

Universidad de Sevilla · Doctoral Thesis

NONLINEAR CONTROL STRATEGIES FOR OUTDOOR AERIAL MANIPULATORS

Carlos Rodríguez de Cos

Directors

Aníbal Ollero Baturone

Catedrático de Universidad

José Ángel Acosta Rodríguez

Profesor Titular de Universidad

Tutor

Aníbal Ollero Baturone

Catedrático de Universidad

Programa de Doctorado en Ingeniería Automática, Electrónica y de Telecomunicación

Escuela Técnica Superior de Ingeniería

2020

Everything changes and nothing stands still.

– Heraclitus of Ephesus

Acknowledgement

First of all, I wish to acknowledge the contribution of my supervisors. José Ángel, your gentle but persuasive guidance, kindness, trust and support has made me a better engineer, without any doubt. Aníbal, you are the researcher we all admire and whose words let us discern what the future is going to look like. I cannot imagine better guides in this adventure.

I would also like to thank *all* the GRVC team for their support and friendliness, especially when the road to this thesis dissertation seemed so uphill. This team feels like a family that you want to be around no matter we are in trouble or celebrating an achievement. I cannot imagine this incredible research group without *any single one* of you.

And finally, I want to express my most sincere gratitude to the ones I love. María, you are my reason to prevail over despair, to work harder and to achieve my goals in the end. The life we share is everything for me. To my family, natural or of adoption, for being an example to follow and for helping me to advance in the right path.

To all of you, thank you.

Abstract

In this thesis, the design, validation and implementation of nonlinear control strategies for aerial manipulators –i.e. aerial robots equipped with manipulators– is studied, with special emphasis on the internal coupling of the system and its resilience against external disturbances. For the first, different decentralised control strategies –i.e. using different control typologies for each one of the subsystems– that indirectly take into account this coupling have been analysed. As a result, a nonlinear strategy composed of two controllers is proposed. A higher priority is given to the manipulation accuracy, relaxing the platform tracking, and hence obtaining a solution improving the manipulation capabilities with the surrounding environment. To validate these results, thorough stability and robustness analyses are provided, both theoretically and in simulation.

On the other hand, a significant effort has been devoted to improving the response and applicability of robot manipulators used in flight via control. In particular, the design of controllers for lightweight flexible manipulators –that reduce the consequences of incidents involving unforeseen contacts– is analysed. Although their inherent nature perfectly fits for aerial manipulation applications, the added flexibility produces unwanted behaviours, such as second-order modes and uncertainties. To cope with them, an adaptable position nonlinear control strategy is proposed. To validate this contribution, the stability of the approach is studied in theory and its capabilities are proven in several experimental scenarios. In these, the robustness of the solution against unforeseen impacts and contact with uncharacterised interfaces is demonstrated.

Subsequently, this strategy has been enriched with –multiaxis– force control capabilities thanks to the inclusion of an outer control loop modifying the manipulator reference. Accordingly, this additional application-focused capability is added to the controlled system without losing the modulated response of the inner-loop position strategy. It is also worth noting that, thanks to the cascade-like nature of the modification, the transition between position and force control modes is inherently smooth and automatic. The stability of this expanded strategy has been theoretically analysed and the results validated in a set of experimental scenarios.

To validate the first nonlinear approach with realistic outdoor simulations before its implementation, a computational fluid dynamics analysis has been performed to obtain an explicit model of the aerodynamic forces and torques applied to the blunt-body of the aerial platform in flight. The results of this study have been compared to the most common alternative nowadays, being highlighted that the proposed model significantly surpasses this option in terms of accuracy. Moreover, it is worth underscoring that this characterisation could be also employed in the future to develop control solutions with enhanced rejection capabilities against wind conditions.

Finally, as the focus of this thesis is on the use of novel control strategies on real aerial manipulation outdoors to improve their accuracy while performing complex tasks, a modular autopilot solution to be able to implement them has been also developed. This general-purpose autopilot allows the implementation of new algorithms, and facilitates their theory-to-experimentation transi-

tion. Taking into account this perspective, the proposed tool employs the simple and widely-known Simulink[®] interface and the highly reliable PX4 autopilot as backup, thus providing a redundant approach to handle unexpected incidents in flight.

Resumen

En esta tesis se ha estudiado el diseño, validación e implementación de estrategias de control no lineales para robots manipuladores aéreos –esto es, robots aéreos equipados con un sistema de manipulación robótica–, dándose especial énfasis a las interacciones internas del sistema y a su resiliencia frente a efectos externos. Para lo primero, se han analizado diferentes estrategias de control descentralizado –es decir, que usan tipologías de control diferentes para cada uno de los subsistemas–, pero que tienen indirectamente en consideración la interacción entre manipulación y vuelo. Como resultado de esta línea, se propone una estrategia de control conformada por dos controladores. Estos se coordinan de tal forma que se le da prioridad a la manipulación sobre el seguimiento de posiciones del vehículo, produciéndose un sistema de control que mejora la precisión de las interacciones entre el sistema manipulador y el entorno. Para validar estos resultados, se ha analizado su estabilidad y robustez tanto teóricamente como mediante simulaciones numéricas.

Por otro lado, se ha buscado mejorar la respuesta y aplicabilidad de los manipuladores que se usan en vuelo mediante su control. Dentro de esta tendencia, la tesis se ha centrado en el diseño de controladores para manipuladores ligeros flexibles, ya que estos permiten reducir el peso del sistema completo y reducen el riesgo de incidentes debidos a contactos inesperados. Sin embargo, la flexibilidad de estos produce comportamientos indeseados durante la operación, como la aparición de modos de segundo orden y cierta incertidumbre en su comportamiento. Para reducir su impacto en la precisión de las tareas de manipulación, se ha desarrollado un controlador no lineal adaptable. Para validar estos resultados, se ha analizado la estabilidad del sistema teóricamente y se han desarrollado una serie de experimentos. En ellos, se ha comprobado su robustez ante impactos inesperados y contactos con elementos no caracterizados.

Posteriormente, esta estrategia para manipuladores flexibles ha sido ampliada al añadir un bucle externo que posibilita el control en fuerzas en varias direcciones. Esto permite, mediante un único controlador, mantener la suave respuesta de la estrategia. Además cabe destacar que, al contar esta estrategia con un diseño en cascade, la transición entre los segmentos de desplazamiento del brazo y de aplicación de fuerzas es fluida y automática. La estabilidad de esta estrategia ampliada ha sido analizada teóricamente y los resultados han sido validados experimentalmente.

Para validar la primera estrategia mediante simulaciones que representen fielmente las condiciones en exteriores antes de su implementación, ha sido necesario realizar un estudio mediante mecánica de fluidos computacional para obtener un modelo explícito de las fuerzas y momentos aerodinámicos a los que se enfrenta la plataforma en vuelo. Los resultados de este estudio han sido comparados con la alternativa más empleada actualmente, mostrándose que los avances del método propuesto son sustanciales. Asimismo, es importante destacar que esta caracterización podría también usarse en el futuro para desarrollar controladores con una respuesta mejorada ante perturbaciones aerodinámicas, como en el caso de volar con viento.

Finalmente, al ser esta una tesis centrada en las estrategias de control novedosas en sistemas reales para la mejora de su rendimiento en misiones complejas, se ha desarrollado un autopiloto modular fácilmente modificable para implementarlas. Este permite validar experimentalmente nuevos algoritmos y facilita la transición entre teoría y práctica. Para ello, esta herramienta se basa en una interfaz sencilla ampliamente conocida por los investigadores de robótica, Simulink®, y cuenta con un autopiloto de respaldo, PX4, para enfrentarse a los incidentes inesperados que pudieran surgir en vuelo.

Contents

Abstract	vii
Resumen	ix
Contents	xi
Abbreviations and acronyms	xv
Notation	xvii
1 Introduction	1
1.1 Context	2
1.2 State of the art	3
1.2.1 Centralised approaches	4
1.2.2 Decentralised approaches	5
1.3 Structure of the thesis	6
1.4 Funding data	7
2 Motivation and contributions	9
2.1 Motivation	10
2.2 Design mission	10
2.3 Research line	12
3 Characterisation of outdoor aerial manipulators	15
3.1 Kinematics and dynamics of the aerial manipulator	16
3.1.1 Multi-rotor platform	16
3.1.2 Robot manipulator	17
3.1.3 Aerial manipulation system	18
3.2 Blunt-body aerodynamics of a multi-rotor UAV	20
3.2.1 Simplified static model	21
3.2.2 Rotatory-wing propulsion model	23
3.2.3 Methodology	25
3.2.4 Explicit aerodynamic model	26
3.2.5 Comparison with constant aerodynamic coefficients model	28
3.2.6 Implementation	30
3.3 Summary of the chapter	33

4	Adaptive position control of lightweight flexible manipulators	35
4.1	Control rationale	36
4.2	Contact model and equivalent manipulator kinematics	37
4.3	Control design	38
4.4	Experimental results	40
4.4.1	Undisturbed scenario	41
4.4.2	Impact scenario	42
4.4.3	Contact scenario	42
4.5	Summary of the chapter	44
5	Adaptive force control of lightweight flexible manipulators	45
5.1	Contact model and equivalent manipulator kinematics	46
5.2	Control design	47
5.3	Experimental results	51
5.3.1	Unperturbed scenario	52
5.3.2	Contact force scenario	53
5.3.3	Mixed scenario	54
5.4	Summary of the chapter	55
6	Robust decentralised control of aerial manipulators	57
6.1	IDA-PBC control rationale	59
6.2	PBC redesign	60
6.3	iCLIK	65
6.4	Cascade nonlinear control strategy	68
6.5	Implementation	68
6.6	Numerical validation	70
6.6.1	Comparison with integral backstepping	71
6.6.2	Collision avoidance	74
6.6.3	Compensation of forces on the EE	75
6.7	Summary of the chapter	76
7	Hardware, software & middleware solutions for aerial robotics	77
7.1	MAS _{PX4} [⊕]	78
7.1.1	Autopilot architecture	80
7.1.2	Experimental validation	85
7.2	Robot manipulator	89
7.2.1	Jormungandr Mk. 1	90
7.2.2	Jormungandr Mk. 2	91
7.3	Summary of the chapter	92
8	Conclusions and future work	93
8.1	Conclusions	94
8.2	Future work	96
8.2.1	Control strategies	96
8.2.2	Novel aerial manipulation applications	97
A	Relative-pose optimisation for decentralised control of aerial manipulators	99
A.1	Optimisation criterion	100
A.2	Recommended poses depending on the environmental conditions	102

B Command-filtered backstepping with RM disturbance rejection capabilities	105
B.1 Command-filtered backstepping rationale	106
B.2 Redesign of the command-filtered backstepping disturbance rejection	108
B.3 Numerical validation	109
List of Figures	113
List of Tables	117
List of Propositions	119
Bibliography	121
Index of terms	133

Abbreviations and acronyms

AM	Aerial manipulator
AMUSE	Aerial manipulator of the University of Seville
AUW	All up weight
BEMT	Blade element momentum theory
BS	Backstepping
BW	Bandwidth
CAC	Constant aerodynamic coefficients model
CAD	Computer-aided design
CFD	Computational fluid dynamics
CLIK	Closed-loop inverse kinematics
CNRS	Centre national de la recherche scientifique
COVID	Coronavirus disease 2019
CPU	Central processing unit
DFC	Differential flatness control
DK	Direct kinematics
DLS	Damped least-squares
DoF	Degree of freedom
DZ	Deadzone
ecl	Estimation and control library
EE	End-effector
EKF	Extended Kalman filter
ERC	European Research Council
EU	European Union
F/T	Force torque
GNSS	Global navigation satellite system
GPIO	General purpose input/output
GPS	Global Positioning System
GPU	Graphics processing unit
GRVC	Grupo de Robótica, Visión y Control
HAC	High-assurance-control
HPC	High-performance-control
IK	Inverse kinematics
I/O	Input/output
iCLIK	Integral closed-loop inverse kinematics
IDA	Interconnection and damping assignment

IoT	Internet of things
JIT	Just-in-time
MAS	Modular autopilot solution
Mk.	Mark
MPC	Model predictive control
MRAC	Model reference adaptive control
NACA	National Advisory Committee for Aeronautics
NED	North, east, down coordinates
PBC	Passivity-based control
PDE	Partial differential equation
PWM	Pulse-width modulation
RAM	Random-access memory
RC	Radio control
RM	Robot manipulator
RMSE	Root-mean-square error
ROS	Robot Operating System
RPM	Revolutions per minute
RTT	Round trip time
SMC	Sliding mode control
SNS	Saturation of the null space
SRAM	Static random-access memory
TN	Technical note
TRL	Technology Readiness Level
UAS	Unmanned aerial system
UAV	Unmanned aerial vehicle
UDP	User datagram protocol
uORB	Micro object request broker
UTM	Unmanned aircraft system traffic management
WiFi	Wireless fidelity
WN	White noise
WP	Waypoint

Notation

In this notation chapter, the general¹ nomenclature and conventions used throughout the thesis are presented. These can be divided into four categories: i) calligraphic symbols, ii) Greek symbols, iii) Latin symbols and iv) general comments.

Calligraphic symbols

\mathcal{B}	Platform body-fixed reference frame.
\mathcal{I}	Inertial reference frame.
\mathcal{R}	Rotation matrix from \mathcal{B} to \mathcal{I} .

Greek symbols

$\bar{\alpha}$	Orientation of the EE, rad.
α_r	Angle of attack of the rotors, rad.
β	Sideslip angle, rad.
γ	Actuated angles of the RM, rad.
γ_h	Climb angle, rad.
δ	Deflection of the flexible joints of the RM, rad.
δ	Flexible deflections of the RM, rad.
δ_r	Airflow deflection angle, rad.
η	Error of the generalised forces applied by the EE, N or N m.
Θ	UAV attitude in Euler angles roll, pitch and yaw, rad.
θ	Pitch angle, rad.
θ_0	Blade pitch angle, rad.
λ	Total inflow ratio.
λ_c	Climb inflow ratio.
λ_i	Induced rotor inflow ratio.
λ_{i0}	Induced rotor inflow ratio in hover.

¹Note that terms defined for a very specific purpose, such as a theoretical demonstrations, are in here omitted to avoid overextending the focus of the notation chapter. Regardless of this omission, these specific symbols are explicitly defined as close as possible to the place in which they are used.

μ_r	Rotor advance ratio.
ρ	Air density, kg m^{-3} .
σ_r	Rotor solidity factor.
τ	Control torques of the UAV in \mathcal{B} , N m.
τ^{aero}	Aerodynamic torques on the UAV in \mathcal{B} , N m.
τ_d	Demanded reaction torque, N m.
τ^{RM}	Control torques of the RM in the joint-space, N m.
ϕ	Roll angle, rad.
ψ	Yaw angle, rad.
ψ_∞	Wind direction angle, rad.
Ω	UAV attitude rates in \mathcal{B} , rad s^{-1}
Ω_r	Rotor angular speed, rad s^{-1} .

Latin symbols

a	Speed of sound, m s^{-1} .
A_r	Area of the actuator disk of the rotors, m^2 .
b_r	Number of rotor blades.
c_r	Blade chord, meter.
C_{L_α}	Blade lift coefficient slope, rad^{-1} .
C_T	Thrust coefficient.
\mathbf{F}	Generalised control input of the AM, N or N m.
\mathbf{F}^{aero}	Aerodynamic forces on the UAV in \mathcal{B} , N.
\mathbf{f}^{EE}	Generalised forces applied by the EE, N or N m.
\mathbf{g}_0	Gravity acceleration vector in \mathcal{I} , m s^{-2} .
h_B	Multi.rotor body height, m.
L	Platform span from rotor hub to opposite rotor hub, m.
\mathbf{m}	RM masses vector, kg.
m_B	Total RM mass, kg.
m_Q	Platform mass, kg.
M	Passive (flexible) DoF of the RM.
M_{tip}	Mach number at the blade tip.
n	Total number of DoF of the AM, including passive ones.
N	Number of actuated DoF of the robot manipulator.
N_r	Number of rotors.
\mathbf{p}	Generalised position of the EE in \mathcal{I} , m.
$\bar{\mathbf{p}}$	Cartesian position of the EE in \mathcal{I} , m.
\mathbf{q}	Generalised coordinates of the AM, m or rad.
\mathbf{q}^{RM}	Joint-space configuration of the RM, rad.
\mathbf{q}^{UAV}	Generalised coordinates of the UAV, m or rad.
R_b	Blade radius, m
\mathbf{s}	Generalised momenta of the AM, kg m s^{-1} or $\text{kg m}^2 \text{rad s}^{-1}$.
S	Total size of the manipulation task-space.
S_α	Size of the orientation task-space of the manipulation system.
S_f	Front area of the UAV for parametrisation of the aerodynamic model, m^2 .
S_p	Size of the position task-space of the manipulation system.
\mathbf{T}	Thrusts of the N_r rotors expressed as a column vector, N.
T	Total thrust of the platform, N.

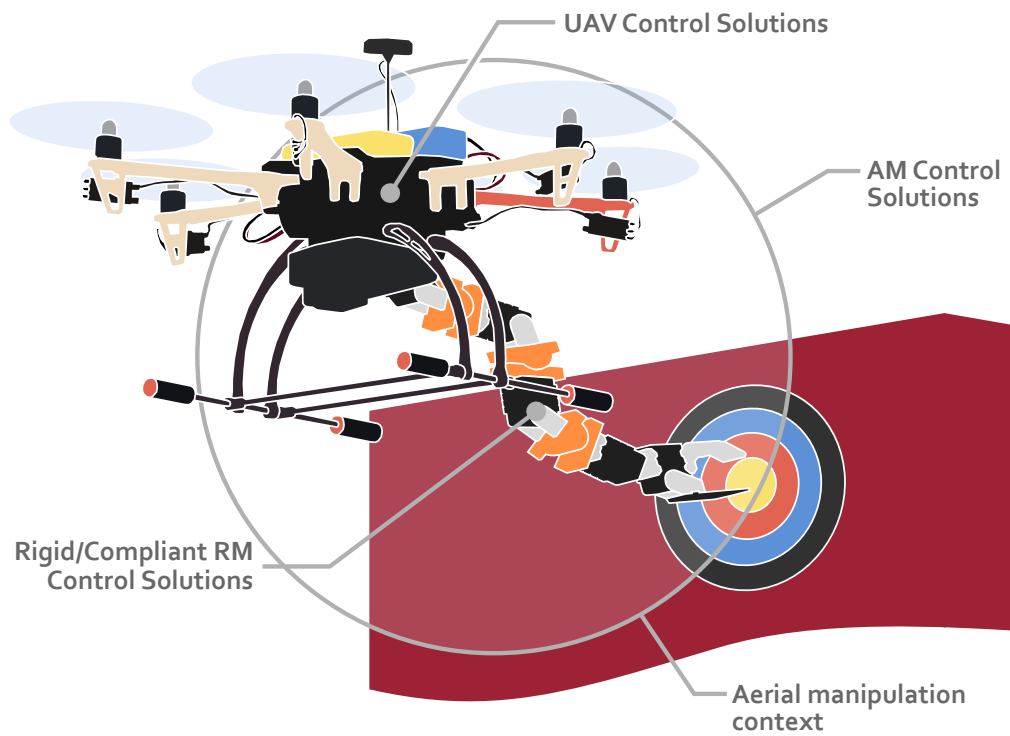
$t_{63\%}$	Time constant of a first-order system, s.
\mathbf{U}	Virtual control force of the UAV in \mathcal{I} , N.
\mathbf{v}	UAV speed in \mathcal{I} , m s^{-1}
v	Airflow total rotor speed, m s^{-1} .
v_c	Climb speed, m s^{-1} .
v_i	Airflow induced rotor speed, m s^{-1} .
v_{i0}	Airflow induced rotor speed in hover, m s^{-1} .
\mathbf{V}_g	Ground velocity, m s^{-1} .
\mathbf{V}_w	Wind velocity, m s^{-1} .
\mathbf{V}_∞	Air velocity, m s^{-1} .
V_∞	airspeed, m s^{-1} .
w_A	Dimension of the platform arm section, m.
w_B	Multi-rotor body width, m.
WF	Weight scale factor.
\mathbf{x}	UAV position in \mathcal{I} , m.

General comments

- All the infographics in this thesis share a common colour pattern: **red** for the robot manipulation, **blue** for the unmanned aerial platform, and **violet** –the result of combining them– for the coupling of these two subsystems.
- Vectors are denoted in bold, in contrast to matrices –regular font weight in capital letters– and scalars –regular font weight as well, but minor case–. The dimensions of these elements is clearly indicated within the text, close to their first use.
- $\mathbf{e}_\mathbf{v}^{\mathcal{A}}$ identifies the unitary vector with direction \mathbf{v} expressed in the frame \mathcal{A} . Accordingly, the unitary vector of direction b belonging to the reference frame \mathcal{A} is denoted $\mathbf{e}_b^{\mathcal{A}}$, e.g. $\mathbf{e}_z^{\mathcal{A}}$ with direction z , and the component of a vectorial variable \mathbf{c} in the axis b is written c_b . For the sake of simplicity, when any equation is fully expressed in the same reference frame, the super-indexes are omitted, e.g. $\mathbf{e}_z = [0 \ 0 \ 1]^T$.
- M^\dagger refers to the Moore-Penrose pseudoinverse of the generic matrix M .
- When writing arrays as arranged expressions, matrix are displayed using parentheses and vectors in brackets.
- The steady-state value of a generic variable $a(t)$ is denoted $a_\infty := a(t \rightarrow \infty)$.
- I_n denotes the identity matrix of size n , $\mathcal{O}_{n \times m}$ the empty matrix of size $n \times m$ (omitting the repetition for square matrices), and \mathcal{O}_n the empty vector of length n .
- Operator $\text{col}(\cdot)$ stands for a column concatenation; and $|\cdot|_P, \|\cdot\|_P$ for vector and matrix norm, respectively, weighted by matrix P .
- While $\text{diag}(\mathbf{v})$ identifies a matrix whose main diagonal is given by the vector \mathbf{v} and whose non-diagonal terms are empty, $\text{diag}(A)$ returns a matrix whose main diagonal coincides with that of A and discards the other elements.
- The Kernel –also named nullspace–, range and rank of any matrix are –in what follows– written as $\ker(\cdot)$, $\text{ran}(\cdot)$ and $\text{rank}(\cdot)$, correspondingly.

Chapter 1

Introduction



Highlights:

- Context of aerial manipulation and its typical applications.
- State of the art of the control of aerial manipulators.
- Structure of the thesis.

1.1 Context

In the last decades, the field of aerial robotics –i.e. *robots that can fly*– has emerged mainly owing to the advance of mechatronics and aerodynamics [1]. The interest on research and development works concerning this technology has increased substantially, as evinced by the number of recent publications in the main robotics journals and conferences [2]. As fully discussed in [3, 4], advances in this field are not only having a significant impact in the research community, but also among other sectors, such as e.g. in [5, 6, 7, 8]. After the initial advances within the defence sector made this technology known to the wide public [2], its popularity¹ has even reached the private sphere, being recreational *drones* common in most developed countries.² The wide range of possible applications of aerial robotics –together with this interest– has led to a significant investment by public and private entities, thus enabling the development of solutions whose focus goes beyond the mere monitoring of the environment. Among these cutting-edge applications, this thesis is focused on aerial manipulation –i.e. unmanned aerial systems equipped with manipulators capable of physically interacting with the environment–, and more specifically on aerial manipulators with multirotor platforms.

This interesting technology combines the 3D range, manoeuvrability and mechanical simplicity of multirotors with the versatility coming from the use of robot manipulators, making tasks such as joint transportation of loads, assembly/disassembly, contact inspection/measurement, grasping, perching, cleaning, capturing other UASs for security reasons, etc. achievable while flying. This is especially useful in those industrial or service applications that are considered hazardous for human operators, either for the proximity of dangerous elements (such as high-voltage lines in [13], as shown in Fig. 1.1c) or for the height at which the operation takes place (as in [12, 14], Figs. 1.1a, 1.1b and 1.1d). Moreover, aerial manipulators can also replace and/or collaborate with human operators in large-scale facilities, such as in [15, 16] –as shown in Figs. 1.1e and 1.1f– or in [13, 17]. Apart from these direct industrial applications, aerial manipulators can be also used for joint transportation of loads [18, 19, 20], collaborative tasks [21], assembly [22, 23], physical interaction with the environment or grabbing objects with a UAV during flight [24, 25, 26, 27], perching on rods or beams to allow UAVs to increase their endurance [24], and lightweight manipulation tasks under severe weight limitations [28, 29, 30, 31, 32].

Although these applications constitute a considerable step forward, some of the challenges of this field are still hindering a generalised implementation of these solutions. Among them, the most relevant for autonomous outdoor applications are:

- The sensitivity of the platform to the coupling with the mission subsystems, both when interacting with its environment or while reconfiguring their relative-pose. The movement of any of these directly affects the stability of the whole system and the accuracy of the manipulation, hence demanding advanced controllers.
- Unlike other mobile manipulation systems, the efficiency and stability of the flight platform is significantly affected by environmental conditions [33, 34] –typically aerodynamic disturbances–, hindering the systematic use of aerial manipulators outdoors. These disturbances can be dominant close to structures –such as walls, ground, ceilings, etc.–, as discussed in [35, 36], or in the presence of wind.
- To avoid limited flight times, the weight of any element onboard must be reduced, being discarded the use of industrial dexterous manipulators to increase the success ratio. Instead, lightweight manipulation systems –usually including flexible modes– are employed. Consequently, controllers with advanced capabilities are required to compensate the lack of hardware robustness via control algorithms.

¹For a detailed analysis of the aerial robotics sectors in the European Union and United States, [9] and [10] are respectively recommended.

²As an example of this tendency, please read specialised newspaper article in [11].



(A) AEROARMS project [12] demonstration, performing inspection tasks in a refinery.



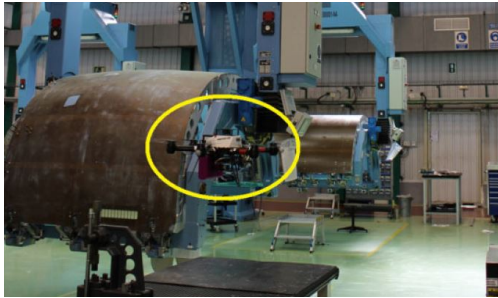
(B) Alexandros dual manipulation system for the AEROARMS project [12].



(C) AM-operator collaboration concept close to a power line in the AERIAL-CORE project [13].



(D) Inspection of bridges in the AEROBI project [14].



(E) Logistic operations in an final assembly line plant in the ARCOW project [15].



(F) Valve tuning task in the ACROSS project [16].

FIGURE 1.1: Some applications of aerial manipulation.

To overcome the limitations associated to these challenges, most integrated solutions tend to be demonstrated in well-conditioned settings –e.g. without significant wind, light conditions maximising the dynamic range of the visual sensors, and adequate GNSS signal– or even indoors. Moreover, the dynamic coupling between the manipulation and transportations systems is generally reduced by design, hence limiting their possible applications.

1.2 State of the art

Once the context of aerial manipulation has been discussed, a succinct state of the art of the applicable control strategies –including robust solutions centred on autonomous platforms and robot manipulators– is in here included. According to the classification in [3], these approaches can be divided –on the base of their control structure– into centralised and decentralised solutions. While

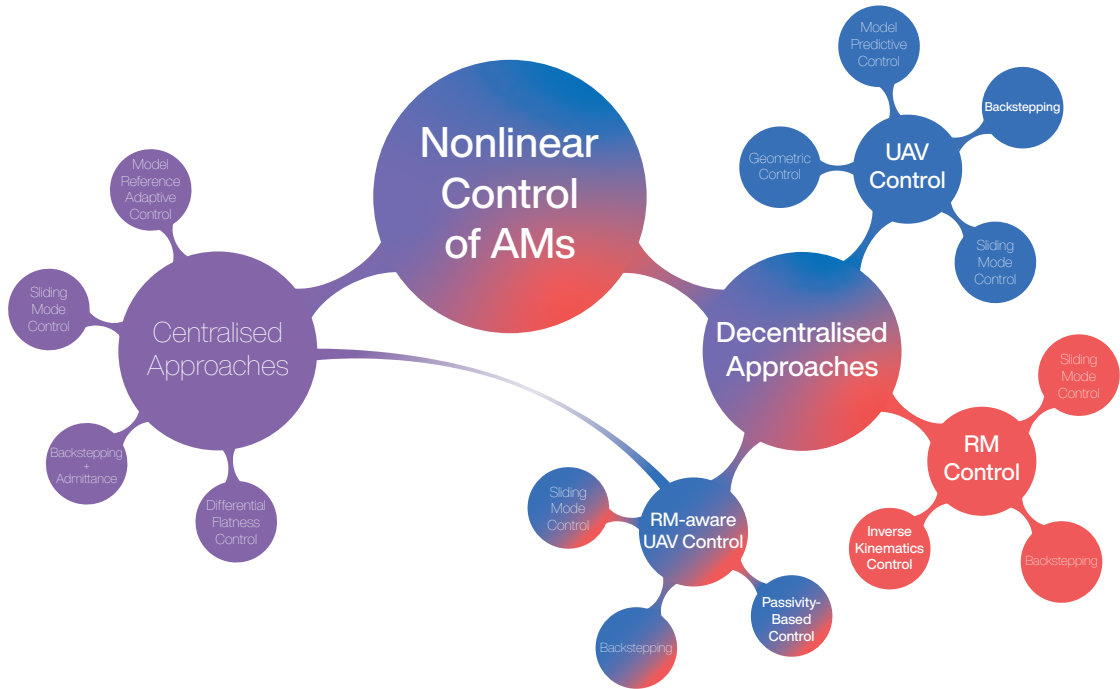


FIGURE 1.2: Concept map with the main trends in what respects to the nonlinear control of aerial manipulators, omitting minor branches –although being mentioned in the body of the text– for simplicity, highlighting the techniques used in this thesis in bold, and using the colour patterns of this thesis: red for RM, blue for UAV, and violet for their coupling in an AM.

the centralised approaches account both the platform and the mission system as a single complex entity, being accordingly controlled; in decentralised solutions these are treated independently, being the coupling either addressed with *ad-hoc* extensions or by enhancing the rejection capabilities of their respective controllers. However, as the main focus of this section is not on a complete survey of these fields, just the most representative approaches (see Fig. 1.2) are discussed.

1.2.1 Centralised approaches

As mentioned above, a single strategy is used to control both the platform and the robot manipulation system in centralised approaches. This results in computationally heavy solutions capable of explicitly handling the coupling of the subsystems. However, this comes at the cost of control specialisation and flexibility. As the platform and robot manipulator are very different in terms of system typology, centralised control solutions –i.e. strategies compatible with the nature of both systems– might not leverage their respective potentials. Moreover, the complexity of these makes theoretical stability analyses significantly more difficult –than decentralised approaches–, and application-focused modifications more involved. Among the current centralised approaches for autonomous aerial manipulation, it is worth highlighting the adaptive SMC in [37]; the complete backstepping strategy in [32, 38, 39]; the backstepping-based approach using a coupled full dynamic model with an admittance controller in [40]; the solution exploiting stable zero dynamics in [41]; the approach combining gain-scheduling and MRAC in [42]; the hierarchical controller with a IK layer in [43]; the impedance-based solution relying wrist sensor feedback and IK in [44]; and the differential flatness-based solution to control AMs tethered by cables [45, 46].

1.2.2 Decentralised approaches

However, this thesis is focused on decentralised approaches –i.e. using different strategies to control the platform and the mission subsystem, either exchanging information between each other or not– due to their reduced computational load and their inherent fitting with the hybrid nature of aerial manipulation systems. These approaches can be divided, in turn, into UAV controllers with disturbance rejection capabilities –but unaware of the manipulation mission–; robust strategies for robot manipulators; and solutions for the control of the platform that are aware of the presence of the manipulation system indirectly –i.e. by a simplified model or estimation–. For instance, a strategy in which the UAV controller is enriched with an adaptive law based on generic disturbances –e.g. constant forces applied to the platform– would be classified in the first category. Nonetheless, this same approach, but being the adaptive add-on focused on the effects of the centre of gravity of the RM on the platform, would be included in the third one. It is also worth noting that RM controllers without moving bases have not been excluded from this state of the art. This is due to the fact that most aerial manipulation applications are designed so that the most accuracy demanding manipulation phases are performed with the platform in hover (or as close as possible). Accordingly, robust manipulation controllers designed for fixed-base implementations but capable of handling oscillations and/or impacts are commonly used in aerial manipulation systems.

UAV control

The most common tendencies for the nonlinear control of autonomous unmanned aerial vehicles [47] are: backstepping techniques, SMC, MPC and geometric control. Backstepping [48], corresponds to a cascade approach where discrepancies between levels are carried out from the inner level to the outer one –in an iterative manner–, until they finally concur at the exterior level, where they are addressed. To cope to the high sensitivity to mistuning and delays of this base backstepping approach, it is usual to reformulate the controller into a command-filtered variant [49], or a command-filtered incremental form [50], hence filtering the interactions between levels. In contrast, SMC is based on shaping the nominal behaviour of the vehicle and applying discontinuous control signals to reject uncertainties. This makes the system slide along the boundaries, as in the incremental SMC with effectiveness loss in actuators in [51], the terminal SMC to reduce the power consumption in [52], or fractional order SMC with a varying mass in [53]. Nonlinear MPC solutions –such as [54]–, on the other hand, take into account future timeslots in the optimisation of the system response via a dynamic model. However, these models tend to be unreliable in aerial manipulation, hence shortening the prediction horizon. For instance, in [55] a robust nonlinear MPC was validated in simulation, being real experiments also performed in [56, 57, 58, 59, 60]. Finally, geometric control avoids problems due to singularities by being formulated in their inherent manifolds, instead of projecting them on a local representation. Subsequently, these control solutions tend to end up having rather compact formulations. Uses of geometric control include, among others, missions demanding high manoeuvrability [61, 62, 63], to cope with configurable tilting rotors [64], to handle their actuation constraints [65] and to avoid obstacles [66].

Additionally, some other solutions not belonging to these trends –or bridging them– are also worth mentioning, such as the linear matrix inequalities approach in [67], the combination of backstepping and sliding mode techniques in [68] and [69], the approach focused on actively rejecting disturbances in [70], the vision-based solution relying on a port Hamiltonian approach in [71], and the solutions based on estimating the external actions to control the platform in [72, 73]. Furthermore, some of the presented techniques can be enriched with adaptive update laws to cope with parametric uncertainties. Nonetheless, this comes on the cost of parametric drift if no robust add-on –such as the σ -modification– is included in the formulation. Among these cases, it is worth highlighting [74] –in which adaptive control is used to cope with thrust saturation–, [75] –coping with attitude saturation–, and [76] –using adaptive incremental nonlinear inversion–.

Control strategies for robot manipulation

The most common approach for manipulation control is the inverse kinematics technique [77]. Among IK solutions, there are, in turn, two main trends: first-order approaches –where the control output is the speed of the servomotors, like in this thesis–, and second-order ones –where this is given as servo accelerations, which can be assimilated to generalised forces–. For instance, first-order solutions include general solutions for redundant manipulators [78, 79], an analysis of the closed-loop stability for redundant systems [80], online approaches to cope with self-imposed joint saturations [81], a general technique to simplify the problem by using a coordinate transformation [82], and approaches for flexible manipulators in which the stiffness of the links is known interacting with a compliant surface –also with known mechanical behaviour–, as in [83, 84].

On the other hand, some second-order solutions are highlighted, such as [85] –where damping is added to the inversion of the Jacobian to handle large control outputs close to singularities– and [86] –which, as happened with some first-order solutions, is focused on redundant manipulators–. Additionally, other control techniques are also used for robot manipulation, such as the adaptive approaches to address uncertainties in [87, 88, 89, 90] (which include backstepping solutions), SMC solutions [91, 92], safe force/impedance compliant controllers [93, 94, 95, 96, 44, 90], and approaches focused on the collision detection rather than in the EE tracking [97, 98].

RM-aware UAV control solutions

Finally, there are solutions for the platform control that include a simplified estimation of the manipulation system to improve their –already robust– behaviour. These constitute a half-way point between centralised and decentralised approaches (as indicated in Fig. 1.2 with a semitransparent link), relaxing the limitations of both. On the one hand, their computational loads are only slightly higher than robust solutions not considering the RM. On the other hand, their RM awareness implies that they avoid choosing behaviours that, due to the configuration of the RM, can lead to oscillatory –if not divergent– regimes. In summary, they can be considered as an evolution of the generic approaches focused on disturbance rejection in which a specific aerial manipulation-focused formulation has been introduced.

Among these solutions, it is worth mentioning the application of the passivity-based control (PBC) concept in aerial robotics, such as in [99, 100]; the solution taking into account the interaction by employing dual quaternions in [101]; the use of an adaptive SMC with super-twisting for a quadrotor with a 2 degree-of-freedom non-redundant manipulator in [102]; the approach employing feedback linearisation with a double integrator to reject parametric uncertainties and external disturbances in [103]; the quaternion-based backstepping approach compensating the disturbances due to the movement of the RM in [104]; the adaptive fuzzy logic approach in [105], capable of achieving acceptable tracking capabilities; and the aerial payload transport with multiple agents considering decentralized strategies by tensegrity muscles in [106].

1.3 Structure of the thesis

To clarify the underlying line of reasoning behind this thesis, it is essential to present its structure. Firstly, Chapter 2 describes the main motivations of the current research line in the context of an aerial manipulation design mission, and briefly presents the most significant contributions obtained during the doctoral studies. Among them, peer-reviewed journal publications are highlighted, but without omitting conference papers and journal contributions yet in the peer-review process. Secondly, Chapter 3 is devoted to the characterisation of the system. It is worth noting that, among the elements discussed in this chapter, there is an explicit blunt-body aerodynamic model of the forces and torques applied to the UAV that constitutes a completely novel tool whose full potential is discussed in Section 2.3.

Then, the major contributions of the thesis are presented in Chapters 4, 5, and 6. On the one hand, in both Chapters 4 and 5 the design of a novel adaptive control strategy for robot manipulation is presented. This new paradigm is proven to be capable of dealing with uncharacterised external conditions ranging from unforeseen impacts –in Chapter 4–, to force control with parametric uncertainties –in Chapter 5–. To validate these strategies, full theoretical and experimental results are reported. On the other hand, Chapter 6 is focused on the study of a complete –but decentralised– aerial manipulation strategy based on prioritising the manipulation task on the cost of the platform tracking capabilities. This is achieved thanks to a passivity-based approach for the control of the platform, obtaining a compliant-like accommodation of this system to the main goal of the mission: the manipulation task. To validate this approach, a theoretical analysis of stability and a set of realistic simulations –including the use of the aerodynamic model in Chapter 3 as a key factor– is included.

Additionally, it is essential to outline the tools and settings used to obtain the experimental results for the adaptive manipulation controllers and other future implementations. This is done in Chapter 7 from the perspective of the hardware, software and middleware solutions employed. Among them, it should be noted that the fast prototyping solution MAS_{PX4}^{\oplus} is also a notable contribution obtained during this thesis.

Finally, the document is wrapped up with the conclusions of the thesis along with some possible future research lines, in Chapter 8. Furthermore, two appendices are added to succinctly include: a criterion to optimise the relative-pose of the platform with respect to the manipulation target according to the control approach in Chapter 6 –in Appendix A–; and the redesign of a command-filtered backstepping UAV controller to enhance its robustness capabilities against significant oscillations of a robot manipulation attached to the platform –in Appendix B–.

1.4 Funding data

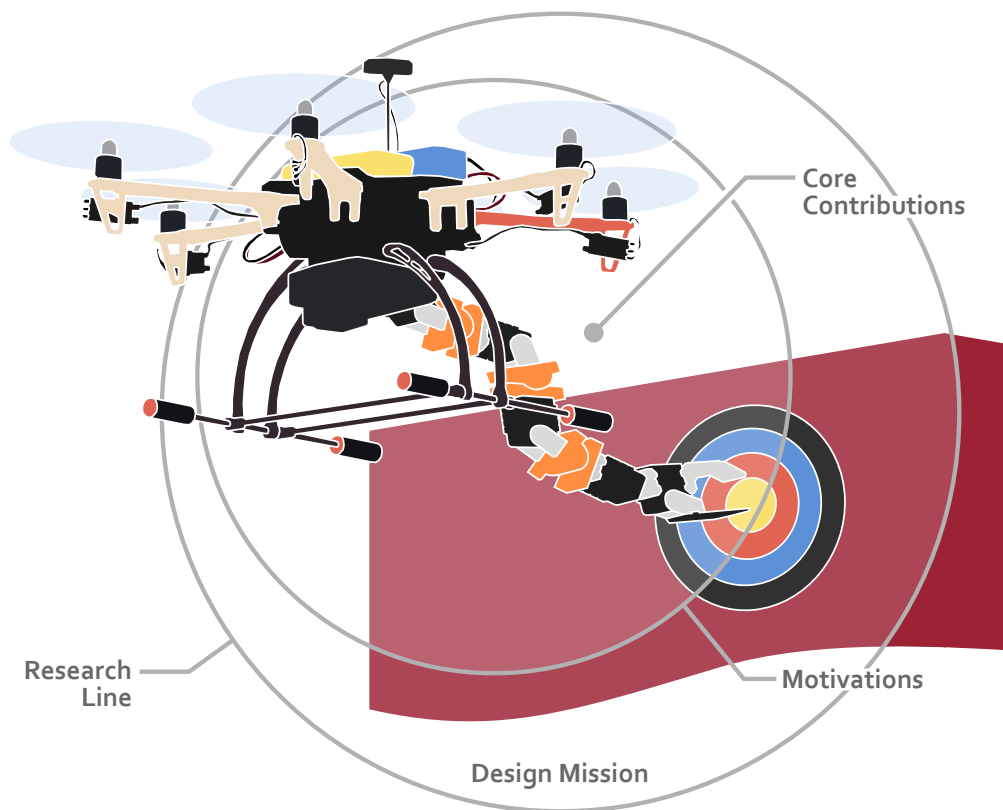
The research activities of the author have been supported by the V Plan Propio de Investigación de la Universidad de Sevilla, under a full-time PIF (Personal Investigador en Formación) fellowship. This includes additional funding for a 4-months-stay with Prof. Tarek Hamel in the I3S group of the Université Côte d’Azur, CNRS (France). Moreover, some of the publications of the thesis have been supported by the following projects of the European Commission and the Spanish Ministerio de Economía, Industria y Competitividad³:

- AEROARMS, from the EU Horizon 2020 Research and Innovation Programme under grant agreement number 644271.
- AERIAL-CORE, from the EU Horizon 2020 Research and Innovation Programme under grant agreement number 871479.
- GRIFFIN ERC Advanced Grant 2017, from the European Research Council under action 788247.
- HYFLIERS, from the EU Horizon 2020 Research and Innovation Programme under grant agreement number 779411.
- ARM-EXTEND, from the Spanish Ministerio de Economía, Industria y Competitividad under grant agreement DPI2017-89790-R.
- AEROMAIN, from the Spanish Ministerio de Economía, Industria y Competitividad under grant agreement DPI2014-59383-C2-1-R.

³The denomination of the Spanish Ministry that conceded the grants for some of these projects has changed since those assignments. For the sake of simplicity, the original name of the Ministry is kept.

Chapter 2

Motivation and contributions



Highlights:

- Motivations behind the research line with respect to a typical aerial manipulation mission.
- Description of the branches of the current research line.
- List of contributions during the PhD.

The main motivations of the current thesis are here presented with respect to the context of aerial robotics in Section 1.1 and a typical aerial manipulation mission. Moreover, the research line followed during this thesis is clearly outlined, being the most significant publications of the author –together with their associated contributions– specifically indicated. It is worth underlining that the ongoing works and future ideas introduced in this chapter are further delineated in Chapter 8.

2.1 Motivation

The promising applications presented in Chapter 1 take place inside unstructured environments –where accurate positioning and state estimation are challenging and disturbances are noticeable–. This implies that the system should be granted a high level of accuracy and repeatability to ensure the safety of the operators, robotic systems and facilities. Moreover, this is even more challenging due to the role of the mission subsystems, i.e. application-focused add-ons attached to the vehicle to perform a specific task. These essential elements –providing real-life application capabilities to otherwise "empty" platforms– tend to add further uncertainty and disturbances to the system. Although some of the latter could be even explicitly calculated using model-reference approaches, the associated computational cost is very significant. Accordingly, aerial manipulation systems undoubtedly benefit from using robust decentralised and explicit nonlinear techniques.

Furthermore, it is also essential to analyse the use of aerial manipulators from a validation perspective. When demonstrating autonomous aerial robotics solutions outdoors –and especially in real industrial environments–, these specific challenges are particularly dominant. To cope with them, the validation experiments are generally accepted to be held either indoors –for lower TRLs or to demonstrate solutions which are not supposed to be significantly affected by outdoor difficulties– or in a well-conditioned outdoor scenario –e.g. with light breezes and acceptable GPS signal–, and the design of prototypes tend to involve reducing the interaction between subsystems. Nonetheless, to make these solutions work on real-world scenarios –where they are being demanded increasingly complex tasks–, it is essential to leave these constraints behind. For that purpose, two main problems should be solved independently:

- i) the estimation of the state variables of the aerial robots from several sources, e.g. using visual odometry or IoT approaches; and
- ii) the development of robust solutions against external –such as wind gusts, or estimation error in GPS-denied zones–, and internal disturbances –for instance, mechanical coupling or opposed goals between subsystems–.

This thesis is focused on the latter.

2.2 Design mission

To contextualise the contributions of this thesis, it is essential to delimit the mission for which these are designed. Among the different possibilities formulated in Section 1.1, a standard benchmark mission for inspection/repair/sensor installation in an industrial facility is proposed (Fig. 2.1). From a general point of view, this mission can be divided into three operational phases:

- P1. *Navigation*, including take-off, landing, payload release and RM-locked flight far from the operation point, all considered relatively low complexity tasks. For this phase, it can be considered that the system is a UAV with a constant disturbance in the form of a fixed arm. Accordingly, the focus of the control strategies for navigation should be in the robust capabilities of the solutions implemented against external disturbances–.
- P2. *Accommodation*, with the RM executing a smooth transition from/to navigation without contact, being this task categorised as medium-high complexity. In contrast to Phase 1, the focus

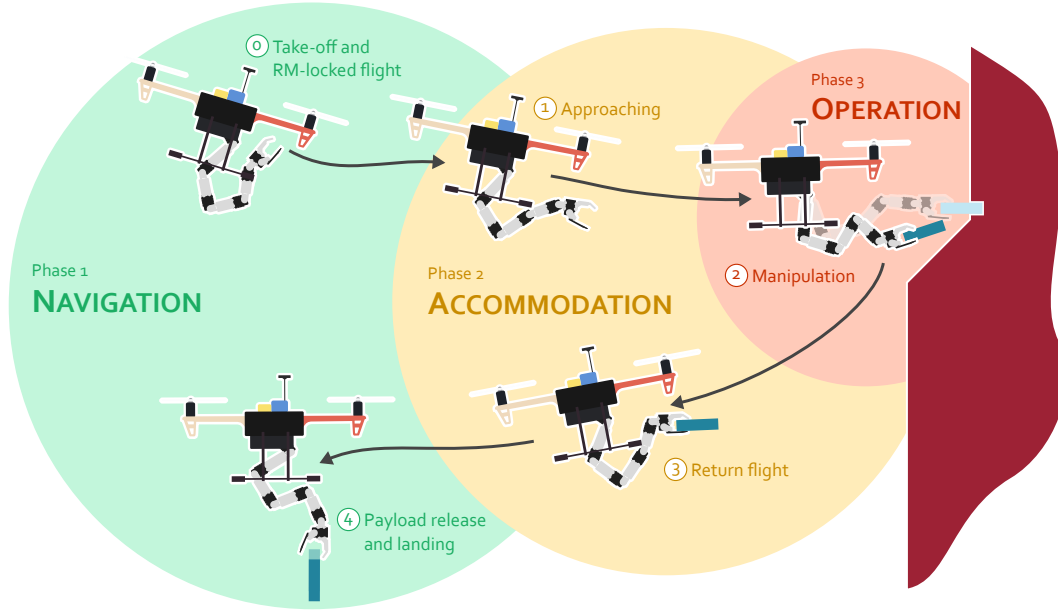


FIGURE 2.1: Phases of an aerial manipulation mission outdoors including interaction tasks with industrial facilities, with colours indicating growing complexity from green to red and being the most relevant tasks enumerated within them.

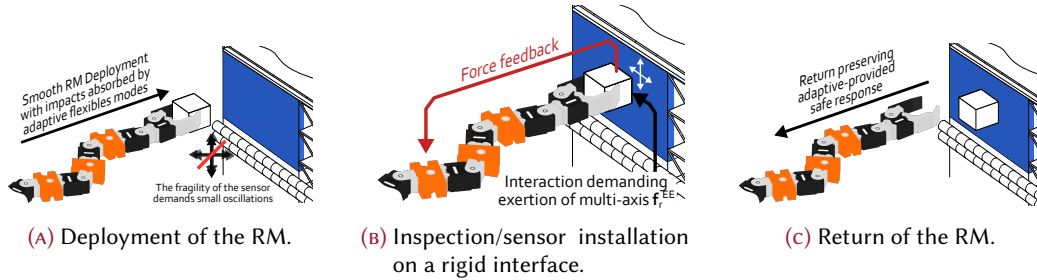


FIGURE 2.2: Steps of the operation phase in the installation of a sensor on a rigid interface or its inspection through contact with force control in several axes.

here should be in the disturbance rejection capabilities against internal disturbances or, alternatively, in shaping these according to a manipulation-aware criterion that improves the stability of the whole system.

- P3. *Operation*, where the focus is set on the force/impedance control of the EE during contact, including gripping and payload grasping, thus involving high complexity tasks. Correspondingly, in this phase the platform is expected to maintain its position or, even more interestingly, to comply with the manipulation tasks.

To further delineate the accommodation and operational phases, in Fig. 2.2 the different steps of within them are detailed. The aerial manipulation system is expected to smoothly deploy the manipulator close to the operation point, perform the dexterous interaction with the target environment –including contact and force/impedance control– and return to the safe position without significant risks that could end up in a flight incident.

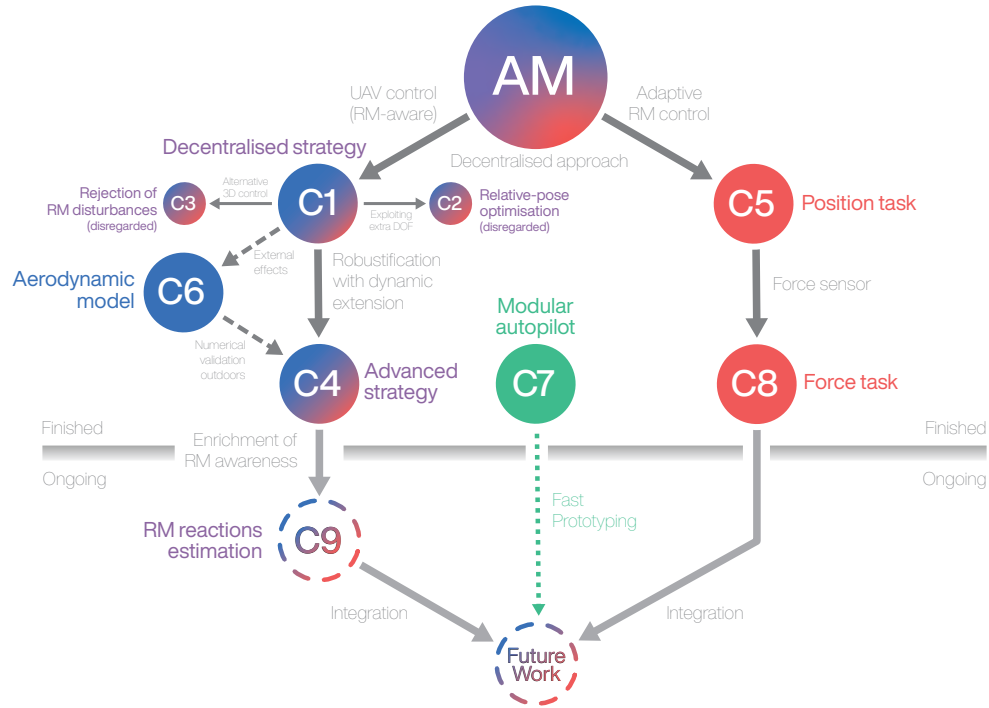


FIGURE 2.3: Schematic depiction of the research line divided into contributions to the manipulation-aware control of UAVs and to the adaptive control of flexible manipulators, with the associated publications labelled according to the list of publications and the ongoing research shown below the line representing the current state.

2.3 Research line

The research line is here presented in terms of two converging research branches –associated to the AM and flexible RM control– and as a detailed chronological list. While the first is focused on introducing the line of reasoning behind the author’s research and highlighting its evolution, the second one offers a detailed account of the publications associated to the thesis.

From a thematic point of view, the end goal of the current research line (see the schematic depiction in Fig. 2.3) is to improve the manipulation capabilities and broaden the range of environmental conditions in which aerial manipulation missions can be performed. For that purpose, two main branches have been studied. On the one hand, significant efforts have been devoted to the development of adaptive nonlinear controllers for flexible lightweight manipulators (see the right ramification in Fig. 2.3). This branch is focused on obtaining solutions capable of handling scenarios with uncertainties –e.g unforeseen impacts and force control against uncharacterised interfaces–, such that the aerial manipulator safely performs complex tasks. On the other hand, control solutions to improve the rejection capabilities of UASs have also been thoroughly studied (see the left branch in Fig. 2.3). These include a decentralised strategy for aerial manipulators that prioritises the manipulation mission on the cost of relaxing the UAV reference tracking, in a compliant manipulation-aware approach. Associated to this idea, the rejection capabilities of the platform ought to be enhanced. For this purpose, an explicit parametric model of the flight aerodynamics of a multirotor –i.e. the external forces applied to the vehicle due to its displacement in a viscous field, indirectly considering the propulsion– is obtained. To connect this approach with the first branch, nonetheless, two additional contributions are essential: i) the modular autopilot solution MAS_{PX4}^{\oplus} , which has been specifically designed for the fast prototyping of novel complex algorithms directly from Simulink[®]; and a geometric estimator of the internal reactions transmitted by the robot manipulator to its platform without using heavy F/T sensors or computation-intensive full model-based calculations.

Moving to a chronological perspective of the research line, a series of core publications¹ are reported:

- [C1] J. Á. Acosta, C. R. de Cos, and A. Ollero, “A Robust Decentralised Strategy for Multi-Task Control of Unmanned Aerial Systems. Application on Underactuated Aerial Manipulator,” in *2016 IEEE International Conference on Unmanned Aircraft Systems (ICUAS)*, Arlington, VA, USA, 2016, pp. 1075–1084.
- [C2] C. R. de Cos, J. Á. Acosta, and A. Ollero, “Relative-pose optimisation for robust and nonlinear control of unmanned aerial manipulator,” in *2017 IEEE International Conference on Unmanned Aircraft Systems (ICUAS)*, Miami, FL, USA, 2017, pp. 999–1005.
- [C3] C. R. de Cos, J. Á. Acosta, and A. Ollero, “Command-filtered backstepping redesign for aerial manipulators under aerodynamic and operational disturbances,” in *Iberian Robotics conference*. Seville, Spain: Springer, 2017, pp. 817–828.
- [C4] J. Á. Acosta, C. R. de Cos, and A. Ollero, “Accurate control of Aerial Manipulators outdoors. A reliable and self-coordinated nonlinear approach,” *Aerospace Science and Technology*, vol. 99, p. 105731, April 2020.
- [C5] C. R. de Cos, J. Á. Acosta, and A. Ollero, “Adaptive Integral Inverse Kinematics Control for Lightweight Compliant Manipulators,” *IEEE Robotics and Automation Letters*, vol. 5, no. 2, pp. 282–289, April 2020.
- [C6] C. R. de Cos and J. Á. Acosta, “Explicit Aerodynamic Model Characterization of a Multirotor Unmanned Aerial Vehicle in Quasi-Steady Flight,” *Journal of Computational and Nonlinear Dynamics*, vol. 15, no. 8, 2020.
- [C7] C. R. De Cos, M. J. Fernandez, P. J. Sanchez-Cuevas, J. Á. Acosta, and A. Ollero, “High-Level Modular Autopilot Solution for Fast Prototyping of Unmanned Aerial Systems,” *IEEE Access*, vol. 8, pp. 223 827–223 836, December 2020.
- [C8] C. R. de Cos, J. Á. Acosta, and A. Ollero, “Adaptive Integral Force Control for Lightweight Flexible Manipulators,” *Preprint submitted to IEEE Robotics and Automation Letters (Under revision) (October 2020)*, 2020.
- [C9] C. R. de Cos, M. D. Hua, J. Á. Acosta, T. Hamel, and A. Ollero, “Nonlinear estimation of the reactions induced by a robot manipulator on an aerial manipulator using distributed sensors,” University of Seville and Université Côte d’Azur, CNRS, Seville, Spain, and Biot, France, Tech. Rep., December 2020.

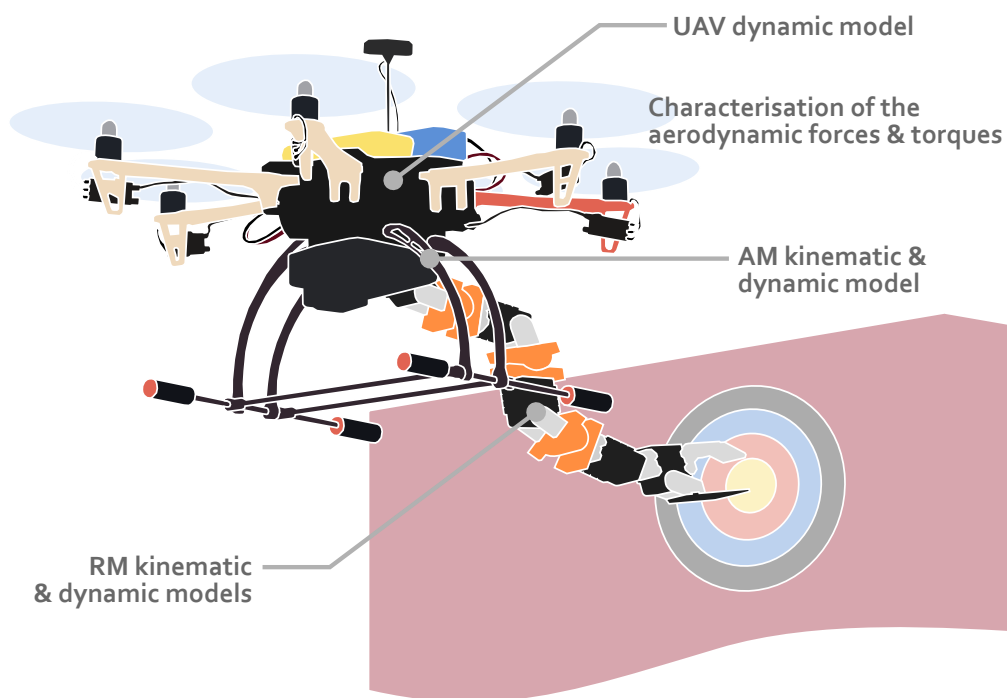
The main contribution from each one of them is here detailed, as well as the chapter in which these are included in the thesis. Firstly, in [C1] (Chapter 6), a control strategy focused on the compliant cooperation of decentralised robust controllers for UAV and RM subsystems via subordinate tasks was presented. As this left an extra degree of freedom associated to the relative-pose between the vehicle and the manipulation system, in [C2] (Appendix A) the author studied the best configurations to improve the performance of the system under external disturbances. Concurrently, the possibility of redesigning a common nonlinear controller for UAVs –a command-filtered backstepping– to enhance its rejection capabilities against RM oscillations was considered in [C3] (Appendix B). The same concept was then applied to the aerial manipulation strategy in [C2], leading to the more advanced approach in [C4] (Chapter 6). This included a robust modification of the manipulation-aware core –dumping the assumption of perfect RM tracking in [C2]– and an in-depth validation of the controller within the design mission in Section 2.2. At the same

¹Please note that when citing these manuscripts, the format [Cn] is used –instead of the standard [n], with n an Arabic numeral– to emphasise their importance and to differentiate them from non-core references.

time, a robust IK solution to reduce the negative impact of introducing flexible modes into lightweight RMs –with special emphasis in unforeseen impacts– was under development, being finally reported in [C5] (Chapter 4). Similarly, the explicit aerodynamic characterisation of the aerodynamic forces and torques applied to the platform in flight in [C6] (Chapter 3) –that had already been used in [C1, C2, C3, C4]– was finally accepted for publication. As a *sine qua non* condition to experimentally validate the results obtained, a highly-customisable autopilot solution based on the Simulink® environment was then developed and tested with real controllers, being its associated results reported in [C7] (Chapter 7). Finally, an extension to force control of the position controller in [C5] in a cascade approach to perform mixed contact/non-contact tasks was submitted in [C8] (Chapter 5). Furthermore, the estimation of the reactions induced by the RM on the aerial platform via lightweight lowcost sensors was studied during the short stay with Prof. Tarek Hamel –I3S group, Université Côte d’Azur, CNRS (France)– leading to the ongoing contribution [C9]. This approach transforming raw data collected from a set of distributed sensors into a theoretically convergent estimator will be reported after the thesis dissertation.

Chapter 3

Characterisation of outdoor aerial manipulators



Highlights:

- Kinematic and dynamic models of the manipulator, the platform and the whole system.
- Novel explicit characterisation of the aerodynamic forces applied to the platform in flight.

As a foundation on which the contributions to the two research branches in Section 2.3 are built, the models of the different systems to be controlled are here presented. For that purpose, several standalone sub-models –corresponding to the adaptive RM control and some UAV control contributions– and an integrated representation –to be used for the manipulation-aware branch– are employed. It is worth mentioning that, although these formulations shown notable structural differences depending on the subsystem, they always share an interconnection bond that comes from the coupling between the platform and the manipulation system. As an interesting addition to these models, a novel explicit characterisation of the flight aerodynamics of UAVs –not to be confused with rotating-wing propulsion aerodynamics– is included to enhance the numerical validation for outdoor aerial manipulation in next chapters.

3.1 Kinematics and dynamics of the aerial manipulator

To represent the system with kinematic and dynamic models, the aerial manipulator is divided into its two main subsystems: the platform and the manipulator. Accordingly, the whole system is presented as a combination of both and the interconnections terms.

3.1.1 Multi-rotor platform

Taking into account that the kinematic configuration of a multirotor is trivial, its dynamic equations flying in a 3D space can be directly written using the Newton-Euler formalism as

$$\dot{\mathbf{x}} = \mathbf{v}, \quad (3.1a)$$

$$\dot{\boldsymbol{\Theta}} = W\boldsymbol{\Omega}, \quad (3.1b)$$

$$m_Q \dot{\mathbf{v}} = m_Q g_0 \mathbf{e}_z^T - T \mathbf{e}_z^B + \mathbf{F}^{aero\mathcal{I}}, \quad (3.1c)$$

$$I_Q \dot{\boldsymbol{\Omega}} = -\boldsymbol{\Omega} \times I_Q \boldsymbol{\Omega} - \mathbf{G}_a + \boldsymbol{\tau}^{aero} + \boldsymbol{\tau} \quad (3.1d)$$

$$I_r \dot{\boldsymbol{\omega}}_r = \boldsymbol{\tau}_r - \mathbf{Q}^{aero}. \quad (3.1e)$$

with the state of the platform given by its position and speed, namely $\mathbf{x}, \mathbf{v} \in \mathbb{R}^3$, attitude and angular rates, denoted respectively $\boldsymbol{\Theta}, \boldsymbol{\Omega} \in \mathbb{R}^3$, and the speed of its rotors $\boldsymbol{\omega}_r \in \mathbb{R}^{N_r}$; and being $T \in \mathbb{R}^+$ the total thrust, $\boldsymbol{\tau} \in \mathbb{R}^3$ the attitude control input, and the aerodynamic model for $\mathbf{F}^{aero}, \boldsymbol{\tau}^{aero} \in \mathbb{R}^3$ discussed in Section 3.2. Moreover, the matrix relating attitude rates and Euler angles derivatives, $W \in \mathbb{R}^{3 \times 3}$, reads

$$W := \begin{pmatrix} -\sin \theta & 0 & 1 \\ \cos \theta \sin \phi & \cos \phi & 0 \\ \cos \theta \cos \phi & -\sin \phi & 0 \end{pmatrix};$$

the UAV and rotor inertias, $I_Q \in \mathbb{R}^{3 \times 3}$ and $I_r \in \mathbb{R}^{N_r \times N_r}$, respectively; and the electric torque transmitted to the rotors and the rotation drag –correspondingly–, $\boldsymbol{\tau}_r, \mathbf{Q}^{aero} \in \mathbb{R}^{N_r}$. Then, by neglecting the gyroscopic terms $\mathbf{G}_a \in \mathbb{R}^3$ and using the rotation matrix from the body frame to its inertial counterpart $\mathcal{R} \in \mathcal{SO}(3)$ reading

$$\mathcal{R} := \begin{pmatrix} \cos \theta \cos \psi & \sin \theta \cos \psi \sin \phi - \sin \psi \cos \phi & \sin \theta \cos \psi \cos \phi + \sin \psi \sin \phi \\ \cos \theta \sin \psi & \sin \theta \sin \psi \sin \phi + \cos \psi \cos \phi & \sin \theta \sin \psi \cos \phi - \cos \psi \sin \phi \\ -\sin \theta & \cos \theta \sin \phi & \cos \theta \cos \phi \end{pmatrix}, \quad (3.2)$$

these equations can be finally expressed in common reference frames (\mathcal{I} for the position dynamics and \mathcal{B} for the attitude one), respectively becoming (3.1c)–(3.1d)

$$m_Q \dot{\mathbf{v}} = m_Q g \mathbf{e}_z - T \mathcal{R} \mathbf{e}_z + \mathcal{R} \mathbf{F}^{aero}, \quad (3.3a)$$

$$I_Q \dot{\Omega} = -\Omega \times I_Q \Omega + \tau^{aero} + \tau. \quad (3.3b)$$

As it is common practice, the rotor dynamics in (3.1e) are considered much faster than its translation and rotation counterparts, hence being neglected in what follows¹. Accordingly, the total thrust and induced torque, T and τ , respectively, are chosen as control inputs for the platform. Associated to this simplification, it should also be highlighted that, depending on the number of rotors and their configuration, the transformation of the chosen control inputs into the thrust commanded to each rotor varies. In here, this control allocation is considered accurate, i.e. the force and torque commands can always be met.

Finally, the characterisation of the aerodynamic effects, i.e. \mathbf{F}^{aero} and τ^{aero} in (3.1c)-(3.1c), is addressed in Section 3.2. These contributions –generally oversimplified in articles focused on control design– are here studied using CFD simulations to improve the robustness of the solution against external disturbances, as e.g. wind. In this analysis, remarkably, the aforementioned transformation between our control inputs and the rotor thrust has some influence on the results, thus being considered.

3.1.2 Robot manipulator

Moving to the manipulation system, two different typologies solely including revolute joints² are considered in this thesis: rigid and flexible robots. In order to reconcile them, a harmonised formulation is proposed.

Rigid manipulators

Let us consider a robot manipulator comprised by N rotation DoF, each one associated to a separate joint actuated by a servomotor. The configuration of this RM can be then either described: i) in the joint-space, by $\gamma \in \mathbb{R}^N$ the angles of the actuated joints; and ii) in the task-space, as $\mathbf{p} := \text{col}(\bar{\mathbf{p}}, \bar{\alpha}) \in \mathbb{R}^S$, with $\bar{\mathbf{p}} \in \mathbb{R}^{S_p}$ and $\bar{\alpha} \in \mathbb{R}^{S_\alpha}$ the Cartesian position and orientation of the EE, respectively. Accordingly, the direct kinematics of the system reads

$$\dot{\mathbf{p}} = J_\gamma \dot{\gamma} = \begin{pmatrix} J_\gamma^t \\ J_\gamma^r \end{pmatrix} \dot{\gamma}, \quad (3.4)$$

where $J_\gamma^t \in \mathbb{R}^{S_p \times N}$ and $J_\gamma^r \in \mathbb{R}^{S_\alpha \times N}$ stand for the Jacobian matrices with respect to the Cartesian DoF –denoted by the super-index t – and to the orientation ones –super-index r –, respectively. Then, by using the Euler-Lagrange formalism, the dynamics of the system becomes

$$B_\gamma \ddot{\gamma} + C_\gamma \dot{\gamma} = \tau^{RM} + \tau_{ext}^{RM} + \mathbf{g}_\gamma,$$

with $B_\gamma, C_\gamma \in \mathbb{R}^{N \times N}$ the inertia and Coriolis terms matrices; $\tau^{RM} \in \mathbb{R}^N$ the servomotor torques; and $\tau_{ext}^{RM} \in \mathbb{R}^N$ the torques produced by the external forces applied to the EE –denoted as $\mathbf{f}_{EE} \in \mathbb{R}^{S_p}$ –, and $\mathbf{g}_\gamma \in \mathbb{R}^N$ the gravitational terms, reading these

$$\begin{aligned} \tau_{ext}^{RM} &:= J_\gamma^t{}^\top \mathbf{f}_{EE}, \\ \mathbf{g}_\gamma &:= J_{B,\gamma}^\top m_B \mathbf{g}_0, \end{aligned}$$

where $J_{B,\gamma} \in \mathbb{R}^{S \times N}$ is the Jacobian of the centre of gravity of the RM, i.e. $\dot{\mathbf{p}}_B := J_{B,\gamma} \dot{\gamma}$.

¹An exception to this consideration is made in Appendix B, where the rotor response is shown in the numerical validation as part of a main contribution of the associated publication.

²In aerial manipulation, prismatic joints are not generally used due to their larger weights and dimensions, thus disagreeing with the low inertia/mass design requirements of flying robots.

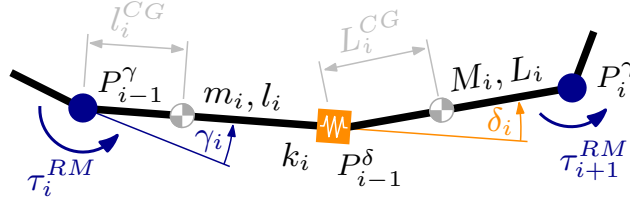


FIGURE 3.1: Definition of the DoF of the flexible manipulator, including the dynamic parameters used.

Flexible manipulators

Let us then modify this rigid formulation by incorporating M flexible rotation DoF in between the actuated ones, as depicted in Fig. 3.1. The configuration of this flexible RM can be, in turn, described: i) in the joint-space, by $\mathbf{q}^{RM} := \text{col}(\boldsymbol{\gamma}, \boldsymbol{\delta}) \in \mathbb{R}^{N+M}$, with $\boldsymbol{\gamma}$ the previously-defined angles of the actuated joints and $\boldsymbol{\delta} \in \mathbb{R}^M$ the flexible link deflections; and ii) in the task-space, with the same form given for rigid manipulators. Hence, the direct kinematics of this system can be written in a block-wise form given by

$$\dot{\mathbf{p}} = J_\gamma \dot{\boldsymbol{\gamma}} + J_\delta \dot{\boldsymbol{\delta}} = \begin{pmatrix} J_\gamma^t & J_\delta^t \\ J_\gamma^r & J_\delta^r \end{pmatrix} \dot{\mathbf{q}}^{RM} = J_{RM} \dot{\mathbf{q}}^{RM}, \quad (3.5)$$

with $J_\delta^t \in \mathbb{R}^{S_p \times M}$, $J_\delta^r \in \mathbb{R}^{S_\alpha \times M}$ the Jacobian matrices of the flexible (passive) modes of the system. Consequently, by using the Euler-Lagrange formalism again, the dynamics of the flexible system can be generically formulated as

$$B_{RM} \ddot{\mathbf{q}}^{RM} + C_{RM} \dot{\mathbf{q}}^{RM} + \nabla V_{RM} = \bar{\boldsymbol{\tau}}^{RM} + \bar{\boldsymbol{\tau}}_{ext}^{RM},$$

with $B_{RM}, C_{RM} \in \mathbb{R}^{(N+M) \times (N+M)}$ the inertia and Coriolis terms matrices of the complete system; $\bar{\boldsymbol{\tau}}^{RM} := \text{col}(\boldsymbol{\tau}^{RM}, \boldsymbol{\varnothing}_M) \in \mathbb{R}^{N+M}$ the control input; $\bar{\boldsymbol{\tau}}_{ext}^{RM} := \text{col}(J_\gamma^{t\top} \mathbf{f}_{EE}, J_\delta^{t\top} \mathbf{f}_{EE}) \in \mathbb{R}^{N+M}$ the external forces applied to the EE; and $\nabla V_{RM} := K \mathbf{q}^{RM} - \mathbf{g}_{RM} \in \mathbb{R}^{N+M}$ the potential terms. The latter includes the flexible modes of the manipulator through the stiffness matrix $K \in \mathbb{R}^{M \times M}$, reading

$$K := \begin{pmatrix} \boldsymbol{\varnothing}_{N \times N} & \boldsymbol{\varnothing}_{N \times M} \\ \boldsymbol{\varnothing}_{M \times N} & K_\delta \end{pmatrix},$$

representing $K_\delta \in \mathbb{R}^{M \times M}$ the stiffness of the passive flexible modes; and the gravitational influence, namely

$$\mathbf{g}_{RM} := J_B^\top m_B \mathbf{g}_0,$$

where $J_B \in \mathbb{R}^{S \times (N+M)}$ stands for the Jacobian of the centre of gravity of the RM, i.e. $\dot{\mathbf{p}}_B := J_B \dot{\mathbf{q}}^{RM}$. Note that, as done with the EE Jacobians, this matrix can be written block-wise as

$$J_B := \begin{pmatrix} J_{B,\gamma} & J_{B,\delta} \end{pmatrix},$$

denoting $J_{B,\delta} \in \mathbb{R}^{S \times M}$ the Jacobian matrix of this point with respect to the flexible modes.

3.1.3 Aerial manipulation system

Taking into account these models, the dynamic formulation of the whole aerial manipulation system is in here studied under the Euler-Lagrange formalism. As done with the RM, the different typologies of the manipulation system result in two models, but with a homogeneous formulation. To obtain this formulation, nonetheless, the coordinates of the system, $\mathbf{q} \in \mathbb{R}^n$, must be classified with respect to

- The division of the aerial manipulator into its vehicle and manipulation subsystems, becoming $\mathbf{q} := \text{col}(\mathbf{q}^{UAV}, \mathbf{q}^{RM})$ –with $\mathbf{q}^{UAV} := \text{col}(\mathbf{x}, \boldsymbol{\Theta})$ the state of the platform and \mathbf{q}^{RM} the join-space configuration of the RM (as already indicated in the Section 3.1.2)–. This approach is used to describe the system dynamics from the point of view of the coupling and to formulate most of the solutions.
- The nature of the DoF, into Cartesian, \mathbf{x} , and angular, $\boldsymbol{\zeta} := \text{col}(\boldsymbol{\Theta}, \mathbf{q}^{RM})$, reading the AM state $\mathbf{q} := \text{col}(\mathbf{x}, \boldsymbol{\zeta})$. In contrast, with this approach the problem can be divided into translations and rotations, thus allowing simpler calculations both in simulation and when implementing the solutions.

Accordingly, consider the direct kinematics of a rigid manipulator (see Section 3.1.2) mounted in an aerial platform, reading

$$\dot{\mathbf{p}} = \underbrace{J_{UAV} \dot{\mathbf{q}}^{UAV}}_{:= -\mathbf{v}_{UAV}} + J_\gamma \dot{\gamma}, \quad (3.6)$$

denoting $J_{UAV} \in \mathbb{R}^{S \times (n-N)}$ the Jacobian matrix associated to the platform position and orientation, and $\mathbf{v}_{UAV} \in \mathbb{R}^S$ the speed of the inertial frame from the point of view of the UAV, i.e. minus the speed of the UAV in the inertial frame. Then, by making use of the Euler-Lagrange formalism, the dynamics of the whole rigid system can be described block-wise as

$$\underbrace{\begin{pmatrix} B_{UAV} & B_\gamma^{UAV} \\ B_\gamma^{UAV} & B_\gamma \end{pmatrix}}_{B(\mathbf{q})} \begin{bmatrix} \ddot{\mathbf{q}}^{UAV} \\ \ddot{\gamma} \end{bmatrix} + \underbrace{\begin{pmatrix} C_{UAV} & C_\gamma^{UAV} \\ C_\gamma^{UAV} & C_\gamma \end{pmatrix}}_{C(\mathbf{q}, \dot{\mathbf{q}})} \begin{bmatrix} \dot{\mathbf{q}}^{UAV} \\ \dot{\gamma} \end{bmatrix} - \underbrace{\begin{bmatrix} \mathbf{g}_{UAV} \\ \mathbf{g}_\gamma \end{bmatrix}}_{\nabla V(\mathbf{q})} = \underbrace{\begin{bmatrix} \mathbf{f}^{UAV} \\ \boldsymbol{\tau}^{RM} \end{bmatrix}}_{\mathbf{u}} + \underbrace{\begin{bmatrix} \mathbf{f}^{aero} \\ \boldsymbol{\tau}_{ext}^{RM} \end{bmatrix}}_{\mathbf{u}_{ext}}$$

with $B, C \in \mathbb{R}^{n \times n}$ the inertia and Coriolis terms matrices of the whole system –with its associated sub-matrices–; ∇V the potential terms –here limited to gravitational contributions, including the one associated to the platform, \mathbf{g}_{UAV} –; $\mathbf{u} \in \mathbb{R}^n$ the control input, where $\mathbf{f}^{UAV} := \text{col}(\mathbf{U}, \boldsymbol{\tau})$ stands for the control input of the UAV –considering the underactuation in \mathbf{U} –; and $\mathbf{u}_{ext} \in \mathbb{R}^n$ the generalised external forces, denoting $\mathbf{f}^{aero} := \text{col}(\mathbf{F}^{aero}, \boldsymbol{\tau}^{aero})$ the external aerodynamic effects on the position and attitude of the platform discussed in the next section.

On the other hand, in the case of using a flexible manipulator, the number of DoF of the system, n , is modified to include the M flexible deflections. Accordingly, the direct kinematics of the system becomes

$$\dot{\mathbf{p}} = \underbrace{J_{UAV} \dot{\mathbf{q}}^{UAV}}_{:= -\mathbf{v}_{UAV}} + J_{RM} \dot{\mathbf{q}}^{RM}, \quad (3.7)$$

with $J_{UAV} \in \mathbb{R}^{S \times (n-N-M)}$, being the new M flexible modes included into n s.t. $n - N - M$ is kept constant with respect to the rigid case. Analogously to the case of rigid manipulators, the result of applying the Euler-Lagrange formalism to obtain the dynamic equations reads

$$\underbrace{\begin{pmatrix} B_{UAV} & B_{RM}^{UAV} \\ B_{RM}^{UAV} & B_{RM} \end{pmatrix}}_{\bar{B}(\mathbf{q})} \begin{bmatrix} \ddot{\mathbf{q}}^{UAV} \\ \ddot{\mathbf{q}}^{RM} \end{bmatrix} + \underbrace{\begin{pmatrix} C_{UAV} & C_{RM}^{UAV} \\ C_{RM}^{UAV} & C_{RM} \end{pmatrix}}_{\bar{C}(\mathbf{q}, \dot{\mathbf{q}})} \begin{bmatrix} \dot{\mathbf{q}}^{UAV} \\ \dot{\mathbf{q}}^{RM} \end{bmatrix} + \underbrace{\begin{bmatrix} -\mathbf{g}_{UAV} \\ \nabla V_{RM} \end{bmatrix}}_{\nabla \bar{V}(\mathbf{q})} = \underbrace{\begin{bmatrix} \mathbf{f}^{UAV} \\ \bar{\boldsymbol{\tau}}^{RM} \end{bmatrix}}_{\bar{\mathbf{u}}} + \underbrace{\begin{bmatrix} \mathbf{f}^{aero} \\ \bar{\boldsymbol{\tau}}_{ext}^{RM} \end{bmatrix}}_{\bar{\mathbf{u}}_{ext}}$$

with $\bar{B}, \bar{C} \in \mathbb{R}^{n \times n}$ the inertia and Coriolis terms matrices of the flexible aerial manipulation system –with its associated sub-matrices–, $\nabla \bar{V}$ the potential terms including the flexible modes, $\bar{\mathbf{u}} \in \mathbb{R}^n$ the complete control input –also underactuated due to the presence of flexible DoF–, and $\bar{\mathbf{u}}_{ext} \in \mathbb{R}^n$ the generalised external forces for this flexible system.

3.2 Blunt-body aerodynamics of a multi-rotor UAV

In both these formulations, the aerodynamic effects are introduced as generic terms to be modelled. It is in order, thus, to analyse the impact of the aerodynamic forces and torques on the dynamics and to propose a model to include them. In this section, two models will be discussed and compared: the well-known constant aerodynamic coefficients model, and the specific approach for multi-rotor UAVs proposed in [C6]. However, before focusing on the modelling, it is essential to put the problem into context.

Multi-rotor UAVs do possess some practical capabilities that are useful for many applications, such as the ones described in Chapter 1. Nonetheless, these come on the cost of a complex nature. Apart from their aforementioned lack of dynamical stability, the aerodynamic field around them is deeply affected by their blunt-body shape (as thoroughly explained in [107]) and the coupling between their propulsive system and the airframe (as analysed in the rotorcraft performance chapters in [108]). This results in the presence of turbulences –i.e. chaotic changes on the fluid motion whose effects have to be studied statistically–, making the accurate dynamic characterisation of the system challenging. This difficulty is, in fact, worsened by the propulsive coupling, as not only does it imply turbulences, but it also results in a *diallelus*: the aerodynamic effects depend on the variations of the fluid field produced by the propulsion and, in turn, the propulsive regime is conditioned by the non-trivial aerodynamic response. To overcome these difficulties, two possible alternatives are considered: i) analysing the system as a whole; or ii) decoupling both problems –by assuming that we are in an equilibrium point– into its propulsion and blunt-body aerodynamic contributions, and then iteratively combining them.

Let us first consider the case of a complete solution. To implement it, a CFD environment must be used, being a preliminary time consumption estimation essential. As the whole fluid dynamics of the UAV is analysed, its rotors –spinning at different speeds– ought to be included. By doing so, however, two of the most important time-saving tools generally used by CFD software have to be discarded: i) the limitation of the fluid field to be contemplated due to the symmetry of the problem, and ii) the consideration of an assimilable time-independent solution. While the first obstacle is trivial due to the non-symmetry of the thrusts, the second should be discussed. In general, rotating blades can be studied in a time-independent manner by using the cylindrical symmetry of the problem, thus choosing a rotating reference frame attached to the blade. For that, accordingly, the contour conditions must respond to that symmetric structure. However, in the case of having more than one rotor the contour conditions are not axisymmetric, hence becoming the solution time-dependant –i.e. needing transient solutions–, and being the mean effects calculated *a posteriori*. Altogether, the CFD simulations must cover all the platform and include transient algorithms, thus demanding important computation times for every single simulation.

Note 1. To illustrate this point, let us use the computation times of a similar problem solved via CFD simulations in the GRVC Robotics Laboratory. This study, focused on the ground effect when flying a multi-rotor over an industrial pipe, demanded about 54 hours to simulate 10 revolutions of the blades at 5600 RPM with a mesh of $2.6 \cdot 10^6$ elements. For the sake of completeness, we should clarify that the computer used to obtain these CFD results mounted an Intel® Xeon® CPU E5-2620 v4 at 2.10 GHz with 32 threads, 128 GB of RAM and an NVIDIA Quadro GPU.

However, the study of this problem does not only involve a single simulation but a batch of them. Therefore, the time to obtain an accurate model depends on the numbers of simulations considered. To determine a significant sample for this problem, we ought to identify the degrees of freedom of the problem and try to reduce their number by using Buckingham II theorem [109]. As a result, a minimal representation of the model to avoid unnecessary simulations is obtained, with $N_r + 2$ parameters (two orientations –not considering the effects of the roll angle– and N_r rotor speeds). Nonetheless, the total simulation time needed to complete this analysis would still be excessive even by assuming a relatively small number of configurations per parameter.

Moving back to the second option, two decoupled solutions must be obtained, together with a proper methodology for their posterior combination. For the propulsion problem, the author opts for a simplistic Blade Element Momentum Theory (BEMT) approach. By simply deriving the equations of this formulation, the relation between thrust, rotation speed and induced speed is calculated from the flight conditions within milliseconds. Then, for the blunt-body aerodynamics, this information is used to obtain the contour conditions for the CFD simulations. Moreover, as no rotating parts are included in this numerical analysis, a time-invariant solution can be used, with the subsequent simulation time reduction. Definitely, the accuracy of this second approach is discussed. As indicated in [110, 111], the coupled BEMT-CFD estimations are not significantly different from the results of integrated CFD simulations, thus confirming the second alternative as the research paradigm.

However, before obtaining the aforementioned contour conditions to run the CFD simulations, some lessons from a preliminary study [112] can be learned. First of all, the need for a cross-validation analysis to assure the concurrence of the results and to prevent counter-intuitive behaviours for extrapolated results. Secondly, some simplifications are needed to obtain a solid model and to reduce the time of simulation up to 45 minutes:³

- S1. The platform dynamics are considered quasi-steady to allow the calculation of the propulsion conditions as a function of the flight conditions. To do so, the rotor speeds are chosen so that the rotor thrusts compensate both the external torques and forces. Additionally, neither the propulsion forces components in the plane of rotation nor the UAV rotations are considered.
- S2. The effects of external contour conditions, such as ground or ceiling effects, are not considering for this section.⁴ This is due to the need for additional degrees of freedom to include them and their limited impact on what is intended to be a general-purpose solution. Additionally, yaw torques are neglected for the propulsion equilibria, i.e. the yaw components of all the rotors are already compensated.
- S3. As usually done in CFD, a delimitation of the studied fluid field is essential. In this case, the control volume is a cube ensuring that each element of the vehicle is at least 5 times the platform span away from the nearest face of the cube. Accordingly, the contour conditions are applied with inlet/outlet surfaces to assure the conservation of the airflow.
- S4. Finally, sharp elements –such as corners– have been either simplified or softened to limit the size of the CFD mesh (see Fig.3.2). Although this assumption can be questionable, the associated reduction of the simulation time is completely essential to carry out the batch of simulations within the time scope devoted to this model in the thesis.

3.2.1 Simplified static model

Before addressing the decoupled models, it is worth analysing the quasi-steady flight conditions of the UAV. To do so, a formulation of the static equilibrium equations directly derived from (3.3a)-(3.3b) is used, namely

$$m_Q g \mathbf{e}_z + \mathcal{R} \mathbf{F}^{aero} - T \mathcal{R} \mathbf{e}_z = \mathbf{0}, \quad (3.8a)$$

$$\boldsymbol{\tau}^{aero} + D \mathbf{T} = \mathbf{0}, \quad (3.8b)$$

with $D \in \mathbb{R}^{3 \times N_r}$ the matrix that transforms the thrusts of the N_r rotors into the generalised torques expressed in the body reference frame. Using the form of the rotation matrix in (3.2), a

³ According to the author's experience in [112], 45 minutes is enough to achieve the desired degree of convergence.

⁴ For those interested in aerodynamic effects close to surfaces, [36] –a thesis dedicated mainly dedicated to these effects– is highly recommended.

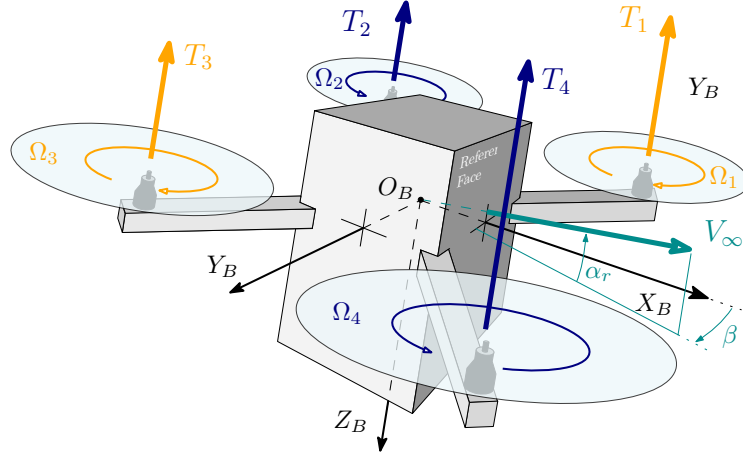


FIGURE 3.2: Characterisation of the studied multi-rotor reference frame, highlighting the reference face – chosen *a priori* for consistency –, the rotor enumeration order and the rotation direction criteria.

succinct formulation of (3.8a) is obtained, namely

$$\begin{bmatrix} 0 \\ 0 \\ T \end{bmatrix} = m_Q g \begin{bmatrix} -\sin \theta \\ \cos \theta \sin \phi \\ \cos \theta \cos \phi \end{bmatrix} + \mathbf{F}^{aero},$$

thus becoming the attitude and thrust references that counterbalance the aerodynamic forces

$$\sin \theta = \frac{F_x^{aero}}{m_Q g}, \quad (3.9a)$$

$$\sin \phi = -\frac{F_y^{aero}}{m_Q g \cos \theta}, \quad (3.9b)$$

$$T = m_Q g \cos \theta \cos \phi + F_z^{aero}. \quad (3.9c)$$

Nonetheless, these forces depend on the air velocity, defined as $\mathbf{V}_\infty := \mathbf{V}_g - \mathbf{V}_w$, thus coupling the aerodynamic model and the attitude of the UAV. To solve this, an iterative approach –which will be discussed in detail in Subsection 3.2.3– is proposed: for each wind condition defined in \mathcal{I} –i.e. as measured in the real world–, the aerodynamic disturbances are obtained for an initial attitude; then, a stable attitude reference is obtained, thus closing the loop. However, to use this solution, an explicit form of the air velocity in both the body and the inertial reference frames is needed. For that purpose, the relation between their respective directions is written as $\mathbf{e}_{\mathbf{V}_\infty}^{\mathcal{I}} = \mathcal{R} \mathbf{e}_{\mathbf{V}_\infty}^{\mathcal{B}}$, being

$$\begin{aligned} \mathbf{e}_{\mathbf{V}_\infty}^{\mathcal{I}} &= \begin{bmatrix} \cos \psi_\infty \cos \gamma_h & \sin \psi_\infty \cos \gamma_h & -\sin \gamma_h \end{bmatrix}^\top, \\ \mathbf{e}_{\mathbf{V}_\infty}^{\mathcal{B}} &= \begin{bmatrix} \cos \beta \cos \alpha_r & \sin \beta \cos \alpha_r & -\sin \alpha_r \end{bmatrix}^\top. \end{aligned}$$

Having this approach provided a solution to counteract the aerodynamic forces, the cancellation of the aerodynamic torques becomes trivial. Using (3.8) and that the total thrust, T , is the sum of the rotor thrusts, these can be obtained for a general number of rotors with

$$\mathbf{T} = \begin{pmatrix} D & & \\ 1 & \cdots & 1 \end{pmatrix}^\dagger \begin{bmatrix} -\boldsymbol{\tau}^{aero} \\ T \end{bmatrix}, \quad (3.10)$$

where –in a general case with $N_r > 4$ –, there would be a kernel associated with the pseudoinverse of this extended matrix, thus allowing us to shape the distribution of thrust among the rotors.

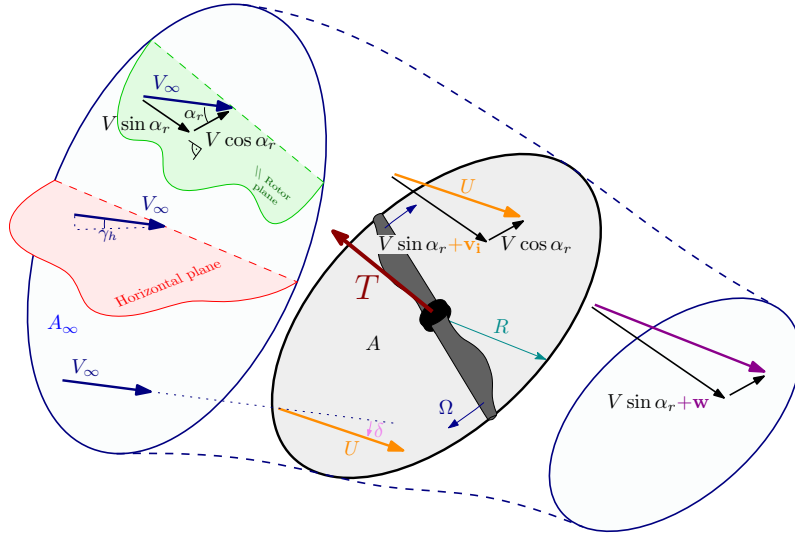


FIGURE 3.3: BEMT actuator disk model of the propulsion system, highlighting the streamtube with its associated far upstream (inlet) and far downstream (outlet) disks of the Glauert's flow model [113].

3.2.2 Rotatory-wing propulsion model

Once the rotor thrusts are obtained, the airflow rotor speeds and the rotor angular speeds should be determined to provide accurate contour conditions for the CFD simulations –with the first ones–, and to set apart unachievable flight conditions from the region of study –using both speeds–. With that purpose in mind, a mixed approach is proposed: i) forward flight and ascent are modelled with a simplistic formulation based on BEMT, while ii) axial descent is incorporated through a continuous empirical regression curve formulated dimensionless-wise. Consequently, the resulting propulsion model covers most of flight conditions without increasing its complexity, thus indirectly enriching the aerodynamic characterisation of the platform.

Firstly, for the simplified BEMT formulation, the well-known actuator disk technique [108, 114] is used. This consists in representing the rotor as a permeable disk through which the air flows with continuous speeds and discontinuous pressures. Accordingly, the streamtube passing over the perimeter of the disk is chosen as the lateral boundary of the control volume, while far upstream and far downstream disks are used as the inlet and outlet for the airflow, respectively, as depicted in Fig. 3.3. Then, applying the conservation of mass, momentum and energy in this control volume leads to the estimation of the disk load given by

$$\frac{T_k}{A_r} = 2\rho v_{ik} \sqrt{(V_\infty \sin \alpha_r + v_{ik})^2 + (V_\infty \cos \alpha_r)^2} \quad (3.11)$$

where the sub-index k refers to the k^{th} rotor values. This equation can be straightforwardly transformed into a quartic in the airflow induced rotor speed given by

$$v_{ik}^4 + 2V_\infty \sin \alpha_r v_{ik}^3 + V_\infty^2 v_{ik}^2 - \left(\frac{T_k}{2\rho A_r} \right)^2 = 0, \quad (3.12)$$

whose real positive root is the parameter needed to calculate the speeds on the actuator disks, the propulsion contour conditions for the CFD simulations.

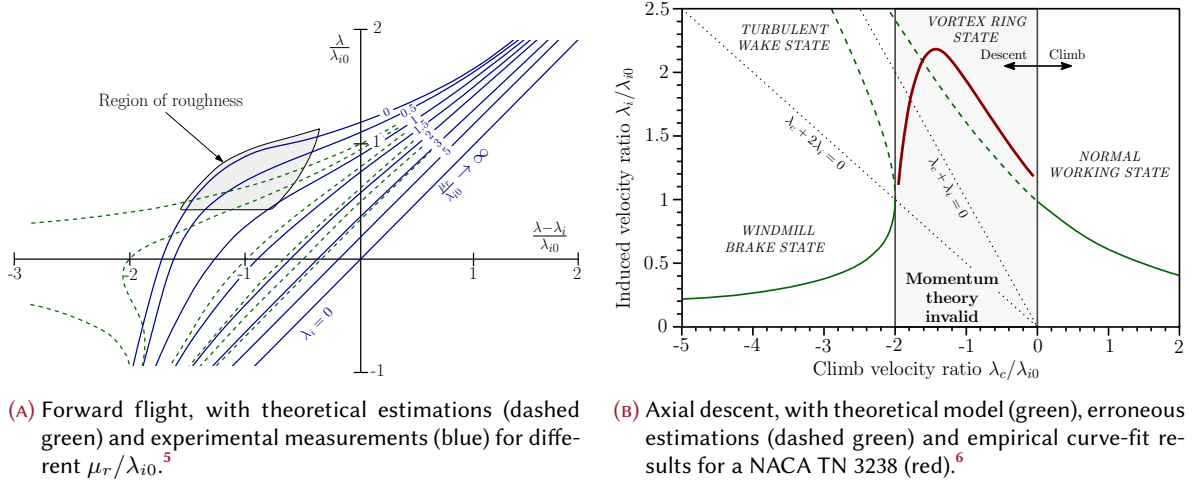


FIGURE 3.4: Deviations of the BEMT in forward flight and axial descent.

Remark 3.1. The quartic in (3.12) is solved using Ferrari's method [115], consistently leading to the following distribution of roots for the complete region under study: two complex roots –which are not of interest in this analysis–, a negative solution –that disagrees with the formulation and, thus, is considered a merely mathematical solution without physical meaning–, and a positive root. The later is used to evaluate (3.11), being in all cases the conditions in this equation met. Consequently, the algorithm used is validated practically, not being within the scope of this thesis the demonstration of the general validity of this approach.

However, the actuator disk approach presents significant estimation deviations for certain flight regimes. To identify these, three parameters are studied: i) the rate between the rotor advance ratio and airflow induced rotor speed in hover, $\mu_r/\lambda_{i0} = V_\infty \cos \alpha_r/v_{i0}$; ii) the climb velocity ratio in axial descend flight, $\lambda_c/\lambda_{i0} = v_c/v_{i0}$; and iii) the blade tip Mach number, $M_{tip} = \Omega R_b/a$. The first, associated to estimation issues when studying forward flight with descent –i.e. $\gamma_h \in (-\pi/2, 0)$ –, indicates significant deviations when $\mu_r/\lambda_{i0} < 1$ (see Fig. 3.4a), as deeply studied in [116]. Nonetheless, this limitation is considered too strict for the studied problem and, thus, it is relaxed to $\mu_r/\lambda_{i0} > 0.7$, as discussed in Remark 3.2.

Remark 3.2. Initially, the theoretical value was directly applied in a preliminary study, being it found to significantly reduce the regimes covered by the subsequent CFD simulations. Accordingly, this requisite for forward flight with descent was relaxed as a trade-off solution to improve the simulation sample on the cost of slightly reducing the accuracy of the contour conditions for these regimes.

Secondly, the parameter λ_c/λ_{i0} is used to identify flight configurations within the well-known vortex ring state inconsistency of the BEMT for axial descent flight, as depicted in Fig. 3.4b. This deviation results from the dominance of turbulent airflow recirculation for intermediate descend speeds, thus reducing rotor efficiency and invalidating the control volume chosen for BEMT, as thoroughly explained in [116]. Accordingly, a curve-fitting solution [117] is generally used to solve this issue in simplistic problems, such as the one studied in this section, namely

$$\frac{v}{v_{i0}} = 1.15 - 1.125 \left(\frac{v_c}{v_{i0}} \right) - 1.372 \left(\frac{v_c}{v_{i0}} \right)^2 - 1.718 \left(\frac{v_c}{v_{i0}} \right)^3 - 0.655 \left(\frac{v_c}{v_{i0}} \right)^4. \quad (3.13)$$

⁵Source: vectorised and coloured from [116, p. 130].

⁶Source: vectorised and coloured from [117, p. 88].

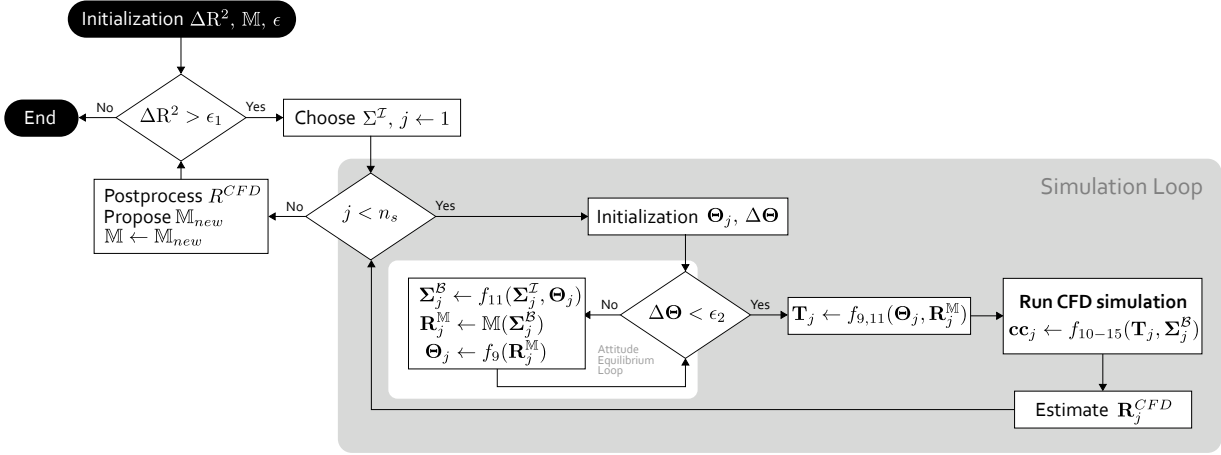


FIGURE 3.5: Recursive methodology to obtain the blunt-body aerodynamic model of a multi-rotor UAV, where f_{eq1}, \dots, eq_n denotes the use of the equations in the sub-index –e.g. if $f_{8,11-13}$ is indicated in within a step, the equations (3.8), (3.11)–(3.13) are needed for that particular step– and the particular nomenclature used for this methodology is defined in the associated text.

Finally, it is also worth studying the blade tip Mach number due to the impact of air compressibility on the foundations of the BEMT: the conservation of mass, momentum and energy. As these are formulated –for the sake of simplicity– using the incompressible fluid hypothesis, high Mach numbers could invalidate the results. Moreover, this parameter is also used to disqualify excessively fast rotation speeds that would not be possible for a lightweight rotor such as the used in aerial robotics. Considering these two goals, a limitation of $M_{tip} < 0.55$ is imposed. Nonetheless, as this parameter cannot be directly obtained from the previously presented formulation, its extension is in order. For that purpose, we will make use of the blade element theory within the BEMT. By supposing that the rotor blades are rectangular and that their twist is constant [108, 114], the thrust coefficient becomes

$$C_{T_k} = \frac{\sigma_r C_{L_\alpha}}{2} \left(\frac{\theta_0}{3} \left(1 + \frac{3}{2} \mu_r^2 \right) - \frac{\lambda_k}{2} \right), \quad (3.14)$$

which, by multiplying by $\Omega_k^2 > 0$, can be rewritten as

$$\Omega_k^2 - \frac{3v_k}{2R_b\theta_0} \Omega_k + \frac{3}{2} \left(\frac{V_\infty \cos \alpha_r}{R_b} \right)^2 - \frac{6T_k}{\rho A_r R_b^2 \sigma_r C_{L_\alpha} \theta_0} = 0. \quad (3.15)$$

Then, the positive root of this second order equation correspond to the rotation speeds, Ω_k , and the associated Mach numbers are finally obtained from $M_{tip} := \Omega_k R_b / a$. It is also worth noting that, in the case of vortex ring state, (3.15) still holds particularising $T_k = T/4$ and $\alpha_r = -\pi/2$.

3.2.3 Methodology

The approach chosen is based on decoupling the propulsion and blunt-body aerodynamics problems and then iteratively coupling them. However, this inner loop only provides the solution for a certain configuration, being a significant sample of these flight conditions essential to enrich the aerodynamic results. After updating the associated model, the same flight conditions can be evaluated again to further improve the results, thus refining the solution until an *accurate* solution is obtained. This recursive methodology is thoroughly explained in this section, being recommended to follow its detailed explanation the use of Fig. 3.5.

Firstly, an initialisation of the coefficient of determination of the batch of results, ΔR^2 , the convergence criteria, $\epsilon := (\epsilon_1; \epsilon_2)$, and the aerodynamic model, \mathbb{M} , is in order. For the latter, a simplistic aerodynamic formulation, the well-known constant-coefficient solution, is chosen. Then, considering the limitations of the aforementioned BEMT formulation, a preliminary set of n_s simulation points in the inertial frame, Σ^I , is selected. Afterwards, this set of simulation conditions is transformed into the body frame, Σ^B , which is used to write the aerodynamic model. However, for each simulation condition, here denoted by the index j , this transformation depends on the platform attitude, Θ_j , and the aerodynamic perturbations estimation, \mathbf{R}_j^M , thus demanding an inner loop. With the resulting conditions, in turn, the rotor thrusts, \mathbf{T}_j , are then calculated, leading to the estimation of the complete contour conditions for the CFD simulations, \mathbf{cc}_j .

Their implementation, nonetheless, demands the use of both CATIA® V5R19 –the standard CAD software tool in aerospace applications– and Autodesk® Simulation CFD 2015 –a reliable CFD tool with favourable license terms for students–. The first is used to include the UAV dimensions and platform attitude with respect to wind, easily exporting this geometry to the second. In this, in turn, the CFD simulations are performed, being the propulsion-related contour conditions applied beforehand. The force and torque estimations of these (which are also obtained after an internal iterative algorithm) are finally stored as \mathbf{R}_j^{CFD} . After collecting data from the n_s simulations to form a simulation set, post-processing is needed to identify a new model that fits better the results, namely \mathbb{M}_{new} . For that purpose, an extensive study of possible support functions under cross-validation considerations is conducted using the Curve Fitting tool of MATLAB® [118], being the optimisation criterion the aforementioned coefficient of determination. Moreover, these results are also employed to modify the set of simulations so that the sample for the iteration of the model is as dimensionlessly diverse and representative as possible.

Finally, the method concludes when the improvements in terms of coefficient of determination are below the criterion ϵ_1 . In the case studied, for instance, after 3 iterations of the aerodynamic model –with $n_s = 150$ – the results were so close to $R^2 = 1$ that the final convergence was assumed (see Table 3.3), resulting in the *accurate* aerodynamic model presented below.

3.2.4 Explicit aerodynamic model

Using the proposed methodology for the aerial platform described in Table 3.1, an *explicit* aerodynamic model in quasi-steady flight conditions is obtained. For the sake of clarity, this model is divided into two sub-models: one for the aerodynamic forces and another one for aerodynamic torques –where their vertical contributions are neglected, as previously explained in depth–. Associated to the support functionals of these two sub-models –which can be initially generalised for similar platforms, as later discussed–, a set of parameters is proposed, being its particularisation for the studied platform shown in Table 3.2.

Mass, kg	Length, m						Surface, m ²	Angle, rad	Dimensionless parameters		
m	L	R_b	w_B	h_B	w_A	c_r	S_f	θ_0	N_r	b_r	C_{L_α}
9.5	0.550	0.203	0.225	0.400	0.020	0.025	0.100	0.141	4	4	5.7

TABLE 3.1: Simulated multi-rotor parameters, corresponding to the AMUSE platform used in the early stages of the AEROARMS project [119].

K_{xy}	K_h		K_z					K_m		
K_1	K_2	K_3	K_4	K_5	K_6	K_7	K_8	K_9	K_{10}	K_{11}
−1.490	52.55	75.50	7.500	8.053	1.218	−2.300	0.286	1.610	0.340	0.540

TABLE 3.2: Parameters of the final blunt-body aerodynamics model for the platform (see Table 3.1).

Aerodynamic forces

The proposed aerodynamic forces sub-model resulting from this study can be expressed in the body reference frame as

$$\frac{\mathbf{F}^{aero}}{\frac{1}{2}\rho S_f} = \underbrace{\begin{pmatrix} \Phi_{xy}(\alpha_r, \beta, V_\infty) & \mathcal{O}_{2 \times 3} \\ 0 & \Phi_z(\alpha_r, \beta, V_\infty) \end{pmatrix}}_{\text{Aerodynamic drag}} \underbrace{\begin{bmatrix} K_{xy} \\ \mathbf{K}_z \end{bmatrix}}_{\text{Varying support functionals}} + \underbrace{\begin{bmatrix} \mathcal{O}_2 \\ K_h \end{bmatrix}}_{\text{Thrust losses}}, \quad (3.16)$$

where the formulation is divided into: an aerodynamic drag contribution –dependant on a series of varying support functionals, similarly to the classic aerodynamic coefficients model–; and the thrust losses –not yet considered in any aerodynamic model for multi-rotor UAVs, to the best of the author’s knowledge–. The support functionals for this model read

$$\begin{aligned} \Phi_{xy}(\alpha_r, \beta, V_\infty) &= \left(1 - \left(\frac{\alpha_r}{\pi/2}\right)^4\right) V_\infty^2 \begin{bmatrix} \cos \beta \\ \sin \beta \end{bmatrix}, \\ \Phi_z(\alpha_r, \beta, V_\infty) &= \sin \alpha_r \begin{bmatrix} V_\infty & V_\infty^2 & V_\infty^2 |\cos 2\beta| \end{bmatrix}, \end{aligned}$$

and the aerodynamic parameters (see Table 3.2) for the force sub-model are given by

$$\begin{aligned} K_{xy} &= K_1, \\ K_h &= \begin{cases} K_3 & \Sigma^{\mathcal{I}} \in \text{axial descend} \\ K_2 & \text{otherwise} \end{cases}, \\ \mathbf{K}_z &= \begin{cases} [K_5 \ K_7 \ 0]^\top & \Sigma^{\mathcal{I}} \in \text{axial descend} \\ [K_4 \ K_6 \ K_8]^\top & \text{otherwise} \end{cases}. \end{aligned}$$

It is worth noting that, among the vertical forces model, some parameters can be interpreted as follows: K_6, K_7 can be seen as aerodynamic coefficients due to the form of their associated support functional –as happens with K_{xy} –; K_8 is assimilable to a wind-direction-dependant disturbance in forward flight; and K_4, K_5 describe the dominance of the linear dependency with respect to the airspeed during the transition between hovering and cruise flight.

Aerodynamic torques

Correspondingly, the aerodynamic torques sub-model in the same body frame reads

$$\frac{\boldsymbol{\tau}^{aero}}{\frac{1}{2}\rho S_f L} = \Phi_\tau(\alpha_r, \beta, V_\infty) \mathbf{K}_\tau, \quad (3.17)$$

being the associated support functional given by

$$\Phi_\tau(\alpha_r, \beta, V_\infty) = \left(1 - \left(\frac{\alpha_r}{\pi/2}\right)^2\right) \begin{bmatrix} -\sin \beta \\ \cos \beta \\ 0 \end{bmatrix} \begin{bmatrix} V_\infty & V_\infty^2 \sin \alpha_r & V_\infty |\sin 2\beta| \end{bmatrix},$$

with the torque model parameters (see Table 3.2)

$$\mathbf{K}_\tau = \begin{bmatrix} K_9 & K_{10} & K_{11} \end{bmatrix}^\top.$$

Analogously to the interpretation of the force parameters, K_{10} can be understood as an aerodynamic coefficient whose support function changes its sign at null values of the angle of attack of the rotor plane, and K_9, K_{11} as linear dependencies with the airspeed –a prevalent term in the transition from low speeds to cruise flight, as in 3.16–.

Remark 3.3. To be best of the author’s knowledge, this is the first *explicit* blunt-body aerodynamic characterisation of a multirotor platform. While most aerial robotics works include oversimplified visions of this complex problem and override the consequences of neglecting this complexity by employing general-purpose robust algorithms, this model presents a realistic –but challenging– depiction of the environmental conditions confronted by aerial robots in outdoor applications, hence enriching numerical validations based on dynamic simulations.

Remark 3.4. Moreover, not only is the proposed model useful as an advanced dynamic simulation add-on, but it is also a key step for outdoor multirotor model-based control techniques –such as robust/adaptive nonlinear control or model predictive control– that can be also used as a pre-training dataset for machine learning algorithms.

Remark 3.5. To obtain this functional solution with broad application capabilities, the *explicit* and *accurate* aerodynamic model must include two additional elements: i) significant improvements in terms of accuracy when compared to well-known simplistic models, and ii) the possibility of using it in other multi-rotors –directly or fine-tuning it with a limited number of CFD simulations–. The fulfilment of these two properties is discussed in depth in the two following subsections.

3.2.5 Comparison with constant aerodynamic coefficients model

To analyse the improvements of the proposed model, it is compared to the well-known constant aerodynamic coefficients approximation (CAC henceforth) for simple geometries (see [120, 121, 122, 123, 124] and references therein), which is the most common option when these effects are considered. The form of this approach is given by

$$\begin{aligned} \frac{\mathbf{F}^{aero}|_{CAC}}{\frac{1}{2}\rho S_f} &= K_f^{CAC} V_\infty^2 \begin{bmatrix} \cos \beta \cos \alpha_r \\ \sin \beta \cos \alpha_r \\ \sin \alpha_r \end{bmatrix}, \\ \frac{\boldsymbol{\tau}^{aero}|_{CAC}}{\frac{1}{2}\rho S_f L} &= K_\tau^{CAC} V_\infty^2 \begin{bmatrix} -\frac{1}{2} \sin \beta \sin 2\alpha_r \\ \frac{1}{2} \cos \beta \sin 2\alpha_r \end{bmatrix}, \end{aligned}$$

where $K_f^{CAC} \in \mathbb{R}^{3 \times 3}$ and $K_\tau^{CAC} \in \mathbb{R}^{2 \times 2}$ are the diagonal constant coefficient matrices for forces and torques, respectively, and the torque support functions are formed multiplying their homologue forces ones by a rotation matrix only dependent on the wind angles. It is worth noting that the constant coefficients have been tuned using the same CFD simulation results to avoid discrepancies with other platforms, thus becoming $K_f^{CAC} = \text{diag}([-1.49 \ -1.49 \ 2.1])$ and $K_\tau^{CAC} = \text{diag}([0.55 \ 0.55])$. However, due to the nature of the comparison –i.e. a vectorial result dependant on 3 variables–, a trade-off solution for the representation of its results is needed. The option chosen is to illustrate the form of both alternatives for a representative value of β –analysing their differences in Fig. 3.6 and 3.7–; and then sum up the complete comparison in Table 3.3. For the first, $\beta = 33.75^\circ$ is chosen, thus including valuable data of all the sub-models away from symmetries, and illustrating the influence of the wind direction.

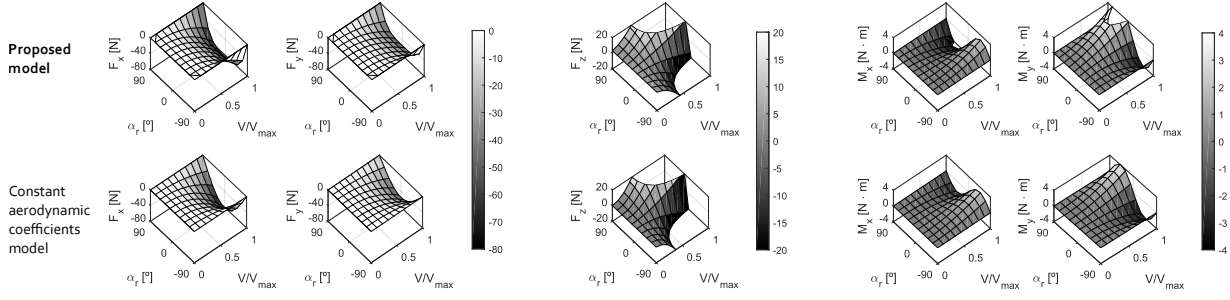


FIGURE 3.6: Structure of the proposed flight aerodynamics model for multi-rotors compared to the CAC approach for $\beta = 33.75^\circ$ as a function of α_r and V_∞ .

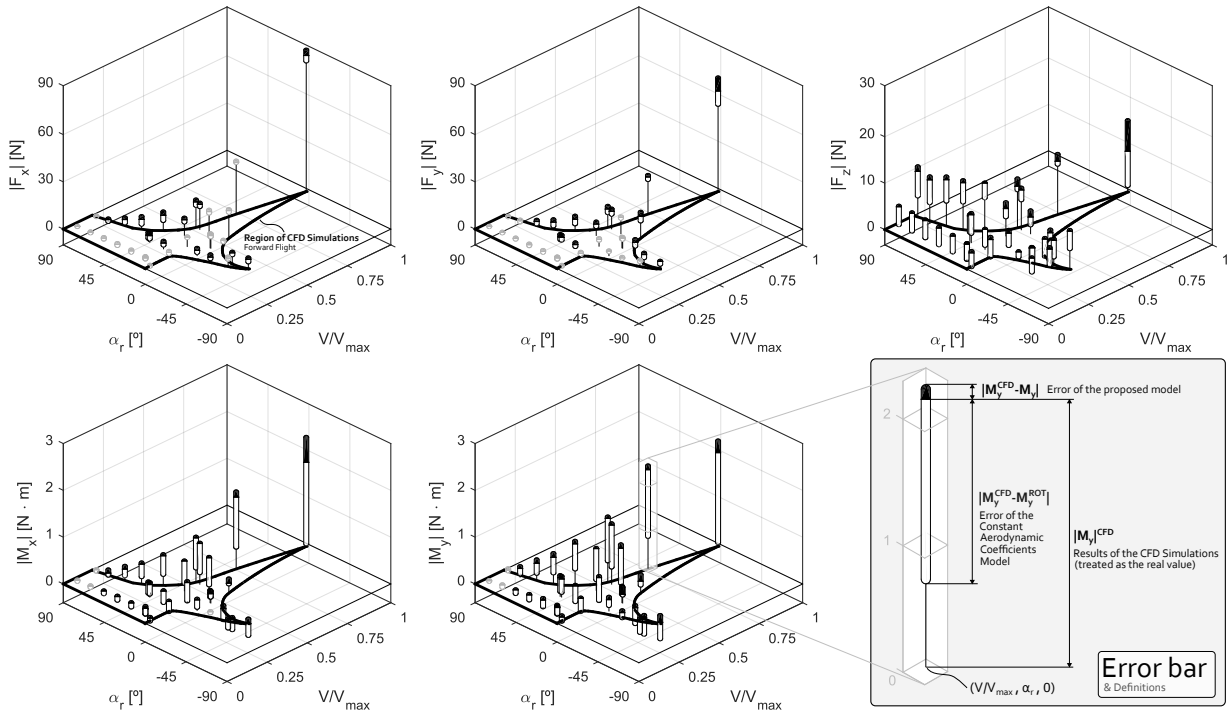


FIGURE 3.7: Comparison in terms of error with respect to CFD simulation results between the proposed aerodynamic model (black segments) and the CAC solution (white segments) as error bars (see their graphical definition on the bottom right corner), being only considered points within the simulable region. Note: error bars in light gray indicate cases in which both solutions show errors below 1 N, for forces, or 0.05 N.m, for torques.

Subsequently, the general form of both alternatives is shown in Fig. 3.6, being worth noting that their structures are similar. Although this resemblance might induce the idea of not having obtained a significant advance, this should be discussed in depth before reaching this conclusion.

To do so, both models are directly compared using error bars, as shown in Fig. 3.7 (see Error bar and Definitions in the bottom right corner). With this alternative point of view, it becomes clear that the subtle changes of the proposed model match the patterns of the CFD results significantly better than the CAC approach in many regimes. For instance, the aerodynamic torque estimation of the proposed solution outperforms this alternative in all flight regimes, with limited cases where both show similar errors. Similarly, the vertical force estimation is generally more accurate than the standard solution used nowadays. On the other hand, the differences with the CAC solution are not appreciable in the case of horizontal forces for this value of β , being needed additional results to determine if the model is more accurate than CAC in these components.

	Component in $\{\mathcal{B}\}$	CAC model	Proposed model	Difference	Variation (%)
COEFFICIENT OF DETERMINATION R^2	F_{xy}	0.991	0.994	0.003	0.3%
	F_z	0.636	0.982	0.346	54.4%
	M_{xy}	0.601	0.983	0.382	63.6%
ROOT-MEAN- SQUARE ERROR RMSE [N] or [N m]	F_{xy}	1.252	1.035	-0.217	-17.3%
	F_z	3.655	0.819	-2.836	-77.6%
	M_{xy}	0.380	0.079	-0.301	-79.2%

TABLE 3.3: Comparison between the CAC model and the proposed solution for the whole spectrum of variables, i.e. $\alpha_r, \beta, V_\infty$, highlighting the significant improvements achieved.

Accordingly, the results of both alternatives for the complete β -spectrum are compared. For that purpose, a set of significant metrics ought to be decided, being finally chosen the coefficient of determination R^2 and the root-mean-square error RMSE. The results of this comparison are then shown in Table 3.3, being evinced that the advances found in the case of $\beta = 33.75^\circ$ could be extended to the whole spectrum. In particular, the characteristic error of the proposed model for vertical forces and torques is a quarter of its equivalent for the CAC approach. Moreover, the advances in the horizontal forces modelling –that were initially thought to be limited according to the results for $\beta = 33.75^\circ$ –, reach a 15% reduction in RMSE. Altogether, the results in Fig. 3.7 and Table 3.3 highlight the weaknesses of the CAC approach –directly related to its oversimplification of the blunt-body aerodynamics–, being the proposed formulation in (3.16)-(3.17) proven to overcome these without substantially increasing the computational complexity of the solution.

3.2.6 Implementation

Finally, the focus of this section is displaced to the implementation of the proposed aerodynamic solution in three cases: i) non-simulable flight conditions, where inter/extra-polation is needed; ii) other platforms assimilable to uniformly scaled vehicles; and iii) multi-rotors with other propulsion configurations, thus affecting the disk load and thrust losses, among others.

Non-simulable flight conditions

Due to the consideration of cross-validation requirements during the selection of support functions, the final aerodynamic model does not provide implausible estimations in those regions not directly covered by CFD simulations. Nonetheless, as these estimations are obtained after either interpolating or extrapolating the results from the simulations, their validity should be initially called into question. The motivation of this subsection, then, is to discuss when these results are recommended and when the estimation should only be used as a last option.

As shown in Fig. 3.8, the simulated region can be divided into two separate cases depending on the propulsion model employed –the general one in (3.12), here denoted as Forward Flight, or the empiric axial descent one in (3.13), identified as Vertical Descent–. Logically, the region between them –labelled as Slow descent– is a perfect candidate for a trade-off solution based on interpolation and its use is recommended for any application in which the region to be covered is not exclusively within the Slow descent regimes. Similarly, the Hovering regimes, i.e. flight conditions close to the collapsed hover model with small speeds in any of the possible directions, correspond to another interpolation case and, as happens with the previous case, its use is recommended in the vast majority of cases. On the other hand, both Fast ascent and Fast descent extrapolations should be generally avoided as their reliability decreases as the condition considered distances from the simulated results. Nevertheless, these regimes correspond to uncommon flight regimes, either faster-than-sedimentation descent or very aggressive ascent, and they are not expected to be needed except in some punctual cases related to aggressive manoeuvring.

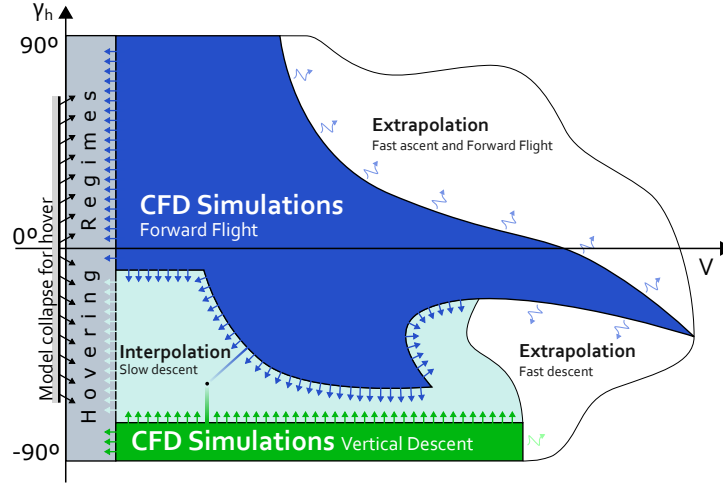


FIGURE 3.8: Simulable and non-simulable regions based on the aforementioned propulsion limitations –being indicated interpolated solutions with straight arrows and extrapolated ones with curved lines– with the model for hover collapsed. Note: these regions can also be identified in Fig. 3.7.

Uniformly scaled platforms

To extend the use of the aerodynamic model in other similar platforms, a first analysis of the impact of the scale of the vehicle in the validity of the solution is conducted. Although this size has been parametrised using the reference face area, S_f , some other factors that are not proportional to that parameter must also be considered. Firstly, the rotor disk load in (3.11) changes linearly with the platform dimensions: the thrust compensates the weight of the platform –which, for constant density, is affected cubically– while the rotor disk area dependency is quadratic–. This implies that the induced flow speeds needed are affected, thus impacting –among others– the thrust losses and the final deflection of the streamtube. On the other hand, aerodynamic forces and torques directly associated with the platform body should evolve linearly with the reference face area. This difference of tendencies between both terms induces deviations from the nominal case that must be analysed. For that preliminary analysis, let us assume that the thrust losses can be modelled as the drag force of four square-section cylinders of the same width of the platform arms under uniform wind with a speed equal to the airflow total speed of the rotors (see [107] for the aerodynamic coefficients). Considering this, an estimation of support arms affected by thrust losses is carried out on the base of the CFD simulation results, leading to an interval of between 90% and 110% of the rotor diameter. Accordingly, we assume for our analysis that the same estimation is still valid for scaled platforms with different induced speeds. Moreover, the deflection of the streamtube, δ_r , is directly considered from the BEMT theory.

The results of this analysis are presented in Fig. 3.9 as a function of the weight scale factor –i.e. the ratio between the simulated platform and the nominal case, denoted as WF – for different percentiles of the set of simulation conditions. Considering that the sensitivity of the module and direction of the aerodynamic effects can be respectively defined as

$$\begin{aligned} \frac{F}{F^n} &:= 1 + \frac{\Delta T(WF)}{F^n}, \\ \frac{\delta_r}{\delta_r^n} &:= 1 + \frac{\Delta \delta_r(WF)}{\delta_r^n}, \end{aligned}$$

with $F := \|\mathbf{F}^{aero}\|$ and the super-index n identifying the nominal case, it becomes clear that the effect of the weight factor on these is significantly different. For instance, while the percentile 90 of the module reaches a deviation of 10% when the scaled platform weight is 140% of the nominal case, the deflection with the same percentile for this platform is below 2%. This identifies the force module as the most affected element, thus being this applicability analysis focused on it.

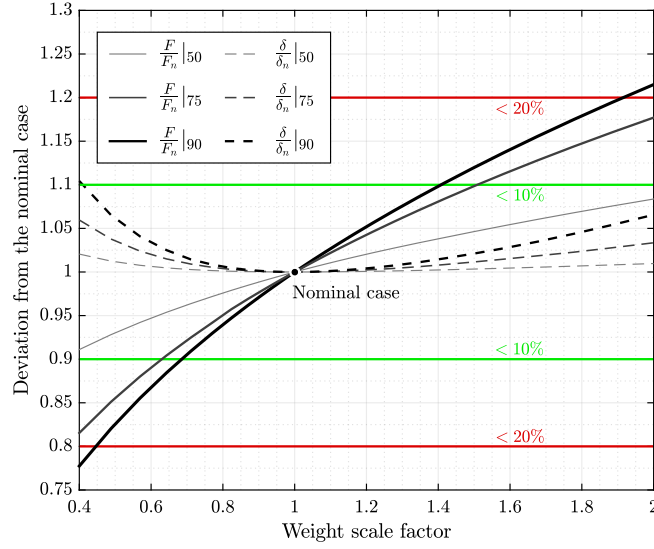


FIGURE 3.9: Influence of the weight factor on the aerodynamic model validity for percentiles 50, 75 and 90 of the simulation configurations.

As previously indicated, the main goal of the study is to extend the applicability of the proposed solution to the widest range of platforms possible. Therefore, we make use of the results of Fig. 3.9 to deduce a limit in weight for the application of the aerodynamic model. The metric chosen for this purpose is the percentile 90 of the module of the forces, being the maximum deviation allowed a 10%. Accordingly, a conservative range would be $WF \in [0.7, 1.4]$, corresponding to platforms from approximately 7 kg to 14 kg. This condition, indeed, includes the vast majority of medium-sized multirotors, thus being the solution extendible to all of them. Moreover, by relaxing the standards to a maximum deviation of 20%, it can be estimated that the model is still acceptable for platforms ranging between 5 and 18 kg. This second interval includes most platforms equipped with advanced sensor/mission systems, hence providing the solution with a fast-to-tune estimation of the blunt-body aerodynamic effects for these. Finally, it is worth noting that those platforms not included in these ranges can also be modelled with the proposed solution after retuning the parameters with a limited set of simulations, thus counterbalancing the effects of the scale.

Other rotor configurations

Additionally, the influence of the rotor configurations on the aerodynamic model is also studied for platforms with the same weight. If the simplistic BEMT is considered a good indicator of the importance of the different parameters, we can deduce that the rotor configuration mainly affects the disk load in (3.11), thus altering the induced flow speed. Accordingly, configurations with similar disk loads –or equivalently similar total rotor area, $N_r A_r$ – should have similar induced speeds. To meet this condition, however, the radii of the rotors should change with $R_b = \sqrt{N_r^n / N_r} R_b^n$, where the super-index n identifies the nominal case. Moreover, if the study of the thrust losses in the previous section is considered, these are proportional to total radii of the rotors, given by $N_r R_b = N_r^n R_b^n \sqrt{N_r / N_r^n}$. Therefore, in configurations with different rotor settings but the same disk load, the parameter associated to thrust losses is recommended to be readjusted as $K_h = \sqrt{N_r / N_r^n} K_h^n$.

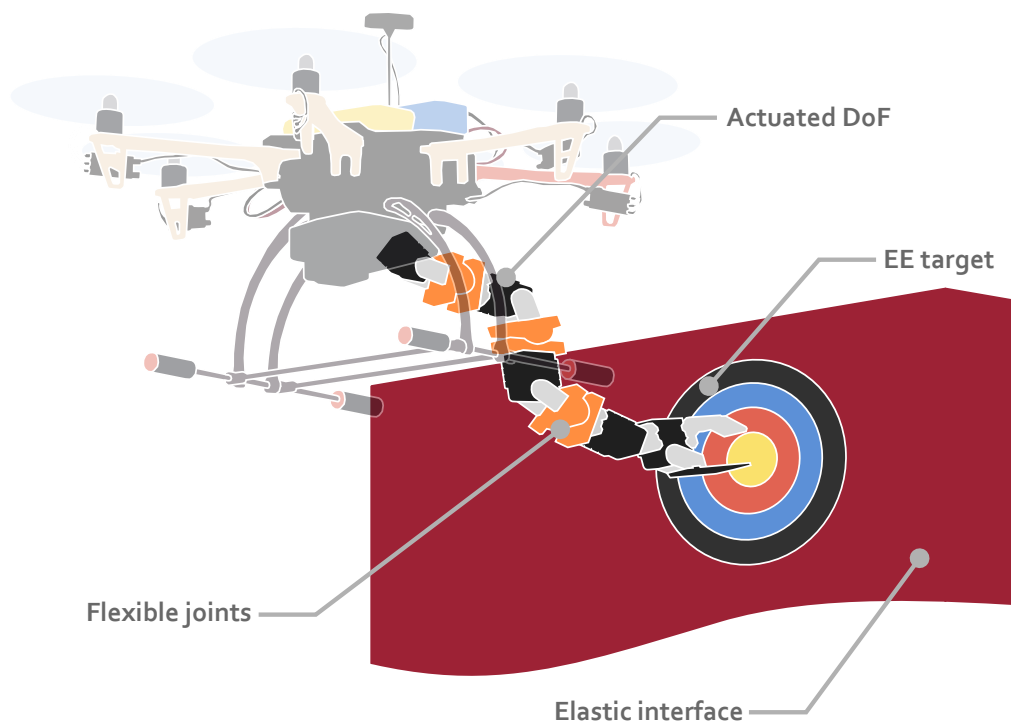
Furthermore, it is also worth analysing the influence of coaxial rotor solutions on the validity of the proposed model. As profoundly studied in [125], these can be assimilated to conventional rotors with the same radius, twist, airfoil sections, root cutout, and total number of blades. By

applying this result to the induced speed calculations, we can ensure that the deviations from the nominal case should be small. Nevertheless, the strict conditions needed to study this problem with a conventional rotor can also be relaxed taking into account the low sensitivity of the induced speed to the rotor solidity. Subsequently, coaxial rotors with a different number of blades or root cutout could also be accepted for this study without additional CFD simulations.

3.3 Summary of the chapter

In this chapter, the characterisation of the systems to be controlled has been presented. Kinematic and dynamic models for the aerial manipulation system –and its main subsystems– are provided. Among them, a special effort has been devoted to the aerodynamic characterisation of the flight platform to enhance the simulations for outdoor missions in next chapters, for which a methodology based on CFD simulations has been employed. Altogether, these models constitute the foundations on which the control contributions are later built.

Adaptive position control of lightweight flexible manipulators



Highlights:

- Novel adaptive nonlinear controller, independent of the stiffness of the flexible modes.
- (Globally) asymptotically stable first-order-like closed-loop response.
- Resilience against unforeseen impacts and contact.

The most common approaches to reduce the impact of oscillations produced by manipulation tasks on aerial missions –such as the one presented in Section 2.2– are: i) to change the mechanical design of RMs in a trade-off solution between compliant oscillations and EE convergence times, or ii) to improve the disturbance rejection capabilities of the controller without downgrading these. The potential of the first, however, is limited in flexible manipulators due to their high sensitivity and inherent delayed response. The latter approach, on the other hand, is studied within the adaptive manipulation control branch outlined in Section 2.3.

As a first step, this chapter is devoted to improving these disturbance rejection capabilities with the adaptive position controller presented in [C5]. This is based on a well-known inverse kinematics approach for compliant manipulators [84], but enhancing it with integral action and an update law for the *a priori* unknown stiffness of the flexible links. As a result, these flexible modes are indirectly taken into account via an equivalent Jacobian matrix. For the sake of comparison, the base approach is succinctly presented with the notation of this thesis in Section 4.1, being the changes with respect to this highlighted in red throughout Sections 4.2 and 4.3.

4.1 Control rationale

A brief summary of [84], which is essential for the adaptive control laws in Chapters 4 and 5, is included here –but with the notation of this thesis–. Consider the flexibility of the manipulator with an elastic contact model, reading

$$K_\delta \delta = J_\delta^t \mathbf{f}^{EE} + J_{B,\delta}^\top m_B \mathbf{g}_0, \quad (4.1)$$

being $\mathbf{f}^{EE} = k_e \mathcal{N}(\bar{\mathbf{p}} - \bar{\mathbf{p}}_s)$ the force applied by the EE, $\mathcal{N} := \mathbf{nn}^\top$ the projection matrix on the outward contact normal $\mathbf{n} \in \mathbb{R}^{S_p}$, $\bar{\mathbf{p}}_s \in \mathbb{R}^{S_p}$ the initial contact point, and $k_e \in \mathbb{R}^+$ the *known* elastic constant of the contact surface (see Fig. 4.1). This model is then used to compute the deflection speeds by deriving (4.1) under the hypothesis of small deflections, thus becoming

$$\dot{\delta} = -J_{fg}(\gamma) \dot{\gamma}, \quad (4.2)$$

where $J_{fg} \in \mathbb{R}^{M \times N}$ denotes the Jacobian taking into account the impact of the external forces applied on the EE on the flexible modes given by

$$J_{fg} := K_\delta^{-1} \left(k_e \frac{\partial J_\delta^t}{\partial \gamma} \bar{N} + J_\delta^t \mathcal{N} J_\gamma^t - \frac{\partial J_{B,\delta}^\top}{\partial \gamma} m_B \tilde{G} \right),$$

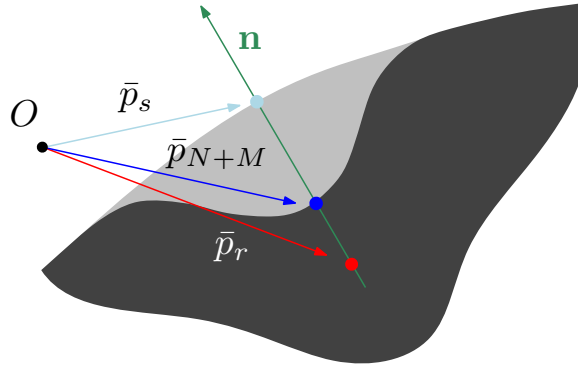


FIGURE 4.1: Definition of the contact parameters using a undeformed/deformed superimposed plot, where the undeformed is in light gray and the deformed in dark grey.

with the extended derivative Jacobian matrices in the derivation defined block-wise as

$$\begin{aligned}\frac{\partial J_\delta^t{}^\top}{\partial \gamma} &:= \begin{pmatrix} \frac{\partial J_\delta^t{}^\top}{\partial \gamma_1} & \dots & \frac{\partial J_\delta^t{}^\top}{\partial \gamma_N} \end{pmatrix}, \\ \frac{\partial J_{B,\delta}^\top}{\partial \gamma} &:= \begin{pmatrix} \frac{\partial J_{B,\delta}^\top}{\partial \gamma_1} & \dots & \frac{\partial J_{B,\delta}^\top}{\partial \gamma_N} \end{pmatrix},\end{aligned}$$

and the contact and gravity extended matrices, $\bar{N}, \bar{G} \in \mathbb{R}^{N S_p \times N}$, as

$$\begin{aligned}\bar{N}_k &:= \text{col}(\boldsymbol{\vartheta}_{(k-1)S_p}, \mathcal{N}(\bar{\mathbf{p}} - \bar{\mathbf{p}}_s), \boldsymbol{\vartheta}_{(N-k)S_p}), \\ \bar{G}_k &:= \text{col}(\boldsymbol{\vartheta}_{(k-1)S_p}, \mathbf{g}_0, \boldsymbol{\vartheta}_{(N-k)S_p}).\end{aligned}$$

Then, by introducing this computed model into the direct kinematics in (3.5), this kinematic formulation can be rewritten as

$$\dot{\mathbf{p}} = J_T(\mathbf{q}^{RM})\dot{\gamma},$$

with $J_T \in \mathbb{R}^{S \times N}$ the equivalent Jacobian introduced to take into account the flexible nature of the compliant RM into the control design, given by $J_T := J_\gamma - J_\delta J_{fg}$. Subsequently, defining the EE tracking error as $\mathbf{e} := \mathbf{p}_r - \mathbf{p} \in \mathbb{R}^S$, the flexible manipulator error kinematics reads

$$\dot{\mathbf{e}} = \dot{\mathbf{p}}_r - J_T \dot{\gamma}, \quad (4.3)$$

being chosen to track the reference \mathbf{p}_r a transpose scheme reading

$$\dot{\gamma} = K_\gamma J_T^\top \mathbf{e},$$

with $K_\gamma \in \mathbb{R}^{N \times N}$ a positive definite gain matrix. Finally, using a Lyapunov argument –as stated in [84]– it can be obtained that tracking error in (4.3) asymptotically tends to the trivial solution if \mathbf{e} is not in the kernel of J_T^\top .

4.2 Contact model and equivalent manipulator kinematics

In order to take into account the flexibility of the manipulator, the elastic contact model in (4.1) is employed, as in Section 4.1. However, this approach yields a pseudo-static assumption whose capabilities in aerial manipulation applications –i.e. robustness against high frequency corrections and interaction with unforeseen external elements– ought to be enhanced. To do so, this model is used to obtain an initial estimation of the deflection speeds depending on a linear set of parameters and then proposing an adaptive update law for these. Firstly, this initial estimation is achieved by deriving (4.1), thus obtaining

$$\dot{\hat{\boldsymbol{\delta}}} = -\hat{\Theta}_K^\top J_{fg}^s \dot{\gamma}, \quad (4.4)$$

where $\Theta_K \in \mathbb{R}^{2M \times M}$ is the parametric uncertainty matrix –to be later updated via an adaptive law– given by

$$\Theta_K^\top := \begin{pmatrix} k_e K_\delta^{-1} & K_\delta^{-1} \end{pmatrix},$$

and $J_{fg}^s \in \mathbb{R}^{2M \times N}$ is a Jacobian taking into account the impact of the external forces applied to the EE on the flexible modes –but having separated the parameters taking into account the stiffness of the interface and the manipulator, unlike J_{fg} in (4.2)– given by

$$J_{fg}^s := \begin{pmatrix} \frac{\partial J_\delta^t{}^\top}{\partial \gamma} \bar{N} + J_\delta^t{}^\top \mathcal{N} J_\gamma^t \\ -\frac{\partial J_{B,\delta}^\top}{\partial \gamma} m_B \bar{G} \end{pmatrix},$$

where the extended derivative Jacobian matrices coincide with the ones in Section 4.1.

Then, upon respectively defining the error of the uncertain matrix and deflection estimations as $\tilde{\Theta}_K := \Theta_K - \hat{\Theta}_K$ and $\tilde{\delta} = \delta - \hat{\delta}$, (3.5) can be rewritten as

$$\dot{\mathbf{p}} = \underbrace{\left(\hat{J}_T(\mathbf{q}^{RM}, \hat{\Theta}_K) \right)}_{\text{Estimate}} - \underbrace{J_\delta \tilde{\Theta}_K^\top J_{fg}^s}_{\text{Uncertain}} \dot{\gamma}, \quad (4.5)$$

being $\hat{J}_T \in \mathbb{R}^{S \times N}$ an estimate of equivalent Jacobian introduced to take into account the flexible nature of the compliant RM into the control design, given by

$$\hat{J}_T := J_\gamma - J_\delta \hat{\Theta}_K^\top J_{fg}^s = J_{RM} \hat{J}_\Theta, \quad (4.6)$$

with

$$\hat{J}_\Theta := \begin{pmatrix} I_N \\ -\hat{\Theta}_K^\top J_{fg}^s \end{pmatrix}. \quad (4.7)$$

Subsequently, using the definition of the EE tracking error –both including position and orientation– given by $\mathbf{e} := \mathbf{p}_r - \mathbf{p} \in \mathbb{R}^S$, the manipulator error kinematics reads

$$\dot{\mathbf{e}} = \dot{\mathbf{p}}_r - \hat{J}_T \dot{\gamma} + J_\delta \tilde{\Theta}_K^\top J_{fg}^s \dot{\gamma}. \quad (4.8)$$

4.3 Control design

Taking into account the form of the error kinematics in (4.8), a nonlinear adaptive control strategy with integral-like action is proposed (see Fig. 4.2), reading

$$\dot{\xi} = K_I \hat{J}_T K_\gamma \hat{J}_T^\top K_P \mathbf{e} - K_\xi \xi, \quad (4.9a)$$

$$\dot{\gamma} = K_\gamma \hat{J}_T^\top (K_P \mathbf{e} + K_I \xi), \quad (4.9b)$$

where $K_\xi, K_I, K_P \in \mathbb{R}^{S \times S}$ and $K_\gamma \in \mathbb{R}^{N \times N}$ are symmetric and positive definite gain matrices, with the associated adaptive update law given by

$$\dot{\tilde{\Theta}}_K = \Gamma_\Theta J_{fg}^s \dot{\gamma} \mathbf{e}^\top K_P J_\delta, \quad (4.10)$$

and $\Gamma_\Theta \in \mathbb{R}^{2M \times 2M}$ is also a positive definite gain matrix.

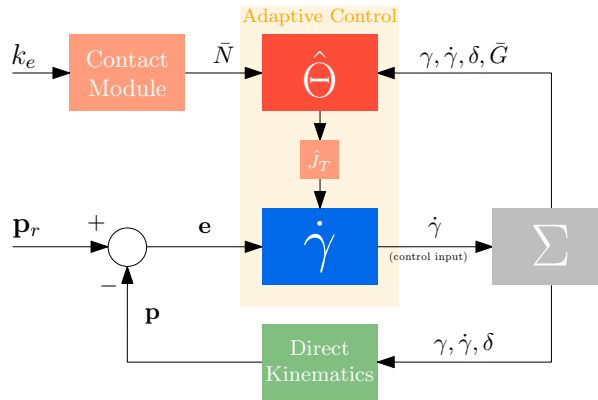


FIGURE 4.2: Close-loop control schematic, including the flexibility-aware actuation (in blue), the adaptive modules (in orange) and the direct kinematics with flexible feedback (in green).

Remark 4.1. Due to the formulation of ξ in (4.9a), this integral-like term clearly shows a nonlinear nature. This behaviour is found to be essential to enhance the robustness capabilities of the strategy and to guarantee the zero steady-state error of the proposed approach when using the interlaced Jacobian in (4.5).

Proposition 4.1. Consider the uncertain system in (4.8) for any $N \geq S$, and assume that $\text{rank}(J_{RM}) = S$, along with the control laws in (4.9) and its associated adaptive update law in (4.10). Then, upon defining the extended system error as $\chi := \text{col}(\xi, \mathbf{e}) \in \mathbb{R}^{2S}$, the closed-loop inverse kinematics of the complete system for $\dot{\mathbf{p}}_r = \mathbf{0}$ becomes

$$\dot{\chi} = \hat{\mathcal{A}}(\mathbf{q}^{RM}, \hat{\Theta}_K) \chi + \tilde{\mathcal{B}}(\mathbf{q}^{RM}, \tilde{\Theta}_K) \dot{\gamma}, \quad (4.11)$$

with

$$\hat{\mathcal{A}} = \begin{pmatrix} -K_\xi & K_I \hat{J}_T K_P \\ -\hat{J}_T K_I & -\hat{J}_T K_P \end{pmatrix},$$

$$\tilde{\mathcal{B}} = \begin{pmatrix} \mathcal{O}_{S \times N} \\ J_\delta \tilde{\Theta}_K^\top J_{fg}^s \end{pmatrix},$$

and $\hat{J}_T := \hat{J}_T K_\gamma \hat{J}_T^\top \in \mathbb{R}^{S \times S}$. Moreover, the zero equilibrium of χ in (4.11) is (globally) asymptotically stable.

Proof. The first claim is straightforward recalling the definition of the EE error in (4.8) and combining it with (4.5) and (4.9). For the second one, let us introduce the radially unbounded and positive definite Lyapunov function candidate given by

$$V := \frac{1}{2} \chi^\top \mathcal{K} \chi + \frac{1}{2} \text{Tr}(\tilde{\Theta}_K^\top \Gamma_\Theta^{-1} \tilde{\Theta}_K), \quad (4.12)$$

with

$$\mathcal{K} = \begin{pmatrix} I_S & \mathcal{O}_S \\ \mathcal{O}_S & K_P \end{pmatrix} > 0.$$

Accordingly, the derivative of (4.12) along the system trajectories reads

$$\begin{aligned} \dot{V} &= \chi^\top \mathcal{K} \dot{\chi} + \text{Tr}(\tilde{\Theta}_K^\top \Gamma_\Theta^{-1} \dot{\tilde{\Theta}}_K) \\ &= \chi^\top \mathcal{K} \hat{\mathcal{A}} \chi + \chi^\top \mathcal{K} \tilde{\mathcal{B}} \dot{\gamma} + \text{Tr}(\tilde{\Theta}_K^\top \Gamma_\Theta^{-1} \dot{\tilde{\Theta}}_K). \end{aligned}$$

Due to the skew-symmetry of the product $\mathcal{K} \hat{\mathcal{A}}$, this derivative becomes

$$\begin{aligned} \dot{V} &= -\xi^\top K_\xi \xi - \mathbf{e}^\top K_P \hat{J}_T K_P \mathbf{e} + \chi^\top \mathcal{K} \tilde{\mathcal{B}} \dot{\gamma} + \text{Tr}(\tilde{\Theta}_K^\top \Gamma_\Theta^{-1} \dot{\tilde{\Theta}}_K) \\ &= -\xi^\top K_\xi \xi - \mathbf{e}^\top K_P \hat{J}_T K_P \mathbf{e} + \mathbf{e}^\top K_P J_\delta \tilde{\Theta}_K^\top J_{fg}^s \dot{\gamma} + \text{Tr}(\tilde{\Theta}_K^\top \Gamma_\Theta^{-1} \dot{\tilde{\Theta}}_K) \\ &= -\xi^\top K_\xi \xi - \mathbf{e}^\top K_P \hat{J}_T K_P \mathbf{e} + \text{Tr} \left[\tilde{\Theta}_K^\top \left(J_{fg}^s \dot{\gamma} \mathbf{e}^\top K_P J_\delta - \Gamma_\Theta^{-1} \dot{\tilde{\Theta}}_K \right) \right], \end{aligned}$$

where the last term is cancelled out with (4.10). Therefore, the derivative of the Lyapunov candidate reads

$$\dot{V} = -\xi^\top K_\xi \xi - \mathbf{e}^\top K_P \hat{J}_T K_P \mathbf{e} \leq 0.$$

Then, since the candidate function is positive definite and the closed-loop system is autonomous, LaSalle's Invariance Principle is invoked. For that purpose, the largest invariant set included in the residual set given by $\dot{V} = 0$ is analysed, namely

$$\Omega_V := \left\{ \chi \in \mathbb{R}^{2S} : \chi \in \mathbb{R}^{2S+S_p} : \xi = \mathbf{0}, \hat{J}_T^\top \bar{\mathbf{e}} = \mathbf{0} \right\},$$

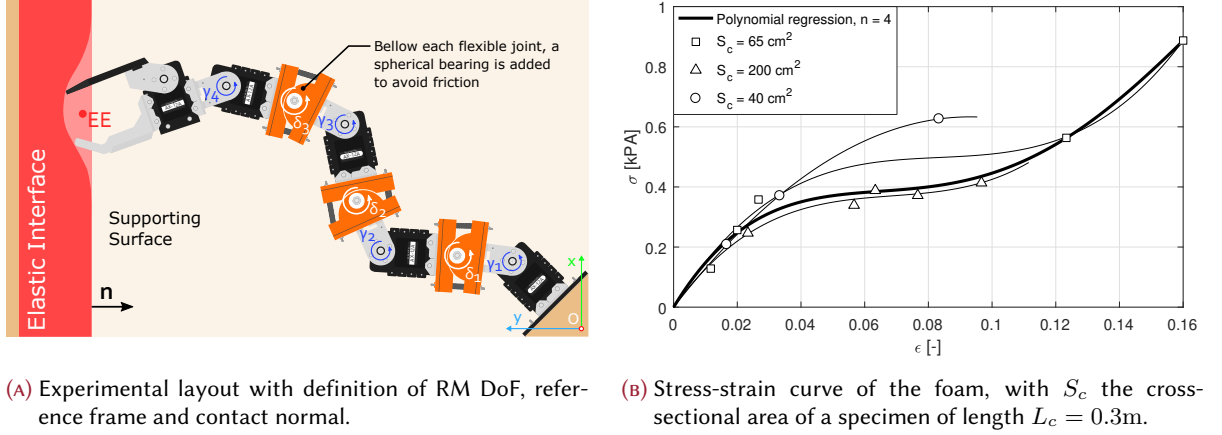


FIGURE 4.3: Experimental setting for the validation of the proposed strategy, including both the experimental layout of the 3 scenarios considered –with or without an elastic interface– and the mechanical characterisation of this element.

with $\bar{\mathbf{e}} := K_p \mathbf{e}$, thus becoming evident that the residual dynamics in this problem are trivial. Accordingly, only fixed points belong to the largest invariant set and the analysis is reduced to determine all non desired equilibria. Since $\hat{J}_T^\top \bar{\mathbf{e}} = \mathbf{0}$ is equivalent to $\bar{\mathbf{e}} \in \ker(\hat{J}_T^\top)$, $\hat{J}_T^\top \bar{\mathbf{e}} = \mathbf{0}$ has the unique trivial solution if and only if $\text{rank}(\hat{J}_T^\top) = S$. Recall from (4.7) that $\text{rank}(\hat{J}_\Theta^\top) = N$, by assumption that $\text{rank}(J_{RM}^\top) = S$ and –by design– $N \geq S$. Therefore, $\text{rank}(\hat{J}_T^\top) = \text{rank}(\hat{J}_\Theta^\top J_{RM}^\top) \leq \min\{N, S\} = S$, concluding the proof. \square

Remark 4.2. Proposition 4.1 relies on the full-rank assumption on the Jacobian J_{RM} , achievable by design as in our benchmark application and in other alternative systems [77].

Remark 4.3. It should be noted that the whole mathematical derivation in Proposition 4.1 results in an algorithm that does not involve any matrix inversion, thus avoiding unbounded responses near singularities.

4.4 Experimental results

To validate this adaptive strategy, the planar RM¹ in Subsection 7.2.1 is employed (see the experimental setting in Fig. 4.3). The gains used in this experiments are shown in Table 4.1, except for K_γ which is chosen equal to the identity. Moreover, it is worth mentioning that due to the limitations of the low-cost board –as its lack of memory–, the inclusion of gravitational terms becomes infeasible and reduces the effective control frequency to 27 Hz (± 2 Hz). Nonetheless, this last challenge allows us to evaluate the robustness of the solution when implemented in discrete time, for which the strategy was not designed.

¹The planar design is chosen to reduce the matrix calculations, being a preliminary analysis of the computational load for 3D configurations provided in Remark 4.4.

K_P		K_I		K_ξ	Γ		
$K_P^{\bar{p}}$	$K_P^{\bar{\alpha}}$	$K_I^{\bar{p}}$	$K_I^{\bar{\alpha}}$	K_ξ	Γ_1	Γ_2	Γ_3
98.40	2.40	0.35	0.30	20.00	0.04	0.07	0.12

TABLE 4.1: Control gains of the benchmark application.

Remark 4.4. In order to determine the best experimental conditions that could be achieved with the aforementioned computer board, a preliminary computational load analysis based on the complexity of the algorithms was conducted. The main conclusions of this study can be divided into:

- a RM with a 6D manipulation space, i.e. $S = 6$ would approximately double the load;
- for the final configuration, an algorithm with damped least-squares (DLS) inverse that does not consider any flexible mode would roughly halve the computational cost of the proposed solution;
- and for a realistic 6D RM ($N = 7$, $M = 4$), the computational load would only scale with a factor 4 in comparison to the benchmark application, being in this case the difference with a DLS solution reduced to a 30%.

Accordingly, we can deduce that although a 6D configuration is infeasible in the current board, the scalability of the approach is promising and its loads are comparable to a well-known solution that does not specifically counteract the flexible modes.

Once the system is presented, let us introduce the validation scenarios. The purpose of all of them is to show the rejection capabilities of the proposed approach when facing different disturbances. According to these, the three scenarios are:

1. A position tracking mission is commanded to the RM without any interference, thus illustrating its nominal behaviour and providing a reference for comparison. As this mission is easily replicable, several consecutive experiments are commanded to obtain an average response and its variability.
2. The same mission is commanded to the RM, but including unforeseen impacts –in time, intensity and direction–. The response against these impacts is then studied to determine if the approach is capable of recovering to its nominal response and track its reference successfully.
3. The RM is commanded to interact with the elastic interface and converge to a waypoint inside it, thus having to overcome the nonlinear response of the foam (see Fig. 4.3b). Nonetheless, as the characterisation of this element is unknown to the control algorithm, it must comply to reach its reference.

Apart from the material included in this thesis, a complete video of these experiments –with link <https://youtu.be/fP3HrJ0x37k>– has been uploaded to the GRVC Robotics Laboratory Youtube Channel.

4.4.1 Undisturbed scenario

Firstly, the results of the undisturbed scenario are presented in Fig. 4.4 for 13 consecutive experiments. As it is clearly visible in the depiction of the mean experiment, the response of the RM controller to step reference changes is similar to a first-order system, but with a slight overshoot in some cases. Considering the ill-conditioning of the system in terms of stiffness, we can conclude that the oscillatory behaviour of the system for fast displacements has been significantly softened. Moving to the adaptive parameters, their mean variation is more subtle. Nonetheless changes of tendency can be appreciated for the moments in which the reference is given one of the

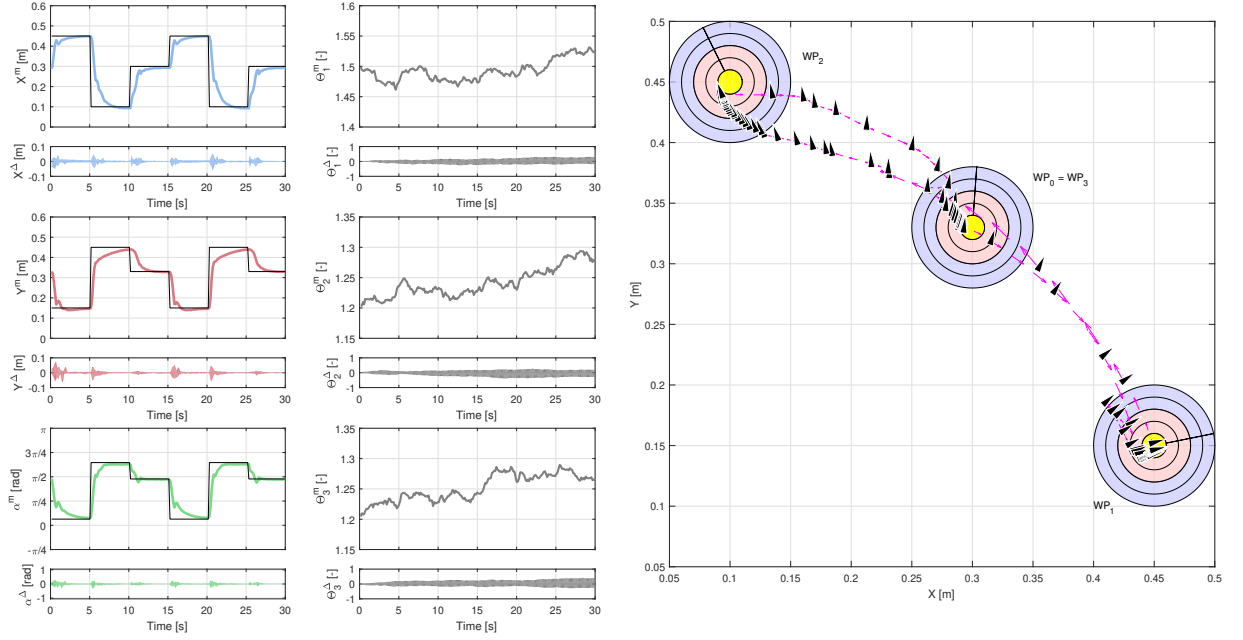


FIGURE 4.4: Results for the repeatability scenario with mean EE position and orientation on the left, mean adaptive parameters on the centre, and XY representation of the mean experiment using black arrows to indicate both position and orientation and targets, with annuli of 1 cm and reference orientation as black radii, for the waypoints on the right. To illustrate the variability in the experimental set, both the position and adaptive parameter plots include their maximum deviations from the mean, here denoted as $(\cdot)^\Delta$.

steps. On the contrary, the variability of the EE positions within the experimental sample is very limited while the adaptive parameters (stimulated via white noise) show significant difference between experiments. Finally, a XY representation of the mean experiment is added to Fig. 4.4, thus illustrating the convergence of the solution in both position and orientation from a more intuitive perspective.

4.4.2 Impact scenario

As previously indicated when presenting the scenarios, the response of the solution to impacts enriches our understanding of its disturbance rejection capabilities. As shown in Fig. 4.5, the manipulator faces 7 impacts during the same mission presented in the previous scenario, achieving a full recovery of its first-order-like behaviour after all of them. To do so, the adaptive capabilities of the proposed solution are employed, as demonstrated by the significant peaks in their values just after each main disturbance. Additionally, it is also worth mentioning that this response is achieved even when the impact occurs during a transient due to reference changes, such as in the last impact, or after a previous disturbance not yet dissipated by the solution, as in the fifth one.

4.4.3 Contact scenario

Finally, the results of the contact scenario are shown in Fig. 4.6. As happened before, the solution provides a first-order-like response when demanded to push into an elastic interface (direction Y), no matter the mechanical behaviour of the material. Obviously, the convergence of the solution is significantly faster in the directions without disturbances. After that, the reference in the pushing direction is tracked, showing the other components of the manipulation space a compliant

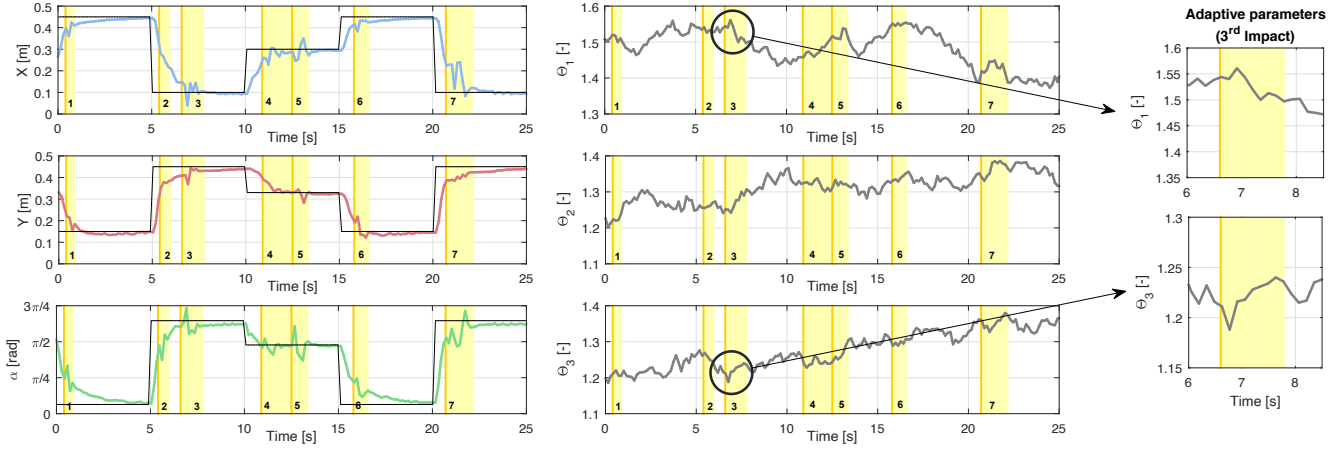


FIGURE 4.5: EE position and adaptive parameters for the impact scenario, where these disturbances are indicated with dark yellow lines –with their associated transients as light yellow rectangles– and labelled from 1 to 7. To facilitate its interpretation, a detail of the third impacts is included on the right.

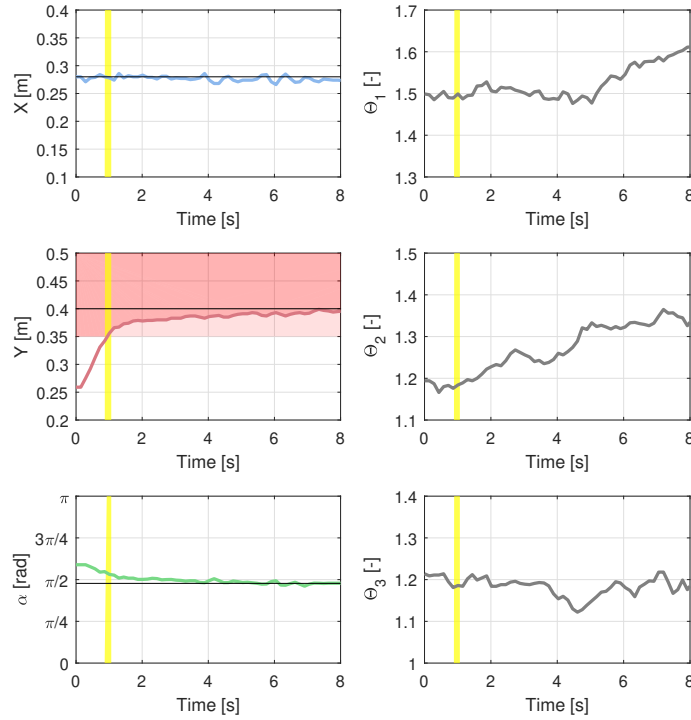


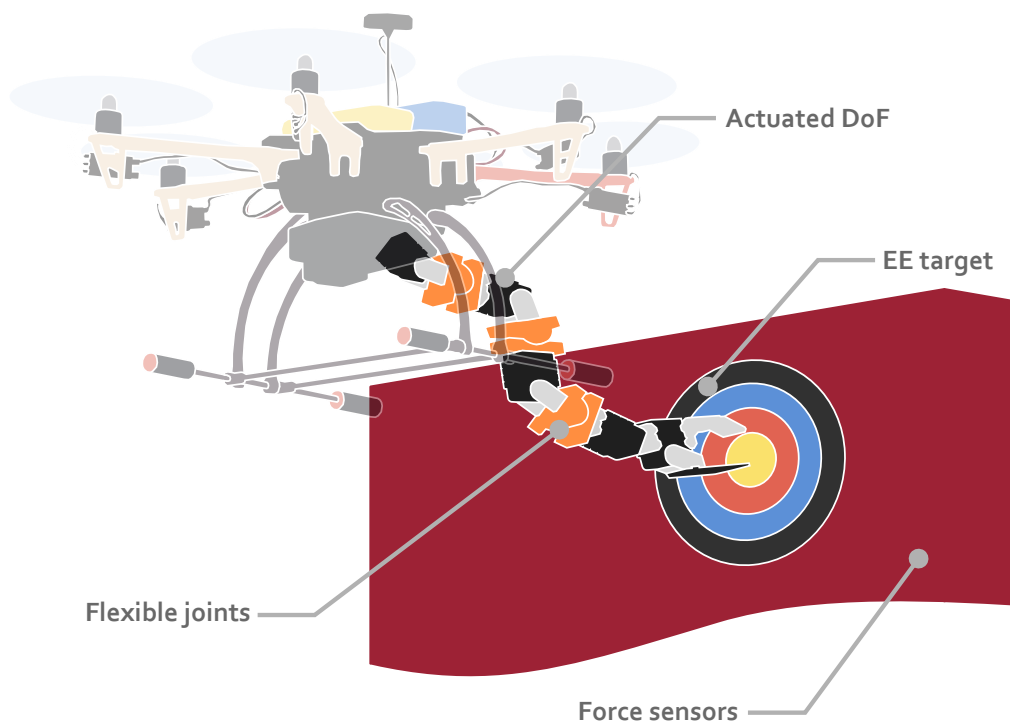
FIGURE 4.6: End-effector position and orientation for the contact scenario, including the variation of the adaptive parameters.

behaviour with some error peaks during this process. Meanwhile, the parameters of the adaptive law evolve to compensate the external disturbance, being their steepest change when the RM is stalled in the Y direction at around 5s.

4.5 Summary of the chapter

In this chapter, a position controller for flexible manipulators under uncertainties has been proposed. Due to its robust formulation relying on adaptive control, this novel strategy has been proven to modulate the oscillations produced by the flexible modes. Furthermore, the proposed strategy has been tested in scenarios including unforeseen impacts and slow contact, maintaining a first-order-like closed-loop response in all cases.

Adaptive force control of lightweight flexible manipulators



Highlights:

- Adaptive force/position controller maintaining the position first-order-like response.
- Automatic force/position reference transitions with the same strategy/tuning.
- (Globally) asymptotically stable closed-loop response and bounded force control capabilities against uncharacterised interfaces.

Following the research branch focused on adaptive manipulation control, the robust position controller in the previous chapter is enriched with force control capabilities [C8]. While an advance in this feature is significant from the operational point of view, it is essential to underscore that the disturbance rejection capabilities already obtained in the position controller must be preserved. Accordingly, the core of the previous controller is maintained and the force control features are added as an outer control loop, in a cascade.

It is also worth commenting that –as a first option– the contact model in Section 4.2 was considered as a basis for this modification. However, this solution would have limited these force capabilities to the normal direction. To capture other behaviours, this contact force is decomposed into two components: the elastic response in the normal direction, and the tangential –elastic and friction– contributions. Subsequently, the previous adaptive control strategy is reformulated for multi-directional contact (with *unknown* mechanical parameters) and the force control loop is designed in a cascade. To present this extension, nonetheless, we firstly have to introduce this new contact model.

For the sake of clarity, the changes with respect to the formulation in the previous chapter are highlighted in **red** –instead of with respect to the non-adaptive control rationale in Section 4.1–. This is intended to facilitate the interpretation of this new solution and to identify the elements that correspond to the new outer force loop. Nevertheless, this extension is far from trivial due to coupling, becoming the theoretical demonstration much more intricate.

5.1 Contact model and equivalent manipulator kinematics

To take into account the contact behaviour of the interface in other directions the same pseudo-static elastic formulation with small deflections in (4.1) is employed, but becoming the force exerted by the EE

$$\mathbf{f}^{EE} = (k_e \mathcal{N} + k_e^\perp \mathcal{N}^\perp) (\bar{\mathbf{p}} - \bar{\mathbf{p}}_s) = K_e (\bar{\mathbf{p}} - \bar{\mathbf{p}}_s),$$

with $\mathcal{N}^\perp := I_{S_P} - \mathcal{N}$ the projection matrix in the orthogonal space of \mathcal{N} , i.e. any tangential direction in Fig. 5.1; $k_e^\perp \in \mathbb{R}^+$ its associated elastic/friction parameter (*unknown*); and K_e the matrix containing both the normal and tangential mechanical behaviour, and that is used in further derivations for brevity. In essence, this decomposition separates the mechanical response of the contact interface into two terms: resistance against direct penetration –with k_e – and resistance against deviation from the axis of penetration –via k_e^\perp –. Then, as previously done in (4.4), the model is used to obtain an enhanced estimation of the deflection speeds, reading

$$\dot{\delta} = -\hat{\Theta}_K^\top J_{fg}^s \dot{\gamma},$$

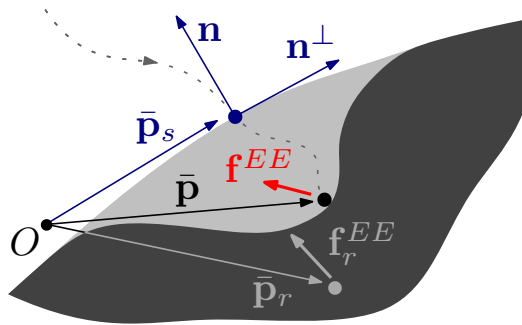


FIGURE 5.1: Definition of the multi-axis contact parameters using a undeformed/deformed superimposed plot, where the undeformed is in light gray and the deformed in dark grey.

where $\Theta_K \in \mathbb{R}^{3M \times M}$ is the new uncertain matrix including the effects of the contact forces in \mathcal{N}^\perp given by

$$\Theta_K := \begin{pmatrix} k_e K_\delta^{-1} & k_e^\perp K_\delta^{-1} & K_\delta^{-1} \end{pmatrix};$$

and $J_{fg}^s \in \mathbb{R}^{3M \times N}$ is the Jacobian considering these effects, namely

$$J_{fg}^s := \begin{pmatrix} \frac{\partial J_\delta^{t^\top}}{\partial \gamma} \bar{N} + J_\delta^{t^\top} \mathcal{N} J_\gamma^t \\ \frac{\partial J_\delta^{t^\top}}{\partial \gamma} \bar{N}^\perp + J_\delta^{t^\top} \mathcal{N}^\perp J_\gamma^t \\ - \frac{\partial J_{B,\delta}}{\partial \gamma} m_B \bar{G} \end{pmatrix},$$

with the extended derivative Jacobian matrices in the derivation maintaining the same form except for the new contact extended matrix, $\bar{N}^\perp \in \mathbb{R}^{N_{S_p} \times N}$, whose column-wise form reads

$$\bar{N}_k^\perp := \text{col}(\mathbf{0}_{(k-1)S_p}, \mathcal{N}^\perp(\bar{\mathbf{p}} - \bar{\mathbf{p}}_s), \mathbf{0}_{(N-k)S_p}).$$

Subsequently, (3.5) can be in turn rewritten as

$$\dot{\mathbf{p}} = \underbrace{\left(\hat{J}_T(\mathbf{q}^{RM}, \hat{\Theta}_K) \right)}_{\text{Estimate}} - \underbrace{J_\delta \tilde{\Theta}_K^\top J_{fg}^s}_{\text{Uncertain}} \dot{\gamma}, \quad (5.1)$$

with $\hat{J}_T \in \mathbb{R}^{S \times N}$ the modified equivalent Jacobian introduced taking into account both the flexible nature of the compliant RM and the response of the contact interface in the tangential directions, given by

$$\hat{J}_T := J_\gamma - J_\delta \hat{\Theta}_K^\top J_{fg}^s = J_{RM} \hat{J}_\Theta,$$

with

$$\hat{J}_\Theta := \begin{pmatrix} I_N \\ -\hat{\Theta}_K^\top J_{fg}^s \end{pmatrix}.$$

Accordingly, leaving the definition of the position error unchanged and defining the force error as $\boldsymbol{\eta} := \mathbf{f}_r^{EE} - \mathbf{f}^{EE} \in \mathbb{R}^{S_p}$ with \mathbf{f}_r^{EE} constant, their respective derivatives become

$$\dot{\mathbf{e}} = \underbrace{\dot{\mathbf{p}}_r - \hat{J}_T \dot{\gamma}}_{\text{Estimate}} + \underbrace{J_\delta \tilde{\Theta}_K^\top J_{fg}^s \dot{\gamma}}_{\text{Uncertain}}, \quad (5.2a)$$

$$\dot{\boldsymbol{\eta}} = - \underbrace{\hat{K}_e J_\gamma^t \dot{\gamma}}_{\text{Estimate}} - \underbrace{\tilde{K}_e J_\gamma^t \dot{\gamma}}_{\text{Uncertain}}, \quad (5.2b)$$

with $\hat{K}_e := \hat{k}_e \mathcal{N} + \hat{k}_e^\perp \mathcal{N}^\perp$ and $\tilde{K}_e := K_e - \hat{K}_e$ used to take into account the adaptive estimation of the parameters k_e, k_e^\perp and its associated error.

5.2 Control design

Considering the changes induced by the contact model into (5.2), the strategy in (4.9) is enhanced with force control (see Fig. 5.2) via the variation of the references, reading

$$\dot{\boldsymbol{\xi}} = K_I \hat{J}_T K_\gamma (\hat{J}_T^\top K_P \mathbf{e} + J_\gamma^\top \hat{K}_e \boldsymbol{\eta}) - K_\xi \boldsymbol{\xi}, \quad (5.3a)$$

$$\dot{\gamma} = K_\gamma \hat{J}_T^\top (K_P \mathbf{e} + K_I \boldsymbol{\xi}) + K_\eta J_\gamma^\top \hat{K}_e \boldsymbol{\eta}, \quad (5.3b)$$

$$\dot{\mathbf{p}}_r = \hat{J}_T (K_\gamma + K_\eta) J_\gamma^\top \hat{K}_e \boldsymbol{\eta} - \sigma_p K_P \mathbf{e}, \quad (5.3c)$$

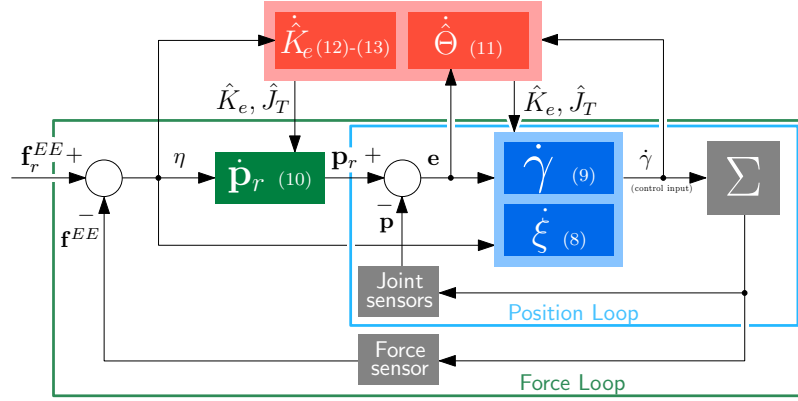


FIGURE 5.2: Close-loop control schematic with the inner position and outer force loops, highlighting the integral inverse kinematics core in blue, the force-aware reference variation law in green, the adaptive parameters (including the new \hat{K}_e) in orange, and the associated equations to obtain each of these in brackets.

where K_ξ, K_I, K_P and K_γ remain positive definite and symmetric, and the definite positive matrix $K_\eta \in \mathbb{R}^{N \times N}$ and the scalar gain $\sigma_p > 0$ are introduced. Associated to these changes, the update law in (4.10) is modified and two adaptive laws more are added to the new adaptive core given by

$$\dot{\hat{\Theta}}_K = \Gamma_\Theta J_{fg}^s \hat{\gamma} \mathbf{e}^\top K_P J_\delta, \quad \hat{\Theta}_K(0) = \Theta_K^0, \quad (5.4a)$$

$$\dot{\hat{k}}_e = \text{Proj}(\varpi_N, \rho(\hat{k}_e)), \quad \rho(\hat{k}_e(0)) \leq 0, \quad (5.4b)$$

$$\dot{\hat{k}}_e^\perp = \text{Proj}(\varpi_{N^\perp}, \rho(\hat{k}_e^\perp)), \quad \rho(\hat{k}_e^\perp(0)) \leq 0, \quad (5.4c)$$

where $\Gamma_\Theta \in \mathbb{R}^{3M \times 3M}$ remains positive definite but changes its size, the function $\varpi_\Xi \in \mathbb{R}$ is defined as

$$\varpi_\Xi(\xi, \mathbf{e}, \eta) := -\Gamma_\Xi \eta^\top \Xi J_\gamma^t \hat{\gamma}, \quad \Gamma_\Xi \in \mathbb{R}^+,$$

with $\Gamma_\Xi \in \mathbb{R}^+$; and the projector operator for scalar parameters $\hat{\kappa} \in \mathbb{R}$ can be written as

$$\text{Proj}(\varpi, \rho(\hat{\kappa})) := \begin{cases} (1 - \rho(\hat{\kappa})) \varpi & \rho(\hat{\kappa}), \rho(\hat{\kappa})' \varpi > 0 \\ \varpi & \text{otherwise} \end{cases},$$

with $\rho: \mathbb{R} \rightarrow \mathbb{R}$ a convex function whose threshold values are given by $\rho(\kappa_t) = 0$ and its upper bound values satisfy $\rho(\kappa_l) = 1$. In particular, a second order polynomial with symmetry around the mean of the maximum and minimum values $\kappa_l = \hat{\kappa}_M, \hat{\kappa}_m$ s.t. $\hat{\kappa}_M > \hat{\kappa}_m > 0$ is chosen for this strategy, reading

$$\rho(\hat{\kappa}) := \frac{\left(\hat{\kappa} - \frac{\kappa_M + \kappa_m}{2}\right)^2}{(1 - \beta^2) \left(\frac{\kappa_M - \kappa_m}{2}\right)^2} - \frac{\beta^2}{1 - \beta^2},$$

being its threshold given by $\kappa_t = (\kappa_M + \kappa_m)/2 \pm \beta(\kappa_M - \kappa_m)/2 > 0$, for $\beta \in (0, 1)$.

Remark 5.1. It is worth highlighting the increase in complexity of (5.3) and (5.4) when compared to (4.9) and (4.10). This necessary change corresponds to the reduction of the information given to the controller. While in the previous position controller the contact stiffness K_e was both unidirectional and *known* from an impedance control point of view, in here the proposed approach is expected to adapt to forces exerted in several directions whose mechanical behaviour is completely unknown, and to converge to a force reference in computable time.

Proposition 5.1. Consider the uncertain system in (5.2), and assume that $\text{rank}(J_{RM}) = S$ and $\text{rank}(J_\gamma^t) = S_p$, along with the control laws in (5.3) and its associated adaptive update laws in (5.4). Then, upon defining the augmented system error as $\chi_a := \text{col}(\xi, \mathbf{e}, \boldsymbol{\eta}) \in \mathbb{R}^{2S+S_p}$, the closed-loop inverse kinematics of the complete system for any constant force reference \mathbf{f}_r^{EE} reads

$$\dot{\chi}_a = \hat{\mathcal{A}}(\mathbf{q}^{RM}, \hat{\Theta}_K, \hat{K}_e)\chi_a + \tilde{\mathcal{B}}(\mathbf{q}^{RM}, \hat{\Theta}_K, \hat{K}_e)\dot{\gamma}, \quad (5.5)$$

with

$$\hat{\mathcal{A}} = \begin{pmatrix} -K_\xi & K_I \hat{J}_T K_P & K_I \hat{J}_{T,\gamma} \hat{K}_e \\ -\hat{J}_T K_I & -(\hat{J}_T + \sigma_p I_{S \times S}) K_P & \hat{J}_{T,\gamma} \hat{K}_e \\ -\hat{K}_e \hat{J}_{T,\gamma}^\top K_I & -\hat{K}_e \hat{J}_{T,\gamma}^\top & -\hat{K}_e \mathcal{J}_\gamma \hat{K}_e \end{pmatrix},$$

$$\tilde{\mathcal{B}} = \begin{pmatrix} \emptyset_{S \times N} \\ J_\delta \tilde{\Theta}_K^\top J_{fg}^s \\ -\hat{K}_e J_\gamma^t \end{pmatrix},$$

and $\hat{J}_{T,\gamma} := \hat{J}_T K_\gamma J_\gamma^t \in \mathbb{R}^{S \times S_p}$, $\mathcal{J}_\gamma := J_\gamma^t K_\eta J_\gamma^t \in \mathbb{R}^{S_p \times S_p}$. Moreover, χ_a , \mathbf{p}_r , $\hat{\Theta}_K$, \hat{k}_e and \hat{k}_e^\perp are globally bounded, and the zero equilibrium of χ_a is asymptotically stable –or equivalently $(\mathbf{p}, \mathbf{f}^{EE})$ is guaranteed to converge to $(\mathbf{p}_r, \mathbf{f}_r^{EE})$ –.

Proof. The first claim is evident considering the definition of the position and force errors in (5.2) and combining it with (5.1) and (5.3). For the second and third ones, let us choose the radially unbounded and positive definite Lyapunov function candidate given by

$$V_a := \frac{1}{2} \chi_a^\top \mathcal{K} \chi_a + \frac{1}{2} \text{Tr}(\tilde{\Theta}_K^\top \Gamma_\Theta^{-1} \tilde{\Theta}_K) + \frac{1}{2} \frac{(\tilde{k}_e)^2}{\Gamma_N} + \frac{1}{2} \frac{(\tilde{k}_e^\perp)^2}{\Gamma_{N^\perp}}, \quad (5.6)$$

with

$$\mathcal{K} = \begin{pmatrix} I_S & \emptyset_S & \emptyset_{S \times S_p} \\ \emptyset_S & K_P & \emptyset_{S \times S_p} \\ \emptyset_{S_p \times S} & \emptyset_{S_p \times S} & I_{S_p} \end{pmatrix} > 0.$$

Subsequently, the derivative of (5.6) reads

$$\begin{aligned} \dot{V}_a &= \chi_a^\top \mathcal{K} \dot{\chi}_a + \text{Tr}(\tilde{\Theta}_K^\top \Gamma_\Theta^{-1} \dot{\tilde{\Theta}}_K) + \frac{\tilde{k}_e \dot{\tilde{k}}_e}{\Gamma_N} + \frac{\tilde{k}_e^\perp \dot{\tilde{k}}_e^\perp}{\Gamma_{N^\perp}} \\ &= \chi_a^\top \mathcal{K} \hat{\mathcal{A}} \chi_a + \chi_a^\top \mathcal{K} \tilde{\mathcal{B}} \dot{\gamma} + \text{Tr}(\tilde{\Theta}_K^\top \Gamma_\Theta^{-1} \dot{\tilde{\Theta}}_K) + \frac{\tilde{k}_e \dot{\tilde{k}}_e}{\Gamma_N} + \frac{\tilde{k}_e^\perp \dot{\tilde{k}}_e^\perp}{\Gamma_{N^\perp}}. \end{aligned}$$

Due to the skew-symmetry of the product $\mathcal{K} \hat{\mathcal{A}}$, this derivative becomes

$$\begin{aligned} \dot{V}_a &= -\xi^\top K_\xi \xi - \mathbf{e}^\top K_P (\hat{J}_T + \sigma_p I_S) K_P \mathbf{e} - \boldsymbol{\eta}^\top \hat{K}_e \mathcal{J}_\gamma \hat{K}_e \boldsymbol{\eta} + \chi_a^\top \mathcal{K} \tilde{\mathcal{B}} \dot{\gamma} \\ &\quad + \text{Tr}(\tilde{\Theta}_K^\top \Gamma_\Theta^{-1} \dot{\tilde{\Theta}}_K) + \frac{\tilde{k}_e \dot{\tilde{k}}_e}{\Gamma_N} + \frac{\tilde{k}_e^\perp \dot{\tilde{k}}_e^\perp}{\Gamma_{N^\perp}} \\ &= -\xi^\top K_\xi \xi - \mathbf{e}^\top K_P (\hat{J}_T + \sigma_p I_S) K_P \mathbf{e} - \boldsymbol{\eta}^\top \hat{K}_e \mathcal{J}_\gamma \hat{K}_e \boldsymbol{\eta} + \mathbf{e}^\top K_P J_\delta \tilde{\Theta}_K^\top J_{fg}^s \dot{\gamma} - \boldsymbol{\eta}^\top \hat{K}_e J_\gamma^t \dot{\gamma} \\ &\quad + \text{Tr}(\tilde{\Theta}_K^\top \Gamma_\Theta^{-1} \dot{\tilde{\Theta}}_K) + \frac{\tilde{k}_e \dot{\tilde{k}}_e}{\Gamma_N} + \frac{\tilde{k}_e^\perp \dot{\tilde{k}}_e^\perp}{\Gamma_{N^\perp}} \\ &= -\xi^\top K_\xi \xi - \mathbf{e}^\top K_P (\hat{J}_T + \sigma_p I_S) K_P \mathbf{e} - \boldsymbol{\eta}^\top \hat{K}_e \mathcal{J}_\gamma \hat{K}_e \boldsymbol{\eta} \\ &\quad + \text{Tr} \left[\tilde{\Theta}_K^\top \left(J_{fg}^s \dot{\gamma} \mathbf{e}^\top K_P J_\delta - \Gamma_\Theta^{-1} \dot{\tilde{\Theta}}_K \right) \right] - \frac{\tilde{k}_e}{\Gamma_{k_e}} \left[\text{Proj}(\varpi_N, \rho(\hat{k}_e)) - \varpi_N \right] \\ &\quad - \frac{\tilde{k}_e^\perp}{\Gamma_{k_e^\perp}} \left[\text{Proj}(\varpi_{N^\perp}, \rho(\hat{k}_e^\perp)) - \varpi_{N^\perp} \right] \end{aligned}$$

$$\leq -\xi^\top K_\xi \xi - \mathbf{e}^\top K_P (\hat{\mathcal{J}}_T + \sigma_p I_S) K_P \mathbf{e} - \boldsymbol{\eta}^\top \hat{K}_e \mathcal{J}_\gamma \hat{K}_e \boldsymbol{\eta} \leq 0,$$

where for the last steps, (5.4) is used and $\hat{\mathcal{J}}_T + \sigma_p I_S > 0, \forall \sigma_p > 0$. Then, since $V_a > 0$ and $\dot{V}_a \leq 0$, the second claim follows.

Let us now move to the third claim. Since the closed-loop system is autonomous and the conditions for the first claim are met, LaSalle's Invariance Principle is invoked. For that purpose, the largest invariant set included in the residual set given by $\dot{V}_a = 0$ is analysed, namely

$$\Omega_V := \left\{ \chi_a \in \mathbb{R}^{2S+S_p} : \xi = \mathbf{0}, \mathbf{e} = \mathbf{0}, J_\gamma^\top \hat{K}_e \boldsymbol{\eta} = \mathbf{0} \right\}.$$

Accordingly, the residual dynamics in this problem are trivial, and only fixed points belong to the largest invariant set and the analysis is reduced to determine all non desired equilibria, only remaining to rule out the equilibrium in $J_\gamma^\top \hat{K}_e \boldsymbol{\eta} = \mathbf{0}$. As $\text{rank}(J_\gamma^\top) = S_p$ by assumption, this Jacobian induces an injective map on $\hat{K}_e \boldsymbol{\eta}$. Moreover, the definition of the projector operators guarantees that $\hat{k}_e, \hat{k}_e^\perp \neq 0$, thus ensuring by the matrix determinant lemma that

$$\begin{aligned} \det(\hat{K}_e) &= \hat{k}_e^\perp \det \left[I_{S_p} + \left(\frac{\hat{k}_e}{\hat{k}_e^\perp} - 1 \right) \mathbf{n} \mathbf{n}^\top \right] \\ &= \hat{k}_e^\perp \left[1 + \mathbf{n}^\top \left(\frac{\hat{k}_e}{\hat{k}_e^\perp} - 1 \right) \mathbf{n} \right] \det(I_{S_p}) \\ &= \hat{k}_e, \end{aligned}$$

and hence, that \hat{K}_e is invertible. Therefore $\hat{K}_e \boldsymbol{\eta} = \mathbf{0} \Leftrightarrow \boldsymbol{\eta} = \mathbf{0}$, thus concluding the proof. \square

Remark 5.2. In contrast to Proposition 4.1, the control strategy in Proposition 5.1 relies on changing the references of the inner position (including orientation) loop, and hence, the assumption on $\dot{\mathbf{p}}_r = \mathbf{0}$ is no longer needed.

Remark 5.3. Interestingly, the conditions found in Proposition 5.1 for the force regulation are –somehow– relaxed with respect to Proposition 4.1 –as evinced from the directly injective map for the position error in \dot{V}_a –. This comes from the extra information fed back by the force sensor and the introduction of the term associated with σ_p in (5.3c).

Remark 5.4. It should be finally highlighted that no matrix inversion is needed in this case neither (see Remark 4.3), thus avoiding unbounded responses near singularities.

K_P		K_I		K_ξ		K_γ				K_γ			
\bar{p}	$\bar{\alpha}$	\bar{p}	$\bar{\alpha}$	\bar{p}	$\bar{\alpha}$	1	2	3	4	1	2	3	4
0.5949	0.0214	0.1610	0.0024	0.1200	0.1200	209.9	220.5	241.4	283.4	20.00	20.00	20.00	20.00

Γ_Θ						Other parameters								
Θ_1	Θ_2	Θ_3	Θ_4	Θ_5	Θ_6	σ_p	σ_Θ	Γ_{k_e}	$\Gamma_{k_e^\perp}$	k_M	k_m	k_M^\perp	k_m^\perp	β
257.1	1929	3857	51.43	385.7	771.4	0.3000	4.000	0.0040	0.0020	0.0120	0.0040	0.0120	0.0040	0.400

TABLE 5.1: Control gains of the modified benchmark application.

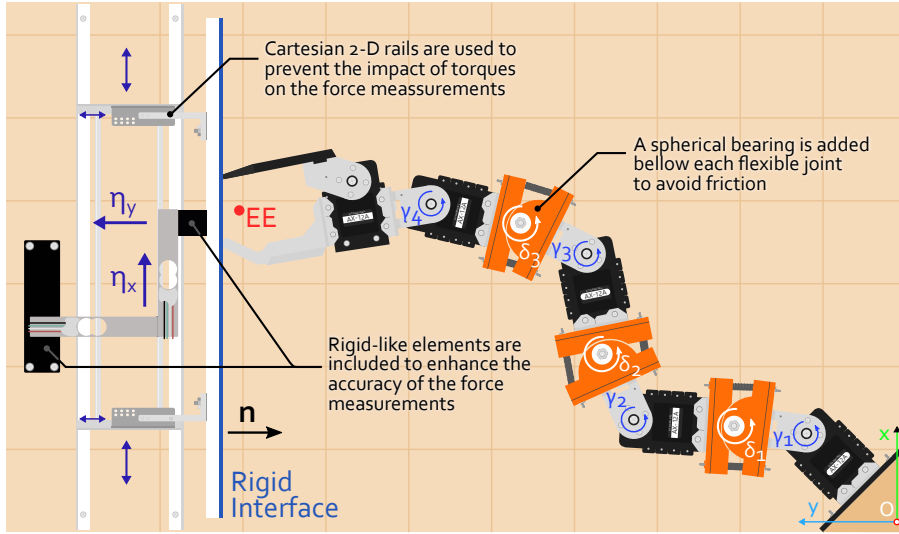


FIGURE 5.3: Experimental setting for the validation of the modified strategy, including the rigid contact interface, the force measuring system, and the consideration of frictionless displacement.

5.3 Experimental results

To demonstrate the force control capabilities while preserving the already proven softened response in Chapter 4, an experimental validation setting for the strategy is presented (see Fig. 5.3 and Section 7.2), being the control gains employed detailed in Table 5.1. The system is comprised of the same low-cost planar RM used in Chapter 4 (see Table 7.3), but adding force control capabilities and changing the computer board to increase the computational power, as discussed in Subsection 7.2.2. This has allowed the implementation of the solution with a stable frequency of 40 Hz throughout the experiment, printing the results stored in the SRAM afterwards to increase the efficiency of the application. Although the impact of this improvement is undeniable, we realised that some negative behaviours that were thought to be derived from the low control frequencies remained. Among them, nonetheless, one stood out: the slow drift of the adaptive parameters in $\hat{\Theta}$ that cause over-damping in the reference tracking. To cope with it, the standard σ -modification for adaptive control [126] is used in (5.4a), namely

$$\dot{\hat{\Theta}}_K = \Gamma_{\Theta} J_{fg}^s \dot{\gamma} \mathbf{e}^T K_P J_{\delta} - \sigma_{\Theta} \hat{\Theta}_K,$$

thus preserving stability.

Once the system is presented, let us introduce the validation scenarios. Their purpose is to evince the force control capabilities while preserving the softened and robust response of the position controller in Chapter 4. Accordingly, the three proposed scenarios are:

1. A position tracking mission that mimics the unperturbed scenario in the unmodified controller (Subsection 4.4.1), focused on proving the robust capabilities –including the modifications above– and studying the implications of the hardware modifications.
2. A simplified force control scenario in which the EE is already close to the contact interface, chosen to validate the main contribution of this modification separately.
3. A mixed mission including both displacement and force control phases with a sole controller organically switching between modes due to its cascade approach, to show an example of application in which other alternatives would have demanded high-level switches –and *ad-hoc* modifications to reduce the risk of their associated transients–.

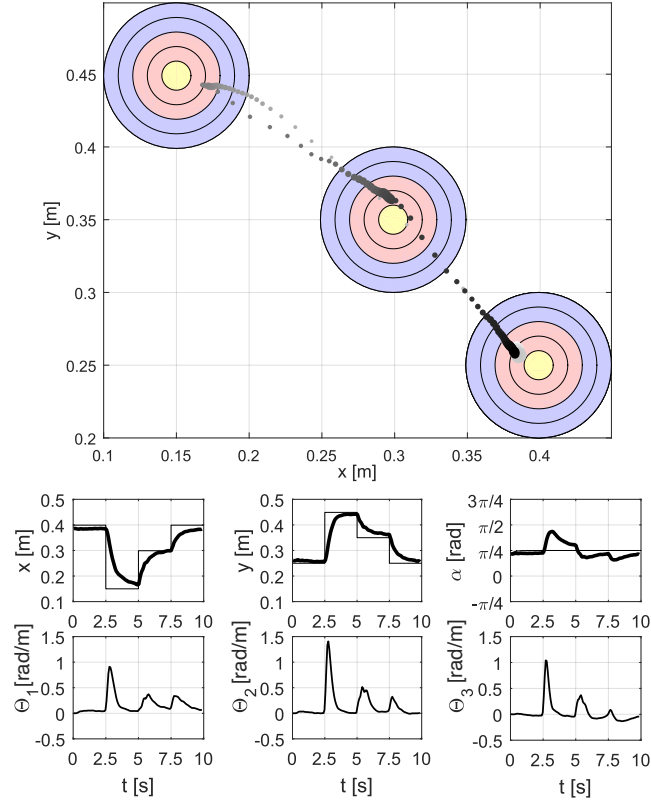


FIGURE 5.4: Results of the unperturbed case with the XY trajectory of the EE represented using equally time-spaced points with different size and lightness to reflect both speed and time (smaller is faster and darker is later), and where waypoints are highlighted as targets, on the top; the Cartesian position and orientation of the EE (being their references identified as thinner lines), on the centre; and the adaptive parameters for \mathcal{N} , on the bottom (their counterparts for \mathcal{N}^\perp were neglectable in this scenario).

Finally, it is worth noting that apart from the figures included in this thesis, a video of the validation experiments can be found in <https://youtu.be/ZtxBORTufP8>.

5.3.1 Unperturbed scenario

Firstly, the controller is tested in a scenario without contact, as in Chapter 4. This analysis is conducted to study the advances derived from the hardware improvements, i.e. the response with the retuned gains for higher control frequencies. As evinced in Fig. 5.4, these include the reduction of the step response time (from ~ 0.9 s to ~ 0.6 s) while retaining the first-order-like behaviour. In turn, it is worth noting that this design behaviour has been also softened when compared to the previous case, both because of the higher control frequencies and of the inclusion of the σ -modification. As the reasons for the former are trivial, let us focus on the latter. The Θ adaptive parameters produce a dampening-like response in brusque displacements, i.e. when $\dot{\gamma}$ is relatively high in modulus. This reduces the oscillations associated to the flexible modes on the cost of slowing down the fine convergence. What the σ -modification produces in the solution is a reduction of these parameters in this last phase (see the bottom plots in Fig. 5.4), thus avoiding their main disadvantage. Moreover, this implies that the gains associated to this adaptive module can be increased to further differentiate these two phases without hindering the manipulation system.

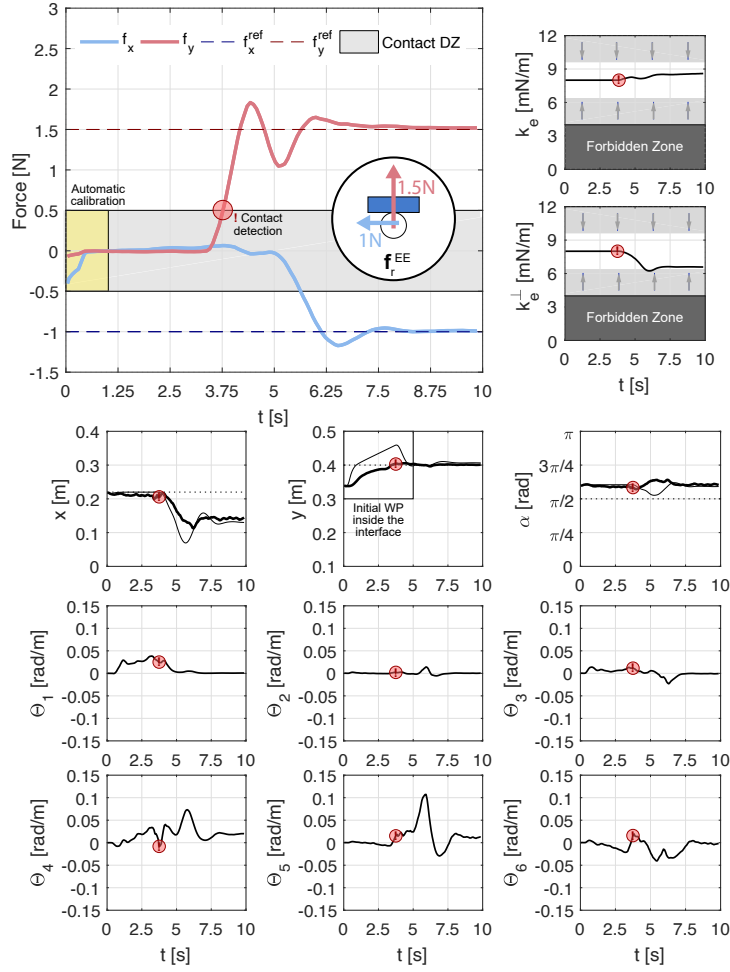


FIGURE 5.5: Results of the simplified contact force scenario: force tracking and adaptive parameters on the top (with projector influence and contact detection highlighted); Cartesian position and orientation on the centre (using thinner lines for modified references according to the outer force control loop in contrast to the original references, dotted); and adaptive parameters on the bottom.

5.3.2 Contact force scenario

Once the basis of the strategy has been validated in a comparison with the already robust solution in Chapter 4, we focus on the main advance of this modification: the force control capabilities. For that purpose, a force reference of $\mathbf{f}_r^{EE} = [-1, 1.5]^T \text{ N}$ is commanded to the system, which is initially close to the contact point. Even for this complex reference, the solution is capable of converging to both force components in less than 10 s, as shown in Fig. 5.5. Meanwhile, the inner position loop converges to the force-shaped position reference, as expected. This process, nonetheless, is not only produced by the concurrence of the position to its reference, but also by the tendency of the reference to the actual position of the manipulator when the force commands are met, in a way that resembles a rendez-vous.

To obtain this coupled convergence, some other factors have a significant –but indirect– impact. Firstly, the contact parameters evolve to change the rates of variation of the reference: smoothing them when the forces are below their references and exciting them when these are excessive so that the over-force is quickly corrected. Secondly, the dampening parameters associated to \mathcal{N} in $\hat{\Theta}$ are substantially smaller than in the oscillation-intensive previous case, mainly damp-

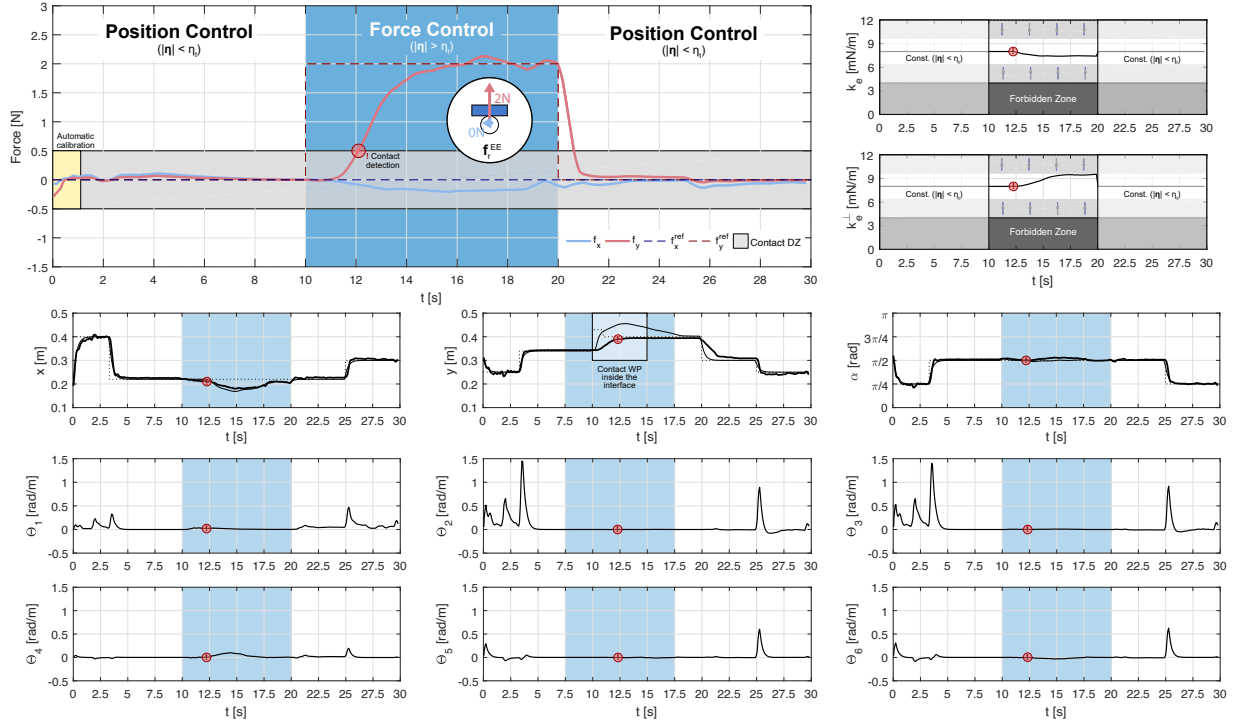


FIGURE 5.6: Results of the mixed contact/non-contact scenario, with the force tracking and its associated adaptive parameters on the top (with highlighted projector influence zones), the Cartesian position and orientation tracking in the centre (with initial references dotted and force-shaped references as thinner lines), and the whole set of adaptive parameters on the bottom.

ening the first contact. Finally, the impact of the novel adaptive parameters for \mathcal{N}^\perp demand a profound analysis. In contrast to their counterpart for the normal direction, these clearly evolve away from the initial contact. However, when the data of the tangential position is considered (in this case, x), it can be deduced that they are responding to the reconfiguration of the EE in that direction after contact. Accordingly, we can conclude that after contact the terms in $\hat{\Theta}$ for both directions soften the oscillations induced by the reconfiguration of the EE pose needed to meet the force demands in all directions, thus extending the already proven robust response in translation to force control. However, this extension is demonstrated in an *ad-hoc* scenario in which other factors, such as the possible discordances between the dampening of abrupt position changes and of reconfigurations for force control, are avoided.

5.3.3 Mixed scenario

To cover these, the final validation experiment is conducted for $\mathbf{f}_r^{EE} = [0, 2]^\top \text{N}$ (pressing without exerting tangential forces, as when attaching a sensor using some adhesive). As exhaustively shown in Fig. 5.6, both unperturbed displacement and force control can be performed using the exactly same strategy –i.e. not changing the control gains or artificially switching between different modules– without the cost of negative alterations during the transition between these phases. Instead, the proposed approach relies on the inherent cancellation of the outer loop when the forces detected are below a threshold imposed to rule out parasitic feedback.

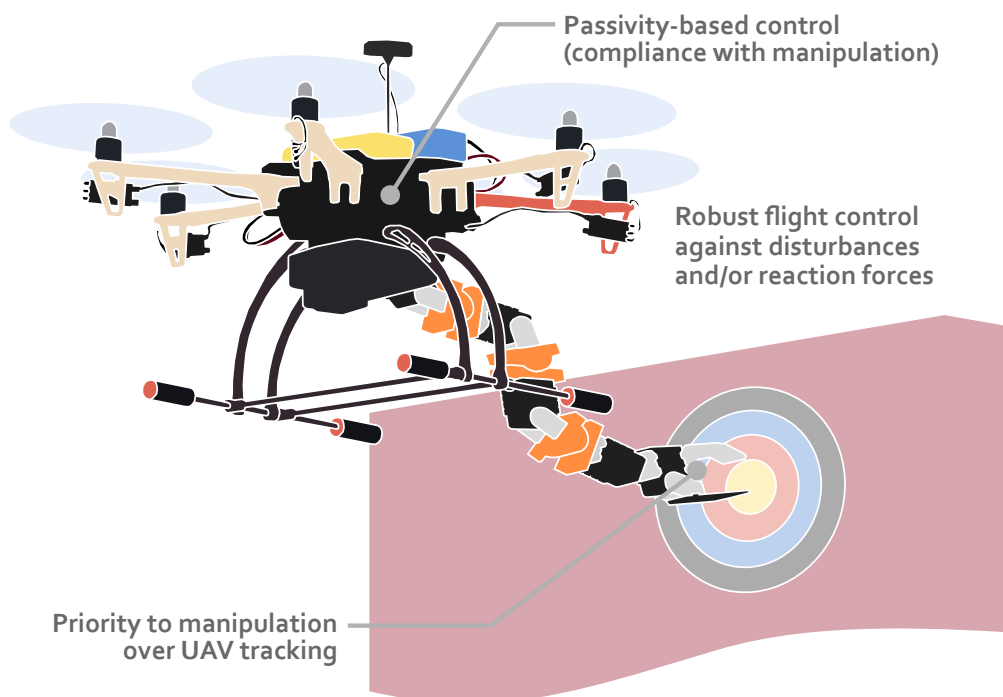
Once the validation in this mixed scenario is presented, we move to analysing the details of the strategy for this experiment. Firstly, it is worth noting that the force response in this case presents more dampening than in the previous scenario. One possible reason for this behaviour

could be that the force reference commanded in this case demands a less involved re-configuration during the contact phase, as evinced by the smoother evolution of the $\hat{\Theta}$ parameters associated to the tangential direction. In turn, this dampening could be the reason behind the more agile variations of the adaptive contact parameters, even to the point of activating the projector operator. Nonetheless, this does not seem to have any significantly negative impact on the convergence of both the position and force loops. Secondly, the results for the $\hat{\Theta}$ parameters are consistent with the previous scenarios, with two minor comments: i) their difference in order of magnitude between contact and displacement make their variation in the former case hard to notice, and ii) the terms associated to \mathcal{N}^\perp in the adaptive matrix are clearly noticeable after contact, in contrast to both the same experiment before this interaction and the results in the unperturbed scenario.

5.4 Summary of the chapter

In this chapter, a strategy including force control capabilities against uncharacterised interfaces is presented. This is achieved by including an outer control loop shaping the position references on top of the already robust controller in the previous chapter, in a cascade approach. Due to this structure, the strategy is capable of automatically transitioning –without changing any control gain– between position and force modes, with the inherent operational benefits.

Robust decentralised control of aerial manipulators



Highlights:

- Decentralised nonlinear strategy based on prioritising manipulation via subordinate tasks.
- Stability analysis throughout AM mission without assuming perfect tracking of the RM state.
- In-depth numerical validation focused on the robustness of the strategy.

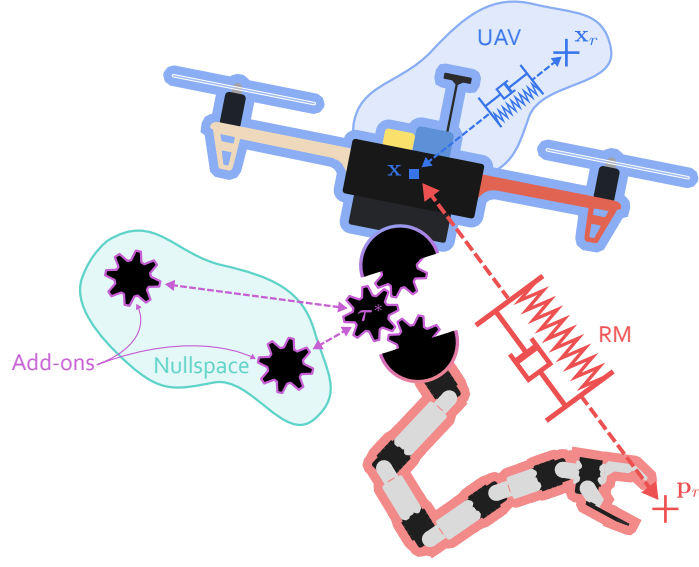


FIGURE 6.1: Coordinate control strategy analogy.

Moving the research branch focused on controlling aerial robots via decentralised paradigms (Section 2.3), a manipulation-aware strategy fitting the coupled nature of these aerial systems is proposed [C1, C4]. This strategy is based on passivity-based control, hence allowing to enrich the UAV controller with a robust formulation while giving priority to the manipulation task, in a compliant-like fashion. Moreover, the controller for fixed manipulators presented in [127] is adapted to this formulation, including a task to minimise the UAV-RM torque mismatch inside a relaxed inverse kinematics formulation. Altogether, the system prioritises the convergence of the EE at the cost of the fine tracking of the UAV, as depicted in Fig. 6.1 in an analogy to springer-dampers compliance, where:

- The platform is allowed to move within a region around its reference (in blue), thus virtually adding extra DoF. These are used for self-accommodation against external disturbances or internal algorithms to prevent incidents, but without negatively impacting the success of the manipulation mission.
- The EE target (in red) acts as the hard constraint of the problem (from a relaxed optimisation point of view, nonetheless), being the whole system accommodated to these commands under strict safety and accuracy conditions.
- The interconnection between these two systems is represented as a gearbox pinpointing the optimal ratio (in purple, representing the optimisation problem), where nullspace control add-ons (region in turquoise) are used for this purpose.

Moreover, the following assumptions are in order to simplify the problem and, hence, obtain the proposed strategy

1. The platform is an underactuated coplanar multirotor.
2. The RM is redundant ($N > S$) with rigid revolute joints controlled in angular speeds by servomotors.
3. The problem is studied in the longitudinal plane of the aerial manipulator, which is considered the main operational direction of the mission.
4. The state of the AM is available and/or measurable.

Remark 6.1. A brief comment on the reasons behind some of these assumptions is in order. Firstly, the coplanarity of the rotors delimits the scope of the analysis, not implying –however– that the proposed solution could not be adapted for other typologies, such as tilted-rotor platforms. Secondly, the rigid and redundant nature of the RM allows the possibility of implementing secondary tasks via its nullspace, one of the main novelties of this strategy. Ultimately, the planar aerial system considered as a benchmark for the longitudinal dynamics captures all the essential nonlinearities of a 3D application. In fact, many practical aerial missions are 2D solutions immersed in a 3D workspace, in which the yaw angle is left as an external parameter to redirect the manipulation plane.

Finally, some practical concerns are discussed to complete the implementation of the solution before conducting a numerical validation based on realistic simulations, for which the blunt-body aerodynamic model of multirotor platforms in Section 3.2 is employed.

6.1 IDA-PBC control rationale

As extensively discussed in [99] and [C1], the Interconnection and Damping Passivity-Based Control (IDA-PBC) was introduced in [128] to regulate underactuated mechanical systems whose form could be described as

$$\dot{\mathbf{x}}_H = \mathcal{S}_{2n} \nabla_{x_H} H + \mathcal{G} \mathbf{F}, \quad (6.1)$$

where the state vector is $\mathbf{x}_H := \text{col}(\mathbf{q}, \mathbf{s}) \in \mathbb{R}^{2n}$ –with $\mathbf{s} \in \mathbb{R}^n$ the generalised momenta¹–, \mathcal{S}_{2n} is the symplectic matrix, $H : \mathbb{R}^{2n} \mapsto \mathbb{R}$ denotes the Hamiltonian, $\mathcal{G} := [\mathcal{O}_{m \times n}, G(\mathbf{q})^\top]^\top$ –being $G \in \mathbb{R}^{n \times m}$, $G^\perp \in \mathbb{R}^{(n-m) \times n}$ a full-rank left annihilator (i.e. $G^\perp G = \mathcal{O}_{(n-m) \times m}$)–, and $\mathbf{F} := \text{col}(\mathbf{T}, \boldsymbol{\tau}^{RM}) \in \mathbb{R}^m$ is the aerial manipulation control input, with $m = N_r + N$. To achieve this regulation, the open loop must be shaped so that it matches a desired and Port-Controlled Hamiltonian closed-loop structure given by

$$\dot{\mathbf{x}}_H = \mathcal{J}_H(\mathbf{x}_H) \nabla_{x_H} H_d, \quad (6.2)$$

with $\mathcal{J}_H \in \mathbb{R}^{2n \times 2n}$ the generalised Hamiltonian matrix and H_d the desired form of H . This reshaping is obtained through the former, that both assures that (6.1) and (6.2) match and that H_d is a Lyapunov function. Then, let us equate these equations and left multiply them by

$$\begin{pmatrix} \mathcal{G}^\top \\ \mathcal{G}^\perp \end{pmatrix} \{ \mathcal{S}_{2n} \nabla_{x_H} H + \mathcal{G} \mathbf{F} = \mathcal{J}_H(\mathbf{x}_H) \nabla_{x_H} H_d \},$$

giving

$$\mathbf{F} = \mathcal{G}^\dagger (-\mathcal{S}_{2n} \nabla_{x_H} H + \mathcal{J}_H \nabla_{x_H} H_d), \quad (6.3a)$$

$$\mathcal{O}_{n-m} = \mathcal{G}^\perp (-\mathcal{S}_{2n} \nabla_{x_H} H + \mathcal{J}_H \nabla_{x_H} H_d). \quad (6.3b)$$

While (6.3a) indicates the required value for the force control input, (6.3b) sets the Partial Differential Equations (PDEs) to be satisfied by \mathcal{J}_H s.t. $\mathcal{J}_H^\top + \mathcal{J}_H \leq 0$.

However, in the case studied here –corresponding to a simple mechanical system–, the Hamiltonian can be written as the sum of the kinetic and potential energy, i.e. $H = 1/2 \mathbf{s}^\top B^{-1}(\mathbf{q}) \mathbf{s} + V(\mathbf{q})$, thus becoming the terms in (6.2)

$$H_d := 1/2 \mathbf{s}^\top B_d^{-1}(\mathbf{q}) \mathbf{s} + V_d(\mathbf{q}), \quad (6.4a)$$

¹Although this is not the conventional notation for momenta in the literature, it has been chosen to avoid any possible confusion with the EE position, \mathbf{p} , in Chapters 4 and 5.

$$\mathcal{J}_H := \begin{pmatrix} \mathcal{O}_{n \times n} & B^{-1}B_d \\ -B_d B^{-1} & J_2 - GK_v G^\top \end{pmatrix}, \quad (6.4b)$$

with $J_2 \in \mathbb{R}^{n \times n}$ a skew-symmetric matrix whose closed form reads

$$J_2(\mathbf{x}_H) = \sum_{i=1}^{n(n-1)/2} \mathbf{s}^\top B_d^{-1} \alpha_i^J W_i,$$

for some functions $\alpha_i^J \in \mathbb{R}^n$ and W_i a basis for skew-symmetric matrices. Finally, after the derivation of the PDEs (see [129, 130]), (6.3) becomes

$$\mathcal{F}(B, V, B_d, V_d, J_2) := \nabla_q H - B_d B^{-1} \nabla_q H_d + J_2 \nabla_p H_d, \quad (6.5a)$$

$$\mathcal{KE}(B, B_d, J_2) := \frac{1}{2} G^\perp [\nabla_q (\mathbf{s}^\top B^{-1} \mathbf{s}) - B_d B^{-1} \nabla_q (\mathbf{s}^\top B_d^{-1} \mathbf{s}) + 2J_2 B_d^{-1} \mathbf{s}] = \mathcal{O}_{n-m}, \quad (6.5b)$$

$$\mathcal{PE}(B, V, B_d, V_d) := G^\perp (\nabla_q V - B_d B^{-1} \nabla_q V_d) = \mathcal{O}_{n-m}. \quad (6.5c)$$

Finally, for any B_d, V_d that satisfy (6.5) and a force input reading $\mathbf{F} = G^\dagger \mathcal{F} - K_v G^\top \nabla_s H_d$, the system in (6.1) is shaped to take the Hamiltonian form in (6.2) with (6.4b); and if K_v is symmetric and definite positive, it also becomes dissipative since

$$\dot{H}_d = -\nabla_s H_d^\top GK_v G^\top \nabla_s H_d \leq 0. \quad (6.6)$$

Furthermore, if B_d is positive definite in the neighbourhood of $\mathbf{q}_* \in \mathbb{R}^n$ and $\mathbf{q}_* = \operatorname{argmin} V_d(\mathbf{q})$ is a stable equilibrium of the desired closed-loop behaviour according to the desired Hamiltonian in (6.4a), \mathbf{q}_* is asymptotically stable –if and only if– it is locally detectable from its natural passive output $G^\top \nabla_s H_d$.

6.2 PBC redesign

To represent the reaction torque demanded by RM, τ_d , a featured distance directly related with it should be selected. Among the possible candidates,

$$\mathbf{L}_{CG}(t) := \overrightarrow{QB}$$

is chosen for compactness, in contrast to [C1] –in which

$$\mathbf{L}(t) := \overrightarrow{P_0 B}$$

was taken– (see Fig. 6.2). Although these two options are associated to different reference points, a mismatch in one implies a mismatch in the other one. Moreover, a passivity-based controller for the aerial manipulation system using the direct coordinates is not explicitly computable –as discussed in [127]– and, hence, a new set of coordinates based on [130] must be introduced. For this purpose, let us consider the longitudinal dynamics of the aerial manipulator depicted in Fig. 6.2, with the rigid N -link RM taken into account solely through its centre of gravity. Then, the new set of coordinates $\bar{\mathbf{q}} \in \mathbb{R}^4$ –with its associated generalised momenta $\bar{\mathbf{s}} \in \mathbb{R}^4$ – reads:

- \bar{q}_1 : the horizontal position of the centre of gravity of the AM, denoted in Fig. 6.2 as CG;
- \bar{q}_2 : the vertical position of the centre of gravity of the AM, positive in the direction of the gravity acceleration;

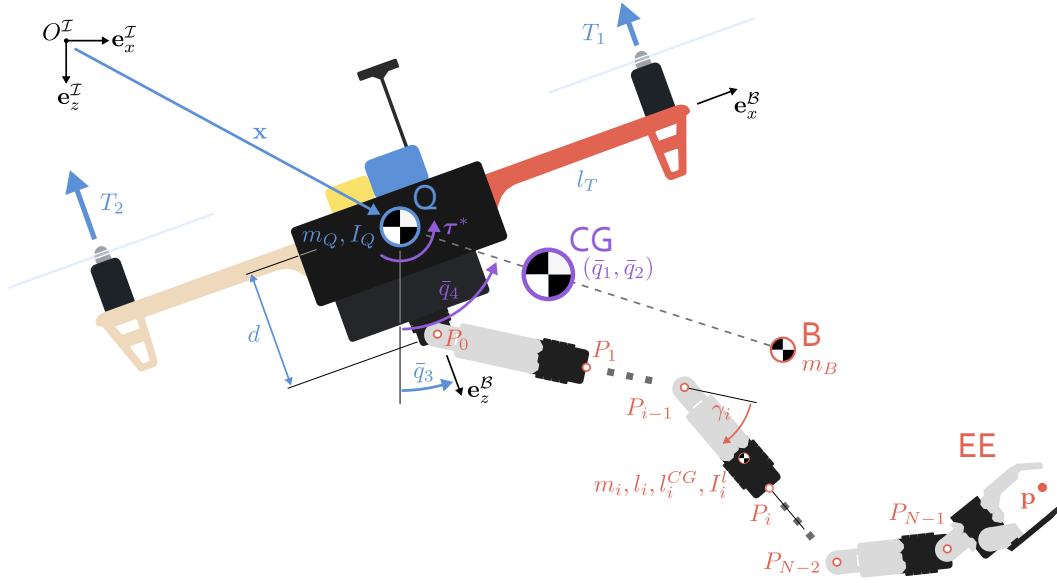


FIGURE 6.2: Sketch of the longitudinal dynamics of the AM.

- \bar{q}_3 : the rotation component of the UAV perpendicular to the OXZ plane with respect to the inertial frame, which in here is assimilated by design to the pitch angle; and
- \bar{q}_4 : its equivalent for the CG of the aerial system.

Correspondingly, the control input in this problem, \mathbf{F} , includes the thrust vector and the demanded reaction torque, i.e. $\mathbf{F} = \text{col}(\mathbf{T}, \tau_d) = \text{col}(T_1, T_2, \tau_d) \in \mathbb{R}^3$. In turn, the underactuation of this input is revealed in the left-hand nullspace of G which is spanned by $G^\perp = [\cos \bar{q}_3, -\sin \bar{q}_3, 0, 0]$. Taking into account these forms, the solution can be summarised (only with the strictly needed relations and parameters) as

$$B_d = \begin{pmatrix} m_Q + m_B & 0 & m_{13} & 0 \\ 0 & m_Q + m_B & 0 & 0 \\ m_{13} & 0 & I_{RM} & 0 \\ 0 & 0 & 0 & (m_Q + m_B) \frac{m_Q}{m_B} L_{CG}^2(\bar{\mathbf{q}}) \end{pmatrix}, \quad (6.7a)$$

$$J_2|_{ij} = \begin{cases} -\frac{m_{13}s_4}{I_{RM}L_{CG}(\bar{\mathbf{q}})} \frac{\partial L_{CG}(\bar{\mathbf{q}})}{\partial \bar{q}_3}, & \text{for } \{i, j\} = \{1, 4\}, \\ 0, & \text{otherwise.} \end{cases} \quad (6.7b)$$

$$V_d = -(m_Q + m_B)g_0 \frac{I_{RM}}{m_{13}} \ln(\cos \bar{q}_3) + \frac{k_1}{2} \left(\bar{q}_2 - \bar{q}_{2*} - \frac{I_{RM}}{m_{13}} \ln(\cos \bar{q}_3) \right)^2 \\ + \frac{k_2}{2} \left(\bar{q}_3 - \frac{m_{13}}{I_{RM}} (\bar{q}_1 - \bar{q}_{1*}) \right)^2 + \frac{k_3}{2} (\bar{q}_4 - \bar{q}_{4*})^2, \quad (6.7c)$$

with $L_{CG} := |\mathbf{L}_{CG}|$, $g_0 = |\mathbf{g}_0|$, I_{RM} the inertia of the whole RM at Q and $m_{13}, k_1, k_2, k_3 \in \mathbb{R}^+$ control gains; and where interested readers are referred to the complete derivation in [130]. For the sake of clarity, let us also define $(\hat{\cdot}) := (\cdot)|_{L_{CG}=\hat{L}_{CG}}$ for \hat{L}_{CG} an estimate of L_{CG} .

Proposition 6.1. The dynamic state feedback given by

$$\mathbf{F} = \hat{G}^\dagger \hat{\mathcal{F}} - K_v \hat{G}^\top \nabla_s \hat{H}_d, \quad (6.8a)$$

$$\dot{\tilde{\sigma}}_0 = -k_\sigma \tilde{\sigma}_0 + k_\sigma \varrho' \sin(\bar{q}_3 - \bar{q}_4) \bar{\mathbf{s}}^\top A \hat{G}^\dagger \hat{\mathcal{F}}, \quad (6.8b)$$

with $\hat{\mathcal{F}}$ from (6.5a) –together with (6.7)–, $\varrho \in \mathcal{K}_\infty$, and the terms $\tilde{\sigma}_0$ and A defined along the proof, ensures that:

- (i) The equilibrium $\text{col}(\bar{\mathbf{q}}, \mathbf{s}, \tilde{\sigma}_0) = \text{col}(\bar{\mathbf{q}}_*, \boldsymbol{\vartheta}_n, 0)$ is uniformly stable for any constants $m_{13} < \sqrt{(m_Q + m_B)I_{RM}}$ and $k_\sigma \in \mathbb{R}^+$, and scalars $k_v^0, k_v^1 \in \mathbb{R}^+$ s.t.

$$K_v > (k_v^0 + k_v^1 |\mathbf{s}|) I_3.$$

Moreover, the domain of attraction is given by

$$\Omega_H := \left\{ \text{col}(\bar{\mathbf{q}}, \mathbf{s}, \tilde{\sigma}_0) \in \mathbb{R}^2 \times \left(-\frac{\pi}{2}, \frac{\pi}{2}\right) \times \mathbb{R}^6 \right\}.$$

- (ii) If $\dot{L}_{CG}, \ddot{L}_{CG} \in \mathcal{L}_\infty$, then all the trajectories satisfy

$$\lim_{t \rightarrow \infty} \left\| \begin{bmatrix} G(\bar{\mathbf{q}}(t))^\top \nabla_s \hat{H}_d(\bar{\mathbf{q}}(t), \mathbf{s}(t)) \\ \tilde{\sigma}_0(t) \end{bmatrix} \right\| = 0, \quad t \geq 0.$$

- (iii) If the RM is locked at a fixed position, the aforementioned equilibrium $\text{col}(\bar{\mathbf{q}}, \mathbf{s}, \tilde{\sigma}_0) = \text{col}(\bar{\mathbf{q}}_*, \boldsymbol{\vartheta}_n, 0)$ is asymptotically stable in the domain of attraction Ω_H .

Proof. Let us firstly pull out the disturbances in (6.8a) with respect to the nominal case by defining the error of estimation $\tilde{L}_{CG} := \hat{L}_{CG} - L_{CG}$, namely

$$\mathbf{F} = \hat{G}^\dagger \hat{\mathcal{F}} + \underbrace{K_v \Pi \bar{\mathbf{s}} - \sigma A \hat{G}^\dagger \hat{\mathcal{F}}}_{=: \mathbf{F}_\sigma},$$

with $\Pi := -(I_3 + \sigma A^\top)$, $\sigma := \tilde{\sigma}_0 \sin(\bar{q}_3 - \bar{q}_4)$, $\tilde{\sigma}_0 := \tilde{L}_{CG}/2l_T$, and

$$A := \underbrace{\begin{bmatrix} 1 \\ -1 \\ 2l_T \end{bmatrix}}_{:=\pi} \begin{bmatrix} 1 & 1 & 0 \end{bmatrix}.$$

Then, as G is full rank m , $GG^\dagger + G^\dagger G^\perp = I_n$ holds directly from the Fundamental Theorem of Linear Algebra, where G^\dagger stands for the right-hand Moore-Penrose pseudoinverse of G^\perp , i.e. $G^\dagger := (G^\perp)^\top (G^\perp (G^\perp)^\top)^{-1}$. Therefore, by propagating the disturbance throughout the closed-loop dynamics, it becomes

$$\begin{aligned} \dot{\mathbf{s}} &= -\nabla_{\bar{\mathbf{q}}} H + G(G^\dagger \hat{\mathcal{F}} + \mathbf{F}_\sigma) \\ &= -\nabla_{\bar{\mathbf{q}}} H + (I_n - G^\dagger G^\perp) \hat{\mathcal{F}} + G \mathbf{F}_\sigma \\ &= -\nabla_{\bar{\mathbf{q}}} H + \nabla_{\bar{\mathbf{q}}} \hat{H} - \hat{B}_d \hat{B}^{-1} \nabla_{\bar{\mathbf{q}}} \hat{H}_d + \hat{J}_2 \nabla_s \hat{H}_d \\ &\quad - G^\dagger G^\perp (\nabla_{\bar{\mathbf{q}}} \hat{H} - \hat{B}_d \hat{B}^{-1} \nabla_{\bar{\mathbf{q}}} \hat{H}_d + \hat{J}_2 \nabla_s \hat{H}_d) + G \mathbf{F}_\sigma \\ &= -\frac{1}{2} \nabla_{\bar{\mathbf{q}}} (\mathbf{s}^\top \tilde{B}^{-1} \mathbf{s}) - \hat{B}_d \hat{B}^{-1} \nabla_{\bar{\mathbf{q}}} \hat{H}_d + \hat{J}_2 \nabla_s \hat{H}_d \\ &\quad - G^\dagger [\mathcal{K} \mathcal{E}(\hat{B}, \hat{B}_d, \hat{J}_2) + \mathcal{P} \mathcal{E}(\hat{B}, V, \hat{B}_d, V_d)] + G \mathbf{F}_\sigma \\ &= -\hat{B}_d \hat{B}^{-1} \nabla_{\bar{\mathbf{q}}} \hat{H}_d + \hat{J}_2 \nabla_s \hat{H}_d - \boldsymbol{\Delta}_s + G \mathbf{F}_\sigma, \end{aligned}$$

with $\boldsymbol{\Delta}_s := \nabla_{\bar{\mathbf{q}}} (\mathbf{s}^\top \tilde{B}^{-1} \mathbf{s})/2$, $\tilde{B}^{-1} := B^{-1} - \hat{B}^{-1}$; and where the last step is obtained using the solutions of nominal cases of (6.5) for $\hat{V} = V$ and $\hat{B}_d \hat{B}^{-1} = B_d B^{-1}$, thus becoming

$\mathcal{PE}(\hat{B}, V, \hat{B}_d, V_d) = \mathcal{PE}(B, V, B_d, V_d) = \emptyset_{n-m}$ and $\mathcal{KE}(\hat{B}, \hat{B}_d, \hat{J}_2) = \emptyset_{n-m}$ –even for $\hat{B} \neq B$ and $\hat{B}_d \neq B_d$ – with the estimated Hamiltonian defined as

$$\hat{H}_d(\mathbf{x}_H, t) := \frac{1}{2} \mathbf{s}^\top \hat{B}_d^{-1}(\mathbf{q}) \mathbf{s} + V_d(\mathbf{q}).$$

Accordingly, the derivative of the estimated Hamiltonian –which is no longer a Lyapunov function– along the closed-loop system trajectories reads

$$\begin{aligned} \dot{\hat{H}}_d &= \nabla_p \hat{H}_d^\top (\hat{J}_2 \nabla_s \hat{H}_d - \Delta_s + G \mathbf{F}_\sigma) + \frac{\partial \hat{H}_d}{\partial t} \\ &= \bar{\mathbf{s}}^\top \underbrace{(K_v \Pi \bar{\mathbf{s}} - \sigma A G^\dagger \hat{\mathcal{F}})}_{\mathbf{F}_\sigma} - \nabla_p \hat{H}_d^\top \Delta_s + \frac{\partial \hat{H}_d}{\partial t}, \end{aligned}$$

where it becomes clear that the purely dissipative form in (6.6) no longer holds due to the mismatch collected in \mathbf{F}_σ –associated to inexact input– and Δ_s –to include the effects of unmatched terms in the PDEs–. Nonetheless, in what follows we will demonstrate that these terms are in the column span of matrix G . For any symmetric matrix $\mathcal{M} \in \text{span}(G)$, there is always a certain matrix $\tilde{\Pi}$ that allows displaying this matrix as $\mathcal{M} = G \tilde{\Pi} G^\top$. Accordingly, let us calculate these factorisations for

$$\begin{aligned} \frac{\partial \hat{H}_d}{\partial t} &= \frac{1}{2} \mathbf{s}^\top \frac{\partial \hat{B}_d^{-1}}{\partial t} \mathbf{s} = -\frac{1}{2} \mathbf{s}^\top \hat{B}_d^{-1} \overbrace{\frac{\partial \hat{B}_d}{\partial t}}^{\in \text{span}(G)} \hat{B}_d^{-1} \mathbf{s} \\ &= -\frac{1}{2} \mathbf{s}^\top \Pi_0 \mathbf{s}; \quad \quad \quad := \frac{\partial \tilde{B}}{\partial \tilde{q}_i} \in \text{span}(G) \\ \Delta_s &= \frac{1}{2} \sum_{i=3,4} \left(\mathbf{s}^\top \frac{\partial \tilde{B}^{-1}}{\partial \tilde{q}_i} \mathbf{s} \right) \mathbf{e}_i = \frac{1}{2} \sum_{i=3,4} \left(\nabla_p \hat{H}_d^\top \hat{B}_d \frac{\partial \tilde{B}^{-1}}{\partial \tilde{q}_i} \hat{B}_d \nabla_p \hat{H}_d \right) \mathbf{e}_i \\ &= \frac{1}{2} \sum_{i=3,4} \left(\bar{\mathbf{s}}^\top \Pi_i \bar{\mathbf{s}} \right) \mathbf{e}_i = \frac{1}{2} \left(\sum_{i=3,4} \mathbf{e}_i \bar{\mathbf{s}}^\top \Pi_i \right) \bar{\mathbf{s}}, \end{aligned}$$

where $\mathbf{e}_i \in \mathbb{R}^n$ denotes the i -th vector of the n -dimensional Euclidean basis. Using these forms, the derivative of the desired Hamiltonian estimate can be written as

$$\begin{aligned} \dot{\hat{H}}_d &= \frac{1}{2} \bar{\mathbf{s}}^\top \left(K_v \Pi + \Pi^\top K_v - \Pi_0 - \sum_{i=3,4} G^\dagger \mathbf{e}_i \bar{\mathbf{s}}^\top \Pi_i \right) \bar{\mathbf{s}} - \bar{\mathbf{s}}^\top \sigma A G^\dagger \hat{\mathcal{F}} \\ &\leq - (k_v^0 + k_v^1 |\bar{\mathbf{s}}|) |\bar{\mathbf{s}}|^2 - \bar{\mathbf{s}}^\top \sigma A G^\dagger \hat{\mathcal{F}}. \end{aligned}$$

The last inequality holds because the matrix Π is Hurwitz $\forall \sigma$, and then by Lyapunov theorem $\exists K_v > 0 : K_v \Pi + \Pi^\top K_v < 0$, hence existing functions k_v^0, k_v^1 that

$$\begin{aligned} k_v^0 &> 0, \\ k_v^1 &> \sum_{i=3,4} \frac{\|\Pi_i\|}{\|\hat{B}_d\|} > 0. \end{aligned}$$

To conclude the proof, let us define the time-varying Lyapunov function

$$V_H(\mathbf{x}_H, \tilde{\sigma}_0, t) := \varrho(\hat{H}_d) + \frac{\tilde{\sigma}_0^2}{2k_\sigma},$$

and calculate a bound for its derivative by using the results above and (6.8b), namely

$$\dot{V}_H \leq \varrho'(\hat{H}_d) (k_v^0 + k_v^1 |\bar{\mathbf{s}}|) - |\tilde{\sigma}_0|^2 \leq 0.$$

Then, the claims of this Proposition can be demonstrated one by one as follows:

- (i) Firstly, it is clear to see that \hat{H}_d is positive definite for RM revolute joints with any $m_{13} < \sqrt{(m_Q + m_B)I_{RM}}$ and $\bar{\mathbf{q}} \in \mathbb{R}^2 \times (-\frac{\pi}{2}, \frac{\pi}{2}) \times \mathbb{R}$; and that for some $\underline{\varrho}, \bar{\varrho} \in \mathcal{K}_\infty$ the Lyapunov function is bounded as $\underline{\varrho}(\mathbf{x}_H, \tilde{\sigma}_0) < V_H(\mathbf{x}_H, \tilde{\sigma}_0, t) < \bar{\varrho}(\mathbf{x}_H, \tilde{\sigma}_0)$. Taking then into account that $\dot{V}_H \leq 0$, any trajectory $(\mathbf{x}_H(t), \tilde{\sigma}_0(t), t)$ is bounded $\forall t \geq 0$ and the equilibrium $\text{col}(\bar{\mathbf{q}}_*, \emptyset_n, 0)$ is uniformly stable. Furthermore, as V_H is radially bounded in the set Ω_H , the trajectories never leave it.
- (ii) Notice that \ddot{V}_H is bounded, and hence, \dot{V}_H is uniformly bounded. Then, since the chosen Lyapunov function is lower bounded and its derivative is semi-definite negative, Barbalat's Lemma ensures that $\lim_{t \rightarrow \infty} \dot{V}_H = 0$.
- (iii) Finally, let us consider the effect of the manipulation system locking on the stability of the system. If the RM is completely locked, the closed-loop of the whole system is autonomous and LaSalle's Invariance Principle can be directly invoked. Accordingly, all trajectories converge to $\lim_{t \rightarrow \infty} \dot{V}_H = 0$, $t \geq 0$, which contains the aforementioned equilibrium. Hence, we should analyse the largest invariant set included in the residual set

$$\Omega_{RM} := \{\Omega_H : \bar{\mathbf{s}} = \emptyset_n, \tilde{\sigma}_0 = 0\},$$

in which the V_H is constant, and hence \hat{H}_d is also constant, for instance $\hat{H}_d = c_{RM}$. Then, let $\bar{\mathbf{s}} := \nabla_s \hat{H}_d$, implying $\bar{\mathbf{s}} = 0$ that $\bar{\mathbf{s}} \in \text{span}((G^\perp)^\top)$, i.e. $\bar{\mathbf{s}} = \varsigma (G^\perp)^\top$ for any $\varsigma \in \mathbb{R}$. Altogether, we obtain that $\hat{H}_d = \varsigma^2(m_Q + m_B)/2 + V_d(\bar{\mathbf{q}}) = c$. Nonetheless, since the equilibrium $\text{col}(\bar{\mathbf{q}}_*, \emptyset_n, 0) \in \Omega_{RM}$ and by construction $V_d(\bar{\mathbf{q}}_*) = 0$, $\varsigma^2(m_Q + m_B)/2 = c$ and, thus, ς must be constant and, in turn,

$$\dot{\hat{H}}_d = \nabla_q V_d^\top \dot{\bar{\mathbf{q}}} = 0.$$

Therefore, either i) $\dot{\bar{\mathbf{q}}} = \bar{\mathbf{s}} = \emptyset_n$, that implies that $\mathbf{s} = \emptyset_n$ and, so, $\varsigma = 0$; or ii) $\nabla_q V_d = \emptyset_n$. In both cases, the state rests at the equilibrium.

Thus, the proof is concluded. \square

Remark 6.2. As already commented, Proposition 6.1 ensures uniform stability in all the cases (i)-(iii) without assuming RM perfect instant tracking, in contrast to [99] and [C1]. It should be noted that this property also provides the ability of withstanding external constant disturbances, such as wind gusts. Moreover, these capabilities are improved with the RM locked –i.e. in the navigation phase–, being even achieved asymptotic stability.

Remark 6.3. It should be highlighted that an estimate for the control gains in Proposition 6.1 is straightforward to obtain, reading

$$\begin{aligned} \Pi_0 &= \frac{2m_Q(m_Q + m_B)}{m_B} \hat{L}_{CG} \dot{\hat{L}}_{CG} \Pi_0^*, \quad \Pi_0^* := \frac{\boldsymbol{\pi} \boldsymbol{\pi}^\top}{(2l_T)^2}, \\ \Pi_i &= - \frac{2m_Q(m_Q + m_B)}{m_B} \hat{L}_{CG}^2 \frac{\partial \ln(L_{CG}/\hat{L}_{CG})}{\partial \bar{q}_i} \Pi_0^*. \end{aligned}$$

6.3 iCLIK

Considering the direct kinematics of the RM in (3.6), a desired speed of the EE, \mathbf{v}_d –later used to track the EE reference \mathbf{p}_r –, and a torque demand emanating from the IDA-PBC solution, τ_d , let us define the relaxed optimisation problem for the aerial manipulation mission as

$$\Psi_{AM}(\mathbf{q}, \dot{\mathbf{q}}, \ddot{\mathbf{q}}) := \frac{1}{2} \left(|\mathbf{v}_d - \dot{\mathbf{p}}|^2 + \alpha_{ID} |\dot{\gamma}|_W^2 + \alpha_\tau \rho_\tau(\tilde{\tau}) \right), \quad (6.9)$$

where $\alpha_{ID}, \alpha_\tau \in [0, 1)$ are the weights of the main tasks accompanying the tracking term, $W \in \mathbb{R}^{N \times N}$ is a diagonal normalising matrix used to shape the distribution of RM speeds according to their associated inertia, and $\rho_\tau : \mathbb{R} \rightarrow \mathbb{R}^+$ is a normalising function for $\tilde{\tau} := \tau_d - \tau^*$ –being τ^* an estimate of the torque transmitted to the platform–. By deriving this criterion with respect to the chosen control input $\dot{\gamma}$, we obtain that the value that solves this optimisation problem can be written as

$$\dot{\gamma} = \underbrace{(J_\gamma^\top J_\gamma + \alpha_{ID} W - \alpha_\tau \rho'_\tau \tau_1^*)^{-1} J_\gamma^\top}_{:= J_\gamma^\# \in \mathbb{R}^{N \times S}} (\mathbf{v}_d + \mathbf{v}_{uAV}),$$

with $\tau_1^* := (\partial^2 \tau^* / \partial \dot{\gamma}^2) / 2$ and \mathbf{v}_{uAV} as defined in (3.6). For the sake of improving the conditioning of the solution, let us define the weighting matrix $W_N := \alpha_{ID} W - \alpha_\tau \rho'_\tau \tau_1^* \in \mathbb{R}^{N \times N}$ and, in turn, express it in its equivalent $\mathbb{R}^{S \times S}$ form, $W_S := (J_\gamma J_\gamma^\top)^{-1} J_\gamma W_N J_\gamma^\top$ –that requires that the solution stays away from singularities, i.e. $\det(J_\gamma J_\gamma^\top) \neq 0$ –, thus reading the pseudoinverse of the solution

$$\begin{aligned} J_\gamma^\# &= J_\gamma^\top (J_\gamma J_\gamma^\top + W_S) \\ &= J_\gamma^\dagger \left[I_S - W_S (J_\gamma J_\gamma^\top + W_S)^{-1} \right] \\ &= J_\gamma^\dagger (I_S - \bar{W}_S), \end{aligned}$$

with $\bar{W}_S := W_S (J_\gamma J_\gamma^\top + W_S)^{-1} \in \mathbb{R}^{S \times S}$ a matrix whose norm is $\|\bar{W}_S\| < 1$ by definition. Furthermore, additional subtasks are included in the nullspace of J_γ to leverage the over-actuation of the manipulation system via its associated projector

$$P_\gamma^\dagger := I_N - J_\gamma^\dagger J_\gamma^\top,$$

hence becoming the controller

$$\dot{\gamma} = \underbrace{J_\gamma^\dagger (I_S - \bar{W}_S)}_{J_\gamma^\#} (\mathbf{v}_d + \mathbf{v}_{uAV}) + \underbrace{P_\gamma^\dagger \sum_i}_{\text{Subtasks}} \dot{\gamma}_{0,i}, \quad (6.10)$$

where we recall that:

- $J_\gamma^\#$ is the pseudoinverse of this IK solution, shaped by the matrix W –introduced to modulate fast movements of the high-inertia joints– and by the interconnection torque –used to soften the coupling between the RM and the platform–.
- \mathbf{v}_d is the input vector, used to include the tracking error.
- $\dot{\gamma}_{0,i}$ encompasses subtasks not modifying the task space state of the AM in (3.6), but affecting the solution of the optimisation problem. They are used to consider additional criteria that cannot be included in the pseudoinverse.

Proposition 6.2. Consider the control law in (6.10) for

$$\mathbf{v}_d = \dot{\mathbf{p}}_r + \kappa(K_P \mathbf{e} + K_I \boldsymbol{\xi}), \quad (6.11)$$

with \mathbf{e} the EE tracking error and $\dot{\boldsymbol{\xi}} := \mathbf{e}$ its integral counterpart²; $K_P \in \mathbb{R}^{S \times S}$, $K_I := 2\epsilon\kappa K_P^2 \in \mathbb{R}^{S \times S}$ definite positive –for $\kappa \in \mathbb{R}^+$ and $\epsilon \in (0, 1)$ –. Then, upon defining the speed of the base³ as $\mathbf{v}_b := \dot{\mathbf{p}}_r + \mathbf{v}_{UAV}$, the degree of convergence of the proposed solution becomes

- (i) If $\mathbf{v}_b \in \mathcal{L}_\infty$, the closed-loop trajectories of the system are uniformly bounded,
- (ii) If \mathbf{v}_b is also bounded, let say $|\mathbf{v}_b| < \delta_d$, $\delta_d \in \mathcal{K}$, the zero equilibrium $\text{col}(\mathbf{e}, \boldsymbol{\xi}) = \mathbf{0}_{2S}$ is uniformly asymptotically stable.
- (iii) If $|\mathbf{v}_b| = 0$, i.e. from the point of view of the manipulator the problem is equivalent to a fixed base, the equilibrium $\text{col}(\mathbf{e}, \boldsymbol{\xi}) = \mathbf{0}_{2S}$ is exponentially stable.

Proof. Let us firstly choose the Lyapunov function given by

$$V_K := \frac{1}{2} \begin{bmatrix} \boldsymbol{\xi} \\ \mathbf{e} \end{bmatrix}^\top \begin{pmatrix} 2\kappa K_I K_P & K_I \\ K_I & K_P \end{pmatrix} \begin{bmatrix} \boldsymbol{\xi} \\ \mathbf{e} \end{bmatrix} > 0, \quad \text{if } \epsilon \in (0, 1),$$

and whose time derivative reads

$$\dot{V}_K = \begin{bmatrix} \boldsymbol{\xi} \\ \mathbf{e} \end{bmatrix}^\top \begin{pmatrix} 2\kappa K_I K_P & K_I \\ K_I & K_P \end{pmatrix} \begin{bmatrix} \mathbf{e} \\ \mathbf{v}_b - J_\gamma \dot{\gamma} \end{bmatrix}.$$

Defining the state vector $\mathbf{y} := \text{col}(K_P^2 \boldsymbol{\xi}, K_I \mathbf{e}) \in \mathbb{R}^{2S}$ and using the form of the control law in (6.10), the derivative of the Lyapunov function becomes

$$\dot{V}_K = -\kappa \mathbf{y}^\top (Q_0 - Q_w) \mathbf{y} + \left(2\kappa \epsilon \boldsymbol{\xi}^\top K_P + \mathbf{e}^\top \right) K_P \bar{W}_S \mathbf{v}_b \quad (6.12a)$$

$$\leq -\kappa \mathbf{y}^\top (Q_0 - Q_w) \mathbf{y} + \frac{\alpha_K}{2} |(2\kappa \epsilon K_P \boldsymbol{\xi} + \mathbf{e}) K_P|^2 + \frac{|\bar{W}_S \mathbf{v}_b|^2}{2\alpha_K} \quad (6.12b)$$

$$= -\kappa \mathbf{y}^\top (Q_\alpha - Q_w) \mathbf{y} + \frac{\|\bar{W}_S\|^2}{2\alpha_K} |\mathbf{v}_b|^2 \quad (6.12c)$$

$$\leq -\kappa \mathbf{y}^\top (Q_\alpha - Q_w) \mathbf{y} + \frac{|\mathbf{v}_b|^2}{2\alpha_K}, \quad (6.12d)$$

with

$$Q_\alpha(\alpha_K) := \begin{pmatrix} (2\kappa\epsilon)^2 \left(1 - \frac{\alpha_K}{2\kappa}\right) I_S & -\alpha\epsilon I_S \\ -\alpha\epsilon I_S & \left(1 - \frac{\alpha_K}{2\kappa} - 2\epsilon\right) I_S \end{pmatrix},$$

$$Q_w := \begin{pmatrix} (2\kappa\epsilon) I_S \\ I_S \end{pmatrix} \bar{W}_S \begin{pmatrix} (2\kappa\epsilon) I_S & I_S \end{pmatrix},$$

and being $Q_0 = Q_\alpha(0)$. Then, let us introduce a basis of the nullspace of Q_w , reading

$$\mathcal{N}_w := \begin{pmatrix} I_S \\ -(2\kappa\epsilon) I_S \end{pmatrix}.$$

The existence of α_K^* s.t. $Q_\alpha(\alpha_K^*) - Q_w > 0$ is hence guaranteed by Finler's Lemma since $\mathcal{N}_w^\top Q_\alpha \mathcal{N}_w > 0$ for any $\epsilon \in (0, 1)$, $\alpha_K > 0$. Altogether, we conclude that there must exist a computable constant c_K s.t.

$$\dot{V}_K \leq -c_K V_K + |\mathbf{v}_b|^2.$$

Taking this into account, the claims above can be proven one by one as follows:

²Not to be confused with its specifically formulated nonlinear homologous $\boldsymbol{\xi}$ in Chapters 4 and 5.

³To analyse the problem from the point of view of a static reference and a moving base.

- (i) If $\mathbf{v}_b \in \mathcal{L}_\infty$ -being $V_K(\emptyset_{2S}) = 0$, $V_K > 0$ for $(\xi, \mathbf{e}) \neq 0$ and radially unbounded-, then $\dot{V}_K < 0$ for $V_K > |\mathbf{v}_b|^2 / c_K$, and hence all trajectories are uniformly bounded.
- (ii) Although the closed-loop system is not autonomous, the Lyapunov function does not explicitly depend on time and it is radially unbounded. Taking this into account, $\delta_d \in \mathcal{K}$ ensures that $\dot{V}_K \leq -c_K^1 V_K$ for some constant $c_K^1 \in \mathbb{R}^+$, thus making the aforementioned equilibrium uniformly asymptotically stable.
- (iii) If $\mathbf{v}_b = \emptyset_S$, then (6.12a) implies that $\dot{V}_K < -c_K^2 V_K < 0$, $c_K^2 \in \mathbb{R}^+$ for any state different from the zero equilibrium, thus being this solution exponentially stable.

Thus concluding the proof. \square

Remark 6.4. It is worth noting that this control design also reduces the negative impact of one of the most critical issues for on-board applications: the sensitivity to numerical error. This phenomenon, in here coped with the strong convergence properties presented above, generally produces drift in the manipulation system positioning and vibrations. While the first affects the convergence to the desired EE pose to proceed with the operation phase; the second complicates any accuracy-demanding operation by reducing their probability of success per attempt, thus being needed to maintain the desired configuration for a time-window wide enough to assure a favourable outcome.

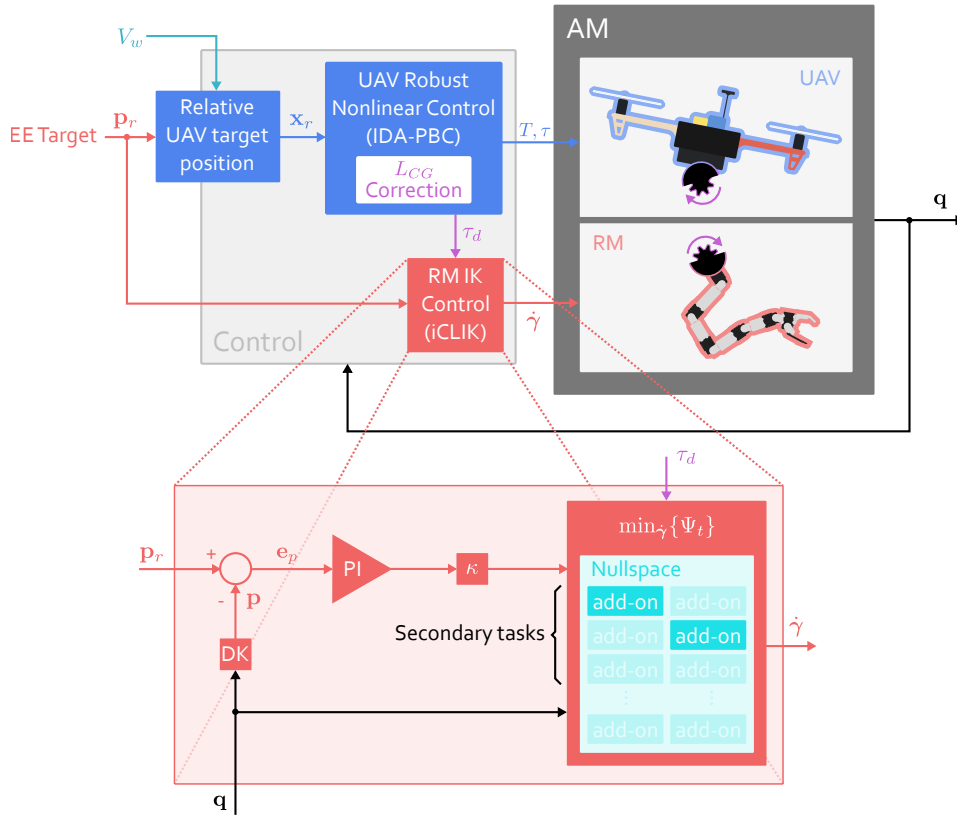


FIGURE 6.3: Block diagram of the whole aerial manipulation strategy.

6.4 Cascade nonlinear control strategy

In the previous sections, the decentralised controller for the subsystems of the AM have been thoroughly discussed. Nonetheless, an analysis of their combined actuation is essential to complete the whole aerial manipulation strategy. For that purpose, a stability analysis of the decentralised strategy, which is depicted as a block diagram in Fig. 6.3, is in here included.

Proposition 6.3. The cascade-like strategy presented in Propositions 6.1 and 6.2 –and more precisely in (6.8) and (6.10)– guarantees that all trajectories are uniformly bounded during the navigation and accommodation phases (Fig. 2.1). Moreover, if $|\mathbf{v}_b| < \delta_d$ for $\delta_d \in \mathcal{K}$, then the EE converges to its reference in finite time.

Proof. The proof is based on the cascade structure of the controller, such that it is a sequential application of Propositions 6.1 and 6.2. Firstly, in the navigation phase the RM is locked, thus being deduced from Proposition 6.1 (iii) that the target equilibrium is asymptotically stable. Accordingly, the AM can reach the approaching zone in finite time, and hence move to the accommodation phase. The whole state is then confined in the approaching zone, thus ensuring boundedness. In this transition, Proposition 6.1 (i) guarantees that the equilibrium is uniformly stable and, with the iCLIK control algorithm active, that $\mathbf{v}_b \in \mathcal{L}_\infty$. With this and Proposition 6.2 claim (i), all trajectories of the RM in this phase are uniformly bounded. Finally, when the system reaches the operation phase, \mathbf{v}_b is bounded and, according to Proposition 6.2 (ii), the EE is guaranteed to converge to this ultimate target in finite time, thus concluding the proof. \square

Remark 6.5. As the uniform stability of the whole solution is guaranteed throughout the design mission, there is no further need of introducing any assumption on instant switch between phases.

6.5 Implementation

Among the possible alternatives for the particularisation of the solution under different criteria, in this section the personal choices of the author are presented and discussed. Firstly, let us consider the cost functional that led to the RM position controller, (6.9). In there, two different elements are yet to be formulated: the diagonal weight matrix, W , and the estimate of the torque transmitted by the manipulation system to the platform, τ^* .

On the one hand, the matrix W is chosen to balance the distribution of the angular speeds commanded to the RM: smoothing the displacements of the high-inertia DoF of the manipulator and producing a more proactive response of the low-inertia ones; as follows

$$W := \frac{B_\gamma^W}{\text{trace}(B_\gamma^W)} \in \mathbb{R}^{N \times N},$$

with B_γ^W a diagonal matrix whose terms read $B_\gamma^W|_{ii} := B_\gamma|_{ii}$ for $i = 1, \dots, N$. On the other hand, the torque estimate is obtained using a concept similar to the structural sub-matrices reduction [131], as thoroughly discussed in [C1], reading

$$\tau^* := B_{\theta x}(\mathbf{q})\ddot{\mathbf{x}} + B_{\theta \gamma}(\mathbf{q})\ddot{\gamma} + \dot{\gamma}^\top c_{\theta \gamma \gamma}(\Theta)\dot{\gamma} + \nabla V_\theta(\mathbf{q}), \quad (6.13)$$

where the sub-indexes delimit the blocks of the inertia matrix used and, for the Christoffel symbol $c_{\theta \gamma \gamma}$, they indicate with respect which components of the AM state its inherent derivation is performed. Although this approach already simplifies the otherwise complex estimation of the

coupling torque, the nonlinearity of the function ρ_τ can still compromise the applicability of the solution. As the implementation of the proposed approach is discrete, the computational cost of $\rho_\tau \tau_1^*$ in (6.10) can be reduced –under the assumption of smooth changes– by using the value of the link torque in the previous sample, τ_0^* , namely

$$\rho'_\tau(\tilde{\tau})\tau_1^* = \rho'_\tau(\tau_d - \tau^*)c_{\theta\gamma\gamma} \approx \rho'_\tau(\tau_d - \tau_0^*)c_{\theta\gamma\gamma}.$$

Subsequently, to complete the cost functional the only factor which has not yet been defined is the normalising function, ρ_τ . Among different studied alternatives, it was finally decided to use a logarithmic function reading

$$\rho_\tau(\tilde{\tau}) := \log \left(1 + \frac{1}{2} \tilde{\tau}^2 \right),$$

for providing a reasonable trade-off between computational complexity and boundedness in both its original and derivative functions. Notice that the nonlinearity induced by this form makes $\rho_\tau \tau_1^*$ dependant on $\dot{\gamma}$, thus causing difficulties for the convergence of (6.10) if the aforementioned simplification is not considered.

Apart from the particularisation of the cost functional to shape the pseudoinverse matrix $J_{\gamma}^\#$, in this section we also propose a set of secondary tasks to be introduced via the homologous solution in (6.10). These can be defined as the gradient of a cost function, w_i , as

$$\dot{\gamma}_{0,i} := k_{0,i} \nabla_\gamma w_i(\gamma),$$

being the criteria chosen to add:

- w_1 , to reduce the quadratic deviation of the angular DoF of the manipulation system, and hence preventing extreme configurations, reading

$$w_1(\gamma) := -\frac{1}{2N} \sum_{j=1}^N \left(\frac{\gamma_j}{2\gamma_j^{max}} \right)^2;$$

- w_2 , to minimise the permanent impact of the coupling torque –not yet considered, as the core controller only perceives its derivative through $\rho_\tau \tau_1^*$ –, reading

$$w_2(\gamma) := -\log \left(1 + \frac{1}{2} (\tau_d - \nabla V_\theta)^2 \right).$$

As an addition to these criteria, a kernel-based collision avoidance solution based on the Saturation of the Null Space (SNS) technique [132] is also implemented. To adapt its approach for complex bounds, each of the (multidimensional) bounds is treated as an equivalent 0D obstacle representing the closest point to the EE, plus additional obstacles associated to the intersection of upper level bounds to improve the conditioning of the approach. Accordingly, the virtual repulsion force of the SNS is determined as the sum of individual repulsion actions and corrected accordingly. Moreover, it is also worth mentioning that additional saturations to the actuated DoF of the RM and its two first derivatives are included for the sake of the safety of the operation and to reflect the real behaviour of servomotor actuators.

Finally, although it is not completely essential for the approach, a normalisation of the controller is implemented via the parameter κ in (6.11). This is done to avoid the need of re-tuning for different operational points, hence simplifying the applicability of the solution. Among the possibilities covered by this modification, it is worth remarking that an appropriate scalar function can substitute this gain, e.g. sigmoid functions, without affecting the stability properties of the solution, as discussed in [C4].

ROBOT MANIPULATOR					UNMANNED AERIAL VEHICLE			
Link	l_i , m	l_i^{CG} , m	m_i , kg	I_i^l , kg m ²	d , m	l_T , m	m_Q , kg	I_Q , kg m ²
1	0.250	0.100	0.40	$8 \cdot 10^{-4}$	0.100	0.500	8.00	$8 \cdot 10^{-2}$
2	0.200	0.090	0.25	$5 \cdot 10^{-4}$				
3	0.150	0.068	0.15	$3 \cdot 10^{-4}$				
4	0.100	0.045	0.10	$2 \cdot 10^{-4}$				
5	0.06	0.036	$0.15 + \Delta m_{EE}$	$1 \cdot 10^{-4}$				

TABLE 6.1: Aerial manipulator model parameters for the benchmark application.

ROBOT MANIPULATOR								UNMANNED AERIAL VEHICLE					
K_P			K_I			$\alpha_{(\cdot)}$		K_v			k		
x	z	α	x	z	α	τ_d	ID	1	2	3	1	2	3
55	40	8.75	0.005	0.003	0.001	0.25	0.30	157.5	168.0	14.0	600	115	11

TABLE 6.2: Control parameters of the proposed solution.

6.6 Numerical validation

After presenting the theoretical contribution and the particularisation of the solution, in here the response of the solution is analysed in simulation. The benchmark application chosen for this purpose is characterised by $S_p = 2$, $S_\alpha = 1$, $N = 5$ and $n = 8$; the parameters in Table 6.1 and the control gains in Table 6.2. The simulation scenarios included in this analysis, which are focused on determining the positive –or negative– impact of using the strategy with the different secondary tasks proposed in outdoor applications, cover:

1. A comparison with a well-known nonlinear strategy for the control of UAVs, which is typically used in real systems not relying on linear controllers.⁴
2. A study of the behaviour of the solution close to obstacles with the SNS, to test its synergy with this task-based solution.
3. An analysis of the robust response of the strategy to EE mass uncertainty.

For the sake of completeness, it is worth detailing the realism-focused add-ons included in the simulation environment. Firstly, the outdoor nature of the mission is considered via the presence of wind disturbances in all the scenarios. For this purpose, both the windspeed and its influence on the system must be modelled. On the one hand, the wind conditions are generated using an approach similar to [133], i.e. an estimation of the power spectral density is used as a normalising transfer function that shapes a white noise source. To particularise this normalisation, the noise power is chosen to approximately coincide with the maximum airspeed resulting from the wind model. On the other hand, the explicit aerodynamic model in Section 3.2, which in turn derives from [C6], is employed to transform this wind model into dynamic disturbances, and its associated propulsive model is introduced to enrich the simulations. Additionally, white noise has been included to the simulated sensors of the solution to mimic the behaviour of the real hardware used in aerial robotics, being these coped with low-pass filters on the cost of producing delays.

⁴This category includes solutions directly evolving from linear controllers in which the inherent deterioration of their properties away from the equilibrium point or lack of disturbance rejection capabilities are mitigated with *ad-hoc* add-ons that do not alter their linear structure.

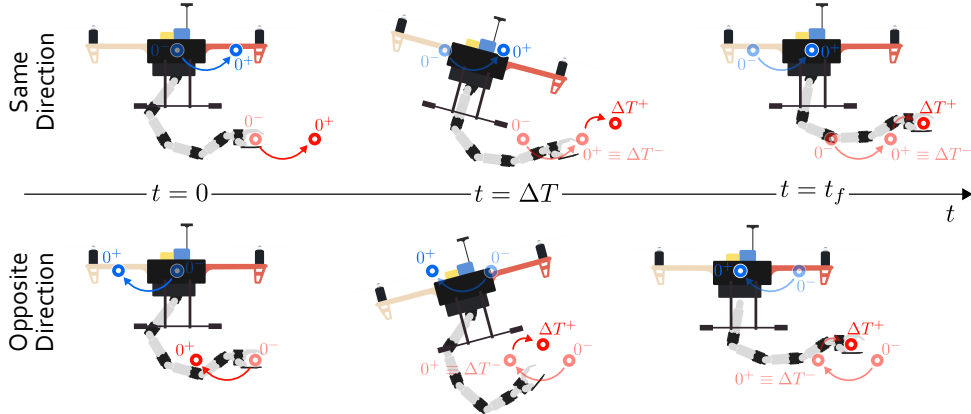


FIGURE 6.4: Reference changes for both UAV and RM in the two sub-cases for the comparison scenario: UAV displacement in the same direction of the RM extension and in the opposite direction. Each reference is labelled with its associated step time, denoting the super-indexes if the reference is pre-step (-) or post-step (+).

Remark 6.6. Before moving the focus into the results of the numerical validation, it is worth discussing the importance of the blunt-body aerodynamic model for this analysis. As already examined in Section 3.2, this characterisation induces realistic –and challenging– disturbances to the aerial robot outdoors. Accordingly, it can be used to estimate the real impact of the proposed controllers on outdoor applications, thus discarding residual improvements more related to the oversimplification of the numerical analysis than to the controllers themselves.⁵

6.6.1 Comparison with integral backstepping

The alternative solution chosen for this comparison is the integral backstepping (which is similar to the command-filtered backstepping in Appendix B, but without the smoothing behaviour of the filter) for the platform, and an inverse kinematics controller without the interconnection task for the RM. Firstly, let us briefly present the alternative control law for the UAV in 2D. If the UAV dynamic equations are written as

$$\begin{aligned} \dot{e}^1 &= e^x, & \dot{e}^x &= e^3, & \dot{e}^3 &= \ddot{x}_r - \mathbf{U}; \\ \dot{e}^4 &= e^\Theta, & \dot{e}^\Theta &= e^6, & \dot{e}^6 &= \ddot{\theta}_r - I_Q^{-1}\tau; \end{aligned}$$

where we recall that the virtual force input reads $\mathbf{U} := g\mathbf{e}_z - (T/m_Q)\mathcal{R}\mathbf{e}_z$, and in which the gyroscopic terms are also neglected; then, for a set of definite positive gain matrices Γ_i^j for $i = \{I, P, D\}$, $j = \{x, \theta\}$ –denoting the integral, proportional and derivative actions, respectively, shown in Table 6.3–, the solution for the position and attitude control loops becomes

$$\begin{aligned} \mathbf{U} &= \ddot{x}_r + \Gamma_I^x e^1 + \Gamma_P^x e^x + \Gamma_D^x e^3, \\ \tau &= I_Q \left(\ddot{\theta}_r + \Gamma_I^\theta e^4 + \Gamma_P^\theta e^\Theta + \Gamma_D^\theta e^6 \right), \end{aligned}$$

where it should be noted that the attitude references satisfy that the virtual control force is aligned with the thrust vector. Moreover, it is also worth recalling that the stability of this approach is only guaranteed when the gains ensure that the convergence of the inner attitude loop is substantially faster than their position equivalent, as in any of these cascade designs.

⁵It is also worth underscoring that this is not the only possible application of the blunt-body aerodynamic model. Apart from as a simulation add-on, the aerodynamic characterisation can be employed –for instance– as a key step in the design of aerodynamics-aware controllers and as a pre-training dataset for machine learning algorithms.

Γ_P			Γ_I			Γ_D		
x	z	θ	x	z	θ	x	z	α
5.0	10.0	250.0	0.1	0.3	150.0	4.5	9.0	90.0

TABLE 6.3: Integral backstepping control gains.

Decoupling step time, s		SAME DIRECTION				OPPOSITE DIRECTION				Mean value ⁶
		0	2.5	5	7.5	0	2.5	5	7.5	
OS, %	IDA-PBC	9.0	4.7	3.5	4.5	6.8	3.0	5.1	5.2	5.2
	Int. BS	11.8	13.1	14.9	9.7	7.2	10.2	7.9	26.2	12.6
	Δ (%)	-2.8	-8.4	-11.4	-5.2	-0.4	-7.2	-2.8	-21.0	-7.4
$t_s^{5\%}$, s	IDA-PBC	4.37	1.22	1.13	1.36	2.78	1.16	2.08	1.72	1.98
	Int. BS	3.20	2.13	2.18	2.08	1.74	2.40	4.75	3.29	2.72
	Δ (%)	36.6	-42.7	-48.2	-34.6	61.6	-51.7	-56.2	-47.7	-27.2
RMSE _s ⁷ , mm	IDA-PBC	1.42	1.57	1.59	1.59	1.56	3.11	1.55	1.73	1.77
	Int. BS	2.64	3.14	3.04	3.33	2.95	1.61	3.15	3.66	2.94
	Δ (%)	-46.2	-50.0	-47.7	-52.3	-47.1	-93.2	-50.8	-52.7	-39.8
t_r , s	IDA-PBC	2.71	1.34	1.21	1.44	2.45	1.27	1.73	1.39	1.69
	Int. BS	2.45	1.45	1.39	1.32	1.24	1.81	1.65	1.53	1.61
	$ \Delta $ (%)	10.6	7.6	12.9	9.1	97.6	29.83	4.8	9.2	5.0

TABLE 6.4: Comparison between the EE tracking of the proposed strategy and of an Integral Backstepping + CLIK decentralised solution without UAV-RM interconnection for similar rise times.

For the sake of a fair comparison, the criterion used to tune the alternative strategy and the simulation scenario must be clarified. On the one hand, as the targets of the UAV and RM controllers are not completely aligned, a trade-off between them –inherently downgrading their separate performances– is in order. To show the advantages of the solution, hence, the alternative controller is tuned to mimic the EE step rise time of the proposed solution, becoming the backstepping gains the ones shown in Table 6.3 and leaving the RM control gains unchanged. On the other hand, the scenario includes step references for both UAV and RM (see Fig. 6.4): 1) the AM, as a whole, is displaced either to the left or the right, and 2) the RM is extended rightwards with a delay $\Delta T = \{0; 2.5; 5; 7.5\}$ s, resulting in a prograde or retrograde deployment. With this approach, the self-accommodation capabilities of both strategies are in here compared in controlled conditions, thus providing enough information to determine the extent of the advances of the proposed solution under external disturbances. The results for this analysis are finally shown via Fig.6.5 –with the EE positions expressed with respect to the platform, i.e. $\mathbf{p}_{rel} := \mathbf{p} - \mathbf{x}$, to obtain clearer plots– and Table 6.4 –with the most significant metrics of both solutions–. Among the conclusions drawn from these results, the following points stand out:

- The compliance behaviour of the solution (Fig. 6.1) relaxes the tracking of the UAV target position to improve its counterpart for the EE reference, hence prioritising the accuracy of the manipulation. This can be seen in the wider oscillations of the platform using the proposed approach when compared to the more consistent tracking performance of the integral backstepping. Nonetheless, these oscillations are compatible with a significant improvement in the EE tracking performance in the permanent regime: the root-mean-square error after settling (5%) is reduced about 40%. From the point of view of application, this change simplifies any mission demanding the EE to be kept as static as possible –e.g. an AM is holding on to a fixed structure in flight or releasing a payload in a limited target space–.

⁶For Δ (%), the variation shown corresponds to the variation of the mean values.⁷Defined as the root-mean-square error once this is below the 5% margin, i.e. $\text{RMSE}_s = \text{RMSE}(t > t_s^{5\%})$.

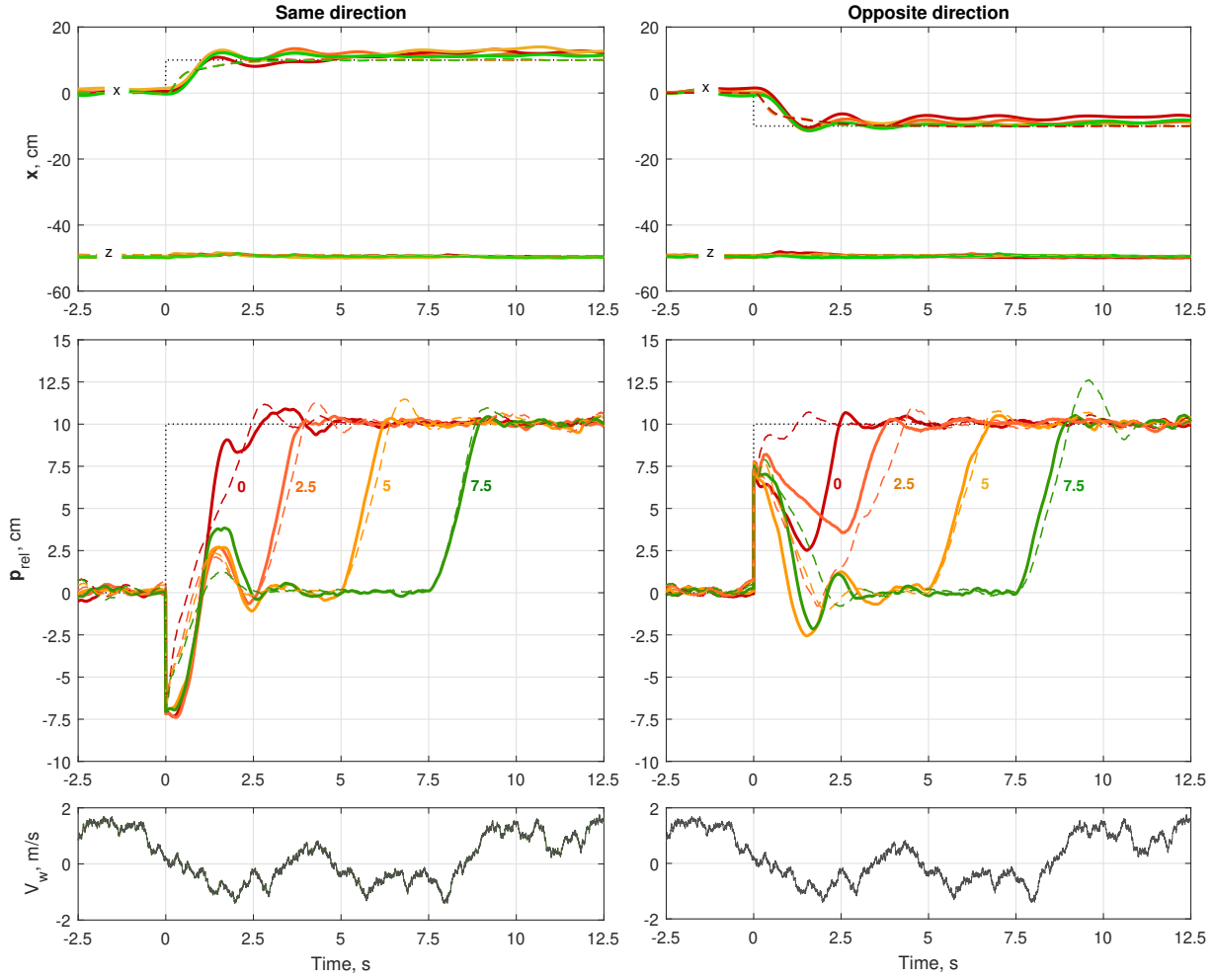


FIGURE 6.5: Comparison between the step response for reference changes of the same and opposite directions of the proposed solution (solid) and of an integral backstepping (dashed) under wind disturbances, with the position references represented with dotted lines and the four step-time offsets ΔT from 0 to 7.5 s labelled with colours ranging from red to green.

- The proposed solution generally displays smoother responses for the EE convergence, both in overshooting (with a reduction of about 7% on average) and settling time (mean reduction of about 30%). It is worth noting that these two metrics are closely related to the probability of succeeding in the capture of the payload, which constitutes one of the most involving challenges of any aerial manipulation mission outdoors.

Taking these advances into account, and specially their implications on the aerial manipulation mission in Section 2.2, we can conclude that the proposed strategy performance should increase the success ratio of the operation while showing safer behaviours when compared to the most used nonlinear controller nowadays. In contrast, the only drawbacks found for the proposed approach are limited to specific applications with limited envelopes for both AM subsystems, such as aerial manipulation in very narrow spaces, or with abrupt simultaneous reference changes for both UAV and RM, such in a mission in which an object is thrown to the AM while avoiding other elements thrown at it.

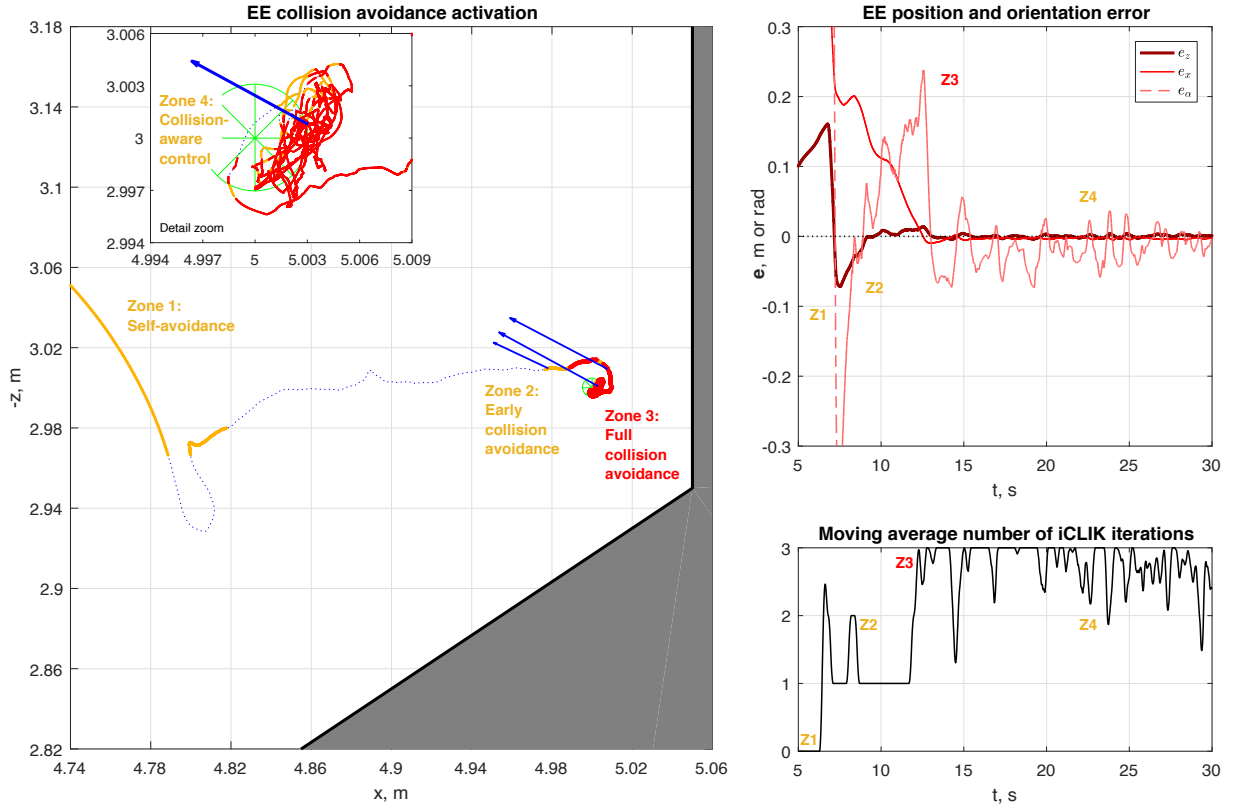


FIGURE 6.6: Collision avoidance results for the operation phase, with EE XZ-trajectory (dotted), highlighted zones of collision avoidance activation (yellow or red for 1 or 2 extra iCLIK iterations, respectively) and blue arrows illustrating virtual rejection forces, on the left; EE error, in the top right corner; and moving average (filter time 0.25 s) number of iCLIK iterations, corresponding 0 to the flight mode, 1 to the normal iCLIK algorithm, and 2 or more to extra iterations, in the bottom left corner.

6.6.2 Collision avoidance

As indicated above, the proposed solution has been enriched with a collision avoidance solution based on the SNS approach. This add-on, which recalculates the solution in the presence of any problematic configuration with the most troublesome DoF locked, increases the computational load of the solution with extra iterations of the RM controller. Accordingly, in here we both analyse the implications on the EE tracking capabilities and on the number of extra iterations needed. For that purpose, let us consider a scenario in which the AM is already in the operation phase –i.e. close to the operational point and with several non-convex polygonal obstacles within its envelope, being the former in one of the inlets of the obstacles– in a configuration that could cause an incident if not rearranged.

According to the results in Fig. 6.6, the SNS-based solution addresses the risks with different degrees of change. During early and self-collision avoidance (zones 1 and 2) only one extra iteration is needed (i.e. the one for the RM control itself and another one for the locking of a single DoF), in a pre-emptive manner. As the gripper gets closer to the more involving inlet in which its target is placed (zone 3), the number of extra iterations rises to 2, hence reflecting a more proactive action but not being detected significant influences on the EE convergence. Finally, when the EE reaches an envelope of about 1 cm of diameter around the target (zone 4), the activity of the algorithm is slightly relaxed –with extra iterations fluctuating between 1 and 2 constantly– as a consequence of the reduction of incident risk. Altogether, the modification is proven to avoid collisions, as expected, without significantly interfering the EE convergence or its steady-state error.

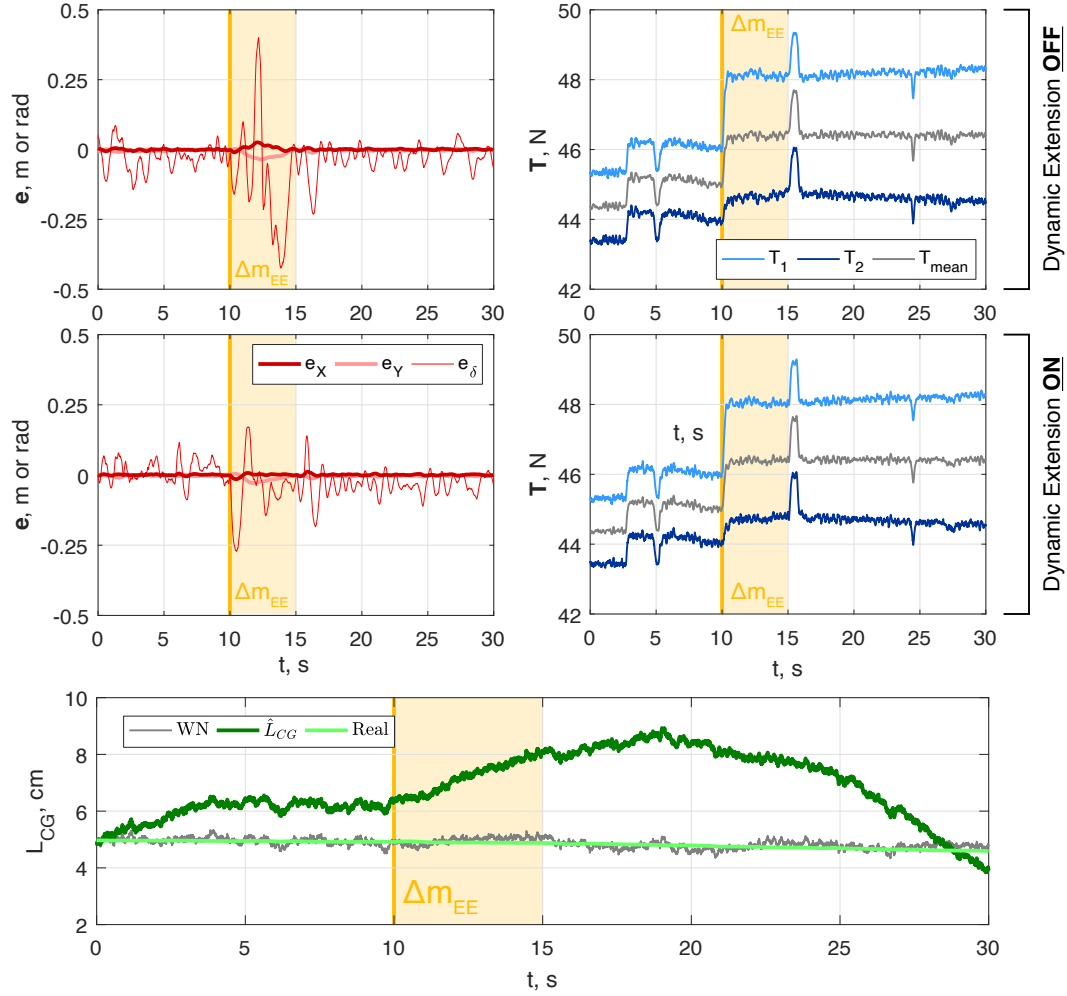


FIGURE 6.7: AM behaviour after a sudden payload increment at 10 s (highlighted in yellow) when the dynamic extension is off (at the top) and on (in the middle), with the dynamic extension results (at the bottom).

6.6.3 Compensation of forces on the EE

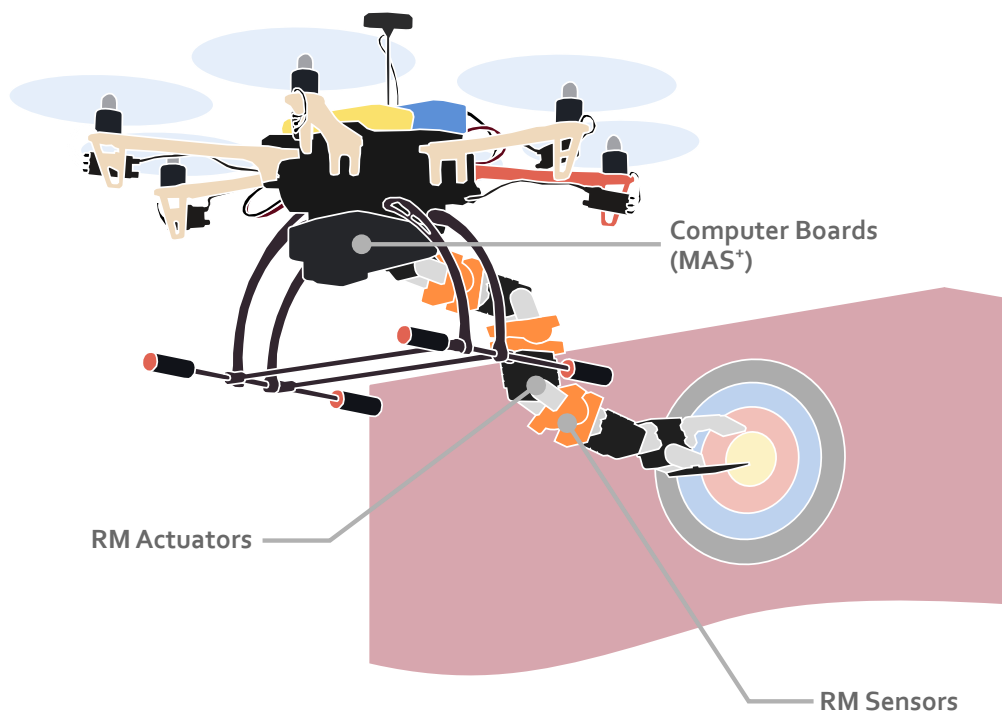
Finally, the robustness of the solution against external forces on the EE is also studied. For that purpose, we consider the case in which –during the release of the mission payload– the EE suffers a sudden mass variation whose extent is *unknown* for the algorithm. We should underscore that such an abrupt and unexpected change could be critical for the stability of the whole system to the point of provoking its collapse. To avoid this extreme case, in here these negative consequences are overcome by the aforementioned dynamic extension. For the sake of completeness, in Fig. 6.7 the responses of the solution with and without this dynamic extension are compared, being $\Delta m_{EE} = 250\text{g}$, and occurring this sudden change at 10 s. From these results, the accuracy of the operation including this dynamic extension is estimated to surpass its unmodified counterpart by a margin of between 20% (EE orientation) and 30% (EE position). Furthermore, it is worth highlighting that –in both cases– the UAV controller counterbalances the effect of the mass change on the whole system by means of the main thrust of the platform, being the differences for the propulsion commands minimal between them.

6.7 Summary of the chapter

In this chapter, a decentralised control strategy for aerial manipulation systems has been presented. Thanks to its relaxed UAV tracking –complying with the priority manipulation task–, and its RM controller –reducing the mismatch in the internal coupling dynamically–, the accuracy of approach is shown to outperform the most common nonlinear alternative.

Chapter 7

Hardware, software & middleware solutions for aerial robotics



Highlights:

- A novel modular autopilot MAS_{PX4}^{\oplus} that expedites the theory-to-validation transitions.
- MAS_{PX4}^{\oplus} autopilot redundancy granted by the use of PX4 as backup.
- Hardware of the robot manipulation system, in its rigid and flexible versions.

In this chapter, the hardware, software and middleware solutions developed to demonstrate the main contributions of this thesis, the $\text{MAS}_{\text{PX4}}^{\oplus}$ autopilot and the Jormungandr lightweight flexible manipulation system, are presented. On the one hand, $\text{MAS}_{\text{PX4}}^{\oplus}$ —a significant contribution to the fast prototyping of novel algorithmia— is intended to bridge the main branches of the research line in Section 2.3 without downgrading any one of them. On the other hand, the Jormungandr system is used to experimentally demonstrate the adaptive controllers in Chapters 4 and 5 under challenging conditions.

7.1 $\text{MAS}_{\text{PX4}}^{\oplus}$



FIGURE 7.1: Logo of the Modular Autopilot Solution, $\text{MAS}_{\text{PX4}}^{\oplus}$.

Among the tools used to implement the strategies presented in this thesis, the novel high-level fast prototyping solution $\text{MAS}_{\text{PX4}}^{\oplus}$ (see Fig. 7.1) stands out. This environment, as thoroughly presented in [C7], provides an ecosystem for fast theory-to-practice transition in outdoor¹ applications based on *flexibility* (both in terms of computational power and interface), *modularity* and *redundancy*. With these, the expansion of project schedules due to the customisation of source codes on open-source software compiled in target computer boards or on *ad-hoc* solutions made by research groups are significantly reduced. To illustrate this point, a comparison between commonly-used autopilots for UAVs² and $\text{MAS}_{\text{PX4}}^{\oplus}$ is shown in Table 7.1.

Autopilot	Modularity & customisability ¹	In flight tuning	Need of <i>full</i> compilation	Redundancy
$\text{MAS}_{\text{PX4}}^{\oplus}$	High Level ⁴	Yes	No ⁵	Yes
PX4	Low Level ⁶	Yes ⁷	Yes	No
ROSflight	Low Level ⁶	Yes	Yes	No
ArduPilot	Low Level	Yes ⁷	Yes	No
DJI	No ⁸	Yes	Yes	No
Paparazzi	Low Level	Yes	Yes	No

TABLE 7.1: Comparison between $\text{MAS}_{\text{PX4}}^{\oplus}$ and alternative autonomous autopilots tested on flight.⁹ Note: some of the footnotes associated to this table can be found in the next page.

¹Applications including wired appliances to support computations offboard –as e.g. [46], [134]– are omitted due to the outdoor and autonomous nature of our design, i.e. with a completely onboard implementation system.

²Only solutions validated in flight are considered, being excluded general purpose and/or educational approaches, such as [135, 136, 137, 138, 139, 140, 141]. In any case, the only redundant alternative is $\text{MAS}_{\text{PX4}}^{\oplus}$.

³Understood as the possibility of actively and directly modifying *all* the control loops, from the ground operator inputs to the generalised force signals.

⁴High level is understood here as including both i) implementing algorithms using an interface which natively does *not* only depend on low-level code, and ii) not demanding the user to get involved into the integration apart from the minimal interconnection variables.

⁵Simulink[®] invokes an internal model interpreter, analogously to a compiler. Nonetheless, this straightforward interpretation is significantly faster (about 2 s, 10 times faster than PX4) and more user-friendly than compiling a standalone executable or a binary file. A detailed and thorough discussion about the differences between compilation and interpretation in this graphical environment is included in Remark 7.1

This comparison is based on the deep knowledge acquired by the GRVC Robotics Laboratory after more than 50 aerial projects along the last 10 years, permitting us to identify usual problematic situations in the early prototyping stages of these autopilot solutions:

- The implementation of customised solutions tends to demand offline *ad-hoc* changes of the native source code, thus expanding the debugging stages during the integration.
- The implementation of increasingly complex algorithms cannot be fully achieved in the existing computer boards due to their low computational-power-to-weight ratios and/or closed nature.

Although the prolongations in the former could be tolerated in theory, they tend to imply limitations in the extension of the advances in complex functionalities to adhere to the project deadlines. On the other hand, the latter is a hard constraint in dexterous manipulation missions, as these also have to cover localisation, vision, flight control and manipulation subtasks. Altogether, this limitation ends up forcing the downgrade of the overall performance. To overcome these limitations, the main contributions of the MAS_{PX4}[Ⓢ] autopilot solution are:

- C1. The drastic reduction of programming and debugging timespans. The full use of the user-friendly and highly *modular* Simulink[®] [143] environment expedites the software development and implementation of complex algorithms.
- C2. High-level in-flight code debugging, tuning and monitoring, while preserving the autopilot *redundancy* for unexpected incidents and/or learning capabilities.
- C3. Enough *computational power* to implement and execute heavy and complex algorithms on-board without downgrading the implementation.
- C4. The possibility of maintaining selected functionalities of PX4 –e.g. in the proposed experimental validation, the EKF and the motor mixer are kept–, hence facilitating a step-by-step implementation of fast-prototyping functionalities.

Remark 7.1. Since the need for compilation in Simulink[®] is not evident, a disambiguation of the difference between *compilation* and *interpretation* in this graphical programming environment is in here included. According to the available documentation, the model is interpreted in Normal mode each simulation run (see 10-11 in [144] and [145]). If only Interpreted Function blocks are used, the execution engine calls these at each simulation time step. Therefore, some kind of *compilation* –i.e. translation of block diagrams to internal representations interacting with the Simulink[®] engine (see 11-26 in [144])– is made in most applications. In what respects to the Accelerator mode [146], Simulink[®] uses by default the Just-In-Time (JIT) *compilation*. This generates an execution engine in memory for the top-level model only, and not for referenced models. As a result, a C compiler is not required during simulations. Additionally, Accelerator mode does not support most runtime diagnostics of Normal mode, which is also useful for prototyping. Finally, in Rapid Accelerator mode, Simulink[®] creates a standalone executable including both the solver and the models interacting via the external mode, with the subsequent lack of debugging options (see [147]).

⁶Simulink[®] external mode can be used with deprecated PX4 versions for Pixhawk, not allowing complex algorithms.

⁷Tuning available via MAVlink using tools such as Mission Planner or QGroundControl (see [142]).

⁸The DJI software in the board cannot be modified directly. References to some of the control levels can be demanded via SDK using another computer board.

⁹This selection does not include: i) applications relying on wired appliances to support computations offboard (e.g. [46],[134]), as these are not designed for outdoor experimentation and they are not *fully* autonomous; nor ii) general purpose and/or educational approaches (such as [135, 136, 137, 138, 139, 140, 141]), as their applicability for aerial robotics has not been experimentally demonstrated.

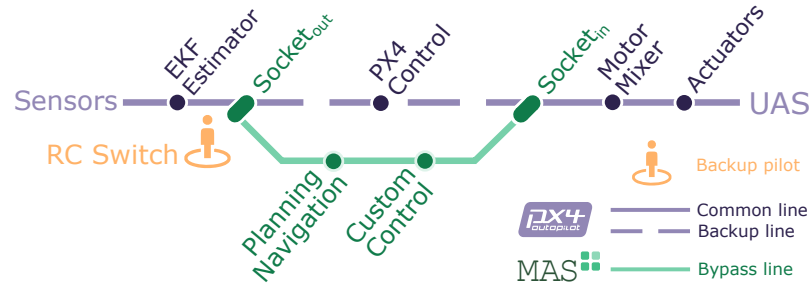


FIGURE 7.2: Redundant MAS_{PX4}^{\oplus} solution, depicted as a schematic diagram similar based on transit maps to underscore the importance of the RC switch (in orange) between the customised line implemented in Simulink[®] (in aquamarine) and the backup line in PX4 (in purple).

In summary, the interpretation made in Normal mode (and in Accelerator mode via JIT) is not comparable to a full compilation obtaining a standalone executable or a binary file, as in Rapid Accelerator mode. The graphical programming, the tools for diagnostics and the possibility of a modular compilation make this approach superior in prototyping stages. On average, our solution takes about 1-2 s to interpret a modified model (Normal mode), while the complete compilation of minimal changes in PX4 last about 20-25 s, 10 times slower in the least favourable case.

Remark 7.2. It should be underscore that the fast prototyping potential relies on two novel specifications: i) the mainframe Simulink[®] environment whose modularity and fast integration capabilities are widely known, facilitating the external validation and/or cooperation between research groups; and ii) to the best of the author's knowledge, MAS_{PX4}^{\oplus} is the first autopilot with in-flight human-in-the-loop redundancy and debug capabilities, drastically reducing the implementation times.

Remark 7.3. Although MAS_{PX4}^{\oplus} is here associated to a fixed hardware configuration, it is worth noting that the framework is flexible in terms of computational power and admits the easy replacement of the proposed Intel[®] NUC. For instance, the All Up Weight (AUW) of the validation system (in Fig. 7.3) is expected to be reduced with the arrival of a new generation of mini computers with enhanced computation power to weight ratios, such as [148, 149].

7.1.1 Autopilot architecture

The main goal of this tool is to provide a safe environment in which the implementation of custom complex algorithms on board is simplified and expedited, thus reducing the timespans for their fully experimental validation. For that purpose, the solution proposed in MAS_{PX4}^{\oplus} integrates the customisation possibilities of Simulink[®] and the reliability of the PX4 stack [150, 151], in a similar manner to the approach *using simplicity to control complexity* in [152]. According to the therein defined concepts, the open-source PX4 plays the role of the high-assurance-control (HAC), being bypassed by the custom algorithms implemented in Simulink[®] as the high-performance-control (HPC), as depicted in Fig. 7.2. In practice, custom daemon modules –after the state estimator and before the motor mixer, as indicated in Fig. 7.2– are chosen to obtain this redundancy.¹⁰ On the one hand, the PX4 ecl/EKF estimation is sent to the customisation environment to take advantage of this highly reliable estimator, thus avoiding to dedicate efforts on a problem out of the main scope of this section. Similarly, by keeping this estimator the researchers that choose this tool will not be forced to develop every single module they need, hence making the implementation of their contribution significantly faster.

¹⁰This modified PX4 version is available at <https://github.com/grvcTeam/MASp>.

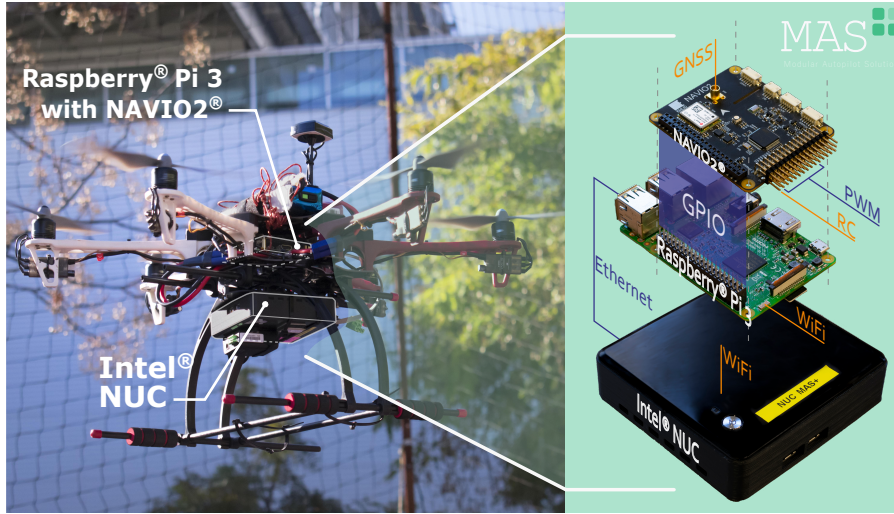


FIGURE 7.3: Validation system during a test flight, with an exploded view of the hardware chosen.

On the other hand, both customised and backup control outputs join at the same command switch, just before the motor mixer (see RC switch in Figs. 7.2 and 7.4). It is in here where the human agents come into action: while the ground operator –an expert engineer developing the algorithm– verifies the response of the system; the backup pilot/pilot in command –an operator with considerable experience flying with PX4– is in charge of guaranteeing the safety conditions of the system during the experiments. If the latter detects any risk to either the platform or the human operators, they would trigger the backup switch to bypass the prototyped solution to the PX4 backup controller and, thus, reduce the risk of an incident. It is worth noting that this backup option must be extensively tested and tuned beforehand to be used as the HAC.

Hardware architecture

The hardware setting proposed for MAS_{PX4}[⊕] consists of a Raspberry Pi[®] 3 [153] equipped with a NAVIO2[®] [154] –serving as both interface board and delegated backup controller–; and an Intel[®] NUC [155] –as the main computer running the customised code directly on Simulink[®] modules (e.g. control, navigation, etc.)–, as depicted in Figs. 7.3 and 7.4. With this approach, the computational capacity left for customisation is maximised and a modular and safe (in the sense of redundancy) environment is obtained.

Remark 7.4. It is essential to underline that MAS_{PX4}[⊕] does not require the use of Simulink[®] external mode. In general, any module of the Library Browser (or any customised module derived from them) can be used to implement personalised solutions, thus providing a broad compatibility. Moreover, accelerator modes can be used for computation-intensive application, with the subsequent limitations in the aforementioned compatibility capabilities.

For the sake of completeness, a comparison with other possible approaches is used to highlight the relationship between this architecture and the main contributions of MAS_{PX4}[⊕]:

- **Dronecode** [151]: the proposed solution has in common with this broad standard ecosystem –that includes PX4– the possibility of using the hardware configuration Raspberry Pi[®] 3 + NAVIO2[®]. However, none of the projects fostered by Dronecode employs an external computer to implement custom complex solutions. In contrast, MAS_{PX4}[⊕] is not initially designed to be used via ROS. Nonetheless, these capabilities can be either enabled through

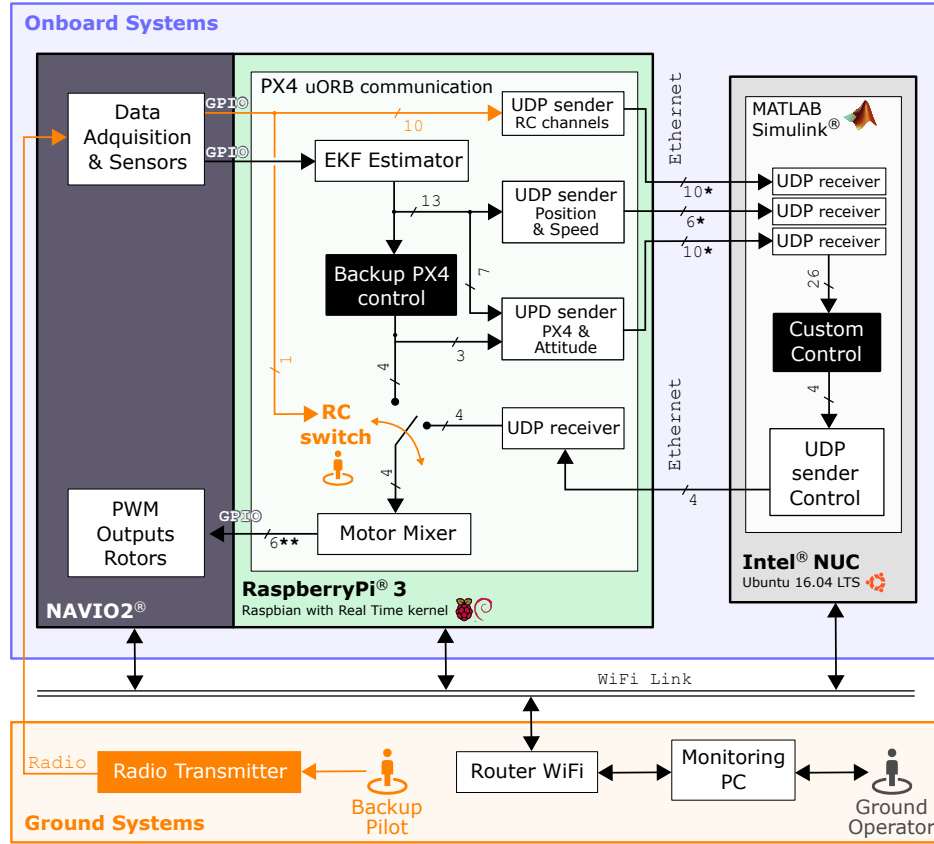


FIGURE 7.4: Architecture of MAS_{PX4}, including the main computer (Intel® NUC, on the right), the backup board (Raspberry Pi® 3, on the left) and the ground systems (at the bottom). Among the latter, both human agents stand out due to their importance for the RC switch and the monitoring of the customised algorithm.

MAVlink/MAVROS or via the ROS toolbox in the Simulink® environment. Furthermore, it is also worth mentioning that MAS_{PX4} also improves the technical specifications of another common solution belonging to the Dronecode suite, Pixhawk [156], as well as it supports Ethernet communications, unlike this.

- **ROSflight** [157]: this recently appeared board concurs with MAS_{PX4} on some characteristics, such as the implementation of new algorithms on a companion computer board, a sensor/actuator interface similar to Raspberry Pi® 3 + NAVIO2® and, most importantly, the focus on easing the development stages. Nonetheless, ROSflight fully depends on ROS, thus lacking the user-friendly graphical interface in Simulink® and the fast theory-to-implementation transition provided by MAS_{PX4}; and does not include the redundancy of a mature backup controller such as PX4, with the associated risk when testing core modifications without progressively implementing them.

Finally, it is worth noting that a trade-off between computational capacity and flight endurance has to be decided *a priori*, as commonly happens in all electrically-powered aerial robotic applications. As indicated in Remark 7.3, the Intel® NUC can be replaced by other boards to reduce the AUW of the validation system (3.2 kg) in lower computational applications, thus improving its current endurance (~8 min).

	Port	I/O	BW [MB/s]	Jitter [ms]	Lost data
INTEL® NUC Main computer	8081	I	1.04	0.49	0/1785
	8082	I	1.04	0.54	0/1785
	8083	I	0.96	1.37	0/1785
	8888	O	0.96	0.56	0/1785
RASPBERRY PI® 3 Backup controller & state estimation	8081	O	1.04	0.49	0/1785
	8082	O	1.04	0.54	0/1785
	8083	O	0.96	1.37	0/1785
	8888	I	0.96	0.56	0/1785

TABLE 7.2: UDP connection analysis for data packages of 25 MB.

Software integration

In MAS_{PX4}[⊕], the integration of PX4 with the customisation environment is essential for the reliability of the whole solution. Hence, a profound analysis of the internal UDP communications is conducted. On the one hand, the quality of this Ethernet UDP connection is studied in terms of bandwidth, jitter and lost datagrams ratio. iPerf [158, 159] is chosen to measure them in a batch of experiments of 20 s of duration with overestimated¹¹ packages. Using this tool, jitter is calculated as the difference between receiving and sending times via timestamps attached to the sent packages, being discrepancies related to clock synchronisation corrected. The results obtained after this batch of experiments are presented in Table 7.2, being confirmed that: i) no datagrams were lost in any of the tests, ii) the bandwidth chosen for the application is adequate, and iii) the jitter is negligible in comparison to the sample time of the fastest processes in PX4, 4 ms.

On the other hand, the delays due to both communications and custom code execution ought to be analysed. These two contributing factors are commonly analysed together due to the difficulties of describing them in detail, but in here we managed to detach their associated delays. Firstly, the impact of the communication delay on the autopilot solution is analysed with the Round Trip Time (RTT). To avoid contaminating the results with the execution times of complex algorithms inside Simulink®, it is decided to measure the time between a simple RC command is given and its impact on the controller output is detected with the simple PID controller in Subsection 7.1.2. With this setting, the mean RTT obtained results to be of around 1235 µs which is clearly below the fastest sample time in PX4 (4000 µs).

Secondly, the influence of custom code complexity on the execution times is examined experimentally. For that purpose, the CPU and RAM are monitored on a ground test for a complex nonlinear flight controller (corresponding to the second experimental scenario) to determine the potential computational capacity left for future application (see Fig. 7.10, after the description of the experimental settings and the form of the controller used). In summary, the results evince that the computational capabilities of MAS_{PX4}[⊕] are well above the current demands of algorithms that are not generally implemented in their full version due to their significant loads on alternative autopilots. Altogether, an increase in the complexity of the custom algorithms could be easily compensated by the computational margins of the proposed environment. Accordingly, the RTT should not have any significant impact on the implemented solution, hence being neglected in what follows.

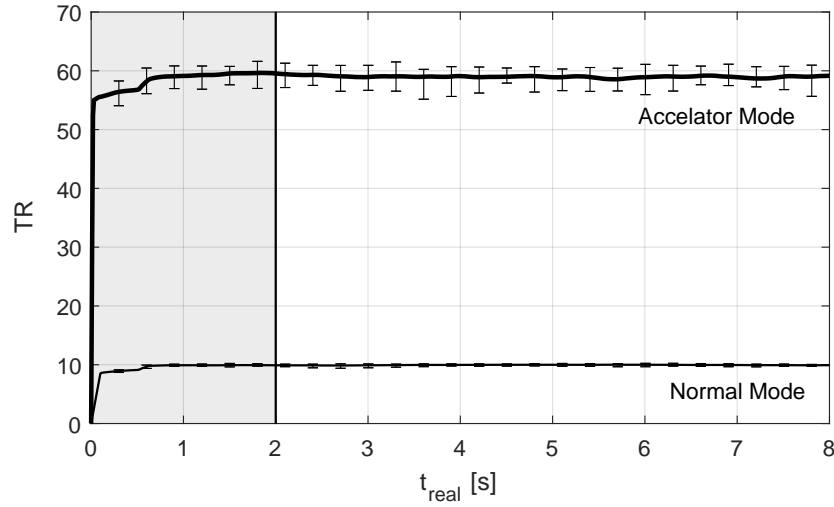


FIGURE 7.5: Mean time ratio during 20 tests of 8 s each, on both normal and accelerator modes, with maximum deviation highlighted as error bars.¹²

Simulation versus real-time oversampling

As already highlighted in Remark 7.4, MAS_{PX4}^{\oplus} is designed to have the broadest compatibility possible with Simulink[®] modules and to significantly reduce the simulation-to-experimentation times. This, however, comes at the expense of real-time. In MAS_{PX4}^{\oplus} , the Simulink[®] simulation time is given as input to time-dependant modules, such as integrators. To test if this approach is safe for the validation of custom solutions, two derived phenomena must be analysed: i) time-variant random disturbances and ii) high-frequency spurious signals. To study both, nonetheless, let us define a unique metric: the time ratio, TR , as the rate between the clock time according to the Simulink[®] simulation records and its *real* value according to the PX4 board clock.¹³

Then, after analysis this ratio in a batch of ground tests (Fig. 7.5), we can identify that it shows a fast first-order response ($t_{63\%} < 0.1s$) that can be assimilated to the initial convergence of the ecl/EKF estimator in PX4. This implies that, except for a first initial transient in which the system is expected to be landed, the TR is kept constant and can be used to correct the time-dependant modules. Nonetheless, this TR_{∞} is consistently above the unity, thus being possible that high-frequency residuals affect the operation. To study this problem, simple signals in a wide range of frequencies were added as inputs/outputs of the different modules used in Simulink[®], looking for behaviours that should not be present. Although some spurious signals were detected in these tests, they all were in frequencies above the real sampling rate limitation imposed by the PX4 motor mixer uORB, i.e. 200-250 Hz, thus being filtered. Moreover, the presence of other filters generally used when implementing UAS solutions and the real rotor dynamics completes the cancellation of these spurious signals. In summary, no incidents were attributed to signal oversampling in the 50 hours of flight needed to perform the experiments for this contribution, and therefore the impact of this issue is considered negligible in UAS applications.

¹¹This consideration is taken to assure the possibility of future scalability.

¹²Experiments carried out in an Intel[®] NUC 5i7RYH.

¹³It is worth noting that the aforementioned time-dependant modules ought to be corrected with this ratio. From a practical point of view, it is recommended to recalculate this ratio after changes that could significantly affect the computational load of the environment, but not after small changes –such as the addition of individual Simulink[®] blocks or the modification of these–.

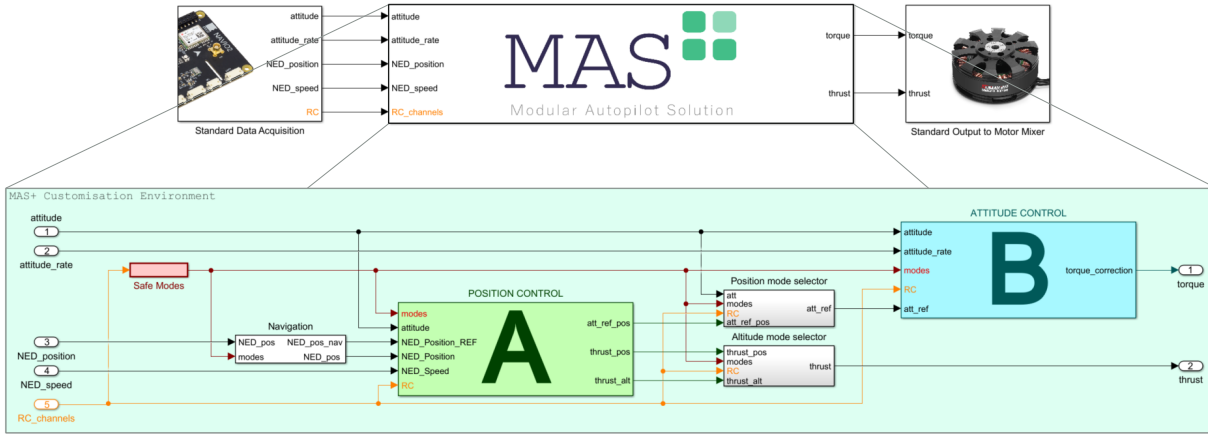


FIGURE 7.6: MAS_{PX4}[Ⓜ] customisation environment in Simulink[®], including the proposed standard communication modules (at the top) and a detail view of the different blocks that comprise the main customisation module (at the bottom). Among these, the position (A) and attitude (B) controllers are highlighted, together with the navigation module and the flight mode switch.

7.1.2 Experimental validation

The validation of the proposed autopilot is demonstrated through three typical implementation cases¹⁴ in a standard DJI[®] F550 frame, thus providing a general overview of the real possibilities of this novel environment. Each one of them is implemented using the Simulink[®] general modular structure depicted in Fig. 7.6, where the content of the position (A) and attitude (B) control modules will be detailed in each experiment. These typical cases are:

- EV1. The progressive development of a cascade PID controller that imitates the control core of PX4, thus illustrating the redundancy and reliability of MAS_{PX4}[Ⓜ], and serving as a basic academic example of the implementation of a full strategy.
- EV2. The implementation of a complex nonlinear control strategy *without any simplification* to illustrate the computational potential of MAS_{PX4}[Ⓜ] (including a test of computational load) while demonstrating its applicability for complex algorithms.
- EV3. A flight navigation module to exemplify other possible implementation cases not concerning control. Accordingly, the controller used underneath this module is the cascade controller in EV1, hence easing the comprehension of this example for those not mainly interested in control.

¹⁴These scenarios are not considered to constitute a sequential validation of the autopilot solution, i.e. each one is independent from the others and the final intention is not to include all of them in a *final* validation.



FIGURE 7.7: Proposed implementation phases for MAS_{PX4}[Ⓜ].

It is worth mentioning that, to avoid incidents while changing the core algorithms in these case, the procedure followed (see Fig. 7.7) consists on three sequential phases:

- P1. Suspended initial tests** (Fig. 7.7a): before testing the whole novel solution, each new basic functionality is tested individually by progressively replacing their homologous algorithm in PX4 during tests conducted in a confined scenario with the system suspended from a solid structure.
- P2. Confined evaluation** (Fig. 7.7b): when all these functionalities have been checked, the experimental setting is relaxed by dropping out the suspension requirement. This improves the realism of the experiments, thus allowing to perform reliable validation experiments for individual functionalities.
- P3. Outdoor validation** (Fig. 7.7c): finally, when each functionality to be included in the final version of the custom solution has been validated in the confined setting, the system is flown outdoors to test the high-level capabilities.

The result of these phases is a reliable full solution directly obtained from a theoretical simulation-based design, in which the safety and redundancy of the procedure are assured.

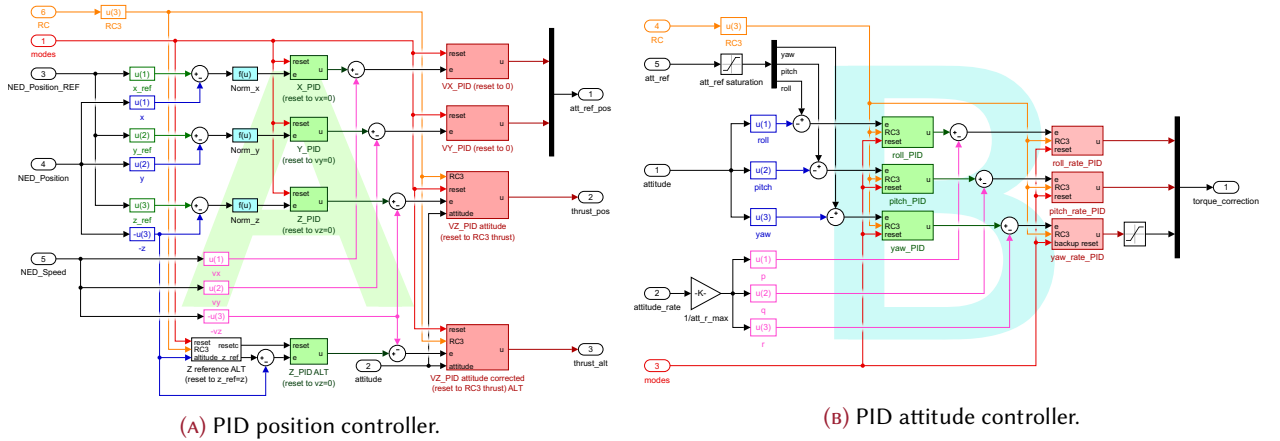


FIGURE 7.8: Cascade PID controller implemented in MAS_{PX4}[Ⓟ], with both position and control loops (see Fig. 7.6) and experimental results for a flight at constant altitude.

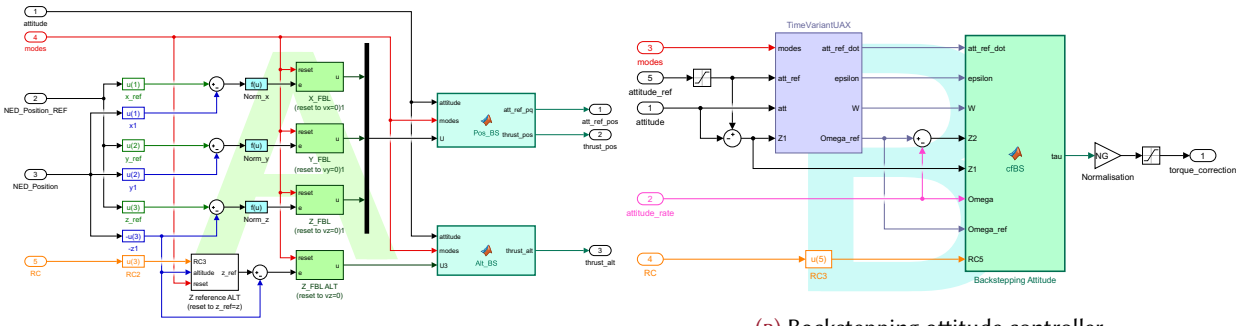
EV1. Simple PID control module

Firstly, a PID controller, mimetic to the PX4 core, is progressively implemented from the inner to the outer loop, as follows: i) attitude rate, ii) attitude, iii) Cartesian speeds, and iv) Cartesian position (see Fig. 7.8, and more specifically Subfigs. 7.8a and 7.8b). The result is a semi-autonomous controller that is used in here to validate the customisation environment and to illustrate the redundancy of the proposed solution.

For that purpose, let us analyse the monitorisation of the system in Subfig. 7.8c. It is clear that the tracking of the four different internal loops is achieved with minimal steady-state error, as expected in a tuned cascade controller. As this result is similar to the response of PX4 in comparable scenarios, the customisation environment is considered validated in terms of reliability and applicability and the capabilities to substitute control modules demonstrated.

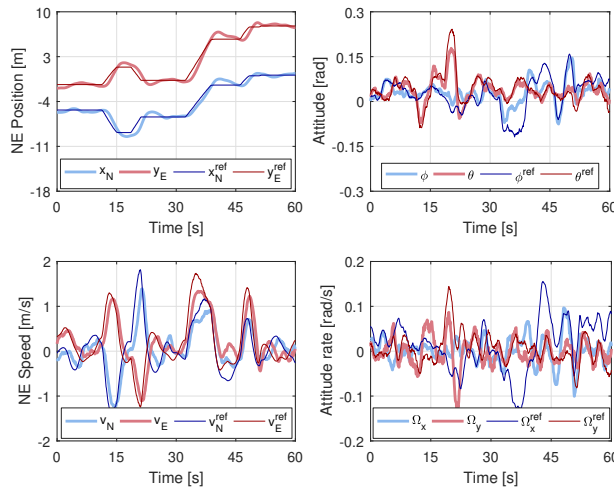
EV2. Complex nonlinear control module

Then, the computational capabilities of MAS_{PX4}[⊕] are illustrated by implementing a complex nonlinear controller. The algorithm chosen here is a standard command-filtered backstepping with feedback linearisation, whose complete formulation is shown in Appendix B (and more precisely in Proposition B.1).



(A) Backstepping position controller.

(B) Backstepping attitude controller.



(c) Experimental results.

FIGURE 7.9: Command-filtered backstepping controller implemented in MAS_{PX4}[⊕], with both position and control loops (see Fig. 7.6) and experimental results for a flight at constant altitude.

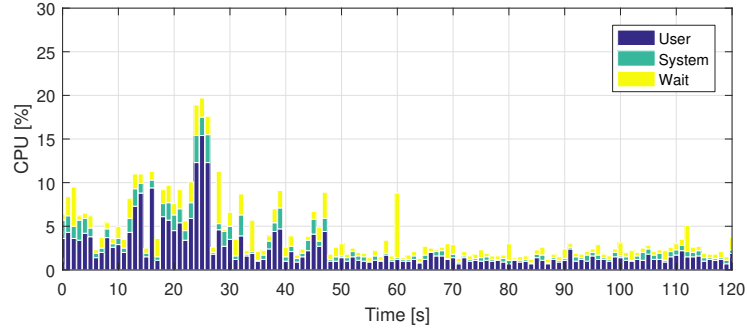


FIGURE 7.10: Stacked CPU load during the execution of the customised code of the command-filtered backstepping in MAS_{PX4}^{\oplus} , being the RAM used steady at 25% throughout the test.

This more involved formulation is, in turn, implemented in the Simulink[®] using the schemes shown in Fig. 7.9 (Subfigs. 7.9a and 7.9b, for position and attitude loops, respectively). When this custom solution is commanded to follow a variable position reference (Subfig. 7.9c), the results evince that the controller tracks it with minimal steady-state error. Nonetheless, it is worth noting this is achieved without full tracking the attitude references derived from the outer position loop. This, however, is an expectable behaviour for a command-filtered approach that has no negative implications on the whole system.

Additionally, a CPU load test is conducted for this algorithm to estimate the computational potential left for future applications (Fig. 7.10). This can be divided into two phases: i) in the first half of the experiment, aggressive RC commands and *ad-hoc* parameter tuning were induced to the environment, thus producing a conservative estimation of the CPU load; and ii) in the second half, these demands were softened and the controller was given normal commands and no intensive online tuning, hence giving a more realistic estimation. Altogether, it becomes clear that the solution equipped with an Intel[®] NUC is capable of running this algorithm and some others with higher computational demands. Moreover, it should be highlighted that this test was performed with the normal simulation mode in Simulink[®]. Accordingly, the computational potential left for future applications is even larger and the applicability of MAS_{PX4}^{\oplus} broader. It is also worth noting that, as shown in the first half of the experiment, the impact of external factors in the CPU is noticeable. However, by combining the CPU margins obtained in the experiment and the time ratio analysis in Fig. 7.5, it can be concluded that their effect on the reliability of the solution is negligible.

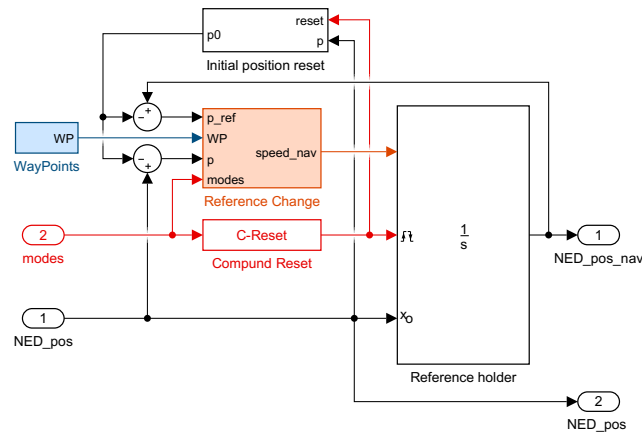


FIGURE 7.11: Navigation module implemented in MAS_{PX4}^{\oplus} (see Fig. 7.6).

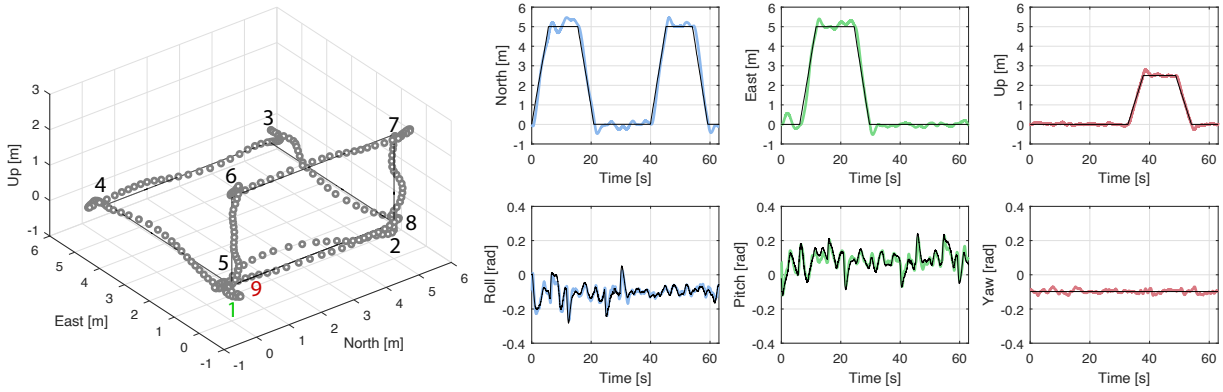


FIGURE 7.12: Results of the experiment including the navigation module on top of the PID cascade controller, with: patch tracking (on the left, using position markers separated by 0.25 s and where the navigation waypoint order is indicated by numbers), global position (in the top right corner, where black lines correspond to the navigation module references) and platform attitude (in the bottom right corner, following the references –in this case derived from the position loop– the same format).

EV3. Autonomous navigation module

Finally, an autonomous experiment is performed outdoors under both minor wind disturbances and GPS inaccuracies to validate the separate navigation module depicted in Fig. 7.11. The flight path of this experiment (Fig. 7.12), consisting of two rectangles –one in the horizontal plane and another one in the vertical plane–, is selected to show the response of the solution for reference changes in different Cartesian directions. As shown by the position tracking subplots, the solution follows the proposed path correctly and, as expected, only produces significant error peaks around the waypoints, being the displayed overshoots in these cases at their typical range in outdoor aerial robotic applications.

7.2 Robot manipulator



FIGURE 7.13: Logo of the Jormungandr lightweight flexible manipulator.

To validate the adaptive strategies aimed at obtaining smooth first-order-like responses and force control capabilities in Chapters 4 and 5, the design of a robot manipulator with adequate sensorisation is essential. For that purpose, two separate re-designs directly evolving from the planar manipulator presented in [160] –the so-called Jormungandr Mk. 1 and Jormungandr Mk. 2 (see the Jormungandr logo at Fig. 7.13 and the prototypes in Fig. 7.14)– are used, being their main parameters shown in Table 7.3.

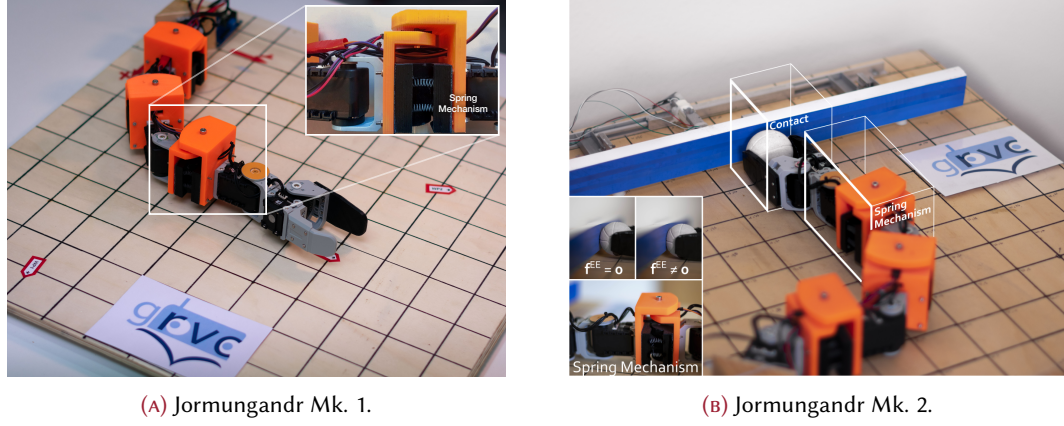


FIGURE 7.14: Jormungandr prototypes.

Compound joints [cm, g, N m rad ⁻¹]							EE joint [cm, g]		
l	L	l^{CG}	L^{CG}	m	M	k	l_{EE}	l_{EE}^{CG}	m_{EE}
4.8	6.2	2.4	3.6	25	64	0.8	12.0	6.0	72

TABLE 7.3: Parameters of the planar RM, where compound joints indexes are omitted due to repetition.

7.2.1 Jormungandr Mk. 1

Firstly, let us describe the original planar manipulator itself before analysing the sensors and the computer board chosen to implement the control solution in Chapter 4. This is comprised of 4 actuated DoF and 3 passive flexible articulations (Fig. 4.3a), with a repetitive actuated-passive design except for the EE link, which is fully actuated (see Fig. 7.14a).



FIGURE 7.15: Dynamixel AX-12A servomotors [161].

For the actuated joints, the servomotors used are the Dynamixel AX-12A [161] (see Fig. 7.15). These have a resolution of 0.3° , a stall torque of 1.5 N m, a no-load speed of 59 RPM and angular feedback. To address their incompatibility with speed control in this application¹⁵, an *ad-hoc* modification of their angular position mode –based on the superposition of speed profiles– is implemented. In what respects to the flexible links –which are designed with a double spring mechanism with low stiffness¹⁶–, the deflection is measured by Murata SV01 rotatory position potentiometers [162] (see Fig. 7.16).

¹⁵The continuous speed mode of the AX-12A is intended as a solution for wheel-driven robots focused on providing high maximum speeds on the cost of torque and response time.

¹⁶This design decision is taken to make the control of the system challenging, thus highlighting the capabilities of the solution. With it, flexible joints are prone to physically saturate and produce significant oscillations while the RM is being operated.



FIGURE 7.16: Murata SV01 rotatory position potentiometer [162].

Finally, to carry out the calculations of the solution in Chapter 4 and to interact with both sensors and actuators, an Arbotix M-Robocontroller microcontroller [163] (see Fig. 7.17) –based on a 16 MHz AVR microcontroller– is used.

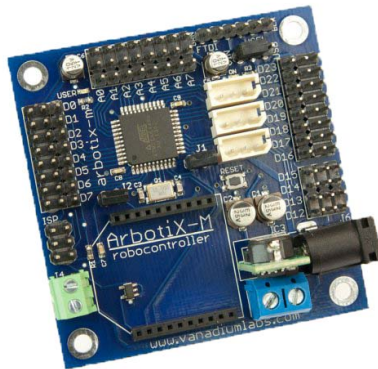


FIGURE 7.17: Arbotix-M Robocontroller [163].

7.2.2 Jormungandr Mk. 2

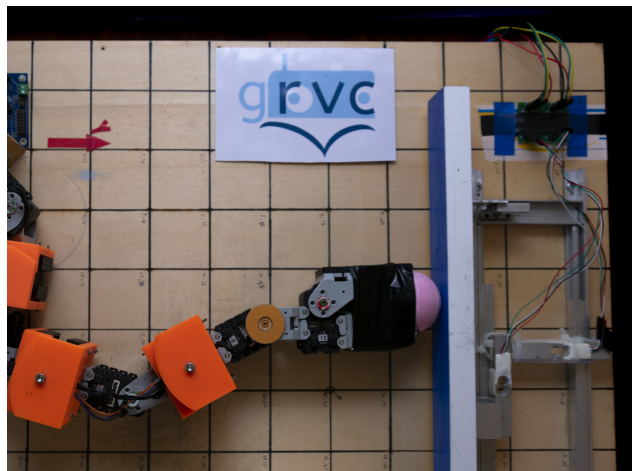


FIGURE 7.18: Dual-axis force sensor setup, with the Jormungandr Mk. 2 pressing in the normal direction.

To obtain the force control capabilities demanded in Chapter 5, two significant novelties in the hardware configuration are essential: i) the use of a dual-axis force sensor formed by two lowcost linear bidirectional load cells (see Fig. 5.3) to obtain relatively clean measurements, thus allowing us

to close the loop with acceptable accuracy; and ii) the substitution of the Arbotix-M Robocontroller with the more powerful –but cheaper– Arduino Mega 2560 [164] (see Fig. 7.19). Among the main features of this board based on a 16 MHz ATmega2560, stand out its flash memory of 256 kB and SRAM of 8 kB. This, nonetheless, comes on the cost of needing a separate SN74LS241N octal buffer to communicate with the servomotors with three-state memory address drivers, while a similar solution was already included in the Arbotix M-Robocontroller.

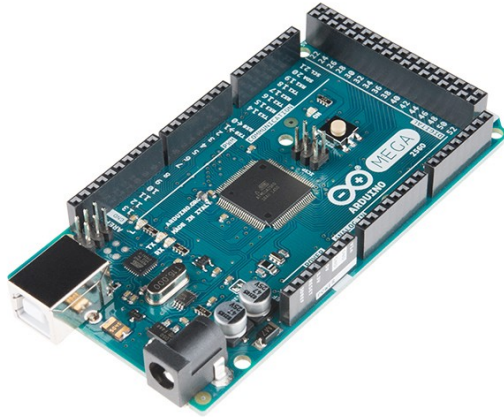


FIGURE 7.19: Arduino Mega 2560 [164].

7.3 Summary of the chapter

In this chapter, the hardware, software and middleware tools used for this thesis have been thoroughly presented. Among them, the MAS_{PX4}^{\oplus} autopilot environment stands out. This new prototyping environment shortens the development timespans for novel algorithmia directly from theory –without downgrading–, while allowing a progressive implementation thanks to its redundant nature. Finally, the benchmark systems employed to demonstrate the manipulation controllers in Chapters 4 and 5 are fully described.

Chapter 8

Conclusions and future work

To wrap up, the main results from this thesis are highlighted, along with some possible lines of research that could emanate from them. Although most of the latter are still in an early stage, they correspond to a long-term research plan.

8.1 Conclusions

This thesis is focused on the study of nonlinear control strategies aimed at aerial manipulation in outdoor scenarios, with special emphasis on the coupling between the platform and the mission system. For that purpose, two main branches have been traversed: the adaptive control of flexible manipulators with uncertainties, and the decentralised control of the aerial manipulation system.

Within the first one, a first controller capable of handling unforeseen impacts and contact with a first-order-like response –i.e. filtering-like the second order oscillations produced by the flexible modes– is fully presented, including both theoretical and experimental results. As an evolution of this controller, an adaptive force controller is presented. This adds to the already robust strategy the possibility of exerting forces in several axis without having to switch between separate modes – or control gains–, by means of a cascade-like approach. As a result, this strategy ends up providing all the capacities needed to perform complex manipulation mission under strict safety conditions, as validated theoretically and experimentally in this thesis.

In what respects to the second branch, a decentralised nonlinear approach relying on the passivity for the platform to give room for the prioritisation of the manipulation tasks is obtained. To do so, a manipulation-aware compliant approach that relaxes in practice the position tracking of the platform is proposed. Moreover, the manipulation mission is performed with a control strategy incorporating secondary tasks –via the nullspace of the task-space–, and whose inverse kinematics formulation is shaped by the coupling with the platform. This facilitates the cooperation between the two subsystems without having to control them with an unified control strategy, what would be computationally intensive. Along with the theoretical formulation of this novel decentralised strategy, that includes a profound stability analysis, a detailed numerical validation under external disturbances is provided. This includes, apart from a operation scenario, a comparison with a common fully-decentralised aerial manipulation strategy –an integral backstepping for the platform and a CLIK for the manipulator–, in which this is clearly surpassed by the proposed strategy; and some additional scenarios focused on demonstrating the robustness of the solution.

To upgrade the realism of the simulations in outdoor scenarios, a necessary contribution has also been developed, a preliminary characterisation of the aerodynamic forces and torques experienced by multirotor platforms in quasi-steady flight based on CFD simulations. Finally, a novel autopilot for aerial manipulators, which will pay the way to the implementation of complex algorithms onboard –as those presented in this thesis–, has also been developed. This simplification of the transition from theoretical formulation to practical implementation is achieved by employing the user-friendly block-based Simulink® environment and a redundant approach relying on PX4. The latter, used as a backup manually activated by an experienced pilot, is used as an auxiliary solution providing reliable base services. Finally, onboard validation of MAS_{PX4}^{\oplus} has been conducted in an outdoor experimental setting including diverse control strategies, hence evincing that complex algorithms can be implemented directly from theory without any downgrade.

Altogether, this thesis includes significant advances for outdoor aerial manipulation from three perspectives (see Table 8.1): i) manipulation control under uncertainties, and ii) manipulation-aware control of AMs to improve the manipulation results.

Moreover, the author also wishes to detail the contributions associated to the ongoing work [C9].¹ This approach provides a robust geometric estimation of the reactions induced by the manipulation system on the platform, thus enriching the awareness of the UAV control solution. As this only relies on distributed lowcost sensors, it perfectly fits with the requirements of weight and costs typically demanded in aerial robotics. It is also worth noting that, although no experimental

¹This publication has not been submitted yet, but the author considers that its contributions are worth discussing here.

results have been yet obtained, the preliminary numerical validation for RMs is promising, being convergence obtained even for cases in which the rotation axis of some of the joints is unknown.

Chapter	Ref.	Contributions
3	[C6]	<ul style="list-style-type: none"> ▷ An explicit mathematical model to characterise the forces and torques applied on a multirotor UAV in flight, obtained from post-processing the results of several iterative batches of CFD simulations. This solution is based on simple support functions and a linear set of parameters. ▷ Full comparison with the most common alternative –being the advances for both vertical forces and horizontal torques substantial–; and analysis of the order of magnitude of the characteristic deviation when the model is employed for other platforms.
4	[C5]	<ul style="list-style-type: none"> ▷ The design of a nonlinear IK controller to reduce the negative impact of introducing flexible modes into lightweight RMs, with a first-order-like closed-loop response. For that purpose, an adaptive update law for the unknown stiffness of the flexible links is employed, thus obtaining an approach valid for soft materials. ▷ An experimental validation of these contributions in a basic controller board running at 27Hz, including unforeseen impacts and contact tasks.
5	[C8]	<ul style="list-style-type: none"> ▷ A nonlinear extension to force control –in both the normal and tangential directions– of the position controller in Chapter 4, including self-tuning update laws, and the possibility of performing mixed contact/non-contact tasks thanks to its cascade design. ▷ Validation of the approach with a board with low computational power and low force sensor accuracy –i.e. closing the loop with cheap load cells–, being also improved the convergence times and oscillation amplitudes with respect to the position controller.
6	[C1]	<ul style="list-style-type: none"> ▷ The cooperation of decentralised robust controllers for UAV and RM subsystems via an optimisation criterion that accounts for their stability margins in real-time. ▷ Compliance of the manipulation and vehicle positioning tasks, being prioritised the former with a subordinate approach.
	[C4]	<ul style="list-style-type: none"> ▷ A decentralised strategy dumping the simplistic and commonly used assumption of perfect RM tracking without losing the passivity property while flying with the RM moving, by means of a dynamic extension. ▷ The theoretical demonstration of the stability of the RM control algorithm taking into account UAV-RM coupling –via the reaction torque– in the optimisation criteria; and of the whole aerial manipulation strategy in all the phases of the design mission. ▷ A thorough numerical validation with the aerodynamic model in [C6], including: i) rejection of external disturbances –such as wind gusts and payload changes–, ii) collision avoidance, iii) target tracking, and iv) a comparison with a well-known decentralised nonlinear strategy for aerial manipulation.
7	[C7]	<ul style="list-style-type: none"> ▷ A user-friendly and modular autopilot that expedites the development of complex algorithms for aerial robots –without downgrades–, and provides enough computational power to implement them onboard. ▷ High-level in-flight code debugging, tuning and monitoring, while preserving the autopilot redundancy –via PX4– for unexpected incidents and/or learning capabilities.
A	[C2]	<ul style="list-style-type: none"> ▷ A study of the UAV-RM relative configurations for fixed manipulation references to improve the performance, safety and robustness of the solution. ▷ An approach to include the recommendations emerging from this study to dynamically optimise the UAV reference under wind gusts and sensor noise.
B	[C3]	<ul style="list-style-type: none"> ▷ The redesign of a common nonlinear control solution for aerial platforms to reduce its sensitivity against manipulation disturbances. ▷ A numerical validation of this redesign for overestimated RM oscillations, showing a significant reduction of the attitude and position oscillations, as well as of the rotor speeds.

TABLE 8.1: List of contributions per core publication, as displayed in the chapters/appendices of this thesis.

8.2 Future work

Although these advances are significant *per se*, the research line of the author is going to be expanded by integrating the different contributions, as already indicated in Chapter 2 (Fig. 2.3). This is expected to lead –with the essential help of the MAS_{PX4}^{\oplus} autopilot solution– to a series of applications, including the following ideas.

8.2.1 Control strategies

The extension of the control research line could be, in turn, divided into: i) the integration of the manipulation-aware paradigm with the adaptive controllers for flexible manipulators, and ii) the use of the proposed aerodynamic model to enhance the disturbance rejection capabilities of UAV control approaches.

Integration of the manipulation-aware line

Firstly, it becomes evident that the decentralised control strategy for aerial manipulators in Chapter 6 should move to an experimental validation phase. Although this was expected to be achieved before the end of this thesis, some delays of the experimental line –produced mostly by the outbreak of the COVID 19 crisis in 2020– has postponed this validation to the post-doctoral stage of the author.

Moreover, the interconnection torque between the manipulation and vehicle systems –chosen in Chapter 6 as the criterion for the internal accommodation– ought to be properly estimated. Although a first approach producing acceptable results based on the structural sub-matrices reduction was presented, its formulation could be significantly improved to enhance this crucial behaviour of the aerial manipulation strategy. For that purpose, a nonlinear estimator for the reactions –forces and torques– between both subsystems based on the use of lightweight and cheap distributed sensors is currently under development. The approach, derived from a short stay in the I3S Laboratory² under the supervision of Prof. Tarek Hamel, estimates the internal reactions in each joint from the EE to the RM base iteratively, being the total computational cost of the estimation significantly lower than any other model-based approach. Altogether, the solution is expected to exceed both approaches relying on F/T sensors –due to the significant reduction in cost and weight– and on complete AM dynamic models –which tend to be very computation-intensive–. Although the theoretical formulation is expected to be finished within the deadline of this thesis, the experimental validation of the solution will be performed after the dissertation.

Subsequently, the strategy in Chapter 6 is planned to be re-scheduled and adapted for a complete 3D implementation relying on this novel estimator. For that purpose, nonetheless, the IDA-PBC solution might need to be changed into a backstepping approach with passivity capabilities, being all the here proposed add-ons validated again accordingly. Altogether, the resulting solution is expected to improve the manipulation performance of current aerial solutions thanks to a low computational load –hence increasing the control frequency– and a robust approach prioritising the manipulation. Furthermore, it is worth highlighting that this solution will be implemented with a significantly reduced computational burden, mainly thanks to: i) the use of MAS_{PX4}^{\oplus} , instead of developing a customised-board to handled the required computations; and ii) the possibility of estimating the main coupling terms via the proposed low-cost distributed sensors estimator instead of using heavy F/T sensors or having to calculate the dynamics of the whole system.

Concurrently, the control laws in Chapter 6 will be modified to be compatible with flexible manipulators. To obtain such results, nonetheless, the far-for-trivial expansion of the strategy and the reaction estimator to flexible manipulators should be deeply studied and a full theoretical validation ought to be obtained –which was out of the scope of this thesis–. This would be followed, as it is expected to happen with its counterpart for rigid aerial manipulators, by the experimental

²Université Côte d’Azur, Institut Universitaire de France, CNRS, Sophia Antipolis, France.

validation of the strategy in flight. It is also worth noting that the controller in Chapter 5 –when integrated within the complete strategy– should provide adaptive force control capabilities on flight. This substantial advance should lead, in turn, to new application possibilities, as the ones presented in Subsection 8.2.2.

Broadening the range of environmental conditions for aerial manipulation

Furthermore, a significant advance for aerial manipulation outdoors is expected to come from the use of the explicit aerodynamic model in Section 3.2. This model provides a first estimation of the wind disturbances –linear to a set of parameters– that can be employed to enhance the UAV control core with adaptive laws. Using this approach, the limited outdoor capabilities of implementable solutions to moderately adverse environmental conditions –generally sidestepped with demonstrations under calm wind conditions– could be significantly improved. This would benefit cutting-edge projects aimed at real outdoor implementation demanding increasingly robust control techniques to improve the operational accuracy and precision under external perturbations.

However, the main drawback of the ongoing work is the need of measuring or estimating the local wind conditions for the AM. To cope with this problem, nonetheless, two different approaches are being studied: i) relaxing the goals of the formulation so the adaptive laws deal with filtered wind inputs –obtained from a fixed ground station–, being the local high-frequency disturbances rejected by the passive robustness of the control core or with robust add-ons; or ii) obtaining an estimate of the wind conditions from distributed sensors –either on ground or on board– so the local inaccuracies of the wind measurement systems are significantly compensated.

Simultaneously, the control allocation of the force and torque control inputs to cope with the disturbances coming from the variations of the rotor efficiency (see Section 3.2.2) are also being studied. To improve its response, a robust approach is expected to be used to create an intelligent motor mixer for the platform. This will include a nullspace-based modification that could shape the distribution of thrusts in case one of the rotors is close to saturation, thus broadening the flight envelope of the multirotor. In what respects to aerial manipulation, this would also extend the practical manipulability region of the mission system. Those configurations that, otherwise, would have saturated the propulsion could now have a small margin left, thus improving the performance, safety and applicability of aerial systems.

8.2.2 Novel aerial manipulation applications

These advances are expected to enable new applications for outdoor aerial manipulation. Among them, the author proposes the use of aerial manipulations to inspect or repair essential infrastructures during emergencies –under negative environmental conditions–; to interact with wildlife in their habitats; and to assist exploration rovers in other planets. Although some of these applications are yet far from becoming real, the approaches above could move them closer.

Emergency inspection/repair of core infrastructures

Due to the enhanced rejections capabilities, aerial manipulators could be used to perform urgent missions in core infrastructures even under severe environmental conditions. On the one hand, they could provide first hand information to evaluate the risks to the infrastructure. If this is used correctly, the efficiency of the early response could be significantly improved, being focused the initially limited resources on dynamically changing key points. On the other hand, punctual actuations could also be performed by these aerial robots if they are equipped with specific mission systems. For instance, chemical agents could be used to extinguish fires located in critical points and manipulation tasks could be performed in otherwise inaccessible locations.

Interaction with wildlife in their habitat

These improved capabilities in outdoor scenarios can also be used to bridge aerial robotics with applications in environmental science, ecology and biology. Nowadays, the collection of samples and the monitoring of organisms/ecosystems is done manually, hence demanding significant human resources and time. By employing aerial robots in these fields, these processes could be –at least partially– automatised. Moreover, if the robotic systems –specifically designed with the safety of the studied environment in mind– could be equipped with different mission systems, these tasks could be expanded. For example, by shooting tranquillisers –i.e. anaesthetic solutions– with a manipulator to incapacitate animals, it could be feasible to assess wounds or monitor pregnant animals of endangered species.

Auxiliary tasks in planetary exploration.

Ultra-lightweight aerial manipulators could also be used in the future as auxiliary systems to autonomous planetary surface exploration vehicles. Among the possible tasks they could perform, the author highlights their potential for inspection, cleaning and repair. These systems could assess damages to their mothership –in this case, the exploration rover– and, if these are limited, even patch them up. In what refers to cleaning, they could potentially improve the energy efficiency of the rover by helping it with the cleaning of the solar panels or the rust attached to any of the mechanisms of the mothership that could induce friction. Additionally, these auxiliary systems could be employed to take samples at inaccessible locations, thus enriching the characterisation of the planetary environment without forcing the rover design to be capable of such missions. Finally, it is worth noting that controllers aimed at such application must be designed with the extreme environmental conditions of planetary exploration –e.g. low/high density of the fluid field, fine dust, high wind speeds and sudden day/night variations– in mind. This would either imply the need of redundancy, or that these aerial systems would need to be automatically manufactured –with 3D printing, for instance–, assembled and recycled.

Appendix A

Relative-pose optimisation for decentralised control of aerial manipulators

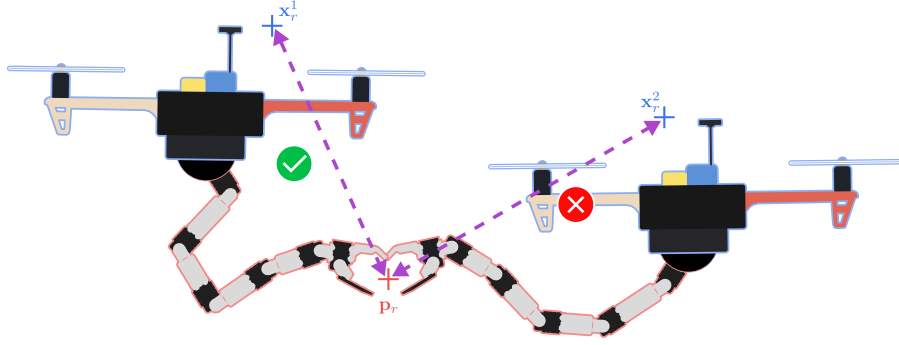


FIGURE A.1: Simplified concept of the pose optimisation: comparison between safe (check-mark) and unsafe (cross-mark) configurations of the platform with respect to the EE reference.

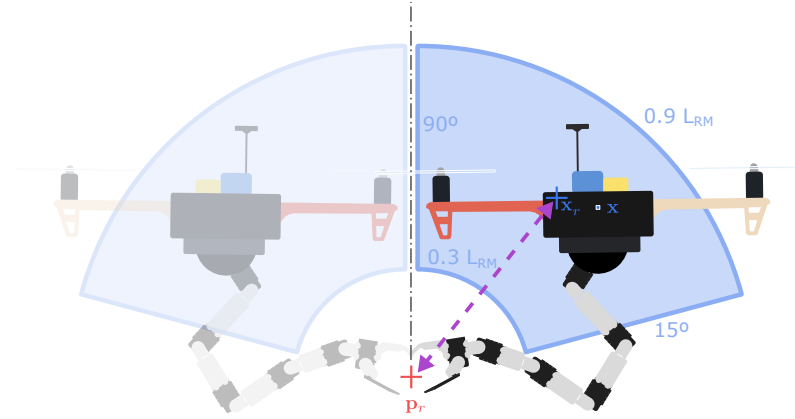


FIGURE A.2: Representation of the simulated conditions, highlighting the symmetry of the analysis.

As thoroughly studied in [C2], the extra DoF resulting from the compliant approach towards platform tracking in [C1, C4] –and reflected in this thesis in Chapter 6– can be exploited to further improve the performance of the system. This is done by optimising the UAV reference position with respect to the fixed manipulation target –here denoted as *relative-pose*, as conceptually shown in Fig. A.1– in terms of safety, performance and robustness against external disturbances.

A.1 Optimisation criterion

For this purpose, a wide set of poses associated to a positioning of the manipulation target within its the reachable region is selected. To delimit these configurations, we should firstly consider that the vertical symmetry of the analysis implies that the direction of the mission –leftwards or rightwards in a plane– has no real effect on the performance. Moreover, the severe limitations to aerial manipulation with the arm above the rotor plane also indicate that these configurations can be omitted. Accordingly, the simulated conditions using the approach in Chapter 6 are inside the sector –from 15° to 90° – of a ring centred in the EE target ranging from 30% to 90% of the total length of the manipulator, L_{RM} (see Fig. A.2). To obtain a significant sample, this region is meshed by intervals of 15° and 20% of L_{RM} , hence being simulated 24 different conditions during the analysis. Once the configurations to be covered are clearly indicated, it is worth detailing the criteria chosen in this case to represent the aforementioned safety, performance and robustness concerns. Among the different possibilities, the chosen criteria are:

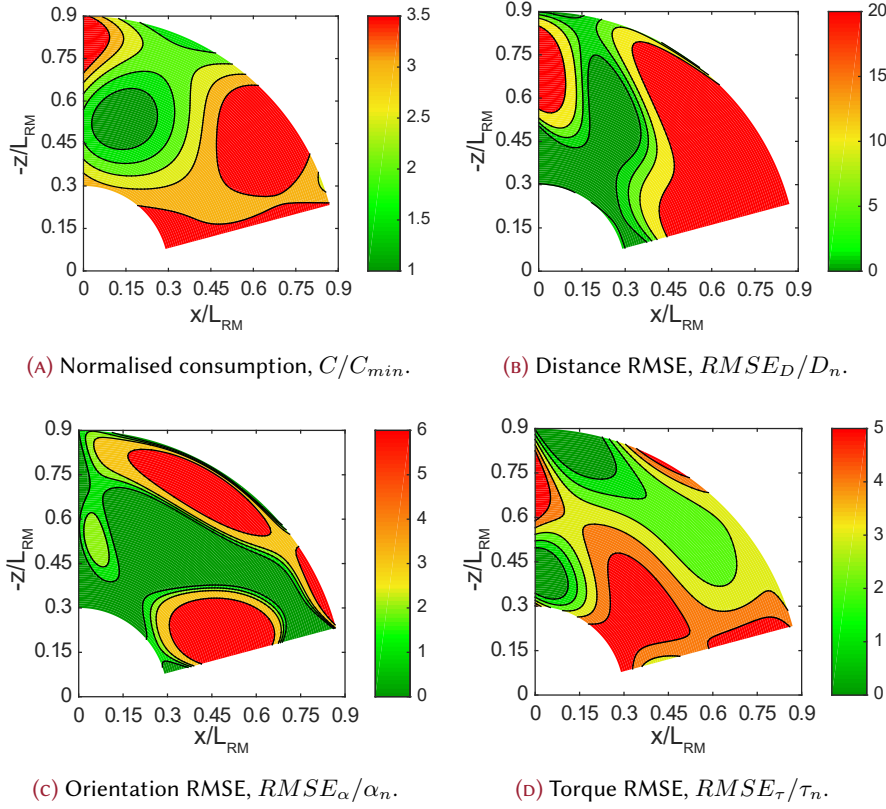


FIGURE A.3: Preliminary maps of the optimisation criteria without wind.

- the energy consumption to complete the manipulation mission, C , reflecting the efficiency of the operation and to penalise convoluted reconfigurations due to extreme poses;
- the position ($RMSE_D$) and orientation ($RMSE_\alpha$) root-mean-square error, both to show the robustness of the solution in terms of manipulation tracking and to clearly highlight those poses resulting in unsafe oscillations and/or steady-state error; and
- the root-mean-square reaction torque transmitted by the manipulator to the platform, $RMSE_\tau$, to display the influence of the pose to the implicit internal disturbances in aerial manipulation and to discard those configurations that are risky from this perspective.

These conditions are, in turn, encapsulated in a single optimisation criterion, reading

$$\Phi_{r-p} := \left| \frac{C}{C_{min}} \right|_{\alpha_C} + \left| \frac{RMSE_D}{D_n} \right|_{\alpha_D} + \left| \frac{RMSE_\alpha}{\alpha_n} \right|_{\alpha_\alpha} + \left| \frac{RMSE_\tau}{\tau_n} \right|_{\alpha_\tau}, \quad (\text{A.1})$$

where C_{min} is the minimum consumption obtained in hover –hence reflecting an approximate lower bound of this metric–, $D_n = 1$ cm is the normalising factor for distance, $\alpha_n = 5^\circ$ its counterpart for angles, and $\tau_n = 0.5$ N m for torques. In order to determine the weights given to each criterion – $\alpha_C, \alpha_D, \alpha_\alpha$ and α_τ –, a preliminary analysis was conducted with reduced simulations of 30 s, resulting in the optimisation criteria maps in Fig. A.3.

As shown by the recommended poses –in deep green–, these criteria significantly differ in their associated recommendations without significant overlapping between any of them. The same happens for alternative solutions in case the most beneficial are not possible (lighter green), non-recommendable configurations (in red), and non-recommendable but feasible poses –generally corresponding to far range capture attempts and nearly vertical or horizontal relative positions of both references– (in orange). Consequently, a trade-off solution is needed. The approach chosen is to

α_C	α_D	α_α	α_τ
0.20	0.65	0.10	0.05

TABLE A.1: Control gains of the benchmark application.

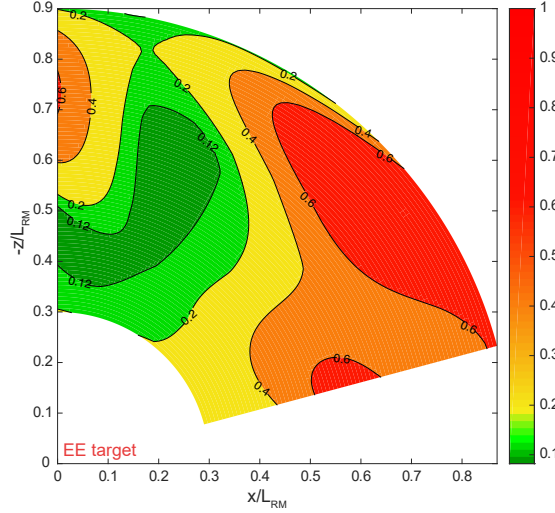


FIGURE A.4: Preliminary optimisation map without wind.

prioritise the position error to ensure that the recommended configuration always ends up in a successful operation. After this, the next criterion is the energy consumption, to avoid reconfigurations as indicated in the enumeration above. Finally, similar weights are given to the orientation and torque error. Altogether, the final weights of the optimisation criteria in (A.1) are presented in Table A.1. According to these weights, the preliminary maps of optimisation criteria result in the unified optimisation map in Fig. A.4. This indicates that –for cases without wind disturbances– it is advised to select configurations with the platform reference with a distance of between 40 % and 70% of the arm length and around an angle of 60° .

A.2 Recommended poses depending on the environmental conditions

Nonetheless, these results only account for cases without significant disturbances, while this appendix is focused on choosing a relative pose that enhances the robustness capabilities of the control strategy in Chapter 6. It is, thus, in order to add this extra layer of complexity to the simulations, both including aerodynamic disturbances produced by wind and white noise in the feedback of the controller. Being the later trivial, we should focus on indicating that the aerodynamic model employed corresponds to the characterisation in Section 3.2.¹ Once this point is clarified, the simulation setting is explained. As the introduction of random wind gusts could end up in completely inconsistent results, a simplified approach was taken. In each of the numerical simulations, the system is placed in a environment with a constant windspeed, being tried different poses –as with Fig. A.3–, where the forces exerted to the system are calculated using (3.16) and (3.17), and where the simulation time is extended to 45 s. Then, for each horizontal wind condition considered, i.e. $V_w = \{-10, -5, 0, 1, 2\} \text{ m s}^{-1}$, the unified criterion in (A.1) is evaluated, resulting in the five maps displayed in Fig. A.5.

¹For a discussion about the importance of this aerodynamic characterisation on the simulation results, please read Remark 6.6.

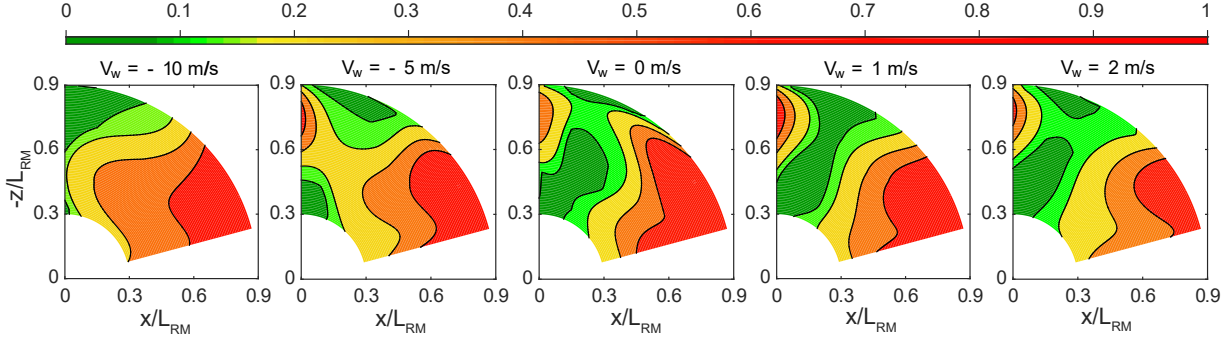


FIGURE A.5: Final optimisation maps for different mean wind speeds, $V_w \in [-10, 2] \text{ m s}^{-1}$.

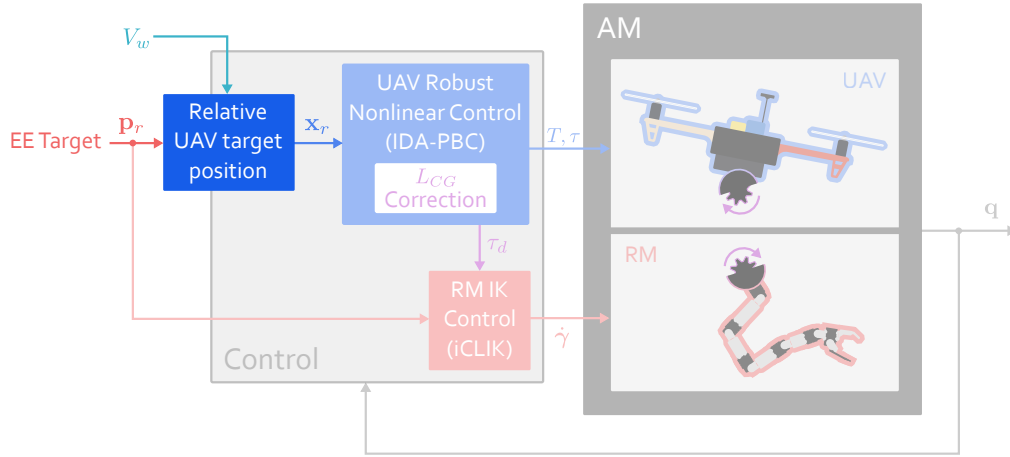


FIGURE A.6: Block diagram of the control solution (see Chapter 6), highlighting the use of the relative-pose optimisation module.

The different maps show that the recommendable poses significantly depend on the wind conditions. For instance, it is advisable stay almost on the vertical of the EE target for strong headwinds, but this configuration should be avoided in other cases. Nevertheless, some consistent recommendations can be given for all wind conditions, such as avoiding horizontal far-range configurations due to their significantly reduced success ratio. On the other hand, close-range poses have displayed acceptable results for all the range of windspeeds here considered, being recommended for operations in which this parameter is hard to estimate, or even has not been estimated at all. This result is specially interesting considering that, according to the unperturbed preliminary analysis in Fig. A.4, this was already recommended if the optimal conditions were not possible.

Finally, in [C2] an optimiser was added to the controller presented in Chapter 6 to reformulate the relative-pose dynamically as a function of the measured windspeed, as highlighted in Fig. A.6. This, nonetheless, showed inconclusive results. Taking into account that changing the UAV reference with respect to a parameter with a small characteristic time, such as wind gusts, reduced the accuracy of the operation, it was chosen instead to account for a filtered value of the windspeed. This, on the other hand, introduces significant delays to the pose recommendation, potentially leading to configurations that inherently contravene the recommendations. As a final approach, the already relaxed formulation was further simplified to obtain what definitely results in a useful tool. Instead of dynamically changing the platform reference, a recommended configuration is calculated offline on the basis of the mean speed of the wind on the location, hence slightly improving the performance.

Appendix B

Command-filtered backstepping with RM disturbance rejection capabilities

As an alternative to the manipulation-aware approach in Chapter 6, the redesign of a command-filtered backstepping UAV controller to enhance its robustness capabilities against RM oscillations was presented in [C3]. Although base command-filtered backstepping (see the rationale in Section B.1) is a robust strategy, it is not designed to cope with such disturbances. To deal with them, accordingly, an integral action is added to the position control, and a derivative-like action is imposed to the attitude rate controller, thus obtaining a dampened response to RM oscillations.

B.1 Command-filtered backstepping rationale

Let us define the UAV position reference as \mathbf{x}_r , with its associated error $\mathbf{e}^x := \mathbf{x}_r - \mathbf{x}$, the virtual control signal for feedback linearisation given by

$$\mathbf{U} := g\mathbf{e}_z - \frac{T}{m_Q} \mathcal{R}\mathbf{e}_z = \ddot{\mathbf{x}}, \quad (\text{B.1})$$

and the associated desired stable linear behaviour in closed-loop

$$\ddot{\mathbf{e}}^x + K_D^x \dot{\mathbf{e}}^x + K_P^x \mathbf{e}^x = 0. \quad (\text{B.2})$$

Then, by combining (B.1) and (B.2) the desired value of this virtual control signal becomes

$$\mathbf{U} = \ddot{\mathbf{x}}_r - \ddot{\mathbf{e}}^x = \ddot{\mathbf{x}}_r + K_D^x \dot{\mathbf{e}}^x + K_P^x \mathbf{e}^x.$$

Correspondingly, after pre and post multiplying the definition of this in (B.1) with the rotation matrix and the UAV mass, and some other straightforward calculations involving the rotation matrix definition in (3.2), the total commanded thrust becomes

$$T = m_Q \|\mathbf{U} - g\mathbf{e}_z\|,$$

and the attitude references result in

$$\begin{aligned} \tan \theta_r &= \frac{U_1 \cos \psi + U_2 \sin \psi}{U_3 - g}, \\ \sin \phi_r &= -\frac{U_1 \cos \psi - U_2 \sin \psi}{T/m_Q}, \end{aligned}$$

where the yaw angle is left unassigned due to its irrelevance on the position loop. Nonetheless, as the direction of the platform is generally significant in Aerial Robotics, its reference is given as an independent reference variable ψ_r . Accordingly to these references, the attitude loop error can be defined as $\mathbf{e}^\Theta := \Theta_r - \Theta$, with $\Theta_r := \text{col}(\phi_r, \theta_r, \psi_r)$, and the attitude rate error as $\mathbf{e}^\Omega := \Omega_r - \Omega$, being Ω_r a reference yet to be defined.

Proposition B.1. Consider the attitude loop of a multirotor UAV defined in (3.3), but omitting the aerodynamic contributions in τ^{aero} , and the proposed control law given by

$$\tau = \Omega \times I_Q \Omega + I_Q \left(\dot{\Omega}_r - W^\top \epsilon + W^\top \mathbf{e}^\Theta + \Gamma_\Omega \mathbf{e}^\Omega \right), \quad (\text{B.3})$$

and its associate filters, namely

$$\dot{\Omega}_r = \Gamma_T (\Omega_d - \Omega_r), \quad (\text{B.4a})$$

$$\dot{\epsilon} = -\Gamma_\Theta \epsilon + W (\Omega_d - \Omega_r), \quad (\text{B.4b})$$

$$\Omega_d = W^{-1} (\dot{\epsilon} + \Gamma_\Theta \mathbf{e}^\Theta), \quad (\text{B.4c})$$

with $\Gamma_\Theta, \Gamma_\Omega \in \mathbb{R}^{3 \times 3}$ definite positive control gains matrices and $\Gamma_T \in \mathbb{R}^{3 \times 3}$ the command filter parameter matrix, also definite positive but also diagonal and with elements large enough to assure a fast transient of the attitude rate reference. Then, upon assuming that the position control loop is significantly faster than its attitude counterpart, the controlled system is (globally) asymptotically stable.

Proof. Let us choose the radially unbounded and positive definite Lyapunov candidate given by

$$V_1 := \frac{1}{2} \|\mathbf{e}^\Theta\|^2,$$

and whose time derivative reads

$$\dot{V}_1 = \mathbf{e}^{\Theta^\top} \dot{\mathbf{e}}^\Theta = \mathbf{e}^{\Theta^\top} (\dot{\Theta}_r - W\Omega).$$

Then, by introducing the virtual control signal given by (B.4c), which can be assimilated to the desired attitude rates to make the whole attitude loop converge, the Lyapunov candidate becomes

$$\dot{V}_1 = -\mathbf{e}^{\Theta^\top} \Gamma_\Theta \mathbf{e}^\Theta + \mathbf{e}^{\Theta^\top} W (\Omega_d - \Omega),$$

where the last term is not yet shaped to become negative definite, thus demanding an add-on to conclude the proof. This is obtained after redefining the attitude error as $\bar{\mathbf{e}}^\Theta := \mathbf{e}^\Theta - \epsilon$, dealing ϵ with the mismatch between the attitude rate reference and its desired value Ω_d . To do so, we also redefine the Lyapunov candidate as

$$V_2 := \frac{1}{2} \|\bar{\mathbf{e}}^\Theta\|^2,$$

being its time derivative

$$\dot{V}_2 = (\bar{\mathbf{e}}^\Theta)^\top \dot{\bar{\mathbf{e}}}^\Theta = (\bar{\mathbf{e}}^\Theta)^\top \left[-\Gamma_\Theta \mathbf{e}^\Theta + W (\Omega_d - \Omega) - \dot{\epsilon} \right].$$

Then, upon using the filter in (B.4b), this derivative becomes

$$\dot{V}_2 = -(\bar{\mathbf{e}}^\Theta)^\top \Gamma_\Theta \bar{\mathbf{e}}^\Theta + (\bar{\mathbf{e}}^\Theta)^\top W \mathbf{e}^\Omega,$$

also being the last term not yet negative definite. Nonetheless, due to its dependency with the attitude rate error it can be shaped in the step associated to this variable. For this purpose, the final Lyapunov candidate is introduced, namely

$$V_3 := V_2 + \frac{1}{2} \|\mathbf{e}^\Omega\|^2,$$

subsequently reading its derivative

$$\begin{aligned} \dot{V}_3 &= \dot{V}_2 + \mathbf{e}^{\Omega^\top} \dot{\mathbf{e}}^\Omega \\ &= -(\bar{\mathbf{e}}^\Theta)^\top \Gamma_\Theta \bar{\mathbf{e}}^\Theta + (\bar{\mathbf{e}}^\Theta)^\top W \mathbf{e}^\Omega + \mathbf{e}^{\Omega^\top} \dot{\mathbf{e}}^\Omega \\ &= -(\bar{\mathbf{e}}^\Theta)^\top \Gamma_\Theta \bar{\mathbf{e}}^\Theta + \mathbf{e}^{\Omega^\top} (W^\top \bar{\mathbf{e}}^\Theta + \dot{\mathbf{e}}^\Omega) \\ &= -(\bar{\mathbf{e}}^\Theta)^\top \Gamma_\Theta \bar{\mathbf{e}}^\Theta + \mathbf{e}^{\Omega^\top} \left[W^\top \bar{\mathbf{e}}^\Theta + \dot{\Omega}_r - I_Q^{-1} (-\Omega \times I_Q \Omega + \tau) \right]. \end{aligned}$$

Thus, using the proposed control law in (B.3), this derivative becomes

$$\dot{V}_3 = -(\bar{\mathbf{e}}^\Theta)^\top \Gamma_\Theta \bar{\mathbf{e}}^\Theta - \mathbf{e}^{\Omega^\top} \Gamma_\Omega \mathbf{e}^\Omega,$$

therefore concluding that the solution asymptotically converges to the equilibrium in $\bar{\mathbf{e}}^\Theta = \mathbf{e}^\Omega = \mathbf{0}$. However, this condition is not the desired outcome of the controller as $\bar{\mathbf{e}}^\Theta \rightarrow \mathbf{0}$ does not directly imply that $\mathbf{e}^\Theta \rightarrow \mathbf{0}$. To finally achieve this result, the command filter in (B.4a) is introduced, therefore granting that the attitude rate reference converges to the aforementioned desired value and, consequently, that the mismatch parameter ϵ tends to converge to the trivial value. Altogether, the only set of equilibria left corresponds to the asymptotic convergence of the system to the zero steady-state error, thus concluding the proof. \square

B.2 Redesign of the command-filtered backstepping disturbance rejection

As commented in the introduction of this appendix, the formulation in Section B.1 is significantly affected by the RM oscillations in AMs. To deal with this situation, a solution to improve the disturbance rejection capabilities against such disturbances is proposed. This modification can be divided in two main contributions: i) the trivial –but essential– introduction of an integral action in the position control, which is based on feedback linearisation; and ii) the addition of derivative-like action on the core controller (B.3), the mismatch filter (B.4b), and the desired attitude rate equation (B.4c), therefore dampening error peaks due to RM oscillations.

On the one hand, the position loop modifications directly emanate from a change in the desired stable behaviour in the close-loop, from (B.2) to

$$\ddot{\mathbf{e}}^x + K_D^x \dot{\mathbf{e}}^x + K_P^x \mathbf{e}^x + K_I^x \int_{t_0}^t \mathbf{e}^x d\zeta = 0, \quad \int_0^{t_0} \mathbf{e}^x d\zeta = \mathbf{e}_{I,0}^x,$$

with $K_I^x \in \mathbb{R}^{3 \times 3}$ a positive definite matrix containing the integral action gains, $\zeta \in \mathbb{R}$ a parametrisation of time and $\mathbf{e}_{I,0}^x$ a feedforward integral action introduced to counteract external forces at the beginning of the operation, typically the weight of the system. Accordingly, the modified virtual control signal reads

$$\mathbf{U} = \ddot{\mathbf{x}}_r + K_D^x \dot{\mathbf{e}}^x + K_P^x \mathbf{e}^x + K_I^x \int_{t_0}^t \mathbf{e}^x d\zeta,$$

being the subsequent steps of the unmodified approach used thereafter. On the other hand, for the derivative-like action in the attitude loop, a similar approach to Proposition B.1 is chosen¹.

Proposition B.2. Consider the dynamic formulation employed in Proposition B.1 –i.e. (3.3), but omitting the aerodynamic contributions– and the modified controller given by

$$\boldsymbol{\tau} = \boldsymbol{\Omega} \times I_Q \boldsymbol{\Omega} + I_Q \left(\dot{\boldsymbol{\Omega}}_r - W^\top \boldsymbol{\epsilon} + W^\top \mathbf{e}^\Theta + \Gamma_\Omega^P \mathbf{e}^\Omega + \Gamma_\Omega^D \dot{\mathbf{e}}^\Omega \right), \quad (\text{B.5})$$

and its associate modified filters reading

$$\dot{\boldsymbol{\Omega}}_r = \Gamma_T (\boldsymbol{\Omega}_d - \boldsymbol{\Omega}_r), \quad (\text{B.6a})$$

$$\dot{\boldsymbol{\epsilon}} = \left(I_3 + \Gamma_\Theta^D \right)^{-1} \left[-\Gamma_\Theta^P \boldsymbol{\epsilon} + W (\boldsymbol{\Omega}_d - \boldsymbol{\Omega}_r) \right], \quad (\text{B.6b})$$

$$\boldsymbol{\Omega}_d = W^{-1} \left(\dot{\boldsymbol{\Theta}}_r + \Gamma_\Theta^P \mathbf{e}^\Theta + \Gamma_\Theta^D \dot{\mathbf{e}}^\Theta \right), \quad (\text{B.6c})$$

where the modifications are highlighted in **dark red**, denoting $\Gamma_\Theta^P, \Gamma_\Omega^P \in \mathbb{R}^{3 \times 3}$ the positive definite proportional control gains matrices already used in Proposition B.1, $\Gamma_\Theta^D, \Gamma_\Omega^D \in \mathbb{R}^{3 \times 3}$ the newly introduced positive definite derivative-like gains matrices, and $\Gamma_T \in \mathbb{R}^{3 \times 3}$ the same command filter parameter matrix defined in Proposition B.1. Then, upon assuming that the position control loop is significantly faster than its attitude counterpart and using estimators for the derivatives of the error variables, the controlled system is (globally) asymptotically stable.

Proof. Let us choose the a new radially unbounded and positive definite Lyapunov candidate, namely

$$V_1 := \frac{1}{2} \left\| \mathbf{e}^\Theta \right\|^2 + \frac{1}{2} \left\| \mathbf{e}^\Theta \right\|_{\Gamma_\Theta^D}^2,$$

¹For the sake of comparison, the names of the Lyapunov candidates used in Proposition B.1 are maintained.

where the sub-index in the new term stands for the Γ_Θ^D -weighted norm. Then, the time derivative of this candidate reads

$$\dot{V}_1 = \mathbf{e}^\Theta{}^\top \dot{\mathbf{e}}^\Theta + \mathbf{e}^\Theta{}^\top \Gamma_\Theta^D \dot{\mathbf{e}}^\Theta = \mathbf{e}^\Theta{}^\top \left(\dot{\Theta}_r - W\Omega + \Gamma_\Theta^D \dot{\mathbf{e}}^\Theta \right).$$

By introducing the virtual control signal (B.6c) in this expression, the Lyapunov candidate derivative reads

$$\dot{V}_1 = -\mathbf{e}^\Theta{}^\top \Gamma_\Theta^P \mathbf{e}^\Theta + \mathbf{e}^\Theta{}^\top W (\Omega_d - \Omega).$$

As happened with the equivalent of this equation in Proposition B.1, an add-on is needed to make the last term negative definite. For that purpose, let us use the redefinition of the attitude error given by $\bar{\mathbf{e}}^\Theta := \mathbf{e}^\Theta - \epsilon$, where ϵ dealt with the mismatch between the attitude rate reference and its desired value Ω_d . Accordingly, we reformulate the second Lyapunov candidate as

$$V_2 := \frac{1}{2} \|\bar{\mathbf{e}}^\Theta\|^2 + \frac{1}{2} \|\bar{\mathbf{e}}^\Theta\|_{\Gamma_\Theta^D}^2,$$

being its time derivative

$$\dot{V}_2 = (\bar{\mathbf{e}}^\Theta)^\top \dot{\bar{\mathbf{e}}^\Theta} + (\bar{\mathbf{e}}^\Theta)^\top \Gamma_\Theta^D \dot{\bar{\mathbf{e}}^\Theta} = (\bar{\mathbf{e}}^\Theta)^\top \left[-\Gamma_\Theta^P \mathbf{e}^\Theta + W (\Omega_d - \Omega) - (I_3 - \Gamma_\Theta^D) \dot{\epsilon} \right].$$

Then, upon using the filter in (B.6b), this derivative becomes

$$\dot{V}_2 = -(\bar{\mathbf{e}}^\Theta)^\top \Gamma_\Theta^P \bar{\mathbf{e}}^\Theta + (\bar{\mathbf{e}}^\Theta)^\top W \mathbf{e}^\Omega,$$

also being in this case the last term not yet negative definite. Nonetheless, as happened in Proposition B.1, this can be shaped in the step associated to the attitude rate error, whose new Lyapunov candidate reads

$$V_3 := V_2 + \frac{1}{2} \|\mathbf{e}^\Omega\|^2 + \frac{1}{2} \|\mathbf{e}^\Omega\|_{\Gamma_\Omega^D}^2,$$

and its derivative

$$\begin{aligned} \dot{V}_3 &= \dot{V}_2 + \mathbf{e}^\Omega{}^\top \dot{\mathbf{e}}^\Omega + \mathbf{e}^\Omega{}^\top \Gamma_\Omega^D \dot{\mathbf{e}}^\Omega \\ &= -(\bar{\mathbf{e}}^\Theta)^\top \Gamma_\Theta \bar{\mathbf{e}}^\Theta + (\bar{\mathbf{e}}^\Theta)^\top W \mathbf{e}^\Omega + \mathbf{e}^\Omega{}^\top \dot{\mathbf{e}}^\Omega + \mathbf{e}^\Omega{}^\top \Gamma_\Omega^D \dot{\mathbf{e}}^\Omega \\ &= -(\bar{\mathbf{e}}^\Theta)^\top \Gamma_\Theta \bar{\mathbf{e}}^\Theta + \mathbf{e}^\Omega{}^\top \left(W^\top \bar{\mathbf{e}}^\Theta + \dot{\mathbf{e}}^\Omega + \Gamma_\Omega^D \dot{\mathbf{e}}^\Omega \right) \\ &= -(\bar{\mathbf{e}}^\Theta)^\top \Gamma_\Theta \bar{\mathbf{e}}^\Theta + \mathbf{e}^\Omega{}^\top \left[W^\top \bar{\mathbf{e}}^\Theta + \dot{\Omega}_r + \Gamma_\Omega^D \dot{\mathbf{e}}^\Omega - I_Q^{-1} (-\Omega \times I_Q \Omega + \tau) \right]. \end{aligned}$$

Finally, using the modified control law in (B.5), the derivative reads

$$\dot{V}_3 = -(\bar{\mathbf{e}}^\Theta)^\top \Gamma_\Theta \bar{\mathbf{e}}^\Theta - \mathbf{e}^\Omega{}^\top \Gamma_\Omega \mathbf{e}^\Omega,$$

just as in Proposition B.1. Correspondingly, the command filter in (B.6a) is introduced to assure that $\bar{\mathbf{e}}^\Theta \rightarrow \mathbf{0}$ implies $\mathbf{e}^\Theta \rightarrow \mathbf{0}$, thus concluding the proof. \square

B.3 Numerical validation

After presenting the theoretical contribution, the associated advances in terms of disturbances rejection are studied in simulation, being the RM considered a disturbance to the operation of the whole AM. For the sake of simplicity, the manipulator motion is modelled using a spherical manipulator that emulates the complete RM complexity via its properties at the centre of gravity instead of assembling individual models for each of the segments of the RM. Additionally, the explicit aerodynamic model in Section 3.2 –which in turn derives from [C6]– is used to include the effects of external aerodynamic effects, thus enriching the simulation scenario.²

²For a discussion about the importance of this aerodynamic characterisation on the simulation results, please read Remark 6.6.

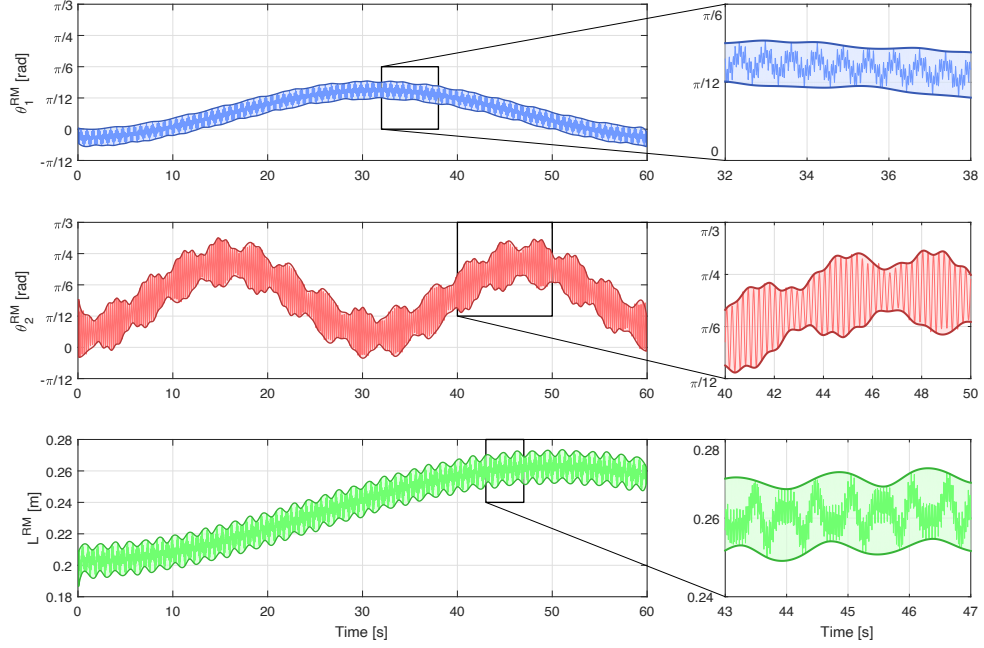


FIGURE B.1: Position of the centre of gravity of the RM in spherical coordinates, with θ_1^{RM} the azimuth, θ_2^{RM} the polar angle and L^{RM} the distance to the centre of gravity of the UAV, including a detail plot of each of the signals and highlighting the envelope of these state variables.

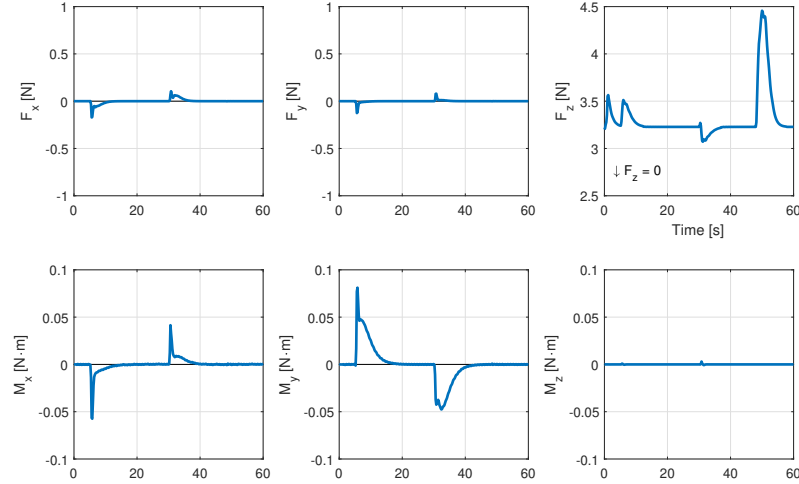


FIGURE B.2: Aerodynamic forces and torques during the numerical validation according to the model in Section 3.2.

Then, before presenting the simulation results, let us firstly characterise these two disturbances. On the one hand, the equivalent manipulator state is represented via the spherical coordinates of its centre of gravity –correspondingly to its configuration–, as depicted in Fig. B.1. It is worth noting that a complex and aggressive motion of this system has been chosen to assure a negative coupling with the platform in a conservative approach. This includes substantial displacements of the centre of gravity (up to 8 cm) and oscillations with diverse amplitudes and frequencies in all the state coordinates. On the other hand, the aerodynamic effects on the platform for the current experiment are shown in Fig. B.2. Note that they essentially depend on the airspeed –in this case without wind disturbances, this is equivalent to the ground speed associated to Fig. B.3–, thus being constant when the platform is in hover and varying for non-steady regimes.

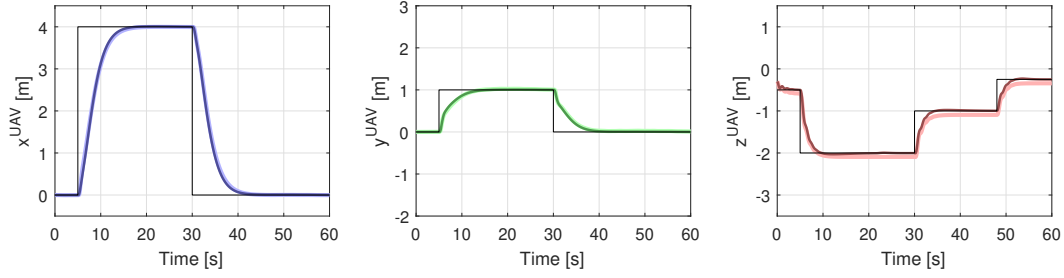


FIGURE B.3: Comparison between the modified solution (darker colours) and the standard command-filtered backstepping one (lighter colours) in terms of UAV tracking, where their respective references are denoted with black lines.

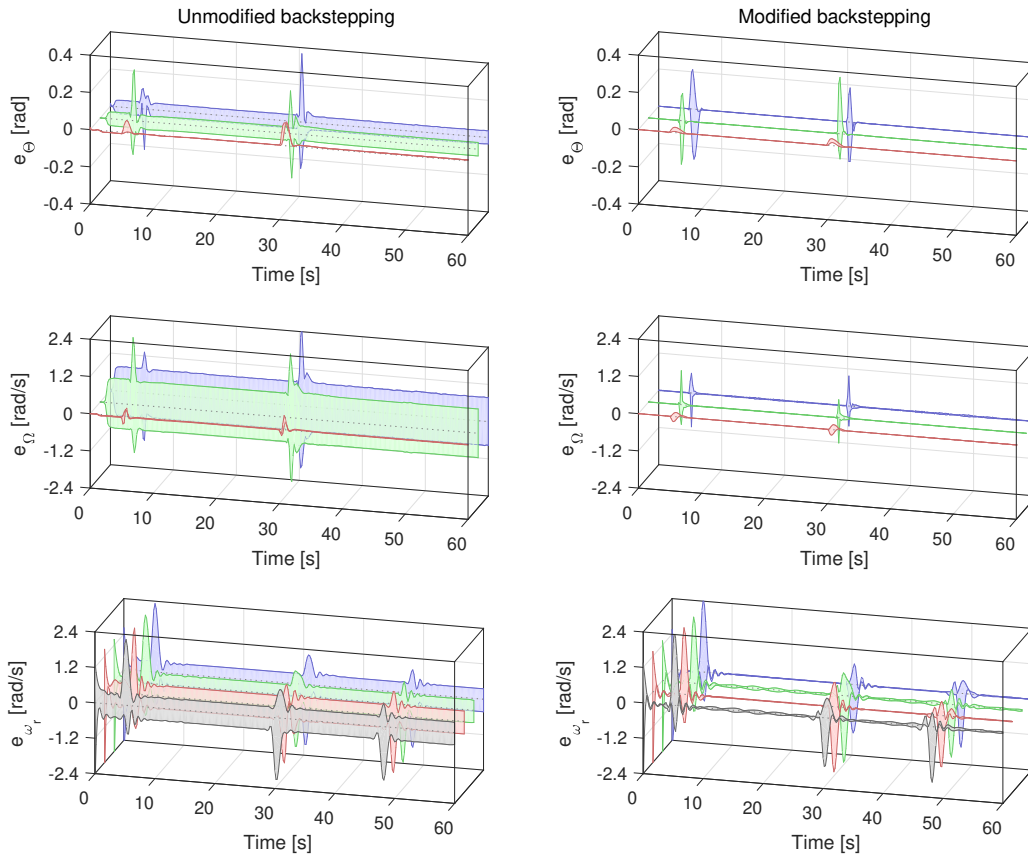


FIGURE B.4: Attitude, attitude rate and rotor speed errors for both the unmodified backstepping and the proposed modification, where each component is identified using colours increasing from blue to gray (i.e. roll error corresponds to the first component, in blue, while the error of the last rotor is its fourth component, accordingly gray).

Finally, the advances obtained have a twofold impact: i) on the overall position AM performance, as depicted in Fig. B.3, and ii) on the attitude oscillations to perform this position tracking (see Fig. B.4), with an evident relation with the power consumption of the system. Although the results of the first do not show ground-breaking improvements, a slightly faster convergence is achieved for the horizontal positions as well as a noticeable correction of the steady-state error in the vertical one, associated to the inclusion of the position integral action. However, the most sig-

nificant improvements are related to the second analysis. In Fig. B.4, we can identify a noticeable reduction of the error oscillations in both the attitude and its rates away from reference changes. This cancellation of disturbances utterly contributes to the accuracy of the manipulation operation and to the power efficiency of the system, thus improving the performance of the whole AM. Additionally, the impact of the solution on the rotor speed error oscillations –in which a simplistic propulsion model, $T_i = k_{\omega_r} \omega_r$ with k_{ω_r} constant, was considered– is also included directly from [C6]. Although this step of the controller has not been considered in the current thesis due to its limited contribution, this particular result evinces that the use of the proposed controller has a significant impact on the variation of the rotor speeds and, therefore, on the power consumption, as aforementioned.

List of Figures

1.1	Some applications of aerial manipulation.	3
1.2	Concept map with the main trends in what respects to the nonlinear control of aerial manipulators, omitting minor branches –although being mentioned in the body of the text– for simplicity, highlighting the techniques used in this thesis in bold, and using the colour patterns of this thesis: red for RM, blue for UAV, and violet for their coupling in an AM.	4
2.1	Phases of an aerial manipulation mission outdoors including interaction tasks with industrial facilities, with colours indicating growing complexity from green to red and being the most relevant tasks enumerated within them.	11
2.2	Steps of the operation phase in the installation of a sensor on a rigid interface or its inspection through contact with force control in several axes.	11
2.3	Schematic depiction of the research line divided into contributions to the manipulation-aware control of UAVs and to the adaptive control of flexible manipulators, with the associated publications labelled according to the list of publications and the ongoing research shown below the line representing the current state.	12
3.1	Definition of the DoF of the flexible manipulator, including the dynamic parameters used.	18
3.2	Characterisation of the studied multi-rotor reference frame, highlighting the reference face –chosen <i>a priori</i> for consistency–, the rotor enumeration order and the rotation direction criteria.	22
3.3	BEMT actuator disk model of the propulsion system, highlighting the streamtube with its associated far upstream (inlet) and far downstream (outlet) disks of the Glauert’s flow model [113].	23
3.4	Deviations of the BEMT in forward flight and axial descent.	24
3.5	Recursive methodology to obtain the blunt-body aerodynamic model of a multi-rotor UAV, where f_{eq_1, \dots, eq_n} denotes the use of the equations in the sub-index –e.g. if $f_{8,11-13}$ is indicated in within a step, the equations (3.8), (3.11)-(3.13) are needed for that particular step– and the particular nomenclature used for this methodology is defined in the associated text.	25
3.6	Structure of the proposed flight aerodynamics model for multi-rotors compared to the CAC approach for $\beta = 33.75^\circ$ as a function of α_r and V_∞	29

3.7	Comparison in terms of error with respect to CFD simulation results between the proposed aerodynamic model (black segments) and the CAC solution (white segments) as error bars (see their graphical definition on the bottom right corner), being only considered points within the simulable region. Note: error bars in light gray indicate cases in which both solutions show errors below 1 N, for forces, or 0.05 N m, for torques.	29
3.8	Simulable and non-simulable regions based on the aforementioned propulsion limitations –being indicated interpolated solutions with straight arrows and extrapolated ones with curved lines– with the model for hover collapsed. Note: these regions can also be identified in Fig. 3.7.	31
3.9	Influence of the weight factor on the aerodynamic model validity for percentiles 50, 75 and 90 of the simulation configurations.	32
4.1	Definition of the contact parameters using a undeformed/deformed superimposed plot, where the undeformed is in light gray and the deformed in dark grey.	36
4.2	Close-loop control schematic, including the flexibility-aware actuation (in blue), the adaptive modules (in orange) and the direct kinematics with flexible feedback (in green).	38
4.3	Experimental setting for the validation of the proposed strategy, including both the experimental layout of the 3 scenarios considered –with or without an elastic interface– and the mechanical characterisation of this element.	40
4.4	Results for the repeatability scenario with mean EE position and orientation on the left, mean adaptive parameters on the centre, and XY representation of the mean experiment using black arrows to indicate both position and orientation and targets, with annuli of 1 cm and reference orientation as black radii, for the waypoints on the right. To illustrate the variability in the experimental set, both the position and adaptive parameter plots include their maximum deviations from the mean, here denoted as $(\cdot)^\Delta$	42
4.5	EE position and adaptive parameters for the impact scenario, where these disturbances are indicated with dark yellow lines –with their associated transients as light yellow rectangles– and labelled from 1 to 7. To facilitate its interpretation, a detail of the third impacts is included on the right.	43
4.6	End-effector position and orientation for the contact scenario, including the variation of the adaptive parameters.	43
5.1	Definition of the multi-axis contact parameters using a undeformed/deformed superimposed plot, where the undeformed is in light gray and the deformed in dark grey.	46
5.2	Close-loop control schematic with the inner position and outer force loops, highlighting the integral inverse kinematics core in blue, the the force-aware reference variation law in green, the adaptive parameters (including the new \hat{K}_e) in orange, and the associated equations to obtain each of these in brackets.	48
5.3	Experimental setting for the validation of the modified strategy, including the rigid contact interface, the force measuring system, and the consideration of frictionless displacement.	51
5.4	Results of the unperturbed case with the XY trajectory of the EE represented using equally time-spaced points with different size and lightness to reflect both speed and time (smaller is faster and darker is later), and where waypoints are highlighted as targets, on the top; the Cartesian position and orientation of the EE (being their references identified as thinner lines), on the centre; and the adaptive parameters for \mathcal{N} , on the bottom (their counterparts for \mathcal{N}^\perp were neglectable in this scenario).	52

5.5	Results of the simplified contact force scenario: force tracking and adaptive parameters on the top (with projector influence and contact detection highlighted); Cartesian position and orientation on the centre (using thinner lines for modified references according to the outer force control loop in contrast to the original references, dotted); and adaptive parameters on the bottom.	53
5.6	Results of the mixed contact/non-contact scenario, with the force tracking and its associated adaptive parameters on the top (with highlighted projector influence zones), the Cartesian position and orientation tracking in the centre (with initial references dotted and force-shaped references as thinner lines), and the whole set of adaptive parameters on the bottom.	54
6.1	Coordinate control strategy analogy.	58
6.2	Sketch of the longitudinal dynamics of the AM.	61
6.3	Block diagram of the whole aerial manipulation strategy.	67
6.4	Reference changes for both UAV and RM in the two sub-cases for the comparison scenario: UAV displacement in the same direction of the RM extension and in the opposite direction. Each reference is labelled with its associated step time, denoting the super-indexes if the reference is pre-step (-) or post-step (+).	71
6.5	Comparison between the step response for reference changes of the same and opposite directions of the proposed solution (solid) and of an integral backstepping (dashed) under wind disturbances, with the position references represented with dotted lines and the four step-time offsets ΔT from 0 to 7.5 s labelled with colours ranging from red to green.	73
6.6	Collision avoidance results for the operation phase, with EE XZ-trajectory (dotted), highlighted zones of collision avoidance activation (yellow or red for 1 or 2 extra iCLIK iterations, respectively) and blue arrows illustrating virtual rejection forces, on the left; EE error, in the top right corner; and moving average (filter time 0.25 s) number of iCLIK iterations, corresponding 0 to the flight mode, 1 to the normal iCLIK algorithm, and 2 or more to extra iterations, in the bottom left corner.	74
6.7	AM behaviour after a sudden payload increment at 10 s (highlighted in yellow) when the dynamic extension is off (at the top) and off (in the middle), with the dynamic extension results (at the bottom).	75
7.1	Logo of the Modular Autopilot Solution, MAS _{PX4} [Ⓜ]	78
7.2	Redundant MAS _{PX4} [Ⓜ] solution, depicted as a schematic diagram similar based on transit maps to underscore the importance of the RC switch (in orange) between the customised line implemented in Simulink [®] (in aquamarine) and the backup line in PX4 (in purple).	80
7.3	Validation system during a test flight, with an exploded view of the hardware chosen.	81
7.4	Architecture of MAS _{PX4} [Ⓜ] , including the main computer (Intel [®] NUC , on the right), the backup board (Raspberry Pi [®] 3 , on the left) and the ground systems (at the bottom). Among the latter, both human agents stand out due to their importance for the RC switch and the monitoring of the customised algorithm.	82
7.5	Mean time ratio during 20 tests of 8 s each, on both normal an accelerator modes, with maximum deviation highlighted as error bars.	84
7.6	MAS _{PX4} [Ⓜ] customisation environment in Simulink [®] , including the proposed standard communication modules (at the top) and a detail view of the different blocks that comprise the main customisation module (at the bottom). Among these, the position (A) and attitude (B) controllers are highlighted, together with the navigation module and the flight mode switch.	85
7.7	Proposed implementation phases for MAS _{PX4} [Ⓜ]	85

7.8	Cascade PID controller implemented in MAS_{PX4}^{\oplus} , with both position and control loops (see Fig. 7.6) and experimental results for a flight at constant altitude.	86
7.9	Command-filtered backstepping controller implemented in MAS_{PX4}^{\oplus} , with both position and control loops (see Fig. 7.6) and experimental results for a flight at constant altitude.	87
7.10	Stacked CPU load during the execution of the customised code of the command-filtered backstepping in MAS_{PX4}^{\oplus} , being the RAM used steady at 25% throughout the test.	88
7.11	Navigation module implemented in MAS_{PX4}^{\oplus} (see Fig. 7.6).	88
7.12	Results of the experiment including the navigation module on top of the PID cascade controller, with: patch tracking (on the left, using position markers separated by 0.25 s and where the navigation waypoint order is indicated by numbers), global position (in the top right corner, where black lines correspond to the navigation module references) and platform attitude (in the bottom right corner, following the references –in this case derived from the position loop– the same format).	89
7.13	Logo of the Jormungandr lightweight flexible manipulator.	89
7.14	Jormungandr prototypes.	90
7.15	Dynamixel AX-12A servomotors [161].	90
7.16	Murata SV01 rotatory position potentiometer [162].	91
7.17	Arbotix-M Robocontroller [163].	91
7.18	Dual-axis force sensor setup, with the Jormungandr Mk. 2 pressing in the normal direction.	91
7.19	Arduino Mega 2560 [164].	92
A.1	Simplified concept of the pose optimisation: comparison between safe (check-mark) and unsafe (cross-mark) configurations of the platform with respect to the EE reference.	100
A.2	Representation of the simulated conditions, highlighting the symmetry of the analysis.	100
A.3	Preliminary maps of the optimisation criteria without wind.	101
A.4	Preliminary optimisation map without wind.	102
A.5	Final optimisation maps for different mean wind speeds, $V_w \in [-10, 2] \text{ m s}^{-1}$	103
A.6	Block diagram of the control solution (see Chapter 6), highlighting the use of the relative-pose optimisation module.	103
B.1	Position of the centre of gravity of the RM in spherical coordinates, with θ_1^{RM} the azimuth, θ_2^{RM} the polar angle and L^{RM} the distance to the centre of gravity of the UAV, including a detail plot of each of the signals and highlighting the envelope of these state variables.	110
B.2	Aerodynamic forces and torques during the numerical validation according to the model in Section 3.2.	110
B.3	Comparison between the modified solution (darker colours) and the standard command-filtered backstepping one (lighter colours) in terms of UAV tracking, where their respective references are denoted with black lines.	111
B.4	Attitude, attitude rate and rotor speed errors for both the unmodified backstepping and the proposed modification, where each component is identified using colours increasing from blue to gray (i.e. roll error corresponds to the first component, in blue, while the error of the last rotor is its fourth component, accordingly gray).	111

List of Tables

3.1	Simulated multi-rotor parameters, corresponding to the AMUSE platform used in the early stages of the AEROARMS project [119].	26
3.2	Parameters of the final blunt-body aerodynamics model for the platform (see Table 3.1).	26
3.3	Comparison between the CAC model and the proposed solution for the whole spectrum of variables, i.e. $\alpha_r, \beta, V_\infty$, highlighting the significant improvements achieved.	30
4.1	Control gains of the benchmark application.	41
5.1	Control gains of the modified benchmark application.	50
6.1	Aerial manipulator model parameters for the benchmark application.	70
6.2	Control parameters of the proposed solution.	70
6.3	Integral backstepping control gains.	72
6.4	Comparison between the EE tracking of the proposed strategy and of an Integral Backstepping + CLIK decentralised solution without UAV-RM interconnection for similar rise times.	72
7.1	Comparison between MAS_{PX4}^\oplus and alternative autonomous outdoor autopilots tested in flight.	78
7.2	UDP connection analysis for data packages of 25 MB.	83
7.3	Parameters of the planar RM, where compound joints indexes are omitted due to repetition.	90
8.1	List of contributions per core publication, as displayed in the chapters/appendices of this thesis.	95
A.1	Control gains of the benchmark application.	102

List of Propositions

4.1	Proposition: Stability of the flexible manipulation system using the proposed adaptive position controller	39
5.1	Proposition: Stability of the flexible manipulation system under contact conditions using the proposed adaptive force controller	49
6.1	Proposition: Stability analysis of the aerial manipulation system using the modified IDA-PBC formulation with a dynamic extension to compensate the lack of perfect RM tracking	62
6.2	Proposition: Stability analysis of the closed-loop manipulation task of the aerial manipulator using the iCLIK controller	66
6.3	Proposition: Stability analysis of the whole aerial manipulation system during all the phases of the design mission in Section 2.2	68
B.1	Proposition: Formulation of the standard command-filtered backstepping	106
B.2	Proposition: Redesign of the command-filtered backstepping to improve the rejection capabilities against manipulation disturbances	108

Bibliography

- [1] European Commission. (2019, May) Unmanned aircraft in the European Union. [Online]. Available: https://ec.europa.eu/growth/sectors/aeronautics/rpas_en
- [2] A. Ollero and B. Siciliano, Eds., *Aerial Robotic Manipulation*, 1st ed., ser. Springer Tracts in Advanced Robotics. Springer International Publishing, 2019, vol. 129.
- [3] F. Ruggiero, V. Lippiello, and A. Ollero, “Aerial manipulation: A literature review,” *IEEE Robotics and Automation Letters*, vol. 3, no. 3, pp. 1957–1964, July 2018.
- [4] H. B. Khamseh, F. Janabi-Sharifi, and A. Abdessameud, “Aerial manipulation—a literature survey,” *Robotics and Autonomous Systems*, vol. 107, pp. 221–235, September 2018.
- [5] Flying-Cam. (2020, December) Flying-Cam Sarah. [Online]. Available: <https://wp.flying-cam.com/>
- [6] Amazon. (2020, December) Amazon Prime Air. [Online]. Available: <https://www.amazon.com/Amazon-Prime-Air/b?ie=UTF8&node=8037720011>
- [7] Alphabet. (2020, December) Alphabet Wing. [Online]. Available: <https://wing.com/>
- [8] J.-P. Aurambout, K. Gkoumas, and B. Ciuffo, “Last mile delivery by drones: An estimation of viable market potential and access to citizens across European cities,” *European Transport Research Review*, vol. 11, no. 1, p. 30, June 2019.
- [9] B. de Miguel Molina and M. S. Oña, “The drone sector in Europe,” in *Ethics and civil drones*. Springer, Cham, 2018, pp. 7–33.
- [10] Federal Aviation Administration. (2020, December) UAS by numbers in the United States of America. [Online]. Available: https://www.faa.gov/uas/resources/by_the_numbers/
- [11] Aviation Week Network. (2015, September) FAA Nightmare: A Million Christmas Drones. [Online]. Available: <https://aviationweek.com/air-transport/faa-nightmare-million-christmas-drones>
- [12] “AEROARMS project: Aerial RObotic system integrating multiple ARMS and advanced manipulation capabilities for inspection and maintenance,” Available: <http://www.aeroarms-project.eu/>, European Commission under the H2020 Framework Programme.
- [13] “AERIAL-CORE: AERIAL COgnitive integrated multi-task Robotic system with Extended operation range and safety,” Available: <https://www.aerial-core.eu>, European Commission under the H2020 Framework Programme.

- [14] “AEROBI: Aerial Robotic System for In-Depth Bridge Inspection by Contact,” Available: <https://www.aerobi.eu/>, European Commission under the H2020 Framework Programme.
- [15] “ARCOW: Aerial Robot CO-Worker in Plant Servicing, within the European Robotics Challenges (EUROC),” Available: <http://aicia.es/proyectos2015/aeronautical/4-arcow.html>, European Commission under the FP7 Programme.
- [16] “ACROSS: Advanced Cockpit for Reduction Of StreSs and workload,” Available: <https://cordis.europa.eu/project/id/314501>, European Commission under the FP7 Programme.
- [17] “AEROWORKS project: Collaborative Aerial Robotic Workers,” Available: <http://www.aeroworks2020.eu/>, European Commission under the H2020 Framework Programme.
- [18] I. Maza, F. Caballero, J. Capitán, J. R. M. de Dios, and A. Ollero, “A distributed architecture for a robotic platform with aerial sensor transportation and self-deployment capabilities,” *Journal of Field Robotics*, vol. 28, no. 3, pp. 303–328, May 2011.
- [19] B. Shirani, M. Najafi, and I. Izadi, “Cooperative load transportation using multiple UAVs,” *Aerospace Science and Technology*, vol. 84, pp. 158 – 169, October 2019.
- [20] M. Bernard, K. Kondak, I. Maza, and A. Ollero, “Autonomous transportation and deployment with aerial robots for search and rescue missions,” *Journal of Field Robotics*, vol. 28, no. 6, pp. 914–931, October 2011.
- [21] I. Maza, J. Kondak, M. Bernard, and A. Ollero, “Multi-UAV cooperation and control for load transportation and deployment,” *Journal of Intelligent and Robotics Systems*, vol. 57, no. 1, pp. 417–449, August 2010.
- [22] A. Jiménez-Cano, J. Martín, G. Heredia, R. Cano, and A. Ollero, “Control of an aerial robot with multi-link arm for assembly tasks,” in *2013 IEEE International Conference on Robotics and Automation (ICRA)*, Karlsruhe, Germany, 2013, pp. 4916–4921.
- [23] R. Cano, C. Pérez, F. Pruano, A. Ollero, and G. Heredia, “Mechanical design of a 6-DOF aerial manipulator for assembling bar structures using UAVs,” in *2013 Workshop on Research, Education and Development of Unmanned Aerial Systems (RED-UAS)*, vol. 218, Compiègne, France, 2013.
- [24] A. Albers, S. Trautmann, T. Howard, Trong Anh Nguyen, M. Frietsch, and C. Sauter, “Semi-autonomous flying robot for physical interaction with environment,” in *2010 IEEE Conference on Robotics, Automation and Mechatronics (RAM)*, Singapore, Singapore, 2010, pp. 441–446.
- [25] C. Korpela, T. Danko, and P. Oh, “MM-UAV: Mobile manipulating unmanned aerial vehicle,” *Journal of Intelligent and Robotics Systems*, vol. 65, no. 1, pp. 93–101, January 2012.
- [26] V. Ghadiok, J. Goldin, and W. Ren, “Autonomous indoor aerial gripping using a quadrotor,” in *IEEE/RSJ International Conference on Intelligent Robots and Systems (IROS)*, San Francisco, CA, USA, December 2011, pp. 4645–4651.
- [27] P. Pounds, D. Bersak, and A. Dollar, “Grasping from the air: Hovering capture and load stability,” in *IEEE International Conference on Robotics and Automation (ICRA)*, Shanghai, China, 2011, pp. 2491–2498.
- [28] A. Suarez, G. Heredia, and A. Ollero, “Lightweight compliant arm for aerial manipulation,” in *2015 IEEE/RSJ International Conference on Intelligent Robots and Systems (IROS)*, Hamburg, Germany, Sep. 2015, pp. 1627–1632.

- [29] A. Suarez, P. R. Soria, G. Heredia, B. C. Arrue, and A. Ollero, "Anthropomorphic, compliant and lightweight dual arm system for aerial manipulation," in *2017 IEEE/RSJ International Conference on Intelligent Robots and Systems (IROS)*, Vancouver, BC, Canada, Sep. 2017, pp. 992–997.
- [30] A. Suarez, A. E. Jimenez-Cano, V. M. Vega, G. Heredia, A. Rodriguez-Castaño, and A. Ollero, "Design of a lightweight dual arm system for aerial manipulation," *Mechatronics*, vol. 50, pp. 30–44, April 2018.
- [31] M. Orsag, C. Korpela, S. Bogdan, and P. Oh, "Lyapunov based Model Reference Adaptive Control for Aerial Manipulation," in *2013 International Conference on Unmanned Aircraft Systems (ICUAS)*, Atlanta, GA, USA, 2013, pp. 966–973.
- [32] M. Kolivarov, "Nonlinear trajectory control of multi-body aerial manipulators," *Journal of Intelligent & Robotic Systems*, vol. 73, no. 1-4, pp. 679–692, January 2014.
- [33] F. Ruggiero, M. A. Trujillo, R. Cano, H. Ascorbe, A. Viguria, C. Pérez, V. Lippiello, A. Ollero, and B. Siciliano, "A multilayer control for multirotor UAVs equipped with a servo robot arm," in *2015 IEEE International Conference on Robotics and Automation (ICRA)*, Seattle, WA, USA, May 2015, pp. 4014–4020.
- [34] X. Li, B. Zhao, Y. Yao, H. Wu, and Y. Liu, "Stability and performance analysis of six-rotor unmanned aerial vehicles in wind disturbance," *Journal of Computational and Nonlinear Dynamics*, vol. 13, no. 3, March 2018.
- [35] P. Sanchez-Cuevas, G. Heredia, and A. Ollero, "Characterization of the aerodynamic ground effect and its influence in multirotor control," *International Journal of Aerospace Engineering*, vol. 2017, 2017.
- [36] P. J. Sanchez-Cuevas, "Modelling and Control of Aerial Manipulators considering Aerodynamic Effects," Ph.D. dissertation, Universidad de Sevilla, Seville, Spain, 2021.
- [37] S. Kim, S. Choi, and H. J. Kim, "Aerial manipulation using a quadrotor with a two DOF robotic arm," in *2013 IEEE/RSJ International Conference on Intelligent Robots and Systems (IROS)*, Tokyo, Japan, 2013, pp. 4990–4995.
- [38] H. Yang and D. Lee, "Dynamics and Control of Quadrotor with Robotic Manipulator," in *2014 IEEE International Conference on Robotics and Automation (ICRA)*, Hong Kong, China, 2014, pp. 5544–5549.
- [39] B. Yang, Y. He, J. Han, and G. Liu, "Rotor-flying manipulator: modeling, analysis, and control," *Mathematical Problems in Engineering*, vol. 2014, May 2014.
- [40] G. Heredia, A. Jiménez-Cano, M. I. Sánchez, D. Llorente, V. Vega, J. Braga, J. A. Acosta, and A. Ollero, "Control of a multirotor outdoor aerial manipulator," in *2014 IEEE/RSJ International Conference on Intelligent Robots and Systems (IROS)*, Chicago, IL, USA, 2014, pp. 3417–3422.
- [41] A. Y. Mersha, S. Stramigioli, and R. Carloni, "Exploiting the dynamics of a robotic manipulator for control of UAVs," in *2014 IEEE International Conference on Robotics and Automation (ICRA)*, Hong Kong, China, 2014, pp. 1741–1746.
- [42] M. Orsag, C. M. Korpela, S. Bogdan, and P. Y. Oh, "Hybrid adaptive control for aerial manipulation," *Journal of intelligent & robotic systems*, vol. 73, no. 1-4, pp. 693–707, January 2014.
- [43] G. Arleo, F. Caccavale, G. Muscio, and F. Pierri, "Control of quadrotor aerial vehicles equipped with a robotic arm," in *2013 IEEE Mediterranean Conference on Control and Automation*, Chania, Greece, 2013, pp. 1174–1180.

- [44] E. Cataldi, G. Muscio, M. A. Trujillo, Y. Rodriguez, F. Pierri, G. Antonelli, F. Caccavale, A. Viguria, S. Chiaverini, and A. Ollero, "Impedance Control of an aerial-manipulator: Preliminary results," in *2016 IEEE/RSJ International Conference on Intelligent Robots and Systems (IROS)*, Daejeon, South Korea, 2016, pp. 3848–3853.
- [45] B. Yüksel, G. Buondonno, and A. Franchi, "Differential flatness and control of protocentric aerial manipulators with any number of arms and mixed rigid-/elastic-joints," in *2016 IEEE/RSJ International Conference on Intelligent Robots and Systems (IROS)*, Daejeon, South Korea, 2016, pp. 561–566.
- [46] M. Tognon and A. Franchi, "Dynamics, control, and estimation for aerial robots tethered by cables or bars," *IEEE Transactions on Robotics*, vol. 33, no. 4, pp. 834–845, Aug 2017.
- [47] T. P. Nascimento and M. Saska, "Position and attitude control of multi-rotor aerial vehicles: A survey," *Annual Reviews in Control*, vol. 48, pp. 129–146, 2019.
- [48] M. Hua, T. Hamel, P. Morin, and C. Samson, "A control approach for thrust-propelled underactuated vehicles and its application to VTOL drones," *IEEE Trans. on Automatic Control*, vol. 54, no. 8, pp. 1837–1853, August 2009.
- [49] J. A. Farrell, M. Polycarpou, M. Sharma, and W. Dong, "Command filtered backstepping," *IEEE Transactions on Automatic Control*, vol. 54, no. 6, pp. 1391–1395, June 2009.
- [50] Y. Wang, W. Chen, S. Zhang, and W. Zhu, "Command-filtered incremental backstepping controller for small unmanned aerial vehicles," *Journal of Guidance, Control, and Dynamics*, no. 4, pp. 952–965, April 2018.
- [51] X. Wang, S. Sun, E. van Kampen, and Q. Chu, "Quadrotor Fault Tolerant Incremental Sliding Mode Control driven by Sliding Mode Disturbance Observers," *Aerospace Science and Technology*, vol. 87, pp. 417 – 430, April 2019.
- [52] R. Miranda-Colorado, L. T. Aguilar, and J. E. Herrero-Brito, "Reduction of power consumption on quadrotor vehicles via trajectory design and a controller-gains tuning stage," *Aerospace Science and Technology*, vol. 78, pp. 280 – 296, July 2018.
- [53] M. Vahdanipour and M. Khodabandeh, "Adaptive fractional order sliding mode control for a quadrotor with a varying load," *Aerospace Science and Technology*, vol. 86, pp. 737 – 747, March 2019.
- [54] M. Bangura and R. Mahony, "Real-time model predictive control for quadrotors," *IFAC Proceedings Volumes*, vol. 47, no. 3, pp. 11 773–11 780, 2014.
- [55] G. V. Raffo, M. G. Ortega, and F. R. Rubio, "An integral predictive/nonlinear \mathcal{H}_∞ control structure for a quadrotor helicopter," *Automatica*, vol. 46, no. 1, pp. 29–39, January 2010.
- [56] Y. Liu, S. Rajappa, J. M. Montenbruck, P. Stegagno, H. Bühlhoff, F. Allgöwer, and A. Zell, "Robust nonlinear control approach to nontrivial maneuvers and obstacle avoidance for quadrotor UAV under disturbances," *Robotics and Autonomous Systems*, vol. 98, pp. 317–332, December 2017.
- [57] C. Liu, W.-H. Chen, and J. Andrews, "Explicit non-linear model predictive control for autonomous helicopters," *Proceedings of the Institution of Mechanical Engineers, Part G: Journal of Aerospace Engineering*, vol. 226, no. 9, pp. 1171–1182, November 2012.
- [58] B. Lindqvist, S. S. Mansouri, A. A. Agha-mohammadi, and G. Nikolakopoulos, "Nonlinear MPC for Collision Avoidance and Control of UAVs with Dynamic Obstacles," *IEEE Robotics and Automation Letters*, vol. 5, no. 4, pp. 6001–6008, July 2020.

- [59] D. Bicego, J. Mazzetto, R. Carli, M. Farina, and A. Franchi, "Nonlinear model predictive control with enhanced actuator model for multi-rotor aerial vehicles with generic designs," *Journal of Intelligent & Robotic Systems*, vol. 100, no. 3, pp. 1213–1247, December 2020.
- [60] M. Neunert, C. De Crousaz, F. Furrer, M. Kamel, F. Farshidian, R. Siegwart, and J. Buchli, "Fast nonlinear model predictive control for unified trajectory optimization and tracking," in *2016 IEEE International Conference on Robotics and Automation (ICRA)*, Stockholm, Sweden, 2016, pp. 1398–1404.
- [61] T. Lee, M. Leok, and N. H. McClamroch, "Geometric tracking control of a quadrotor UAV on SE(3)," in *IEEE Conference on Decision and Control (CDC)*, Atlanta, GA, USA, 2010, pp. 5420–5425.
- [62] F. Oliva-Palomo, A. Sanchez-Orta, P. Castillo, and H. Alazki, "Nonlinear ellipsoid based attitude control for aggressive trajectories in a quadrotor: Closed-loop multi-flips implementation," *Control Engineering Practice*, vol. 77, pp. 150–161, August 2018.
- [63] N. Raj, R. N. Banavar, M. Kothari, *et al.*, "Attitude tracking control for aerobatic helicopters: A geometric approach," in *2017 IEEE Conference on Decision and Control (CDC)*, Melbourne, Australia, 2017, pp. 1951–1956.
- [64] M. Ryll, D. Bicego, and A. Franchi, "Modeling and control of FAST-Hex: A fully-actuated by synchronized-tilting hexarotor," in *2016 IEEE/RSJ International Conference on Intelligent Robots and Systems (IROS)*, Daejeon, South Korea, 2016, pp. 1689–1694.
- [65] D. Invernizzi and M. Lovera, "Geometric tracking control of a quadcopter tiltrotor UAV," *IFAC-PapersOnLine*, vol. 50, no. 1, pp. 11 565–11 570, July 2017.
- [66] H. L. N. N. Thanh, N. N. Phi, and S. K. Hong, "Simple nonlinear control of quadcopter for collision avoidance based on geometric approach in static environment," *International Journal of Advanced Robotic Systems*, vol. 15, no. 2, p. 1729881418767575, March 2018.
- [67] D. Kun and I. Hwang, "Linear matrix inequality-based nonlinear adaptive robust control of quadrotor," *Journal of Guidance, Control, and Dynamics*, vol. 39, no. 5, May 2016.
- [68] Z. Jia, J. Yu, Y. Mei, Y. Chen, Y. Shen, and X. Ai, "Integral backstepping sliding mode control for quadrotor helicopter under external uncertain disturbances," *Aerospace Science and Technology*, vol. 68, pp. 299–307, September 2017.
- [69] T. Madani and A. Benallegue, "Sliding mode observer and backstepping control for a quadrotor unmanned aerial vehicles," in *2007 IEEE American Control Conference*, New York City, NY, USA, 2007, pp. 5887–5892.
- [70] Y. Zhang, Z. Chen, X. Zhang, Q. Sun, and M. Sun, "A novel control scheme for quadrotor UAV based upon active disturbance rejection control," *Aerospace Science and Technology*, vol. 79, pp. 601–609, August 2018.
- [71] R. Mahony, S. Stramigioli, and J. Trumpf, "Vision based control of aerial robotic vehicles using the port hamiltonian framework," in *2011 IEEE Conference on Decision Control and European Control Conference (CDC-ECC)*, Orlando, FL, USA, 2011, pp. 3526–3532.
- [72] F. Ruggiero, J. Cacace, H. Sadeghian, and V. Lippiello, "Impedance control of VTOL UAVs with a momentum-based external generalized forces estimator," in *2014 IEEE International Conference on Robotics and Automation (ICRA)*, Hong Kong, China, 2014, pp. 2093–2099.
- [73] Y. E. Tlatempa-Osorio, J. J. Corona-Sánchez, and H. Rodríguez-Cortés, "Quadrotor control based on an estimator of external forces and moments," in *2016 IEEE International Conference on Unmanned Aircraft Systems (ICUAS)*, Arlington, VA, USA, 2016, pp. 957–963.

- [74] F. Gavilan, R. Vazquez, and J. Á. Acosta, "Adaptive Control for Aircraft Longitudinal Dynamics with Thrust Saturation," *Journal of Guidance, Control, and Dynamics*, vol. 38, no. 4, pp. 651–661, April 2015.
- [75] C. Fu, W. Hong, H. Lu, L. Zhang, X. Guo, and Y. Tian, "Adaptive robust backstepping attitude control for a multi-rotor unmanned aerial vehicle with time-varying output constraints," *Aerospace Science and Technology*, vol. 78, pp. 593 – 603, July 2018.
- [76] E. J. J. Smeur, Q. Chu, and G. C. H. E. de Croon, "Adaptive Incremental Nonlinear Dynamic Inversion for Attitude Control of Micro Air Vehicles," *Journal of Guidance, Control, and Dynamics*, vol. 39, no. 3, pp. 450–461, December 2016.
- [77] B. Siciliano, L. Sciavicco, L. Villani, and G. Oriolo, *Robotics. Modelling, planning and control*. Springer-Verlag (UK), 2009.
- [78] S. Chiaverini, G. Oriolo, and I. Walker, "Kinematically redundant manipulators," in *Handbook of Robotics*. Berlin Heidelberg: Springer, 2008, pp. 245–268.
- [79] H. Das, J. Slotine, and T. Sheridan, "Inverse kinematic algorithms for redundant systems," 1988 *IEEE International Conference on Robotics and Automation (ICRA)*, pp. 43–48, 1988.
- [80] P. Falco and C. Natale, "On the stability of closed-loop inverse kinematics algorithms for redundant robots," *IEEE Transactions in Robotics*, vol. 27, no. 4, pp. 780–784, August 2011.
- [81] G. Antonelli, S. Chiaverini, and G. Fusco, "A new on-line algorithm for inverse kinematics of robot manipulators ensuring path tracking capability under joint limits," *IEEE Transactions on Robotics and Automation*, vol. 19, no. 1, pp. 162–166, February 2003.
- [82] L. Sciavicco and B. Siciliano, "Coordinate transformation: A solution algorithm for one class of robots," *IEEE Transactions on Systems, Man, and Cybernetics*, vol. 16, no. 4, pp. 550–559, July 1986.
- [83] B. Siciliano, "Parallel force and position control of flexible manipulators," *IEEE Control Theory and Applications*, November 2000.
- [84] B. Siciliano and L. Villani, "An inverse kinematics algorithm for interaction control of a flexible arm with a compliant surface," *Control Engineering Practice*, vol. 9, no. 2, pp. 191–198, February 2001.
- [85] F. Caccavale, S. Chiaverini, and B. Siciliano, "Second-order kinematic control of robot manipulators with Jacobian damped least-squares inverse: Theory and experiments," *IEEE/ASME Transactions on Mechatronics*, vol. 2, no. 3, pp. 188–194, September 1997.
- [86] A. De Luca, G. Oriolo, and B. Siciliano, "Robot redundancy resolution at the acceleration level," *Laboratory Robotics and Automation*, vol. 4, no. 2, pp. 97–97, 1992.
- [87] Y. Pan, H. Wang, X. Li, and H. Yu, "Adaptive command-filtered backstepping control of robot arms with compliant actuators," *IEEE Transactions on Control Systems Technology*, vol. 26, no. 3, pp. 1149–1156, May 2018.
- [88] K. P. Tee, R. Yan, and H. Li, "Adaptive admittance control of a robot manipulator under task space constraint," in *2010 IEEE International Conference on Robotics and Automation (ICRA)*, Anchorage, AK, USA, 2010, pp. 5181–5186.
- [89] B. Siciliano and L. Villani, "Adaptive compliant control of robot manipulators," *Control Engineering Practice*, vol. 4, no. 5, pp. 705 – 712, May 1996.

- [90] R. C. Luo, Y. W. Perng, B. H. Shih, and Y. H. Tsai, "Cartesian position and force control with adaptive impedance/compliance capabilities for a humanoid robot arm," in *2013 IEEE International Conference on Robotics and Automation (ICRA)*, Karlsruhe, Germany, 2013, pp. 496–501.
- [91] I. El Makrini, C. Rodriguez-Guerrero, D. Lefeber, and B. Vanderborght, "The variable boundary layer sliding mode control: A safe and performant control for compliant joint manipulators," *IEEE Robotics and Automation Letters*, vol. 2, no. 1, pp. 187–192, January 2016.
- [92] N. Kashiri, N. G. Tsagarakis, M. Van Damme, B. Vanderborght, and D. G. Caldwell, "Enhanced physical interaction performance for compliant joint manipulators using proxy-based sliding mode control," in *2014 IEEE International Conference on Informatics in Control, Automation and Robotics (ICINCO)*, vol. 2, Vienna, Austria, 2014, pp. 175–183.
- [93] A. Suarez, G. Heredia, and A. Ollero, "Physical-virtual impedance control in ultralightweight and compliant dual-arm aerial manipulators," *IEEE Robotics and Automation Letters*, vol. 3, no. 3, pp. 2553–2560, July 2018.
- [94] F. Ficuciello, L. Villani, and B. Siciliano, "Variable impedance control of redundant manipulators for intuitive human–robot physical interaction," *IEEE Transactions on Robotics*, vol. 31, no. 4, pp. 850–863, August 2015.
- [95] A. Colomé, D. Pardo, G. Alenyà, and C. Torras, "External force estimation during compliant robot manipulation," in *2013 IEEE International Conference on Robotics and Automation (ICRA)*, Karlsruhe, Germany, 2013, pp. 3535–3540.
- [96] L. Roveda, N. Pedrocchi, F. Vicentini, and L. M. Tosatti, "An interaction controller formulation to systematically avoid force overshoots through impedance shaping method with compliant robot base," *Mechatronics*, vol. 39, pp. 42 – 53, November 2016.
- [97] A. D. Luca, A. Albu-Schaffer, S. Haddadin, and G. Hirzinger, "Collision Detection and Safe Reaction with the DLR-III Lightweight Manipulator Arm," in *2006 IEEE/RSJ International Conference on Intelligent Robots and Systems (IROS)*, Beijing, China, 2006, pp. 1623–1630.
- [98] A. Suarez, A. M. Giordano, K. Kondak, G. Heredia, and A. Ollero, "Flexible link long reach manipulator with lightweight dual arm: Soft-collision detection, reaction, and obstacle localization," in *2018 IEEE International Conference on Soft Robotics (RoboSoft)*, Livorno, Italy, 2018, pp. 406–411.
- [99] J. Acosta, M. I. Sánchez, and A. Ollero, "Robust Control of Underactuated Aerial Manipulators via IDA-PBC," in *2014 IEEE Annual Conference on Decision and Control (CDC)*, Los Angeles, California, USA, 2014, pp. 673–678.
- [100] J. G. Romero and H. Rodríguez-Cortés, "Asymptotic stability for a transformed nonlinear UAV model with a suspended load via energy shaping," *European Journal of Control*, vol. 52, pp. 87 – 96, March 2020.
- [101] H. Abaunza, P. Castillo, A. Victorino, and R. Lozano, "Dual quaternion modeling and control of a quad-rotor aerial manipulator," *Journal of Intelligent & Robotic Systems*, vol. 88, no. 2-4, pp. 267–283, December 2017.
- [102] M. F. Ballesteros-Escamilla, D. Cruz-Ortiz, I. Chairez, and A. Luviano-Juárez, "Adaptive output control of a mobile manipulator hanging from a quadcopter unmanned vehicle," *ISA Transactions*, vol. 94, pp. 200–217, November 2019.
- [103] D. Bazylev, A. Kremlev, A. Margun, and K. Zimenko, "Design of control system for a four-rotor UAV equipped with robotic arm," in *2015 IEEE International Congress on Ultra Modern Telecommunications and Control Systems and Workshops (ICUMT)*, Brno, Czech Republic, 2015, pp. 144–149.

- [104] S. Di Lucia, G. D. Tipaldi, and W. Burgard, "Attitude stabilization control of an aerial manipulator using a quaternion-based backstepping approach," in *2015 IEEE European Conference on Mobile Robots (ECMR)*, Lincoln, UK, 2015, pp. 1–6.
- [105] A. Khalifa, M. Fanni, A. Ramadan, and A. Abo-Ismael, "Adaptive intelligent controller design for a new quadrotor manipulation system," in *2013 IEEE International Conference on Systems, Man, and Cybernetics*, Manchester, UK, 2013, pp. 1666–1671.
- [106] H. Rastgoftar and E. M. Atkins, "Cooperative aerial lift and manipulation (CALM)," *Aerospace Science and Technology*, vol. 82 - 83, pp. 105 – 118, November 2018.
- [107] F. White, *Fluid Mechanics*, 7th ed., ser. McGraw-Hill series in mechanical engineering. McGraw Hill, 2011.
- [108] J. Seddon, *Basic Helicopter Aerodynamics*, 1st ed., ser. AIAA education series. American Institute of Aeronautics and Astronautics, 1990.
- [109] E. Buckingham, "The principle of similitude," *Nature*, vol. 96, no. 2046, pp. 396–397, December 1915.
- [110] R. Malki, A. J. Williams, T. N. Croft, M. Togneri, and I. Masters, "A coupled blade element momentum–Computational fluid dynamics model for evaluating tidal stream turbine performance," *Applied Mathematical Modelling*, vol. 37, no. 5, pp. 3006–3020, March 2013.
- [111] I. Masters, R. Malki, A. J. Williams, and T. N. Croft, "The influence of flow acceleration on tidal stream turbine wake dynamics: A numerical study using a coupled BEM–CFD model," *Applied Mathematical Modelling*, vol. 37, no. 16, pp. 7905–7918, September 2013.
- [112] C. R. de Cos, "Modelo de la Aerodinámica Estacionaria de un Quadrotor mediante CFD," MSc Thesis, Escuela Técnica Superior de Ingeniería, Universidad de Sevilla, Seville, Spain, 2015.
- [113] H. Glauert, *Airplane Propellers*. Berlin, Heidelberg: Springer Berlin Heidelberg, 1935, pp. 169–360.
- [114] A. R. S. Bramwell, G. T. S. Done, G. Done, and D. Balmford, *Bramwell's Helicopter Dynamics*. American Institute of Aeronautics and Astronautics, 2001.
- [115] S. Neumark, *Solution of Cubic and Quartic Equations*, ser. Commonwealth and international library of science, technology, engineering and liberal studies. Pergamon Press, 1965.
- [116] W. Johnson, *Helicopter Theory*, ser. Dover Books on Aeronautical Engineering. Dover Publications, 2012.
- [117] G. J. Leishman, *Principles of Helicopter Aerodynamics with CD Extra*, ser. Cambridge aerospace series. Cambridge University Press, 2006.
- [118] MathWorks®. (2020, December) MATLAB Curve Fitting app. [Online]. Available: <https://www.mathworks.com/help/curvefit/curvefitting-app.html>
- [119] A. Ollero, G. Heredia, A. Franchi, G. Antonelli, K. Kondak, A. Sanfeliu, A. Viguria, J. R. Martinez-de Dios, F. Pierri, J. Cortes, A. Santamaria-Navarro, M. A. Trujillo Soto, R. Balachandran, J. Andrade-Cetto, and A. Rodriguez, "The AEROARMS Project: Aerial Robots with Advanced Manipulation Capabilities for Inspection and Maintenance," *IEEE Robotics & Automation Magazine*, vol. 25, no. 4, pp. 12–23, December 2018.
- [120] G. Hoffmann, H. Huang, S. Waslander, and C. Tomlin, "Precision flight control for a multi-vehicle quadrotor helicopter testbed," *Control engineering practice*, vol. 19, no. 9, pp. 1023–1036, September 2011.

- [121] W. Dong, G. Gu, X. Zhu, and H. Ding, "Modeling and control of a quadrotor UAV with aerodynamic concepts," *World Academy of Science, Engineering and Technology (WASET)*, vol. 7, no. 5, 2013.
- [122] M. De Simone, S. Russo, and A. Ruggiero, "Influence of aerodynamics on quadrotor dynamics," *Recent Researches in Mechanical and Transportation Systems Influence*, pp. 111–118, 2015.
- [123] X. Zhang, X. Li, K. Wang, and Y. Lu, "A survey of modelling and identification of quadrotor robot," in *Abstract and Applied Analysis*, vol. 2014. Hindawi, 2014.
- [124] N. K. Tran, E. Bulka, and M. Nahon, "Quadrotor control in a wind field," in *2015 IEEE International Conference on Unmanned Aircraft Systems (ICUAS)*, Denver, CO, USA, 2015, pp. 320–328.
- [125] R. Brown and K. H.W., "A comparison of coaxial and conventional rotor performance," *Journal of the American Helicopter Society*, vol. 55, no. 1, January 2010.
- [126] P. Ioannou and J. Sun, *Robust Adaptive Control*, ser. Dover Books on Electrical Engineering Series. Dover Publications, Incorporated, 2012. [Online]. Available: https://books.google.es/books?id=pXWfy_vbg1MC
- [127] M. I. Sánchez, J. Acosta, and A. Ollero, "Integral action in first-order Closed-Loop Inverse Kinematics. Application to aerial manipulators," in *2015 IEEE International Conference on Robotics and Automation (ICRA)*, Seattle, WA, USA, 2015, pp. 5297–5302.
- [128] R. Ortega and M. W. Spong, "Stabilization of underactuated mechanical systems via interconnection and damping assignment," *IFAC Proceedings Volumes*, vol. 33, no. 2, pp. 69–74, March 2000.
- [129] J. Acosta, R. Ortega, A. Astolfi, and A. M. Mahindrakar, "Interconnection and damping assignment passivity-based control of mechanical systems with underactuation degree one," *IEEE Transactions on Automatic Control*, vol. 50, no. 12, pp. 1936–1955, December 2005.
- [130] G. Viola, R. Ortega, R. Banavar, J. Acosta, and A. Astolfi, "Total Energy Shaping Control of Mechanical Systems: Simplifying the Matching Equations Via Coordinate Changes," *IEEE Transactions on Automatic Control*, vol. 52, no. 6, pp. 1093–1099, June 2007.
- [131] M. Paz and W. Leigh, *Integrated Matrix Analysis of Structures. Theory and Computation*. Springer US, 2001.
- [132] F. Flacco, A. De Luca, and O. Khatib, "Motion Control of Redundant Robots under Joint Constraints: Saturation in the Null Space," in *2012 IEEE International Conference on Robotics and Automation (ICRA)*, Saint Paul, MN, USA, 2012.
- [133] A. G. Davenport, "The spectrum of horizontal gustiness near the ground in high winds," *Quarterly Journal of the Royal Meteorological Society*, vol. 87, no. 372, pp. 194–211, April 1961.
- [134] M. Jafarinasab, S. Sirouspour, and E. Dyer, "Model-Based Motion Control of a Robotic Manipulator With a Flying Multirotor Base," *IEEE/ASME Transactions on Mechatronics*, vol. 24, no. 5, pp. 2328–2340, August 2019.
- [135] Y. S. Lee, B. Jo, and S. Han, "A light-weight rapid control prototyping system based on open source hardware," *IEEE Access*, vol. 5, pp. 11 118–11 130, June 2017.
- [136] D. Hercog and K. Jezernik, "Rapid control prototyping using MATLAB/Simulink and a DSP-based motor controller," *International Journal of Engineering Education*, vol. 21, no. 4, p. 596, 2005.

- [137] R. Grepl, "Real-Time Control Prototyping in MATLAB/Simulink: Review of tools for research and education in mechatronics," in *2011 IEEE International Conference on Mechatronics*, Istanbul, Turkey, 2011, pp. 881–886.
- [138] S. Rebeschief, "MIRCOS-microcontroller-based real time control system toolbox for use with MATLAB/Simulink," in *1999 IEEE International Symposium on Computer Aided Control System Design*, Kohala Coast, HI, USA, 1999, pp. 267–272.
- [139] R. Bucher and S. Balemi, "Rapid controller prototyping with MATLAB/Simulink and Linux," *Control Engineering Practice*, vol. 14, no. 2, pp. 185–192, February 2006.
- [140] G. Skiba, T. Zabinski, and A. Bozek, "Rapid control prototyping with Scilab/Scicos/RTAI for PC-based ARM-based platforms," in *2008 IEEE International Multiconference on Computer Science and Information Technology*, Wisia, Poland, 2008, pp. 739–744.
- [141] Y. S. Lee, J. H. Yang, S. Y. Kim, W. S. Kim, and O. K. Kwon, "Development of a rapid control prototyping system based on MATLAB and USB DAQ boards," *Journal of Institute of Control, Robotics and Systems*, vol. 18, no. 10, pp. 912–920, October 2012.
- [142] A. Koubaa, A. Allouch, M. Alajlan, Y. Javed, A. Belghith, and M. Khalgui, "Micro air vehicle link (MAVlink) in a nutshell: A survey," *IEEE Access*, vol. 7, pp. 87 658–87 680, June 2019.
- [143] MathWorks®. (2019, May) Simulink. [Online]. Available: <https://www.mathworks.com/products/simulink.html>
- [144] MathWorks®. (2020, November) Simulink Reference. [Online]. Available: https://www.mathworks.com/help/pdf_doc/simulink/simulink_ref.pdf
- [145] MathWorks®. (2020, November) Improving Simulation Performance in Simulink. [Online]. Available: <https://es.mathworks.com/company/newsletters/articles/improving-simulation-performance-in-simulink.html>
- [146] MathWorks®. (2020, November) How Acceleration Modes Work. [Online]. Available: <https://www.mathworks.com/help/simulink/ug/how-the-acceleration-modes-work.html>
- [147] MathWorks®. (2020, November) Choosing a Simulation Mode. [Online]. Available: <https://www.mathworks.com/help/simulink/ug/choosing-a-simulation-mode.html>
- [148] Intel®. (2019, May) Intel® Compute Card. [Online]. Available: <https://www.intel.com/content/www/us/en/products/boards-kits/compute-card>
- [149] KHADAS®. (2019, May) KHADAS® Vim Boards. [Online]. Available: <https://www.khadas.com/vim>
- [150] L. Meier, D. Honegger, and M. Pollefeys, "PX4: A node-based multithreaded open source robotics framework for deeply embedded platforms," in *2015 IEEE International Conference on Robotics and Automation (ICRA)*, Seattle, WA, USA, May 2015, pp. 6235–6240.
- [151] Dronecode®. (2020, May) Dronecode® Project. [Online]. Available: <https://www.dronecode.org/>
- [152] L. Sha, "Using simplicity to control complexity," *IEEE Software*, vol. 18, no. 4, pp. 20–28, 2001.
- [153] Raspberry®. (2019, May) Raspberry® Pi 3 Model B. [Online]. Available: <https://www.raspberrypi.org/>
- [154] Emlid®. (2019, June) NAVIO2. [Online]. Available: <https://emlid.com/navio/>

- [155] Intel®. (2019, June) NUC Boards and Kits. [Online]. Available: <https://www.intel.com/content/www/us/en/products/boards-kits/nuc.html>
- [156] Dronecode®. (2019, May) Pixhawk – the hardware standard for open source autopilots. [Online]. Available: <https://pixhawk.org/>
- [157] J. Jackson, G. Ellingson, and T. McLain, “ROSflight: A lightweight, inexpensive MAV research and development tool,” in *2016 International Conference on Unmanned Aircraft Systems (ICUAS)*, Arlington, VA, USA, 2016, pp. 758–762.
- [158] A. Tirumala, L. Cottrell, and T. Dunigan, “Measuring end-to-end bandwidth with Iperf using Web100,” in *Passive and Active Monitoring Workshop*, San Diego, CA, USA, 2003.
- [159] iPerf. (2019, May) iPerf – The ultimate speed test tool for TCP, UDP and SCTP. [Online]. Available: <https://iperf.fr/>
- [160] J. Tormo-Barbero, “Diseño y control de un robot manipulador,” BSc Thesis, Escuela Técnica Superior de Ingeniería, Universidad de Sevilla, Seville, Spain, 2018.
- [161] Robotis®. (2019, April) Dynamixel Actuators. [Online]. Available: http://en.robotis.com/subindex/dxl_en.php
- [162] Murata®. (2019, April) Rotary Position Sensors. [Online]. Available: <https://www.murata.com/en-sg/products/sensor/rotaryposition/>
- [163] Vanadium Labs. (2019, January) Dynamixel Actuators. [Online]. Available: <http://www.vanadiumlabs.com/arbotix>
- [164] Arduino. (2019, January) Arduino Mega 2560 Rev3. [Online]. Available: <https://store.arduino.cc/arduino-mega-2560-rev3>

Index of terms

- Accommodation, 10, 58, 68, 72, 100
- Accuracy, 10, 26, 72
- Adaptive, 5, 12, 36, 37, 39, 46, 48
- Aerodynamic coefficient, 28
- Aerodynamics, 12, 20, 110
- Application, 2, 78
- Assumption, 17, 21, 24, 37, 39, 40, 49, 58, 66, 68, 69, 100, 106, 108
- Autopilot, 12, 78, 80

- Backstepping, 4–6, 71, 87, 106
- Backup, 80, 81
- Barbalat’s Lemma, 64
- BEMT, 23
- Blunt-body, 20

- Centralised, 3, 4
- CFD, 20, 28
- Challenge, 2, 10, 79
- Closed-loop, 39, 59, 62, 66, 106
- Comparison, 28, 70, 71, 75, 78, 81
- Compilation/interpretation, 79
- Compliance, 11, 36, 58, 100
- Compressibility, 25
- Computational load, 4, 6, 10, 12, 41, 69, 74, 78, 79, 82, 83, 85, 88
- Computer board, 40, 78, 79, 90–92
- Contact, 2, 11, 12, 36, 37, 41, 46
- Contribution, 13
- Coupling, 2, 4, 16, 20, 58, 65, 69

- Decentralised, 3, 5, 10, 12, 68
- Design, 89
- Design mission, 10, 65, 68, 73
- Differential flatness, 4
- Direct kinematics, 17, 19, 37

- Disturbance rejection, 4–6, 11, 12, 36, 37, 108, 109
- DLS, 41
- Dynamic extension, 75

- Efficiency, 112
- EKF, 80, 84
- Environmental conditions, 2, 10, 12, 64, 70, 89, 102, 110
- Estimation, 12, 61, 68
- Euler angles, 16
- Euler-Lagrange, 17–19
- Explicit, 12, 26

- Feedback linearisation, 6, 87, 106
- Finler’s Lemma, 66
- Flexible, 2, 6, 18, 36, 37, 47, 80, 90
- Force, 12, 27, 36, 37, 46, 75, 110
- Force/impedance control, 11, 12, 41, 46, 51, 91
- Fundamental Theorem of Linear Algebra, 62
- Funding, 7

- Geometric control, 5
- Grasping, 2

- Hamiltonian, 59, 60, 63
- Hurwitz, 63

- Implementation, 30, 51, 68, 79, 80, 85, 90
- Inspection and repair, 10
- Integral action, 36, 38, 106, 108
- Interpolation/extrapolation, 30
- Inverse kinematics, 4, 6, 36, 65, 71

- Jacobian, 6, 17–19, 36–38, 47

- LaSalle’s Invariance Principle, 39, 50, 64

- Lightweight, 2
Lyapunov, 39, 49, 59, 63, 66, 107, 109

Manipulation-awareness, 5, 6, 11, 12, 58
Methodology, 21, 25, 86
Model, 16, 20, 26, 27, 46, 70, 109
Modularity, 78, 80
MPC, 5
MRAC, 4

Navigation, 10, 68
Newton-Euler, 16

Obstacle, 69, 70, 74
Operation, 11, 74, 102
Optimisation, 58, 65, 68, 100

PBC, 6, 58–60
Post-processing, 26
Propulsion, 12, 16, 20, 21, 23, 32, 75, 106, 112

Recursive/iterative, 25
Redundancy, 6, 58, 65, 69, 78–81, 85
Reference frame, 16
Reliability, 83, 85
Research line, 6, 12
Robust, 5, 10, 36, 37, 40, 51, 58, 70, 75
Rotation matrix, 16

Sensitivity, 2, 5, 36, 67
Sensor, 12, 58, 89–91
Servomotor, 69, 90
Simulation, 21, 26, 70, 109
Singularity, 5, 6, 40, 50
SMC, 4–6
SNS, 69, 74
Stability, 39
Steady-state error, 39, 88, 107, 111
Stiffness, 6, 18, 36, 37
Structure, 6
Support function, 27
Symmetry, 20, 100

Task, 11, 12, 58, 59, 65
Theoretical demonstration, 4, 39, 49, 62, 66, 68, 106, 108
Time dependence, 20, 84
Torque, 12, 27, 60, 65, 68, 69, 110
Tracking, 37, 38, 41, 50, 51, 64, 66, 72, 74, 88, 89, 111
Trade-off, 28, 69, 72, 82, 101
Turbulence, 20, 24

Uncertainty, 5, 12, 39, 49, 70

Validation, 10, 41, 51, 70, 80, 85, 109